② **LEVEL** Ⅲ

ADA076941

THE FIRE ENVIRONMENT OF A SOLID ROCKET PROPELLANT BURNING IN AIR

E. W. Price, et al.

Georgia Institute of Technology
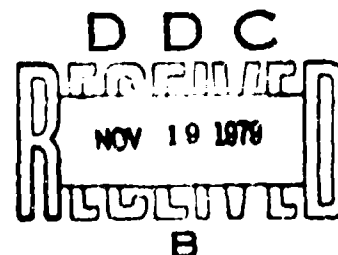Atlanta, GA 30332

March 1979

Final Report

DDC FILE COPY

D D C

NOV 19 1979

RECEIVED

B

AIR FORCE WEAPONS LABORATORY
Air Force Systems Command
Kirtland Air Force Base, NM 87117

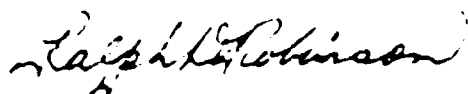79 08 20 067

Best
Available
Copy

This final report was prepared by the Georgia Institute of Technology, Atlanta, Georgia, under Contract F29601-75-C-0119, Job Order ILIR7605 with the Air Force Weapons Laboratory, Kirtland Air Force Base, New Mexico. Lieutenant Michael L. Crawford (DYV) was the Laboratory Project Officer-in-Charge.

When US Government drawings, specifications, or other data are used for any purpose other than a definitely related Government procurement operation, the Government thereby incurs no responsibility nor any obligation whatsoever, and the fact that the Government may have formulated, furnished, or in any way supplied the said drawings, specifications, or other data, is not to be regarded by implication or otherwise, as in any manner licensing the holder or any other person or corporation, or conveying any rights or permission to manufacture, use, or sell any patented invention that may in any way be related thereto.

This report has been authored by a contractor of the United States Government. Accordingly, the United States Government retains a nonexclusive, royalty-free license to publish or reproduce the material contained herein, or allow others to do so, for the United States Government purposes.
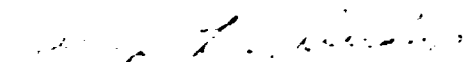
This report has been reviewed by the Office of Information (OI) and is releasable to the National Technical Information Service (NTIS). At NTIS, it will be available to the general public, including foreign nations.

This technical report has been reviewed and is approved for publication.

RALPH D. ROBINSON, GS-11
Project Officer

FOR THE COMMANDER

GEORGE L. WILLIAMS
Major, USAF
Chief, Environment and Effects Branch

THOMAS W. CIAMBRONE
Lt Colonel, USAF
Chief, Applied Physics Division

REPORT DOCUMENTATION PAGE	READ INSTRUCTIONS BEFORE COMPLETING FORM

1. REPORT NUMBER	2. GOVT ACCESSION NO.	3. RECIPIENT'S CATALOG NUMBER
AFWL-TR-78-34		

4. TITLE (and Subtitle)	5. TYPE OF REPORT & PERIOD COVERED
THE FIRE ENVIRONMENT OF A SOLID ROCKET PROPELLANT BURNING IN AIR	Final Report.
	6. PERFORMING ORG. REPORT NUMBER

7. AUTHOR(s)	8. CONTRACT OR GRANT NUMBER(s)
E. W. Price S. S. Samant J. C. Handley W. L. Mayer E. A. Powell W. C. Strahle	F29601-76-C-0119

9. PERFORMING ORGANIZATION NAME AND ADDRESS	10. PROGRAM ELEMENT, PROJECT, TASK AREA & WORK UNIT NUMBERS
Georgia Institute of Technology Atlanta, GA 30332	62601F

11. CONTROLLING OFFICE NAME AND ADDRESS	12. REPORT DATE
Air Force Weapons Laboratory (DYV) Kirtland Air Force Base, New Mexico 87117	March 79
	13. NUMBER OF PAGES
	248

14. MONITORING AGENCY NAME & ADDRESS(if different from Controlling Office)	15. SECURITY CLASS. (of this report)
	Unclassified
	15a. DECLASSIFICATION DOWNGRADING SCHEDULE

16. DISTRIBUTION STATEMENT (of this Report)

Approved for public release; distribution unlimited

17. DISTRIBUTION STATEMENT (of the abstract entered in Block 20, if different from Report)

18. SUPPLEMENTARY NOTES

19. KEY WORDS (Continue on reverse side if necessary and identify by block number)

Fire   Solid Rocket Propellant
Combustion   Launch Safety

20. ABSTRACT (Continue on reverse side if necessary and identify by block number)

A study was made of the fire environment of UTP 3001 propellant burning at atmospheric pressure in air, with particular emphasis on the conditions likely to affect objects immersed in the fire. The studies involved measurements of conditions using propellant samples with planar burning surfaces from 2 to 120 cm². Early tests indicated that deposition of condensed material was a critical factor in heat-up of immersed objects. Several methods of observation were used to determine temperatures, flow variables, nature of condensed ...

DD FORM 1473   EDITION OF 1 NOV 65 IS OBSOLETE

UNCLASSIFIED
SECURITY CLASSIFICATION OF THIS PAGE (When Data Entered)

20. ABSTRACT (Continued).

material and spatial distributions of these variables. Analyses were made of chemical equilibrium conditions, burning of aluminum droplets, and of size distribution of condensed material versus location in the flow.

TABLE OF CONTENTS

1 INTRODUCTION

1.1 General Statement of the Practical Problem

Among the hazards of large rocket launches is the possibility of a propulsion failure that leaves parts of the vehicle exposed to burning propellants. While the probability of such failures is very low, it cannot be totally discounted if the consequences are serious. Thus it is a matter of concern that some vehicle components such as radioisotope power sources would survive a propellant fire environment without release of toxic material. This imposes a rather stringent requirement, which can be met more reliably if the fire environment itself is adequately characterized. Ideally, it would be desirable to be able to calculate in advance the thermochemical and flow environment that would be encountered by an object in the fire. Because the effect of this environment on the object is also determined by properties of the object, it is also desirable to be able to run reasonably reproducible and inexpensive tests on specimens in the fire environment to screen designs and materials that are chosen to survive the fire environment.

1.2 Goal of Present Investigation

The purpose of the present investigation was to adapt, develop, and apply laboratory scale methods to characterize the fire environment of UTP 3001 propellant burning in an ambient atmosphere. Particular emphasis was placed on those aspects of the fire environment that seemed to be most important to deteriorative effects on objects immersed in the fire. To this end, the experiments included limited tests on immersed objects.

Properties of the fire environment that were assumed to be important included flow velocity, temperature, density, gas composition, and droplet size and composition (aluminum (Al) and aluminum oxide (Al_2O_3)). It was recognized that the chemical reaction zone of the propellants was localized near the propellant surface, except as modified by the long burning time of aluminum droplets in the combustion plume. Considerable emphasis was given to this latter attribute of the combustion zone because it was the least well understood factor in the fire environment, and was expected to

3

be a critical factor in effect on immersed objects. As will be seen later in the report (Section 4.3, 4.4), the state of the aluminum combustion is indeed a critical factor in immersed object response, which must be characterized in detail as a function of location in the fire. Considerable effort was devoted to this task.

1.3 Previous Information Regarding the Fire Environment

The general nature of the fire environment has been determined previously in terms of rocket motor conditions, but only for specific propellants and environments, and only in qualitative terms (References 1 through 3). This knowledge was used to forecast the nature of the present problem (below), but could not supply the quantitative data applicable to atmospheric pressure with UTP 3001 propellant.

Tests have been run on large blocks of propellant (References 4 through 6), usually to determine the deterioration of test objects in the fire

1.   Pokhil, P. F., A. F. Belyayev, Yu V. Frolov, V. S. Logachev, and A. I. Korotko, "Combustion of Powdered Metals in Active Media," *Goreniye Poroshkovbraznykh Metallov v Aktivnykh Sredakh*, 1972, (translation from U. S. Air Force Foreign Technology Division, WP-AFB, Ohio, FTD-MT-24-551-73).

2.   Price, E. W., *Combustion Instability in Rocket Motors with Aluminized Solid Propellants*, Naval Weapons Center Technical Publication 5505, June 1973.

3.   Price, E. W., "Comments on 'Role of Aluminum in Suppressing Instability in Solid Propellant Rocket Motors,'" *AIAA Journal*, Vol. 9, No. 5, May 1971, pp. 987-990.

4.   General Electric Space Division, *Final Report, Safety Test No. S-3, Solid Propellant Fire*, Document No. GEMS-414, July 1973.

5.   Snow, E. C., *Safety Test No. S-6, Launch Pad Abort Sequential Test Phase II: Solid Propellant Fire*, Los Alamos Scientific Laboratory, Los Alamos, New Mexico, LA-6034-MS, August 1975.

6.   Snow, E. C., *Solid Propellant Impact Tests*, Los Alamos Scientific Laboratory, Los Alamos, New Mexico, LA-6283-MS, March 1976

environment. While these tests obviously come closer to simulating the conditions of concern in a launch accident, tests are costly, and it is difficult to generalize the results because of the problems of making systemmatic measurements of fire conditions in large fires.

Much of the information describing the fire environment can be calculated with existing computer codes. In the case of nonaluminized propellants, these computations often provide more accurate information on gas composition and temperature than one can expect to measure--and at much lower cost. However, such computer codes are based on existence of chemical equilibrium. In the case of aluminized propellants, the slowly burning aluminum droplets prevent chemical equilibrium in much of the volume of the fine environment of interest here. As a result, the thermo-chemical equilibrium calculations are helpful in determining a picture of how compositions and temperatures go in the fire environment, but only after the spatial distribution of the aluminum combustion has been independently established by other means.

One other source of information on the fire environment is that obtained by observation of rocket exhaust plumes. The references on this subject gives some idea of radiation and Al_2O_3 product droplet size. No attempt was made to review this literature because the information was considered to be of doubtful relevance (i.e., does not simulate the interior of the atmospheric pressure combustion zone).

1.4   General Nature of the Combustion Zone

From previous studies of combustion of aluminized propellants, a reasonable advance description could be constructed, and is described here to assist in understanding the subsequent studies and results.

Because of slow aluminum combustion, the combustion zone has the macro-scopic structure shown in Figure 1. In a thin region (roughly 1-cm thick) adjoining the propellant surface, the oxidizer and polymeric binder decompose and interact. This is followed by an extended Region A, (Figure 1) in which the aluminum droplets are burning, and the gaseous products are near to equilibrium composition (i.e., equilibrium for the amount of aluminum burned at that point). Region B corresponds to a distance from

5
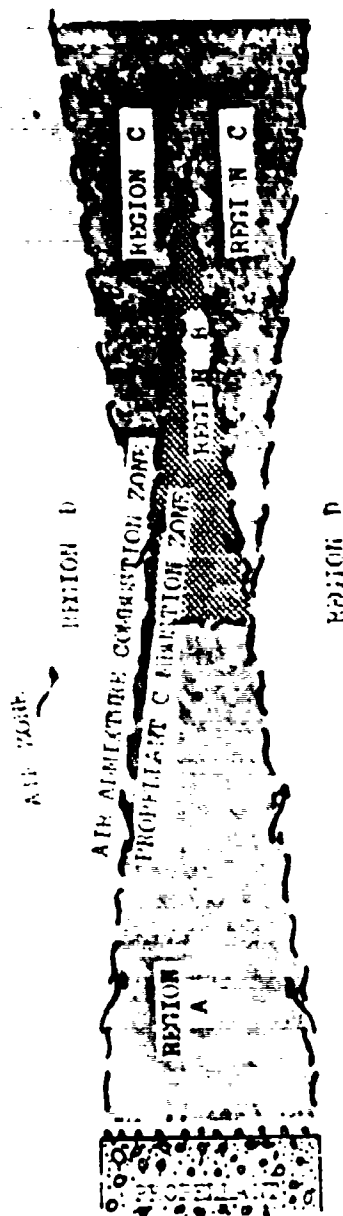
REGION A: Oxidizer and binder reacted, aluminum oxidation proceeding. Temperature roughly 2400°K, rising to about 3000°K.

REGION B: Oxidizer, binder and aluminum reacted, no air admixture. Temperature roughly 3000°K.

REGION C: Oxidizer, binder, aluminum and air in equilibrium, stoichiometric mixtures. Temperature roughly 3050°K.

REGION D: Mixing region, with unreacted aluminum present (outer boundaries uncertain, state dependent on relation of mixing rate and aluminum combustion rate).

Figure 1. General structure of the combustion plume.

the burning surface great enough so that all aluminum is burned. Along
the sides of the combustion plume there are regions where the environmental
air has mixed with propellant products. Because the propellant products
are highly fuel-rich, air admixture leads to further reaction and heat
release, concurrent with dilution and cooling with atmospheric nitrogen.

The important aspect of this macroscopic description of the combus-
tion zone is recognition of the difference in reaction rate-controlling
processes in the different regions. Near the propellant surface, the
dominant rates involve binder and oxidizer decomposition and mixing. In
Region A, the rate is limited by the aluminum droplet combustion. In
Region B, composition is constant. In Regions C and D, the rate is limited
by air mixing. The principal scale effect in going to large propellant
samples is the decreasing importance of edge effects (Regions C and D).
Region A remains the same thickness for all sample sizes that are large
enough for complete aluminum combustion before appreciable air admixture.
Determination of these sample sizes is one objective of the investigation.

The macroscopic structure of the combustion zone is substantially
determined by microscopic details, as is the nature of the two-phase flow
seen by an object immersed in the fire. Looking at the combustion sequence
on a more microscopic scale, the oxidizer and binder on the propellant sur-
face decompose to gases, while the aluminum particles (10 to 30-μm) accumu-
late and adhere to form larger agglomerate droplets up to 200 μm in diameter
and more (Figure 2). The oxidizer and binder gases mix and react near the
burning surface. The aluminum agglomerate droplets ignite, and burn briefly
on the surface (Figure 3), then move out into the gas flow. There they burn
so slowly that they produce an extended combustion zone roughly one meter in
thickness. The final product flow is roughly 30% aluminum oxide, which is
in liquid droplet form. The foregoing complex of processes is described in
Figures 3 and 4.

Figure 4 shows the course of the combustion of the aluminum droplet
cloud in more detail. Starting with a variety of agglomerates in the
20 to 200-μm-diameter range, the droplets burn by two paths that produce
distinctive product oxide droplets (Figure 2). Fine (< 2 μm) smoke

7
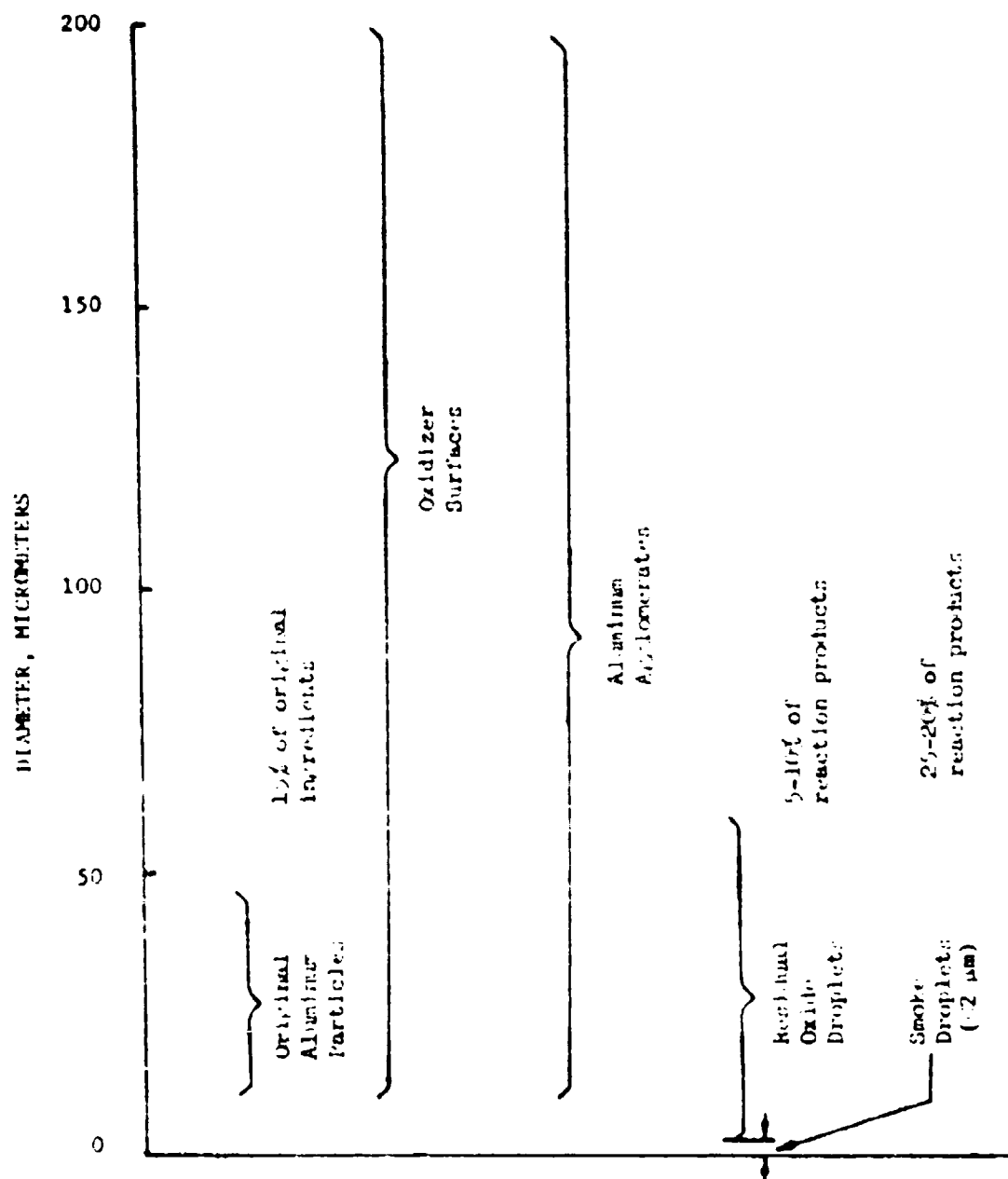
Figure 2. The size of things in the combustion zone.
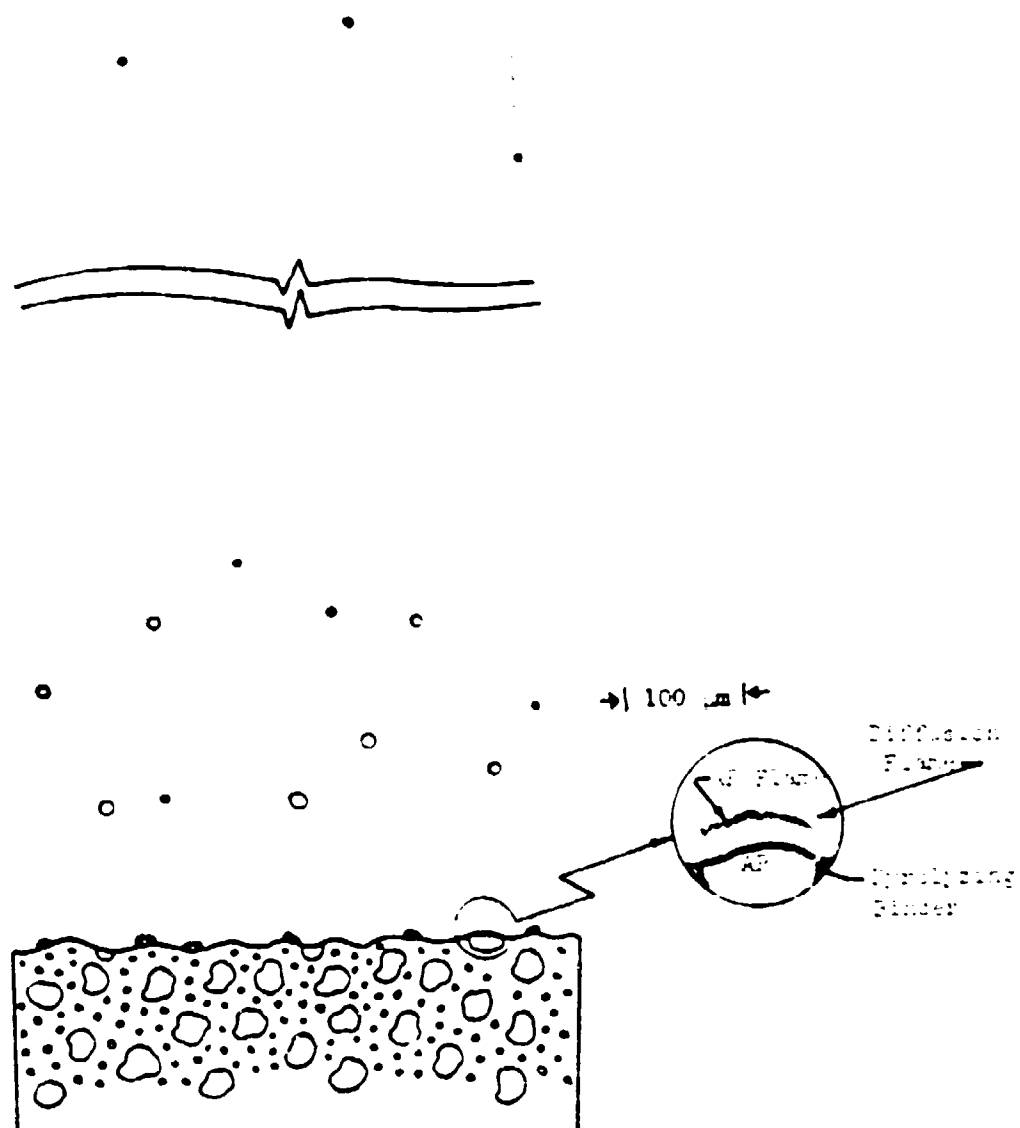
Figure 3. Details of the combustion zone.
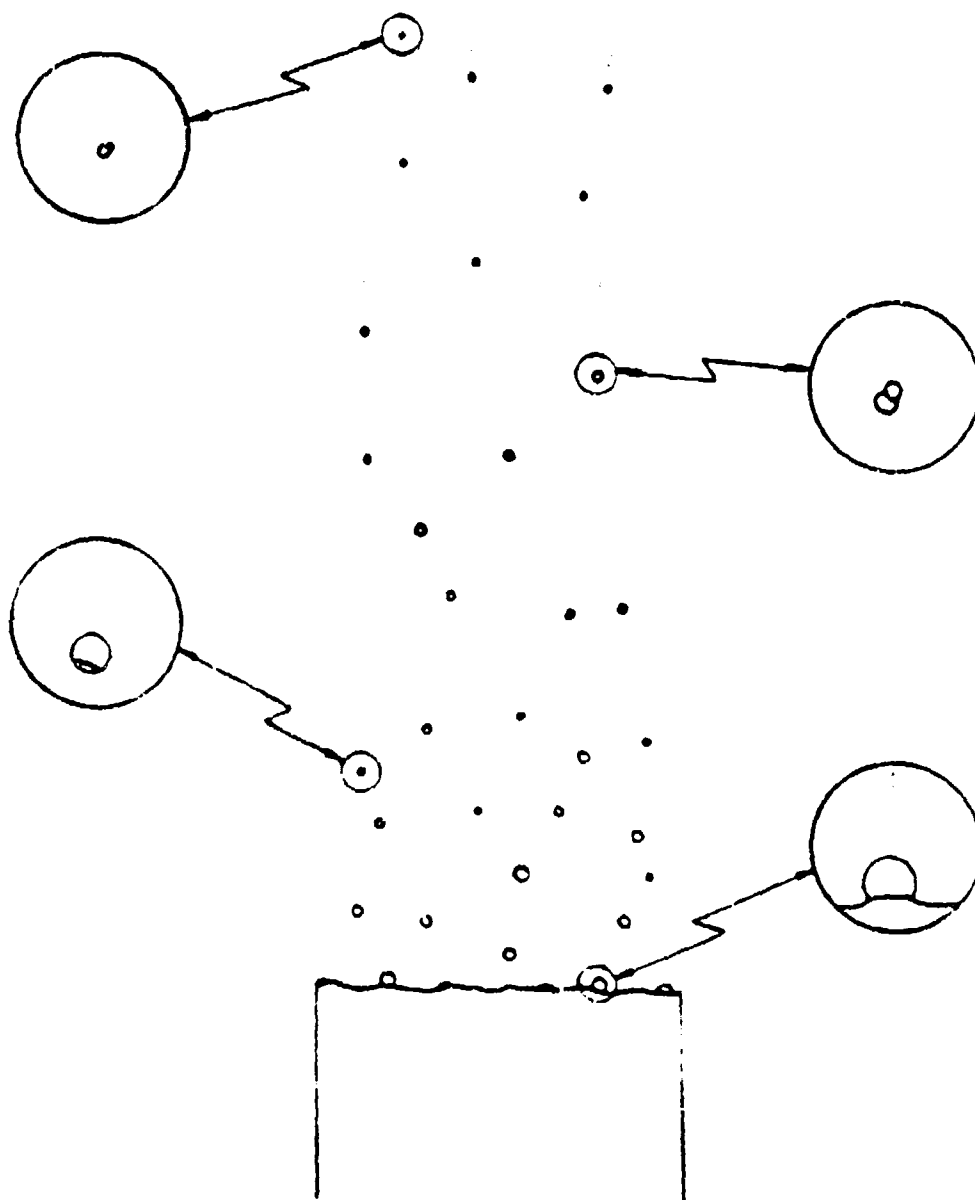
4a. General progress of agglomerate
formation and combustion in the
plume.

Figure 4. Details of aluminum combustion.

Oxide Smoke Trail

Oxide Smoke
(Flame Envelope)

Aluminium Droplet

Oxide Lobe
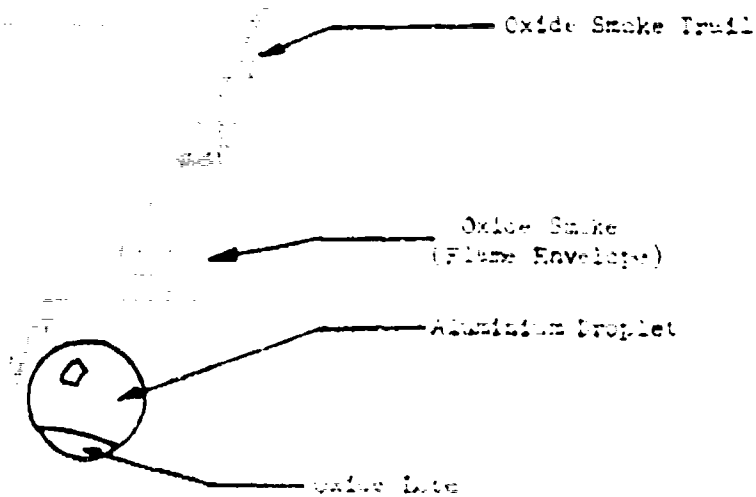
4b. Agglomerate early in burning.

Smoke Trail
(Vaporized Aluminium,
Droplets of Oxide)

Aluminium Droplet

Oxide Envelope
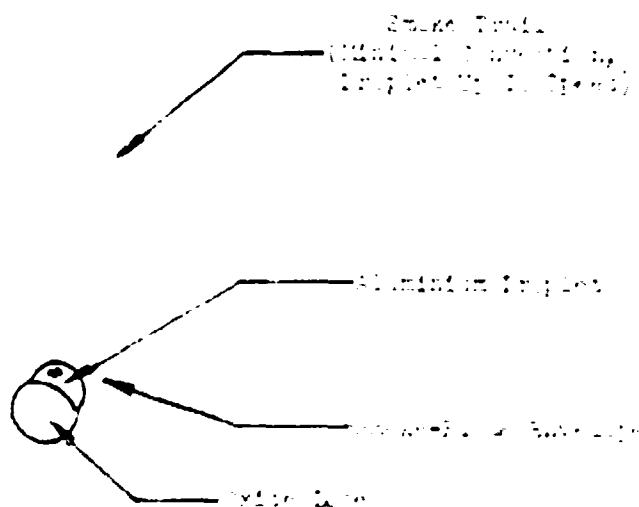
Oxide Lobe

4c. Agglomerate late in burning.

Figure 4. Details of aluminum combustion.

11

droplets are formed in a flame envelope around each aluminum droplet. Oxide also forms and accumulates on the aluminum. This in turn forms a distinctive oxide lobe that eventually becomes a residual droplet when the aluminum is consumed. Thus an increasingly dense oxide cloud develops as the burning aluminum droplets and smoke move away from the propellant surface, with the initial residual oxide consisting of relatively small droplets, and larger ones being formed later as the larger aluminum droplets burn out.

It is not entirely clear to what extent the microscopically complex, spatially nonuniform aluminum combustion field must be characterized, but the results in this report indicate that the detail is very important to the plume effect on immersed objects. This explains the consideration of detail in the foregoing, and a subsequent impact on the investigations and the approach used here in reporting results.

1.5 Strategy in Reporting Results

The structure of this report was governed by three widely different motivations:

1. Much of the work was exploratory in nature, because of the limited amount of advance information on experimental methods, or on identity of dominant mechanisms. For this reason the project work statement started with a topic entitled "Screening Studies". These are summarized early in the report for further orientation on the problem and motivation of later work.

2. The physicochemical processes involved are so complex and interactive that no simple sequential description of the investigations or their significance is possible.

3. While the objective of the investigations and this report is to describe the fire environment, this is an artificially limited goal; the line of investigation is continually oriented towards those factors controlling the effect of the fire environment on objects immersed in the fire--even to the point of preliminary observations of immersed objects.

Following this Introduction, the results of the chemical equili-
brium calculations are summarized in a way intended to show how the com-
position and temperature in the fire environment would vary (over the
Regions in Figure 1) if one knew the spatial distribution of the aluminum
combustion and air admixture. This is followed by a summary of the
Screening Studies, which include (among other things) preliminary evaluation
of the dimensions of the aluminum combustion zone. Following this, a brief
section discusses the aspects of the heat transfer to an immersed object,
with a summary of direct observations made during the investigations.
The results of these observations brought forth the weakness of the concept
of temperature during heat transfer in a two-phase reacting flow of this
kind. This led to the next section, which is a discussion of the microscopic
temperature distribution in the combustion zone. The following sections
concern radiation in the fire environment, variables concerned with flow
rates, and determination of size and composition of droplets in the com-
bustion zone. Detailed discussion of experiments and analysis are pre-
sented in the appendices.

13

2 FIRE ENVIRONMENT BASED ON CHEMICAL
EQUILIBRIUM CALCULATIONS

2.1 Applicability of the Method

Chemical equilibrium calculations have been used effectively in predicting rocket motor performance, and the method is highly perfected. In the present problem, the method is suitable for those situations where gas combustion is complete and air admixture minimal. Such calculations would give the composition, temperature, density and viscosity in Region B of Figure 1, but would provide no information about the size distribution of the Al_2O_3 droplets.

In regions where the aluminum droplets are still burning, chemical equilibrium calculations have some value because equilibrium is approximated in most of the volume--i.e., everywhere, except very near each burning aluminum droplet. This is the situation in Region A of Figure 1 where useful calculations could be made if one knew how much of the aluminum was consumed at each point in the Region. Lacking that information, the calculations can be made anyway, using percent aluminum reacted as a parameter. Such calculations help to illustrate how the aluminum ingredient contributes to gas composition and temperature, but leave the combustion zone undescribed as far as its spatial distribution is concerned, because that is determined by unknown rate processes in the aluminum droplet combustion.

Applicability of equilibrium calculations is more limited in the regions of the combustion zone where air admixture is appreciable (Regions C and D of Figure 1). Reaction rates are governed not only by molecular collision rates, but by relatively slow overall diffusion rates of air and propellant species, in addition to the slow combustion of the aluminum droplets. Further, the aluminum and its oxide product droplets do not diffuse into the air in the same way as the gaseous propellant products, posing a very complex problem. The equilibrium calculations do provide a means to explore the approximate effect of air admixture on gas composition and temperature.

18

During the project, a series of chemical equilibrium calculations were made for UTP 3001 propellant at one atmosphere. These calculations, made with the ACE computer program at the Air Force Weapons Laboratory, involved calculations using percent aluminum reacted, and percent air admixture as parameters. Results are described in the following.

2.2 Equilibrium Conditions for Adiabatic Combustion

Combustion of UTP 3001 propellant at one atmosphere leads to the product composition in Table 1.

Table 1. Composition of Reaction Products as Given by Chemical Equilibrium Calculations with the ACE Computer Program (Adiabatic Composition of UTP 3001 Propellant at One Atmosphere).

Product Specie	Mol Fraction	Weight Fraction	State
Al_2O_3	0.0748	0.3997	Liquid
H_2O	0.1123	0.1060	Gas
H_2	0.2815	0.0297	Gas
CO_2	0.0147	0.0339	Gas
CO	0.2635	0.3868	Gas
HCl	0.1207	0.2306	Gas
N_2	0.0788	0.1157	Gas

Other properties of the equilibrium products are summarized in Table 2. The results in Tables 1 and 2 are applicable to Region B in the combustion zone as described in Figure 1. This is a major part of the fire environment of a large piece of propellant, encompassing that region more than one meter or so from the burning surface, out to those regions where air admixture has become important. For a large propellant sample (e.g.,

15

Table 2. Properties of Reaction Products in Table 1.

Temperature	$2990°K$
Average molecular wt	
excluding Al_2O_3	19.082
including Al_2O_3	26.707
Density	
excluding Al_2O_3	$0.778 \times 10^{-4} g/cm^3$
including Al_2O_3	$1.088 \times 10^{-4} g/cm^3$

1 meter across the burning surface), the temperature   culated by this means is probably more accurate than can be measu   tly.

2.3 Effect of Incomplete Aluminum Combustion

Closer to the burning surface, the aluminum is not all burned. Equilibrium composition was calculated for several assumed values of percent aluminum burned, as suggested in Section 2.1. The results are shown in Figures 5 and 6, the latter showing the temperature. In these calculations, some assumptions had to be made as to the temperature of the unburned aluminum (the computer program simply ignored the unburned aluminum and corrections in temperature were made by hand calculations for Figure 6. Of the three assumed aluminum temperatures referred to in Figure 6, the value $2535°K$ is most plausible for Region A, while lower values are appropriate near the burning surface (which corresponds to near 0% aluminum reacted).

From Figure 6, it can be seen that the aluminum combustion brings the temperature in Region A up from about $2350°K$ at about 1 cm above the burning surface, to $2990°K$ at the start of Region B (Figure 1) where aluminum combustion is complete. In the process, H_2O and CO_2 are reduced to H_2 and CO, as indicated by Figure 5. Concentration of other gases in Table 1 are relatively constant. The calculations are instructive,
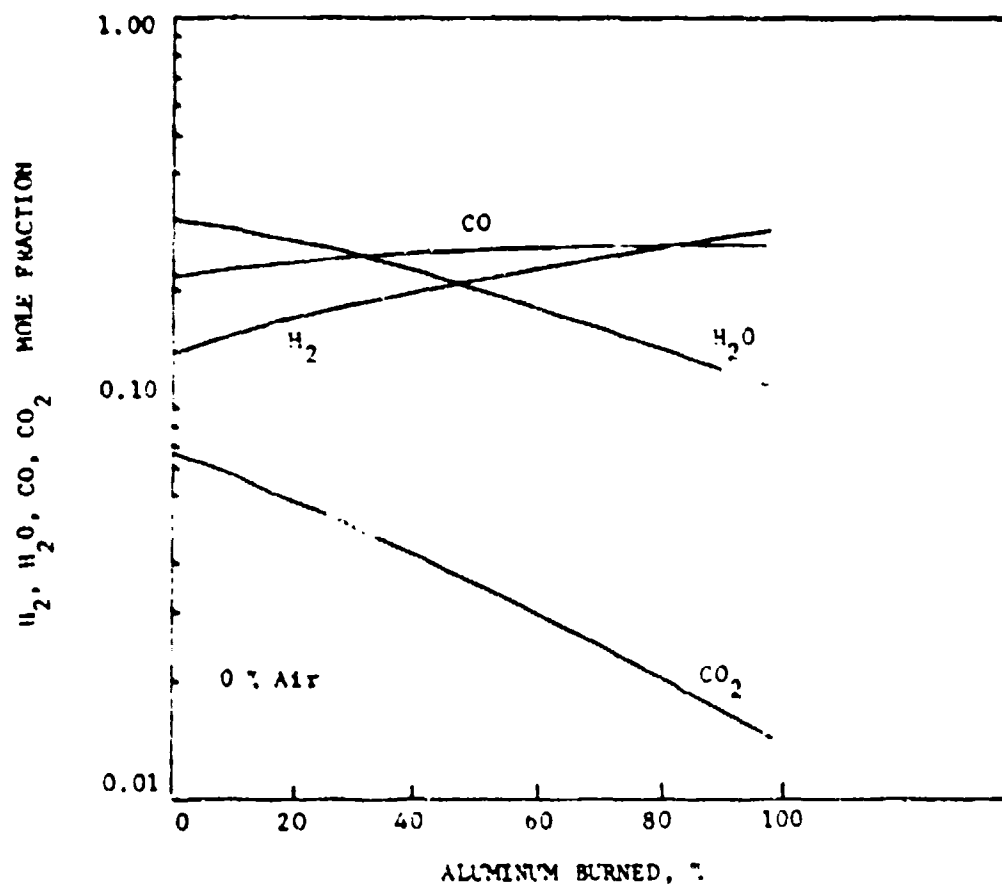
16

Figure 5. Principal effect of aluminum combustion on composition of gaseous reaction products, based on chemical equilibrium except as indicated by percent aluminum reacted.
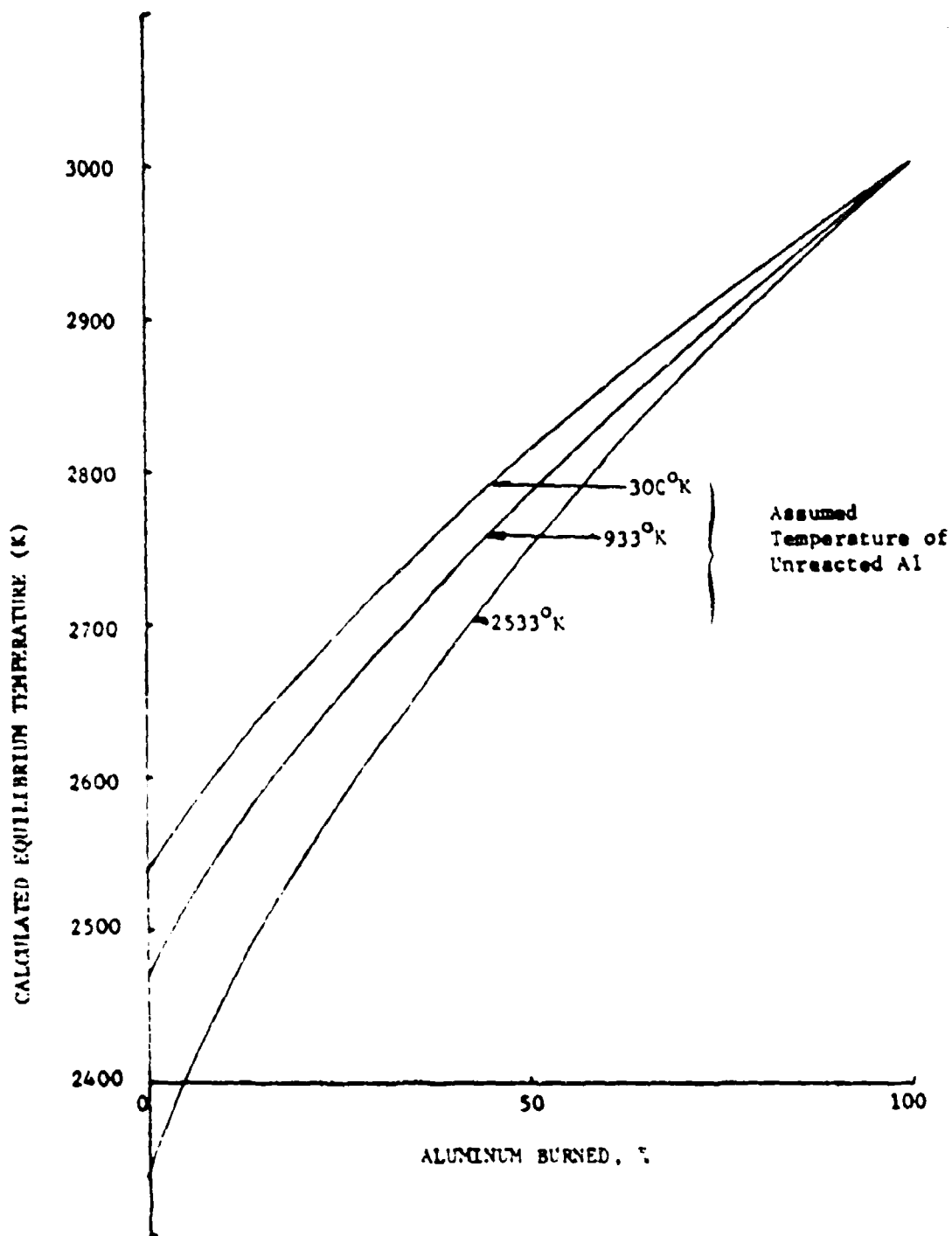
Figure 6. Calculated combustion zone temperature -- effect of percent
aluminum burned and assumed temperature of unreacted alumi-
num.

18

but tell nothing about the droplet size distributions at each point in the combustion zone (Figure 4) or the dimensions of the combustion zone. Dimensions noted above were estimated from experimental observations.

2.4 Effect of Air Admixture

As noted in Section 2.1, some estimate can be made of this effect in Regions C and D from equilibrium calculations. The primary effects of air admixture are to dilute the plume with cold nitrogen, and to oxidize the H_2 and CO back to H_2O and CO_2. The first effect cools the plume and the second heats it, so modest air admixture does not have a critical effect on temperature. Further out in the mixing region, the temperature must drop off, indicating depletion of fuel species from the plume, continued mixing with air, and a shift to lower temperatures and an oxidizing atmosphere. This trend is reflected in Figure 7, which shows how the temperature changes with percent air admixture for equilibrium composition. The different curves are for different percents of aluminum burned. The curves show the low sensitivity of temperature to air admixture up to about 50% concentration of air.

It should be stressed that the chemical equilibrium calculations are relevant and give accurate predictions in those regions of the combustion zone where the gas-phase reactions proceed much more rapidly than aluminum droplet combustion (Region A of Figure 1) or air mixing (Region D of Figure 1). In the mixing region, equilibrium between gaseous species may be approached, but it is uncertain what the state of the aluminum will be, primarily because it does not diffuse laterally with the product gases, but does react with the air-enriched mixture. In view of the uncertainty of the aluminum and aluminum oxide concentrations in the air admixture region, the equilibrium calculations serve there primarily as a means of setting limits on the uncertainty regarding temperature. This will be discussed further in the context the air-plume mixing problem in Appendix A.

Turning to the effect of air admixture on composition, the condition 0% aluminum burned was chosen to illustrate the effect of air concentration (Figure 8). This corresponds to the mixing region immediately above the
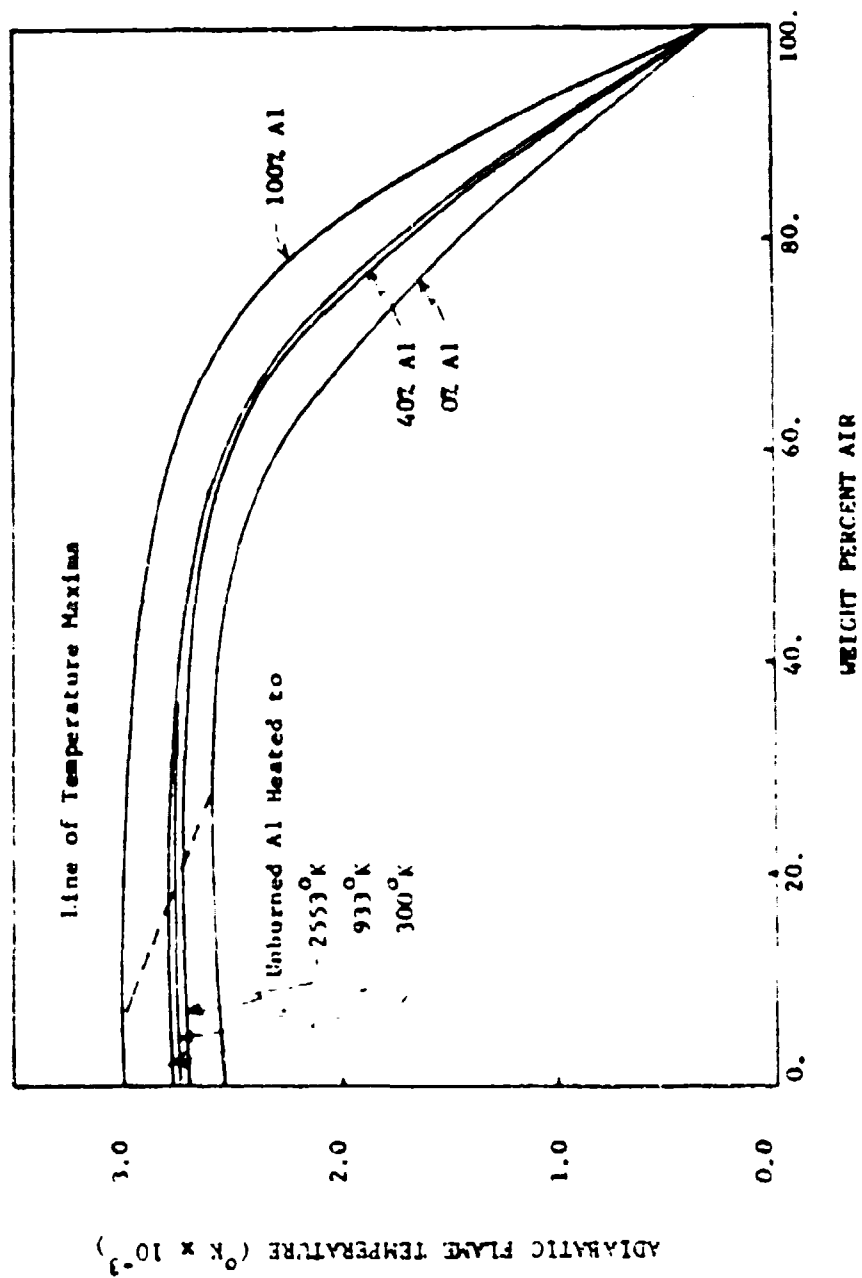
Figure 7. Adiabatic flame temperature vs percent aluminum burned and percent air admixture (calculated for equilibrium except as indicated by percent and temperature of aluminum).

20
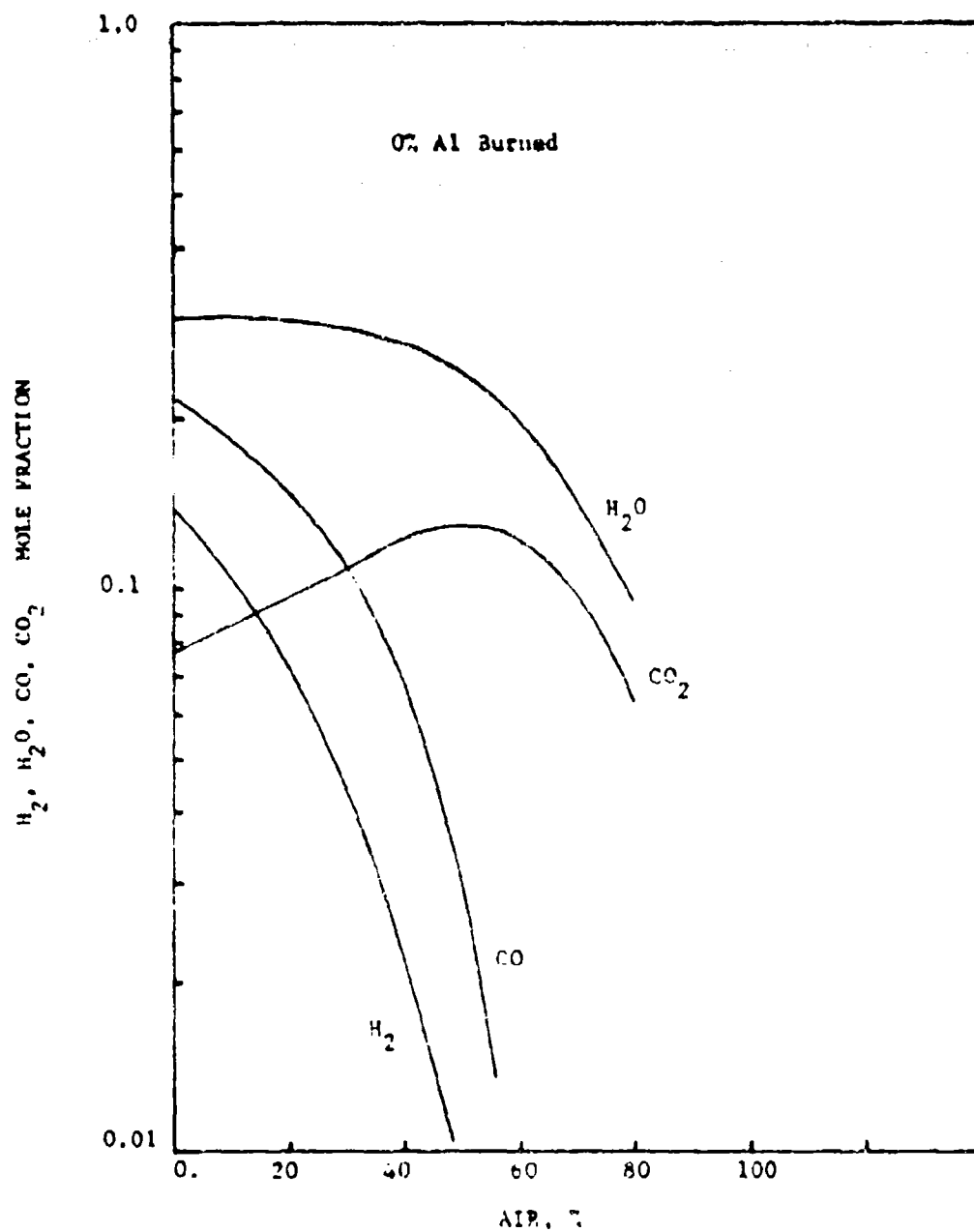
Figure 8. Principal effect of air admixture on concentration of reaction products -- case for 0% aluminum burned.

21

edge of the burning sample, but may approximate much of mixing Region D, in view of the slow lateral diffusion of condensed material. In the figure, all concentrations go to the composition of air as the abscissa approaches 100% (low concentrations for the gases shown). However, starting at 0% air, the H_2O concentration initially holds steady in spite of dilution, as the H_2 reacts with the incoming oxygen. The CO_2 concentration actually increases up to 50% air admixture, due to oxidation of CO. At higher air concentration, the concentrations in the figure drop off rapidly due to dilution. The subject of the dimensions of this mixing zone is touched on in Sections 1, 2 and 5, and in Appendix A.

3 SCREENING STUDIES

3.1 Introduction

At the outset of this study, a considerable backlog of information was available on combustion of aluminized solid propellants, but the applicability of that information to burning under atmospheric conditions, or for UTP 3001 propellant, was unknown. Further, there were some critical unresolved issues, such as the size of aluminum agglomerates of the particular propellant, the burning rate of the droplets, and the relative amounts of oxide formed as fine smoke and as surface oxide on burning droplets (which forms much larger oxide droplets in the plume). Since these questions were considered to be critical to the effect of the fire on immersed objects, it was essential that methods be developed and applied to make such observations. Before initiating quantitative measurements, it was proposed to do a series of screening studies designed to obtain additional qualitative insight and evaluation of candidate experimental techniques.

3.2 Test Sample Preparation and Preliminary Photographic Studies

Initial testing was directed at narrowing the scope of the problem by experimental observation of combustion of various size samples with various ignition methods and various processes of coating the sides of the sample other than the burning surface. It was desired to use small samples for as much of the work as possible, because it simplified testing. Screening tests with propellant cubes, burned in an ambient atmosphere, led to the choice of 5-cm diameter samples because photographs (Figure 9) showed that this resulted in a fairly one-dimensional flow away from the burning surface, hopefully simulating a columnar section above the burning surface of a large sample. Some smaller samples served well to demonstrate the details of the two-phase nature of the "plume" and the prolonged burning of the aluminum droplets (Figure 10).

It was found that care in ignition and inhibiting of the sample was required to obtain columnar combustion plumes. Uniform ignition was accomplished by using an electrically heated loop of wire (Figure 11), and a coating of igniter paste consisting of potassium perchlorate with titanium

23

Figure 9. Columnar combustion plume from a 5-cm diameter
sample of UTP 3001 in air.

Figure 10. Blown plume from a 2.5-cm sample, showing response of products other than aluminum agglomerates to cross flow. (Streaks in the upper plume indicate motion of burning agglomerates during the time the camera shutter was open; intermittent nature of the streaks is produced by a 1000 Hz chopper in the light path to facilitate velocity determinations).

Figure 11. Photograph of a 5-cm-diameter sample with igniter wire and igniter paste.

and boron powders, in a polybutadiene binder thinned to the desired
consistency with toluene. The sides of the sample were inhibited by a
smear of petroleum jelly, which had the virtue of melting and flowing away
from the burning surface, giving a clean edge. Other inhibitors either
failed to prevent burning down the sides (Figure 12), or accumulated on the
periphery in such a way as to modify combustion or obstruct the view of
the surface (Figure 13).

The early studies showed that camera settings equivalent to 0.01 sec
at f/32, with ASA 160 color film yielded satisfactory exposure of the plume.
However, it will be noted later that the bright, burning aluminum agglom-
erates tend to be obscured by the smoke cloud unless exposure time can
be reduced to about 0.0002 sec (with corresponding increases in aperture
and/or film speed). Close-up pictures of the burning surface and plume
structure were taken with a 35-mm Nikon camera with a 200 to 600-mm zoom
telephoto lens (further details of photographic methods are presented in
Appendix B).

The plume pictures showed that burning aluminum droplets are present
in the plume for as much as 1 meter above the burning surface. Near the
burning surface (Figure 14) the plume is dominated by streaks resulting
from smoke trails (Al_2O_3 particles in the < 2 μ-diameter range), trails
formed from aluminum agglomerates burning on the propellant surface.
Previous studies have shown that the burning agglomerates form very fine
Al_2O_3 smoke droplets in a detached flame envelope around agglomerate drop-
lets, and also form oxide on the droplet surfaces (References 7 and 8;
Figure 15). Thus one expects the aluminum droplets to continue to form
smoke after departure from the burning surface, and to produce larger oxide

---

7.   Prentice, J. L., "Combustion of Single Aluminum Droplets in Various
     Oxidizing Gases Including CO_2 and Water Vapor," Chemical Propulsion
     Information Agency Publication 243, Vol. III, December 1973, pp 279-
     295.

8.   Price, E. W., H. C. Christensen, R. H. Knipe, C. M. Drew, J. L. Prentice,
     and A. S. Gordon, Aluminum Particle Combustion: Progress Report, Naval
     Ordnance Test Station Technical Publication 3916, April 1966.
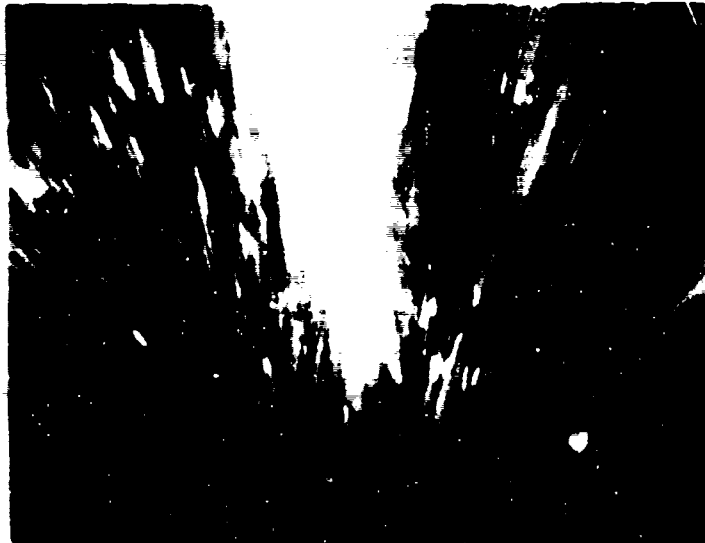
Figure 12. Photograph of a 2.5-cm sample with nonuniform edge
burning and divergent plume, unsuitable for test work.

Figure 13. Photograph of a 2.5-cm sample with accumulating
inhibitor obstructing edge burning and viewing.
Generally unsuitable for test work.
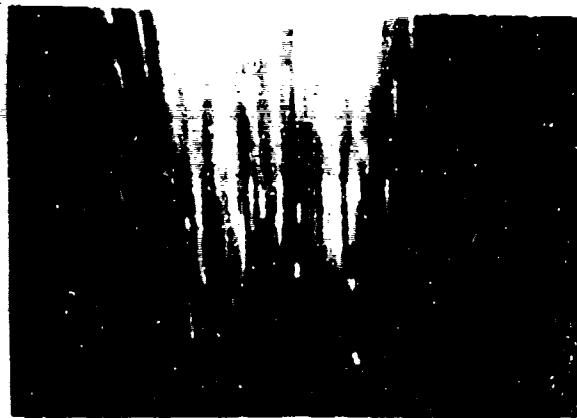
Figure 14. Photograph of plume near surface showing smoke trails
from aluminum agglomerates burning before detachment
from the propellant surface.

Figure 15. Picture illustrating the surface oxide lobe on quenched agglomerates (SEM).

Figure 16. Picture of deflected flow in the combustion plume. Note the condensed material splattered out of the plume.

droplets upon burn out, droplets consisting of all the surface oxide
accumulated before burn out. The photography shows the burning agglomerates
-- especially when the obscuring smoke is blown away by transverse flow
(Figure 10). The residual oxide droplets (which are much larger than the
smoke droplets, and probably not blown away by the cross flow), do not show
in photographs because they are cooler than the droplet flame, and corre-
spondingly less luminous (See also Sections 5 and 6). As noted in later
discussion, the residual oxide droplets are observed in direct sampling
of the plume.

3.3 Mixing and Atmospheric Effects

As noted in the Introduction, the propellant plume is fuel-rich and
reacts with air. This results in a mixing reaction region around the
plume which may be a factor in some fire situations. Further, the alumi-
num droplets burn vigorously in air, and can be predominant in the pictures
of the plume because agglomerates in the interior of the plume tend to be
obscured by smoke. The combustion of agglomerates in air is best demonstra-
ted in the present work by samples with nonflat burning surfaces (Figure 12)
and by droplets deflected out of the plume (Figure 16).

Early results indicated that, however columnar the flow from the
burning surface appeared, mixing of air into the plume was rapid, being
substantial (for 5-cm samples) at the center of the plume at a distance
of 15-cm from the burning surface (see later discussion of temperature
measurement). The mixing is by circulation as well as molecular diffusion,
as illustrated in tests on large samples (12.7-cm diameter) as in
Figure 17. Tests were run with the 5-cm samples and plumes inside a
15-cm pyrex tube with flow of different gases (Ar and O_2) to clarify the
role of mixing and reaction in the plume boundary. While only preliminary
in nature, photographs during these tests on 2.5-cm samples showed the plume
to be greatly suppressed in brightness in an argon atmosphere (Figure 18).
These results support the interpretation of rapid plume mixing and dictated
use of samples at least 5-cm diameter in the subsequent investigation, with
most being burned in 5-cm-diameter tubes to confine the plume.
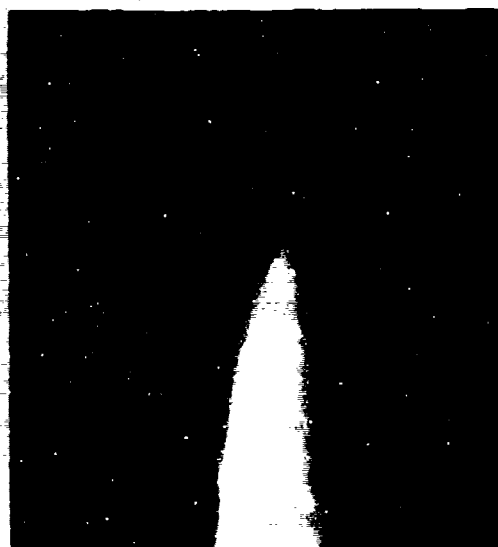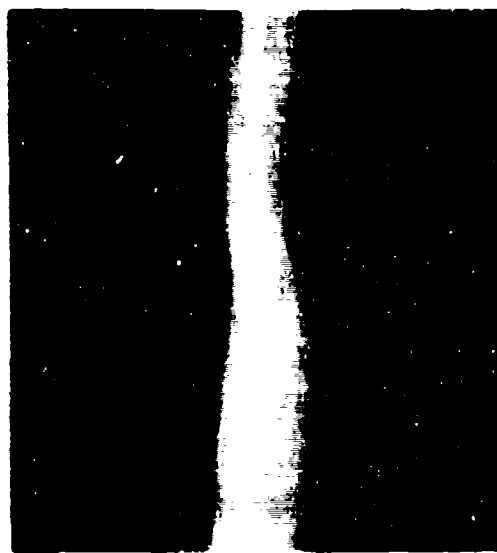
(a)

(b)

Figure 17.   Photographs of plume from a 12.5-cm sample, showing
             convective mixing at the periphery of the plume.
             Part a, full plume, and Part b, close-up with vortex
             ring.

31

(a)

(b)

Figure 18. Photographs of sample burning in a column of
flowing gas: (a) Argon, (b) Oxygen.

3.4 Collection of Condensed Material In Open Plumes

In order to establish the burning rates and size distribution of
agglomerates in the plume directly, it was proposed that burning agglom-
erates be quenched and collected at various locations in the plume. Pre-
liminary calculations indicated that if the burning surface were oriented
to give a horizontal plume, the agglomerates would fall out of the plume
due to gravity, and earlier tests on a different propellant had shown
that the burning agglomerates would then quench if allowed to fall on a
metal plate. However, screening tests on UTP 3001 in open plumes showed
that the aluminum agglomerates were not quenched on the plate, but instead
usually bounced and continued to burn (Figure 19). Various schemes were
used to achieve good quenching and collection from open plumes (inclined
plates, trays of water, nitrogen flushing), with only limited success.
Some agglomerates were captured and photographed (Figure 20), illustrating
the expected configuration and size. However, it was decided during these
studies that the rapid mixing of the atmosphere with the open plume would
lead to deceptive results even if successful open plume quenching were
achieved. As a result, systematic studies were made later by tests on
samples burned in tubes (see below).

During the efforts to quench-sample agglomerates, copious quantities
of aluminum oxide were collected. These samples revealed the expected com-
bination (Figure 21a) of fine oxide smoke and larger residual oxide spheres
(as well as the oxide caps on the agglomerates; (Figures 21b, 21c). In
later studies, efforts were made to determine the weight-distance distri-
bution of aluminum, smoke and residual oxide, as well as their size distri-
butions. This will be discussed below and in Sections 8 through 11, and in
Appendix C.

3.5 Collection of Condensed Material in Tube Burners

Because of the problem of rapid air admixture in the combustion plume,
testing was eventually shifted to confined flow, where the sample was fitted
in a tube, and observations were made at the tube exit. In the case of
collection of condensed material, the tube was oriented open-end-down. The
out-flow was then quenched by various means such as discharge into a pool of
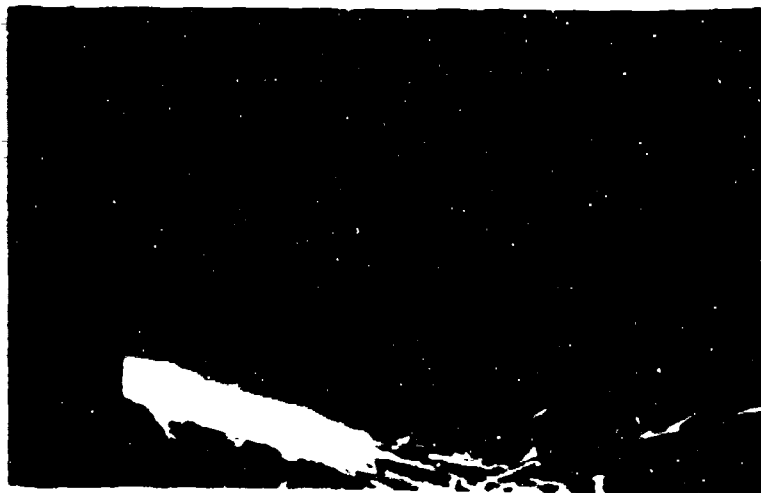
Figure 19. Photograph showing burning agglomerates falling out of a horizontal plume, impinging and bouncing on a quench-collection plate.

Figure 20. Picture of an agglomerate that quenched on a metal plate (SEM).

34
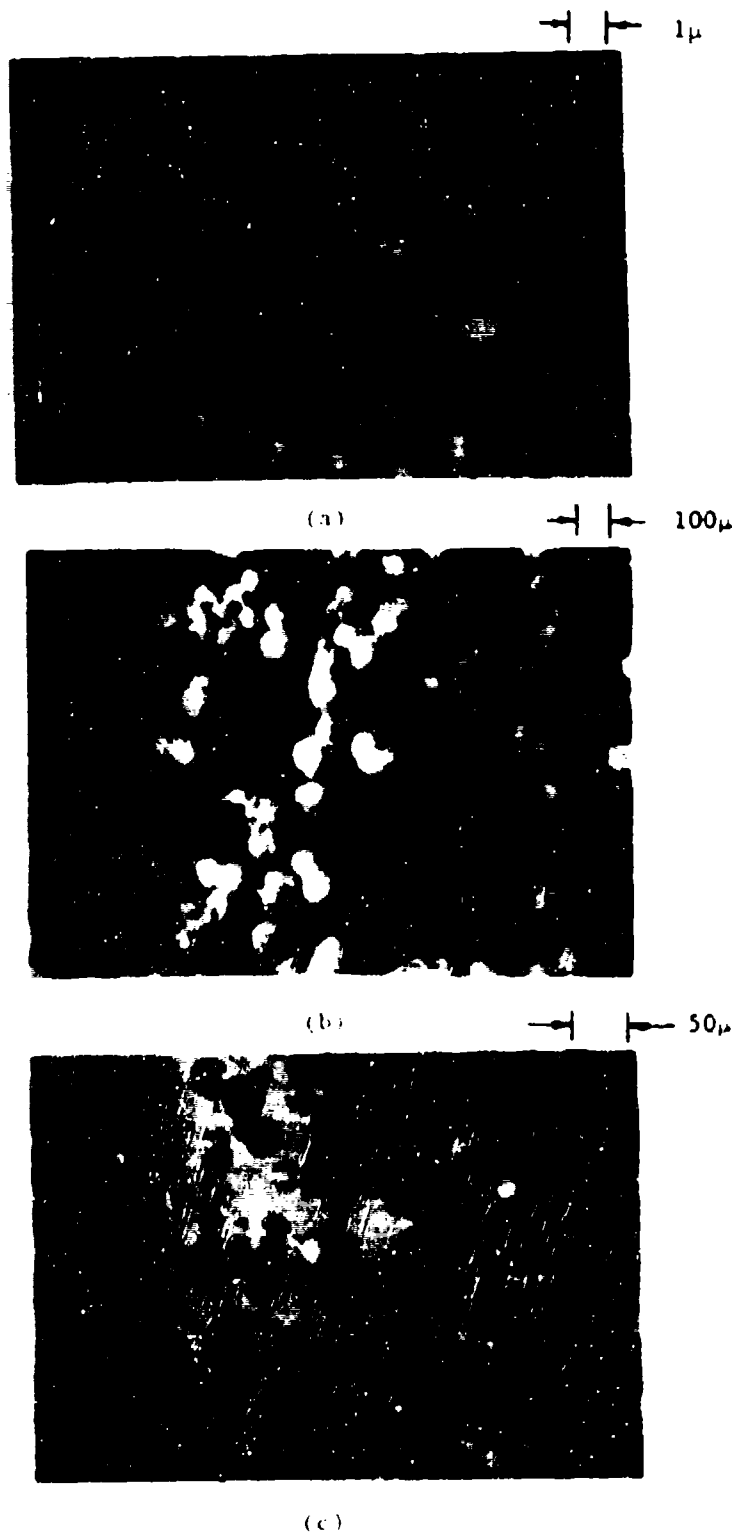
Figure 21. Forms of oxide droplets in the combustion plume:
(a) oxide smoke; (b) quenched aluminum agglomerates
with lobe of surface oxide (precursor of residual oxide
droplets), and (c) residual oxide droplets (formed from
oxide lobe of agglomerate).

35

alcohol. These methods were explored in the screening studies and found to yield quenched material in good condition (Figures 21 and 22). Later, more complete testing is discussed in Section 11.

3.6 Combustion Zone Size and Structure

The collected measurements of the screening studies indicate that the experiment can be conducted so as to yield a columnar flow from the burning surface, essential to laboratory simulation of fire environments of practical concern. Microscopic detail of the burning surface shows protruding oxidizer particles (Figure 23a) and burning agglomerates of aluminum particles (up to 500 μm; Figure 23b). In the region near the surface, smoke streamers from the burning aluminum agglomerates suggest laminar flow (remarkably so considering the irregular nature of the surface). Aluminum agglomerates leave the burning surface already burning, in a wide range of sizes, and move away in the direction of the plume column. The density and luminosity of the smoke plume increases rapidly as the material flows away from the surface.

Preliminary results suggest that 50% of the aluminum is reacted within about 15-cm of the propellant surface, with the remainder (large agglomerates) burning for up to 1 meter. Plumes from laboratory scale samples (5-cm diameter) appear to experience rapid mixing with entrained air, as evidenced by their sensitivity to atmospheric environment. All measurements on open plumes beyond 6 or 7-cm from the surface (i.e., measurements of temperature, composition, agglomerate sizes etc.) are presumably affected by mixing, and the test procedure was modified because of this (by conducting the tests in tubes). Mixing was apparently less rapid on the axis of the plume with 12.5-cm diameter samples, simply because of the larger radial mixing distances (hence the highly luminous upper plume with large samples; Figure 17a). Nonetheless, the mixing processes with the large samples were sometimes large scale, as indicated by the apparent recirculation in the plume boundaries (Figure 17b). It is judged that the 12.5-cm sample can be used for tests of plume effects on immersed objects in the region up to 50-cm from the propellant burning surface if the immersed objects are small (e.g., ~ 2.5-cm). Most of the tests run on 12.5-cm samples were run in

─┤├─ 100μ

Figure 22. Typical sample of condensed material collected by the alcohol quench method.
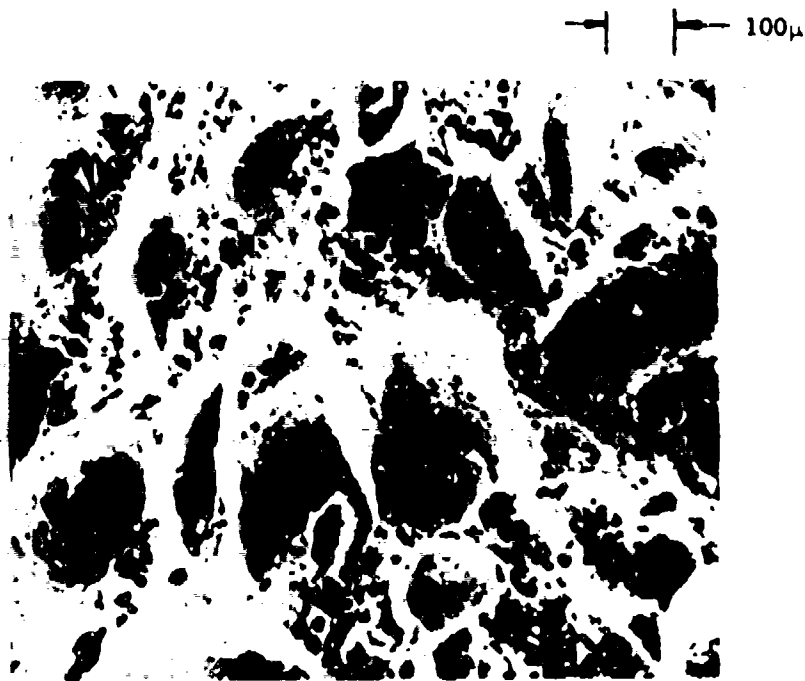
(a)
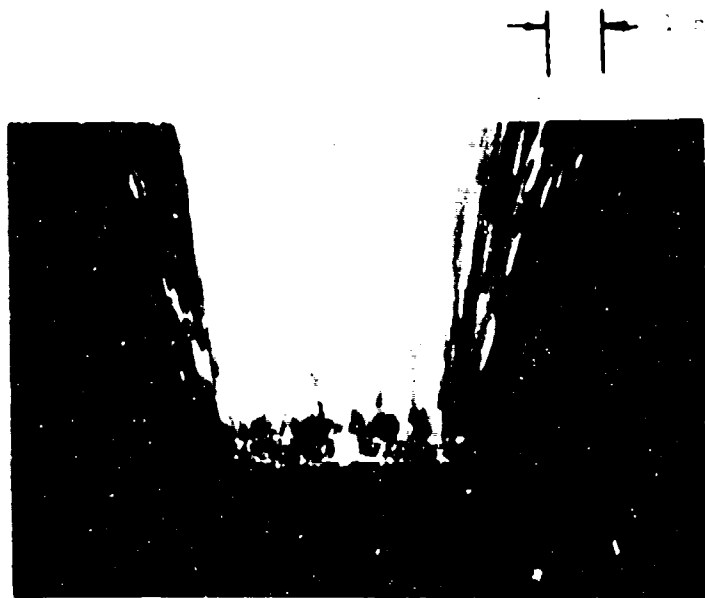
(b)

Figure 23. Details of propellant burning surface: a) SEM
of a sample quenched by impingement of freon jet,
showing protruding oxidizer particles; b) photograph
of a burning sample, showing aluminum agglomerates
burning on the surface.

stainless steel tubes, and tubes were used on almost all tests on 5-cm samples where quantitative measurements were reported.

The burning rate of the propellant could be estimated from test duration, since initial sample thickness was normally measured. The rate was qualitatively reproducible, and averaged 0.127 cm/sec. The propellant density was measured, and was 1.76 g/cm^3. Thus the mass flow rate in the efflux from a surface one cm^2 was 0.223 g/sec.

Assuming an equilibrium composition of products (after complete combustion of the aluminum) as indicated in Table 1, and a temperature of 2990°K, the mass flow velocity would be 28 cm/sec (see Section 7 for details). Velocities in the plume could be estimated from the length of streaks in photographs made by motion of images of agglomerates during the exposure time. Velocities obtained in this way varied widely, and it was concluded that the most visible agglomerates were in the reduced velocity, front and lateral boundaries of the combustion plume where obscuration by smoke was minimal. The higher observed velocities were around 15 m/sec. For this velocity and the plume height of about 1 meter seen for 12.5-cm diameter samples, the largest agglomerates must have burned about 0.07 second.

In summary, the qualitative properties of the combustion plume as estimated above are collected in Table 3.

Table 3. Estimates of Reaction Zone Characteristics Obtained
from Screening Studies (Augmented by Use of Results
of Chemical Equilibrium Calculations).

Propellant burning rate (measured)	0.127 cm/sec
Propellant density (measured)	1.76 g/cm^3
Propellant mass burning rate ($\rho_p r$)	0.233 g/sec/cm^3
Combustion zone thickness, (Figure 1); (Region A, observed values)	1.0 m
Burning time of large agglomerates	0.07 sec
Temperature after burning of Al is complete (from Table 1)[*]	2990°K
Gas density in the combustion zone[*]	0.78×10^{-4} g/cm^3
Mass of Al$_2$O$_3$ per unit volume in the product flow[*]	0.31×10^{-4} g/cm^3
Flow velocity[**]	15-30 m/sec

[*] Based on chemical equilibrium data actually applicable
     to region of complete reaction, Region B of Figure 1.

[**] Based on several methods of determination.

4 HEAT TRANSFER

4.1 Introduction

The primary effect of the fire environment on immersed objects is temperature rise. Accordingly, heat transfer is the physical process of primary concern (if the immersed object is chosen to be reasonably resistant to chemical attack). The present project was concerned with characterization of the fire environment responsible for the heat transfer. However, the ultimate application of concern was heat transfer, and some consideration of it was necessary to assure proper emphasis in the fire environment investigation.[*] Indeed, heat transfer measurements were undertaken from the outset of the project, measurements in the form of immersion calorimeter probes.

It should be stressed that heat transfer in the fire environment is a very complex process, primarily because of the (uncharacterized) two-phase nature of the medium, and the reactive and reacting conditions in the combustion zone. That is precisely why the first effort, the effort chosen for this project, was to characterize the medium. The second phase problem of heat transfer is discussed at this point in the report primarily to explain some qualitative findings about it and how they affect the allocation of effort in the study of the fire environment.

4.2 Heat Balance for an Immersed Object in a Gas Flow

When an object is immersed in a gas flow, a flow field is established around the object, from which heat of the gas is transferred to the object. Depending on the shape and size of the object, heat is transferred at different rates at different locations on the surface, and a transient temperature field develops in the object while it is heating up. If the propellant yielded only gaseous combustion products (and the immersed object were geometrically simple and located outside the combustion zone),

---

[*] A further objective was to establish a modest size experiment in which exploratory tests could be made on various test objects without excessive cost of tests.

41

then the heat-up of the immersed object could be calculated by any of several existing computer programs. Characterization of the fire environment would consist of determination of propellant flame temperature, density and burning rate; of product molecular weight, density, velocity, heat capacity, thermal conductivity, and viscosity. All of these quantities can be determined with sufficient accuracy from known propellant characteristics and results of chemical equilibrium computer programs.

The heat transfer argument is simplified further if the immersed object is small and is a good heat conductor, because it can be assumed to be at uniform temperature. This condition can be approximated if the immersed object is a temperature probe, designed to conform to a simple representation of the heat transfer problem. In that case, heat transfer can be described by a heat balance equation

$$H_g (T_g - T_p) + H_r T_g^4 = C_p \frac{dT_p}{dt} + H_r T_p^4 + H_o (T_p - T_o) \quad (1)$$

| Heat in by convection | Heat in by radiation | Heat stored | Heat out by radiation | Heat out through probe support |

where T_g, T_p, and T_o are the temperatures of the gas, immersed probe, and ambient environment respectively; H_g, H_r, and H_o are bulk heat transfer coefficients (that depend on the detailed flow field and gas properties) for heat in from the flow field, heat radiation and heat out through the probe support: C_p is the bulk heat capacity of the calorimeter part of the probe. For a specific flow situation and a specific probe, this equation can relate the gas temperature to the object temperature if the coefficients are known. The coefficients can be determined by running a test in a known gas flow field, measuring T_p vs time, and determining the best combination of the parameters for fitting Equation (1) to the observed $T_p(t)$. Then when T_g is not known, but is believed to be constant, the same calculation can be made to determine T_g as well. In Section 4.4, Equation (1) is used to interpret probe temperature measurements made in the fire environment of UTP 3001. The results are wholly unsatisfactory unless one considers the two phase nature of the fire environment. The

complications of the condensed phase products are discussed next.

4.3 Complications Due to Condensed Phase Reaction Products

As noted in Table 1, the condensed phase material in the combustion zone of UTP 3001 propellant consists of about 15% aluminum near the propellant, which changes to about 28% aluminum oxide in the final reaction products. As was seen in Figure 16, condensed phase material impinges directly on immersed objects in the flow, which was observed to cause cumulative build-up of material. This is demonstrated by Figure 24, which shows a refrasil rod placed longitudinally in the plume with the end located 7 cm from the propellant burning surface. Accumulation of deposit on the end of the rod over a 15 second interval is conspicuous. The brightness of this accumulated material suggests that it is very hot, and post-test examination indicates that substantial aluminum is present. Thus it seems likely that the depositing material not only deposits heat, but the aluminum continues to add heat by oxidation.

From the foregoing it is evident that the process of heat transfer involves not only convection from the gas flow, but also direct deposition with impinging condensed phase material, along with heat release by this material through chemical reaction. Further, the accumulating material changes the heat transfer characteristics into the solid, in a time-dependent way due to deposit accumulation. These effects pose a heat transfer problem for the future. For the present, effort is concentrated primarily on characterizing those properties of the fire environment that determine these heat transfer effects. As far as the condensed phase material is concerned, it can be assumed that the critical considerations are the relative amounts of aluminum and aluminum oxide, and the droplet size distributions and temperatures, subjects of Sections 5 and 8 through 11. In the meantime, attention is turned next to the actual heat transfer, and an estimate of the role of the condensed phase.

4.4 Calorimeter Measurements

After relatively uninformative measurements with bare thermocouples in the plume (Appendix D), primary effort was devoted to design and use of

t = 0

t = 7 sec

t = 15 sec

Figure 24.   Photographs of accumulation of Al_2O_3 and Al on a refrasil
rod immersed in the combustion zone.

a probe consisting of a thermocouple-equipped copper tip and a shank constructed from coaxial sleeves of ceramic, inconel, and stainless steel (Figure 25). Figure 26 shows typical temperature-time curves for the probe, recorded in tests at different heights in open plumes from 5-cm samples. From one such temperature-time curve (combined with similar ones from tests in a clean flame of known temperature), a local effective plume temperature can be calculated (Appendix D). Figure 27 and Table 4 show the temperatures calculated from three tests at different distances from the

Table 4. Calculated Temperatures, °K; Based on Immersion Probe Heat-up and Equation (1) -- Assuming No Heat Transfer by Impingement of Condensed Material.

Time Interval During Heat-up (sec)	Distance from Burning Surface	7.62 cm (3 in.)	15.2 cm (6 in.)	22.9 cm (9 in.)
10		12 300	11 280	6050
11		13 770	12 240	6060
12		14 860	13 170	6003
13		15 540	13 520	5970

burning surface. The multiple points at each distance correspond to different times during the burn.

The most notable features of the measurements are the very high indicated temperatures, and the trend to lower temperatures at greater distance from the burning surface. The chemical equilibrium calculations (Section 2) indicate that the temperatures should range between about 2400°K (near the surface where very little combustion of the aluminum has occurred) and 3000°K (where aluminum combustion is complete). Since the values in Table 4 are calculated on the basis of the assumptions that the

Two Hole Ceramic
Protector &
Insulator
(Alumina)

Closed End
Tube
(Inconel)

S - Type Thermocouple Bead
(Plat -- Plat 10% RH)

0.95 cm

Copper
Cap

Stainless Steel Tubing

Figure 25.   Sketch of calorimeter immersion probe.
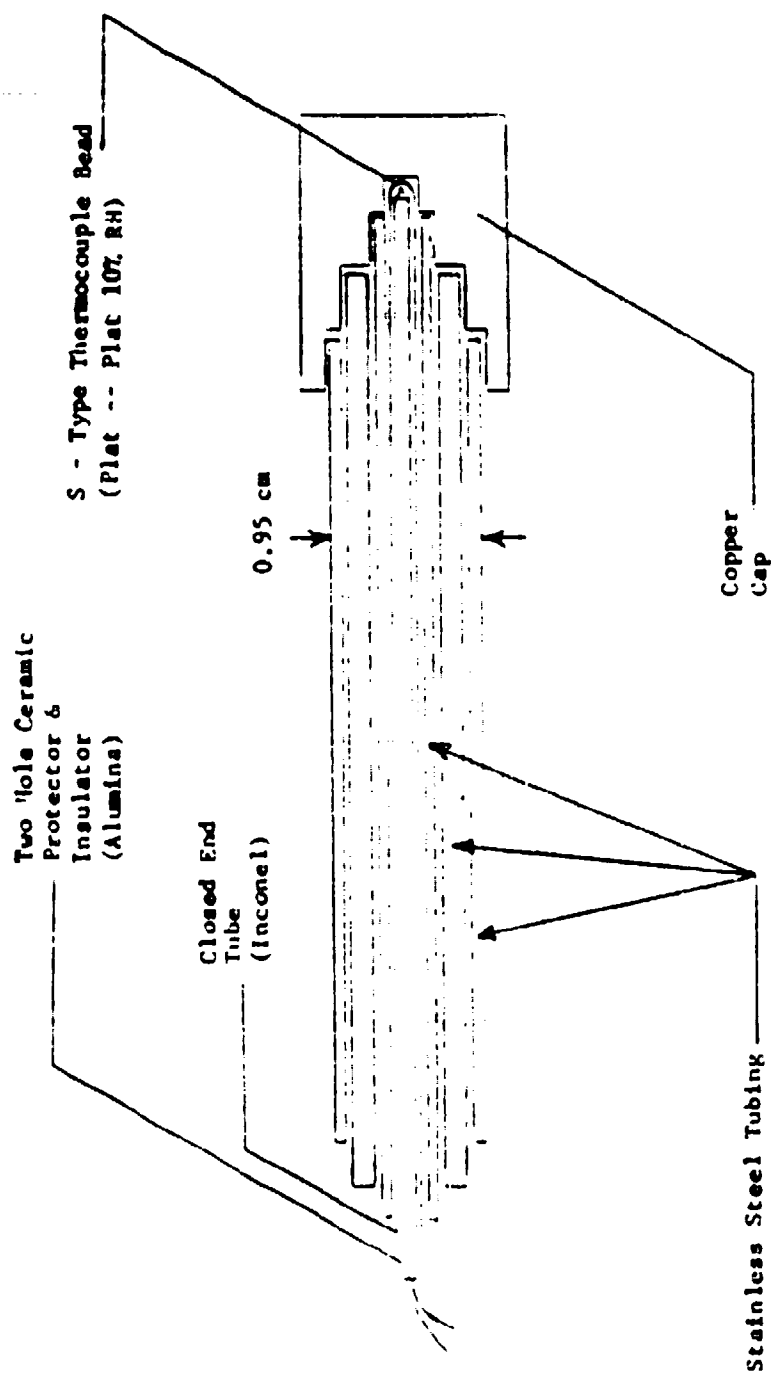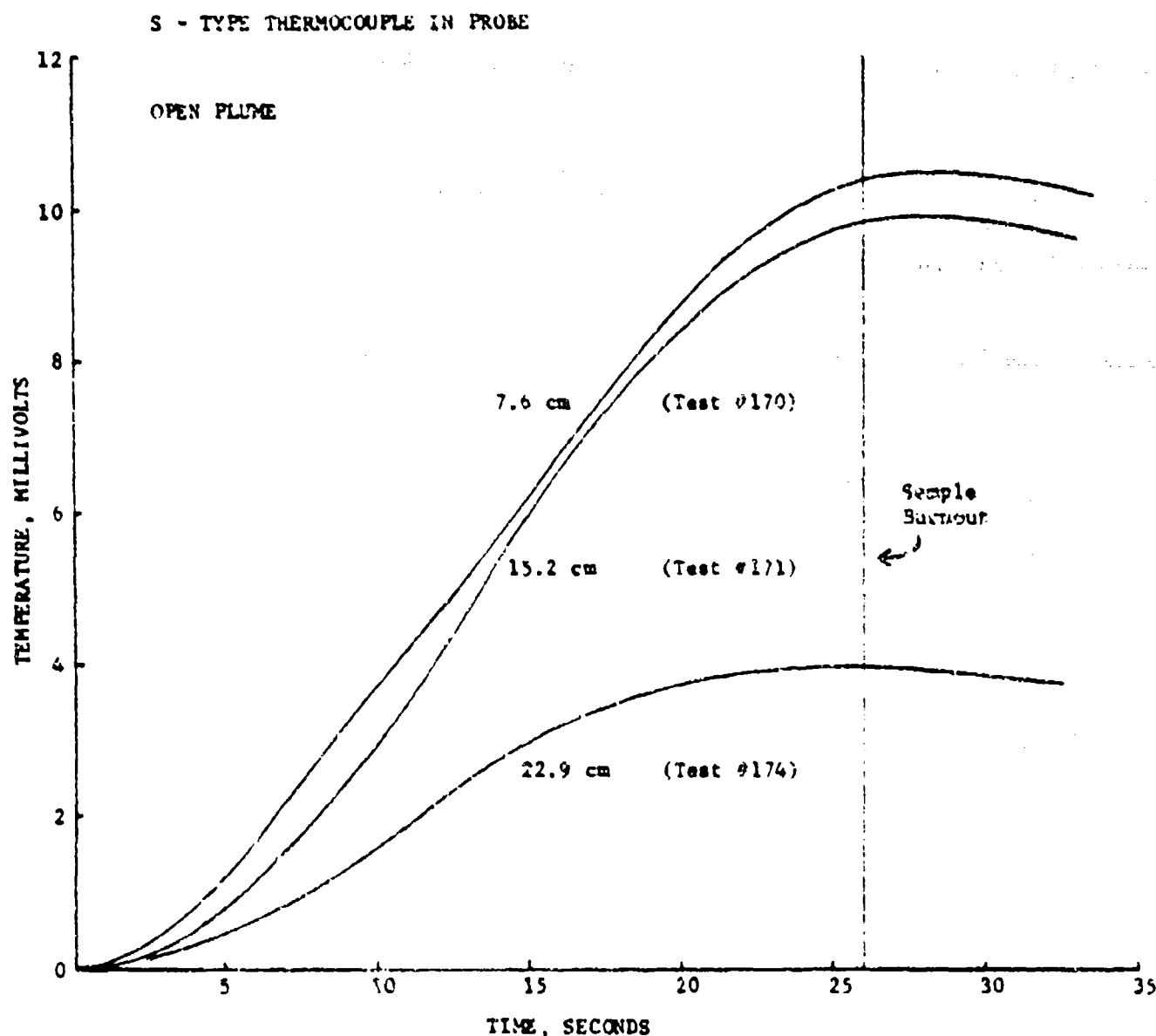(Drawn to scale.)

46

Figure 26. Temperature-time curves for an immersion probe used in
the calorimeter mode. The different curves correspond to
different distances from the burning surface. Tests were
in open plumes from 5-cm diameter samples.
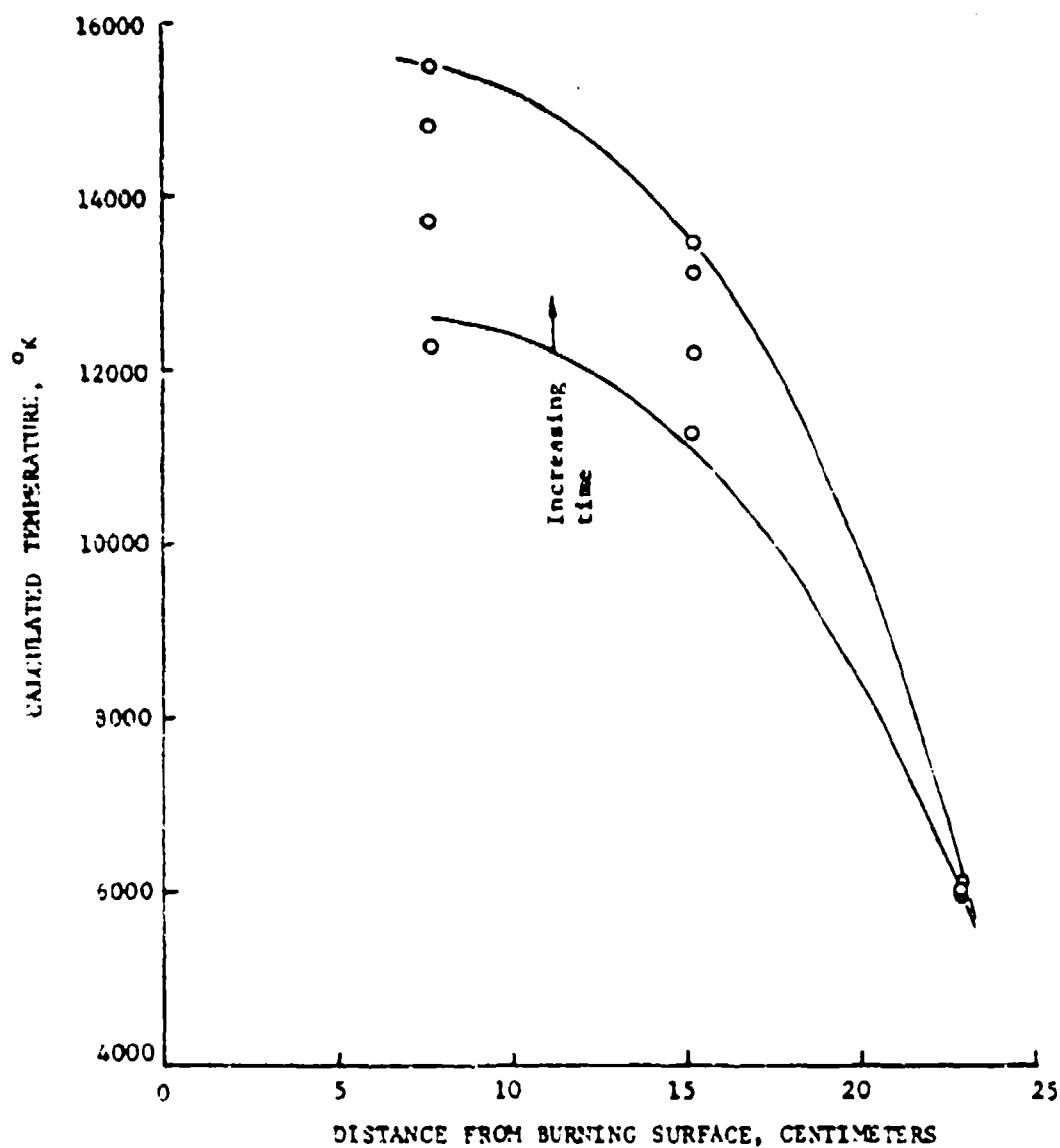
Figure 27. Indicated temperatures vs distance from the burning surface based on heat-up curves in Figure 26 and on Equation 1.

heat transfer is described by Equation (1) and that the heat transfer coefficient is the same as in the calibration tests in a clean flame, the inordinately high indicated temperatures apparently reflect heat transfer by deposition and reaction of condensed material on the probe, which is not accounted for in Equation (1). While this is a critically important result, it also emphasizes that there are serious troubles with any conventional heat transfer coefficient-free stream temperature concept in characterizing heating of objects immersed in the flow.

Referring to the trend of calculated temperature with distance from the burning surface, the decreasing indicated temperatures suggest that air admixture has appreciably cooled the plume at 23 cm from the burning surface. An alternate interpretation is that the nature or temperature of condensed material evolves in such a way as to reduce deposition-reaction heating further from the burning surface. Direct observation of the probes after tests indicated less deposit, mostly oxide, on probes when they were heated at the 23-cm station. When the probe was near the propellant surface, it exhibited extensive metallic deposit after the test. Thus one might infer that the indicated temperature drop-off with distance from the propellant surface was because of an actual plume temperature drop-off (air admixture), but also because the heat transfer due to deposition-reaction decreases. The trend with time during individual tests is probably due to time dependence of retention and reaction of condensate, and corresponding time dependence of the heat transfer into the deposit-coated probe (see Appendix D). The trend of the indicated temperature towards expected flame equilibrium values at greater distance from the propellant surface is consistent with the observed decrease in deposition, as is the relatively time-independent temperature there.

4.5 Water-Cooled Probe

The procedure for interpreting the temperature-time curve from the original immersion probe involved a calibration in a clean flame before and after a test in the propellant fire (Appendix D), this procedure being motivated by the realization that the heat transfer coefficient must change as a function of time due to accumulation of deposited material.

49

Since such deposition is a fundamental aspect of the effect of the fire environment, some consideration was given to a probe concept that would more clearly show the effect of accumulation of deposits. For this purpose, preliminary tests were run on a probe consisting of a stainless steel tube with a outside diameter of 0.63-cm and an inside diameter of 0.32-cm, extending through the plume, and cooled by a constant water flow rate. The increase in water temperature is a measure of heat transfer rate to the tube. With a water flow rate sufficient to give a temperature rise of $30^\circ C$, the water temperature came to equilibrium in less than 2 seconds. This result indicated that the probe could be used to monitor the change in heat transfer coefficient as proposed. Further development of this concept holds promise.

4.6 Summary of Heat Transfer Measurements

The results of these experiments establish the importance of condensed phase material in the fire environment as a major factor in heat transfer. The results indicate a complex impingement of the droplets on the exposed object, with appreciable accumulation, and apparently very extensive heat deposition (References 9 and 10). Further, the deposited aluminum probably oxidizes, delivering still more heat to the exposed object. While no measurements were made to demonstrate the relative importance of fine and coarse droplets of condensate, fundamental considerations dictate that the coarser droplets will be more likely to impinge on immersed objects. These results dictate that more basic information must be obtained on droplet size distribution and deposition-retention characteristics versus immersed object size, material, shape, and duration of exposure. In the present investigations, particular attention was given to the size of the droplets, as discussed in Sections 8 through 11.

9. Shchubin, V.K., A.I. Mironov, V.A. Filin and N.N. Koval'nogov, "Intensity of Heat Transfer Between Two-Phase Flow and Nozzle Walls as Function of Particle Motion Parameters," Izvestiya VUZ, Aviationnaya Tekhnika, Vol. 19, No. 1, pp. 109-114, 1976.

10. Kuznetsov, V.A., and O.E. Kashireninov, "Specialties of Thermocouple Measurements of Temperature Into the Flame at the Condensed Product Formation," presented at the AIAA Aerospace Sciences Meeting, Jan. 1976.

5 TEMPERATURE

5.1 Introduction

In Section 4, it was emphasized that the heat transfer could not be characterized in a simple way as a function of temperature in the fire environment, because of the complex way in which heat is transferred from the two-phase flow and dependence on its microscopic details. It was not meant to imply that temperature was ill-defined (although there are problems), or that the concept is not useful. Rather, it was meant to state that the medium is not microscopically uniform, and is thermally nonuniform in the same way as it is physically and chemically nonuniform. Specifically, the temperature is very high in the flame envelope around the aluminum droplet, lower in the gas-smoke field, and still lower in the aluminum droplets. The purpose of this Section is to describe what we know about these temperatures.

5.2 The Temperature Zones

The extended region of the combustion zone of the propellant in which the aluminum droplets burn is a region where chemical heat release continues locally around the aluminum droplets and flows to the surrounding media; with corresponding temperature gradients. The most intense heat release is in a high temperature zone which is a detached flame envelope around each aluminum droplet (References 11 and 12). In this flame envelope, the most energetic step is the formation of Al_2O_3 in liquid form, primarily on the surface of existing smoke droplets in that envelope. It is the resulting energy of that reaction, and the corresponding high temperature of these smoke droplets, that makes the combustion so luminous. Indeed, these droplets are near their boiling temperature (Reference 11), and it is partly

11. Christensen, H.C., R. H. Knipe, and A. S. Gordon, "Survey of Aluminum Particle Combustion," _Pyrodynamics_, Vol. 3, published by Gordon and Breach, 1965, pp. 91-119.

12. Friedman, R., and A. Maček, "Combustion Studies of Single Aluminum Particles," from _Ninth Symposium (International) on Combustion_, Academic Press, 1963, p. 709.

because of the radiative disposal of energy that the rate of formation of liquid Al_2O_3 can exceed the rate of its vaporization (dissociation).[*] At one atmosphere this process maintains the Al_2O_3 temperature at about 3800°K (Figure 28). The region involved is an envelope surrounding all of the burning agglomerate, except that portion covered by an oxide lobe (that portion of the envelope is deficient in fuel species (Al, AlO, etc.)). In a convective environment the flame envelope may be drawn out by convection of Al and lower oxides into a tail as in Figure 29. It will be noted in the figure that the luminosity of the convective tail quickly decreases in the bulk gaseous environment, reflecting rapid equilibration with the lower temperature of that bulk environment when the supply of Al_2O_3-forming reactants is depleted. From a practical viewpoint, it should be stressed that the high temperature zone arcund the burning agglomerates, while the source of a large part of the radiant energy and heat, contains very little mass, and only small droplets that may not deposit extensively on objects in the flow.

Inside the flame envelope, the aluminum droplet constitutes a second zone, which is necessarily at a temperature below the aluminum boiling point (~2740°K) and above the Al_2O_3 melting point (2318°K). The reason is that the flame cannot support the high vaporization rate of the boiling point, while the combustion would be arrested or drastically reduced if the oxide were frozen (because it would encapsulate the agglomerate). Thus one may regard the aluminum droplet as a second temperature zone in the aluminum combustion which contains substantial mass, at a temperature of about 2500°K, in a droplet form that impinges readily on immersed objects. Further, the impinging material will almost surely react exothermally on the immersed object if retained. These effects would be major when the test object is near the propellant burning surface where the alluminum concentration is high.

_____

[*] Al_2O_3 dissociates instead of boiling, and the high energy of formation can be realized only if heat is being removed to keep the temperature down.

52

Zone # 1 (Detached Flame)
3800°K

Oxide
Lobe

Zone # 3
2300 - 3000°K

Zone # 2
~ 2500°K
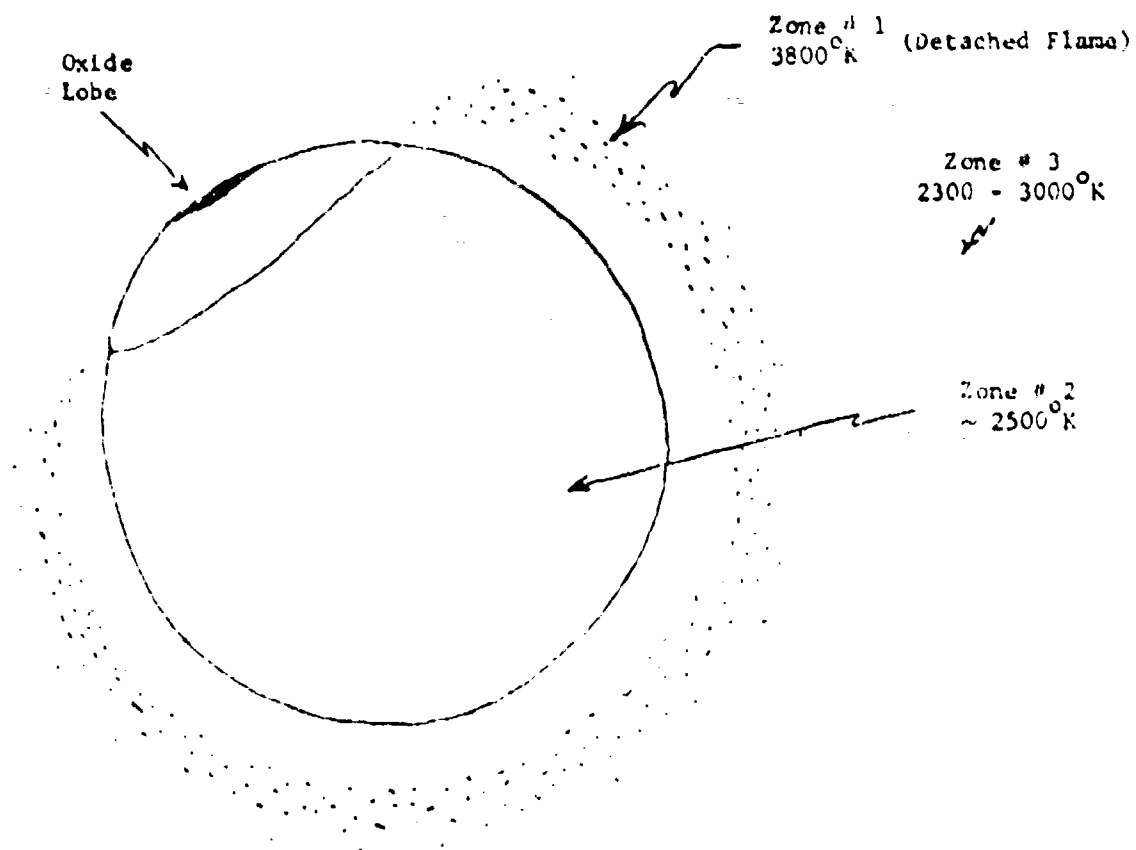
Figure 28. Features of the burning aluminum droplet, and its associated
temperature zones for a typical solid propellant combustion
zone.
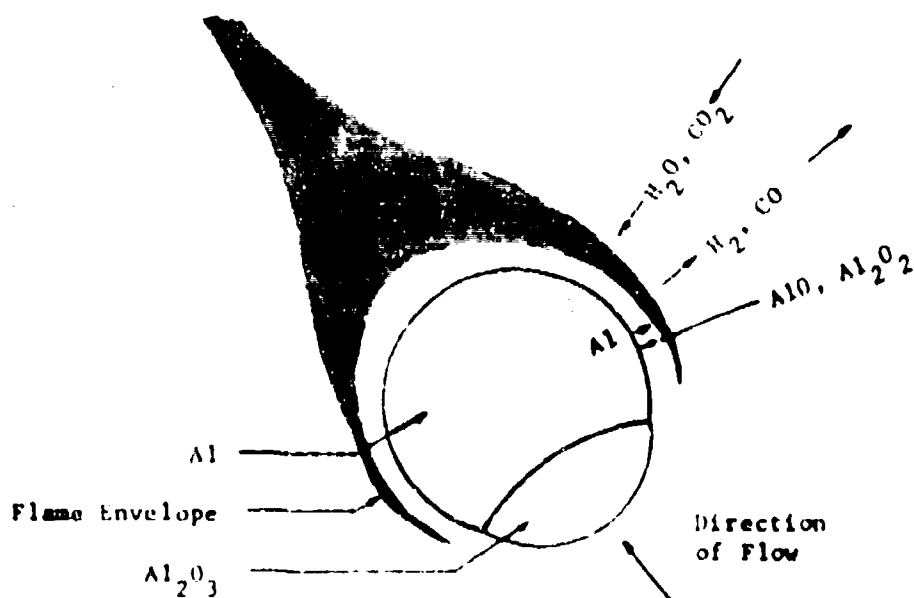
(a) Sketch of agglomerate combustion.
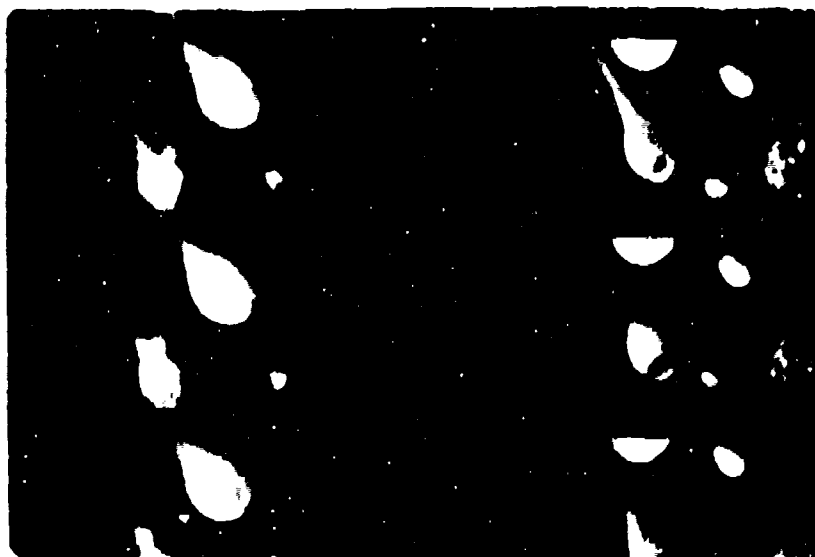
(b) Photograph of agglomerate combustion.

Figure 29. Effect of a convective environment on the aluminum flame.

The third temperature zone of the aluminum combustion is all that volume outside the droplet flame envelope, where the temperature is something like a flame temperature of the propellant (with due regard for the percent aluminum consumed at the particular location). The temperature ranges from $2350^\circ K$ near the propellant surface, to $3000^\circ K$ further out where the aluminum is 100% consumed (as shown in Figure 6 and described in Section 2.2), with the temperature rise being due to heat flow from the first temperature zone (aluminum combustion zone) described above.

From the foregoing, it can be concluded that most of the volume of the fire environment consists of the following material at the indicated temperatures (assuming no air admixture):

1. The bulk of the volume (gas, smoke, and residual oxide droplets) is at temperatures ranging from $2350^\circ K$ to $3000^\circ K$. Only the residual oxide droplets are large enough for impingement.

2. The unreacted aluminum in burning droplets is at about $2500^\circ K$. Droplets are large enough for impingement.

3. The flame envelope around the aluminum droplet, containing a very small mass of very hot gases and Al_2O_3 smoke droplets, is at about $3800^\circ K$. It is highly visible because of high temperature.

5.3 Spatial Distribution of Temperature

The experimental methods of this investigation have not yet established the temperature distribution unequivocally, and from the discussion in Sections 5.2, 6, and 9, it is clear that to do so could be prohibitively difficult because of the nonuniformity on a microscopic scale due to presence of burning metal droplets. However, in this context it is worth recapitulating the concepts of the microscopic temperature zones of Section 5.2, in the context of the general Regions of the plume shown in Figure 1.

Near the propellant burning surface (lower Region A) there is a heavy flow of burning aluminum (temperature zone 2, droplet temperature about $2500^\circ K$); with a correspondingly large flame envelope radiation (zone

55

1, temperature about $3800^\circ K$); and with a correspondingly low smoke density in the rest of the volume (zone 3, temperature 2400 to $2500^\circ K$). As the material flows further from the surface (outer Region A), the aluminum droplets (zone 2) decrease in size and total mass while remaining at about $2500^\circ K$; the total volume and radiation of the flame envelopes (zone 1, temperature $3800^\circ K$) decreases; the population of both smoke and residual oxide droplets increases in zone 3, and the temperature rises towards $3000^\circ K$ if air admixture does not intervene unduly; beyond about 1 meter (Region B), the aluminum droplets (zone 2) and their flame envelopes (zone 1) disappear, leaving only a homogeneous flow of gas, oxide smoke, and residual oxide droplets at about $3000^\circ K$ as described in Section 2.

The regions of air admixture (Regions C and D of Figure 1) are less well characterized, although the qualitative trends with air admixture are discussed in Section 2.4 and in Appendix A. The same microscopic details occur as in Regions A and B, with the amount of burning aluminum decreasing with distance away from the plume axis and the burning sur' e. In view of the uncertain radial component of aluminum motion and the presence of vortex flow, it will be difficult to characterize this air admixture region. Since the behavior is less important in full-scale fire events, and since it is feasible to suppress its unwanted effect with a combustion tube in laboratory tests, no further study of the temperature in the air admixture region was made.

5.4   Temperature Measurement

This subject has been touched on in the preceding Sections, and is discussed in References 13 to 17. It has been noted that the temperature

13.   Dodge, L. G., "Optical Absorption and Emission Measurements in Flames," in Experimental Diagnostics in Gas Phase Combustion Systems, Vol. 53 of Progress in Aeronautics and Astronautics, AIAA, 1977, p. 155-175.

14.   Tourin, R. H., Spectroscopic Gas Temperature Measurement, Elsevier Publishing Co., 1966.

15.   Gaydon, A. G., The Spectroscopy of Flames, Chapman and Hall, 1974.

is nonuniform on both microscopic and macroscopic scales. In Section 5.3 some limiting arguments regarding temperature were used to estimate the microscopic temperature distributions (temperature zones) and the macroscopic temperature distribution (plume regions, Figure 1). It has been noted that immersion type temperature detectors tend to respond to the condensed phase in the flow in a complex way that defies interpretation in terms of any characteristic temperature. Under these conditions, recourse can be taken to optical methods.

The optical methods are usually based on one of three techniques, which possess some capability of specialization of specific temperature zones, as follows:

1. Resonance absorption (line reversal): This method uses observation of transmitted monochromatic light having the wavelength of a particular excited specie in the flame gas (usually sodium). By adjusting the source light so that its brightness is neither enhanced or reduced relative to adjoining wavelengths when passed through the plume, it is known that the temperature of plume gas is the same as that of the light source (which is calibrated). This method would be useful for determing temperatures in temperature zone 3, but the smoke may be too dense for this method in its brightest region.

2. Spectral line intensity: This method involves comparison of brightness of certain spectral lines, and comparison with tabulated relations of spectral line brightness and temperature. This method might provide means to measure temperatures in zones

16. Reef, I., V. A. Farsel and R. N. Kniseley, "Spectroscopic Flame Temperature Measurements and Their Physical Significance," Spectrochemica Acta, Vol. 28B, March 1973, Vol. 29B, March 1974, Vol. 30B, May 1975 (3 parts).

17. Millikan, R. C., "Measurement of Particle and Gas Temperature in a Slightly Luminous Premixed Flame," Journal of the Optical Society of America, Vol. 51, May 1961.

1 and 3 (zone 1, using spectral lines of lower oxides of
aluminum, present primarily in the flame envelope).

3. Particle radiation: This method involves comparison
of brightness of the smoke cloud with that of a calibrated
tungsten filament lamp. This method is discussed further in
Section 6. From the description of the temperature zones of
the aluminum combustion, it is evident that most of the smoke
is in zone #3, i.e., the same temperature as the gas. In
Region B of the plume, where combustion is complete, this is the
temperature of everything present, and would be the same as
that given by chemical equilibrium calculations (Figure 7) if
there were no heat loss or inaccuracy in methods. In Region A
of the plume, the meaning of thermal radiation measurements
is complicated by uncertainty of smoke emissivity and plume
density, and presence of radiation of a different temperature
coming from temperature zone 1 of the aluminum combustion
(see Section 5.3).

From the foregoing it is evident that no definitive optical pro-
cedure for temperature measurement was found entirely suitable, nor is
one likely to emerge in the near future because of the microscopically
nonuniform nature of the medium and of its temperature. This is dis-
cussed further in Section 6.

5.5   Status of Temperature Information and Measurement

While definitive temperature determination by direct measurements
is still a remote prospect, the various sources of information permit a
fairly complete description of the temperature field. The information
and mechanistic arguments available from Sections 2, 4, 5, and 6 are
collected here to summarize the temperature field and the basis for the
temperature information.

5.5.1 Immediately above the propellant surface, where aluminum is largely
unburned, the thermochemical equilibrium calculations are probably the
best means of determining temperature, and indicate a temperature of

58

about 2350°K. The aluminum droplets would be at about the same temperature, with flame envelopes at about 3800°K. Because of low smoke density, line reversal methods would probably be useful to confirm the temperature of 2350°K.

5.5.2 **Proceeding outward in Region A**, the bulk temperature increases rapidly for roughly 20 to 30-cm because of heat release from aluminum combustion, with the temperature of the (shrinking) aluminum droplets remaining around 2500°K and the flame envelopes of the droplets running around 3800°K. The increasing amount of Al_2O_3 is mostly at the bulk temperature, except for the oxide on the burning agglomerates, which is at the droplet temperature of about 2500°K. These temperatures are based on thermodynamic arguments and constraints imposed by combustion dynamics. Measurements are reported in Section 6 based on measurement of thermal radiation, which support the above temperature estimates (particularly the bulk temperature). The temperature of the flame envelope could probably be determined by the spectral line method, and such measurements would probably help to evaluate the thermal radiation measurements of Section 6. Such measurements have been made in simple aluminum combustion situations (Reference 18), and support of flame envelope temperature 3800°K given below.

5.5.3 **At the outer limit of Region A and in Region B**, the aluminum is all burned and the temperature becomes microscopically uniform. In a large propellant sample where heat loss to the surroundings is minimal, the thermochemical equilibrium calculations are relatively accurate, and predict 3000 K. Measurement by the thermal radiation method (Section 6) on laboratory size samples yields somewhat lower temperatures, although the measurements were not made far enough out from the burning surface to avoid the difficulties of concurrent radiation from hotter flame envelopes (further measurement by this method seems desirable). Other optical methods of measurement are ot particularly promising in this region because

---

18. Mitchell, A. C. C., and M. W. Zamansky, _Resonance Radiation and Excited Atoms_, Cambridge University Press, London, 1971.

of the smoke density, while uncertainties in the smoke particle size distribution (Sections 8 through 11) complicate even the thermal radiation method (Section 6 and Appendix E).

5.5.4 <u>Temperatures in the air admixture Regions</u> (C and D) were not measured (because of limited interest) beyond the preliminary estimates implicit in thermochemical calculations (Figure 7), the photographs of plume spreading (Section 3), and the calculations of the mixing region (Appendix A). These inputs indicate that temperature change in the radial direction due to air admixture is gradual if air admixture does not involve breakdown of the plume because reaction with air initially counteracts cooling by the air (no temperature rise is indicated). In the current tests on laboratory scale samples, the complicating plume breakdown was so rapid that air was excluded by use of a combustion tube. In larger samples (e.g., 0.5 meter or so) the air admixture region is not likely to be important except as a possible barrier to optical measurements of the propellant combustion zone.

6 RADIATION

h.1 Introduction

Radiation in the combustion environment is of interest for two reasons, first because it is a cause of energy transfer to objects immersed in the fire environment, and second as a means of diagnosing the state of the environment. It was expected that the radiation would consist of emission lines of excited species in the gas (including aluminum flame envelopes), and of thermal radiation from the Al_2O_3. Further, the optical density of the fire environment due to Al_2O_3 droplets is a factor in all radiation. In the present work a rather superficial examination of the overall spectrum was made, and subsequent measurements were aimed at description of the emissivity and temperature of the primary radiators, the Al_2O_3 smoke droplets.

b.2 Spectrum

The overall spectrum was examined for open plumes with no attempt towards spatial resolution in viewing the plume. A wavelength-scanning spectrograph was used in the photographic mode, with repeat tests in different wavelength intervals. Figure 30 shows the resulting spectra. The various families of spectral lines were compared with lines tabulated for species expected in the flame, and lines due to chlorine, AlO, and iron were identified. A strong sodium doublet was also present, although sodium is present in the propellant only as an impurity.

The spectrograms were also recorded by graphs of the output of a photomultiplier unit. This type of record showed a great deal of fluctuation in brightness during the time of a wavelength scan (about 20 sec), with the spectral lines not always resolved from the bright continuum radiation and with more-or-less random superimposed fluctuations (Figure 31). This observation indicated that

a) the continuum radiation involved much more energy than the line spectra (Figure 31a)

b) the plume luminosity varied appreciably with time due to
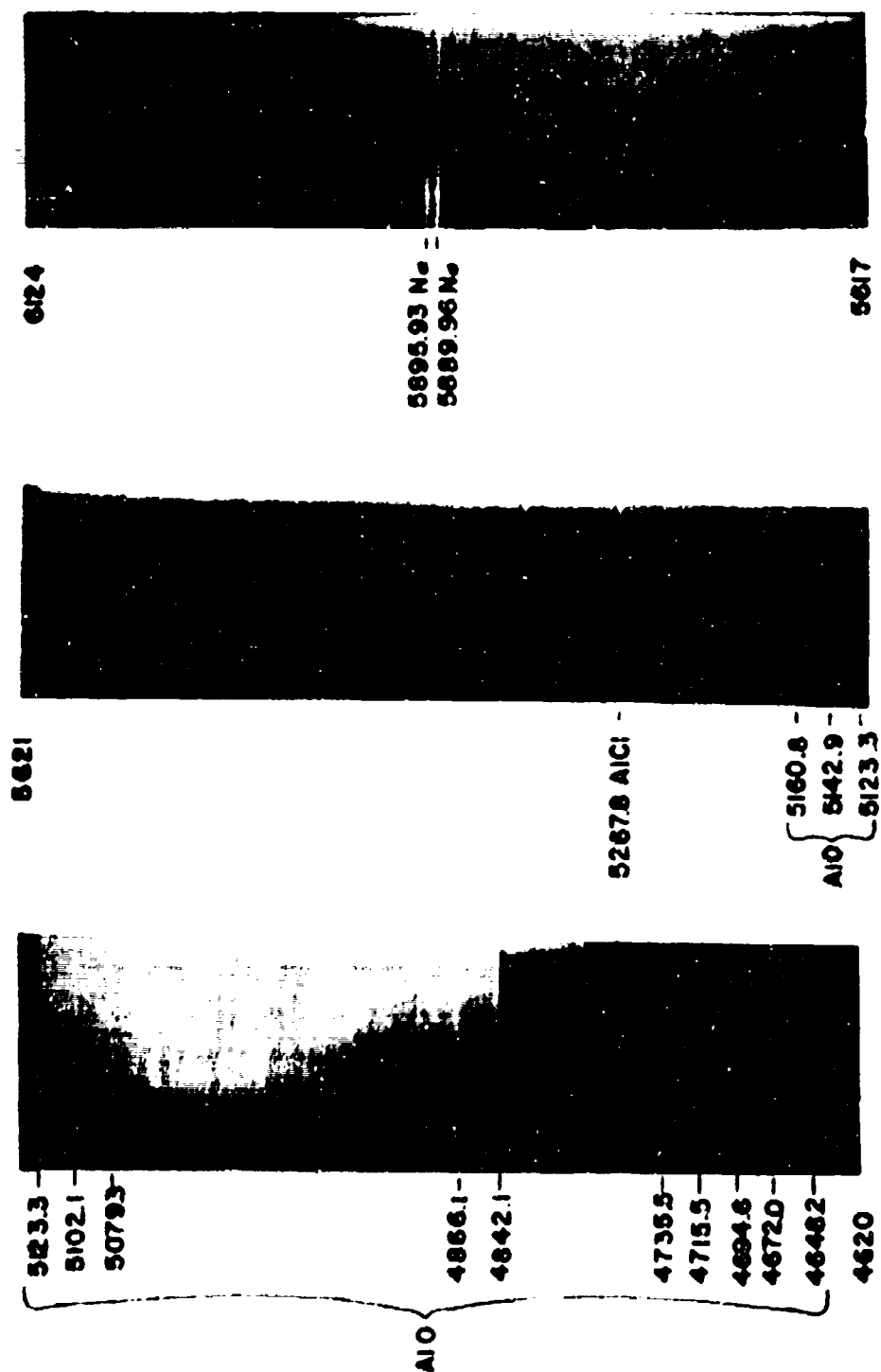
SPECTRA FROM 6124 TO 4620Å

Figure 30. Spectra from combustion plume of TP-300H at one atmosphere in air.
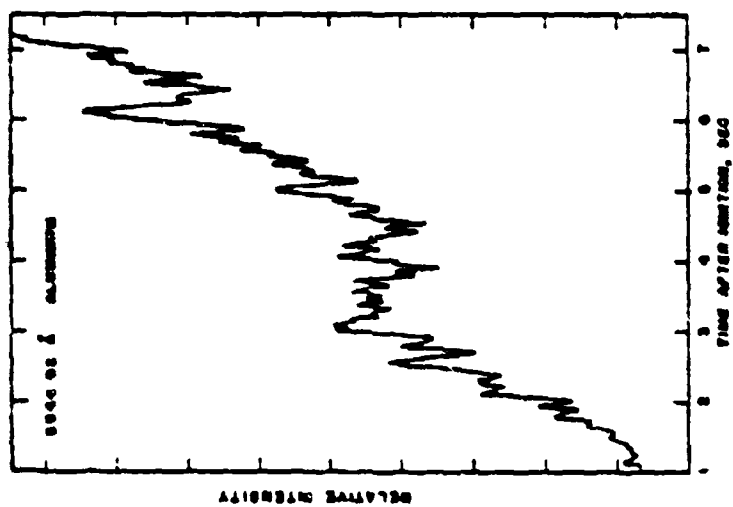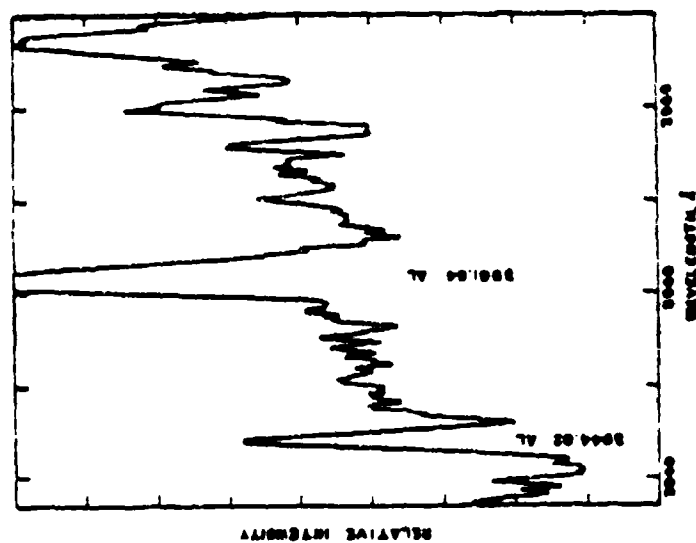
(b) Constant wavelength mode.

(a) Wavelength scanning mode.

Figure 31. Plume intensity recorded from photomultiplier output.

unknown causes (Figure 31b).

Because of the dominance of the continuum radiation, subsequent studies concentrated on it. From such studies one might hope to determine the emissivity and temperature of the bulk smoke cloud and plume gas, and at least probe the question of whether the numerically small but optically bright smoke droplets in the flame envelopes contribute appreciably to the radiation field. In the process it was necessary to consider also the random fluctuations in luminosity noted in the photometer records, a subject discussed in Section 6.4.

6.3 Continuum Radiation

The radiation from the bulk smoke cloud might be expected to conform to a black, or gray body radiation law relating radiation intensity, wavelength and temperature, given by Equation (2):

$$I = C_1 / \lambda^5 \left(e^{C_2 / \lambda T} - 1 \right) \tag{2}$$

In Equation (2), the coefficient C_1 contains a factor ϵ which is an unknown effective emissivity, equal to one for black bodies (refer to Appendix E for further details). Figure 32 shows the relation in Equation (2) for $\epsilon = 1$. From the figure it is evident that an intensity measurement at any particular wavelength establishes the temperature, if the emissivity is one. Concurrent measurements at more than one wavelength should then give the same temperature, as only one constant temperature curve goes through a given intensity-wavelength point, and all other intensity-wavelength points from that radiator temperature will be on the same constant temperature curve in Figure 32.

However, concurrent measurements were made at three wavelengths in order to deal with practical problems such as the following:

    a) Emissivity is usually not 1.0, is likely to be in the range of 0.10-0.80.

    b) For droplets in the size range of the oxide smoke, the
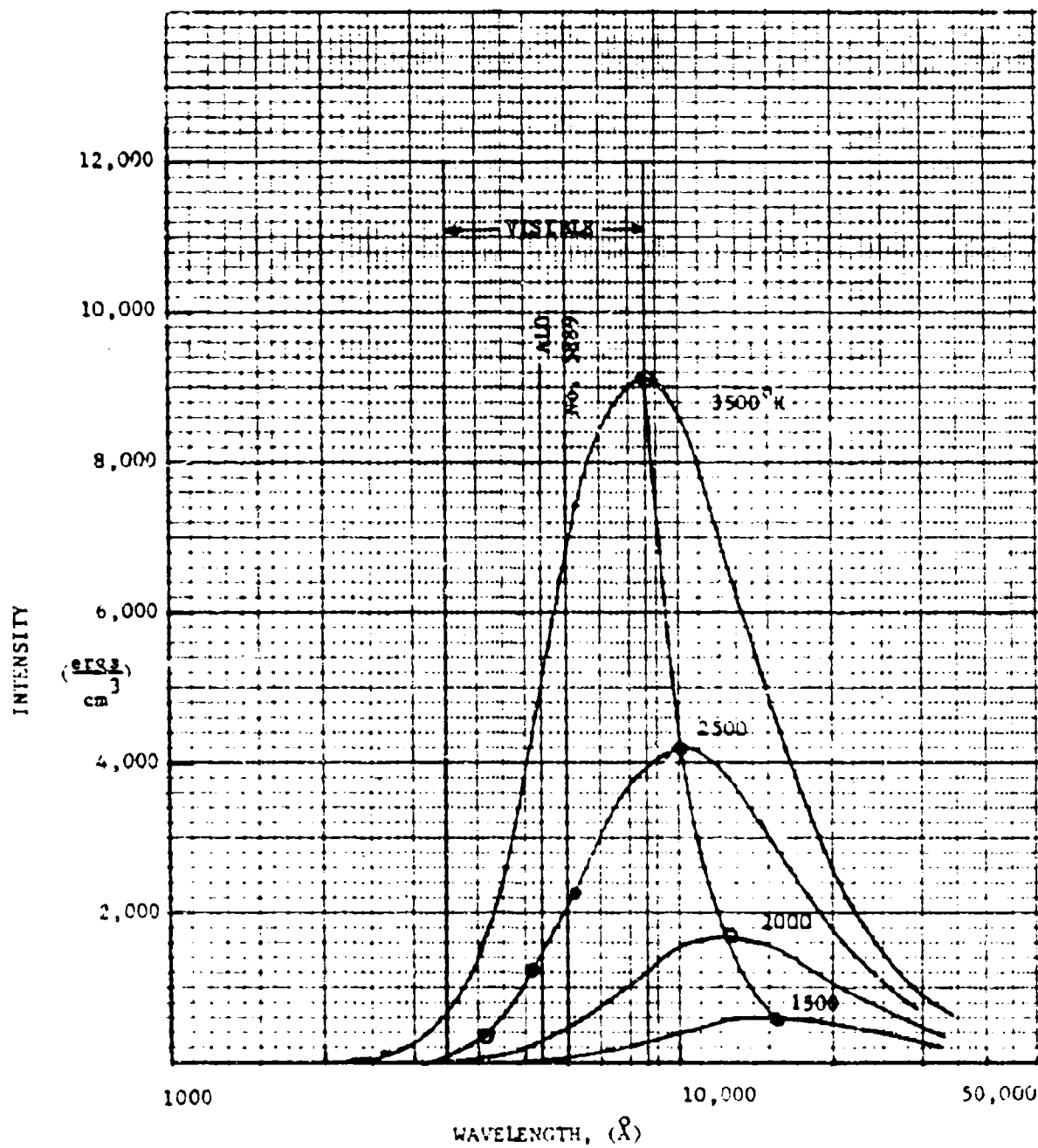
Figure 32. Black body radiation curves.

emissivity is dependent on wavelength.

　　　c)　In the present study the intensity of the source
is nonuniform.

Use of the 3-color measurements to correct for a and b is discussed in Appendix E. Problem c is discussed further in the next section, and appears to have affected test results considerably.

　　　As to the results (Appendix E), Table 5 summarizes typical temperatures determined from the intensity measurements. An emissivity of about

Table 5.　Summary of Temperature--Emissivity Calculations From Intensity of Continuum Radiation Measurements.

Wavelength pair used	Temperature calculated	Emissivity corresponding to listed temperature
5050 Å and 6000 Å	2840°K	0.030
4050 Å and 6000 Å	3330°K	0.006 to 0.025
4050 Å and 5050 Å	3750°K	0.001 to 0.008

0.030 and a temperature of about 2800°K are indicated in the basis of intensity measurements at 6000 and 5050 Å. This temperature agrees moderately well with calculated values (Section 2.3). However, the temperatures based on the wavelength combination 4050 and 5050 Å are higher. This result may be due to either problem b or c above. However, a correction (Appendix E) for problem b above, using concurrent intensity measurements at three wavelengths failed to resolve the problem, suggesting that problem c, the nonuniformity of temperature due to the hot flame envelopes around burning agglomerates, is complicating interpretation of the measurements. Consideration is now being given to a two-temperature interpretation

of measurements. In the meantime, the temperatures indicated by combination of the measurements at 6020 and 5050 Å are in reasonable agreement with other indicators of bulk smoke and gas temperature, and the higher indicated temperature calculated from the measurements at the shorter wavelengths of 4050 and 5050 Å suggest presence of a higher temperature source in the field of view.

6.4 Observation of Optically Heterogeneous Flows

The contrast in brightness of the bulk of the flow and that of the flame envelope around the burning agglomerates was a complexity of the fire environment that was consistently difficult to observe; as a result it was considered in some detail. Specifically, calculations were made of the effect of agglomerates passing in the field of view of the photometer system, and a qualitative diagnosis was made of the resolution of agglomerates in photography (Appendix B).

6.4.1 The Appearance of Agglomerates in the Photometer System

The photoelectric monitoring in the plume was accomplished by viewing the plume through a tube having one end opening inside the plume. This light tube limited the field of view seen by the photomultiplier tube. Initially it was assumed that the smoke would be too dense to see many agglomerates (i.e., that only those close to the light tube opening would be visible). Under these conditions, the occasional passage of an agglomerate through the field of view would produce a very brief (approximately 0.05 milliseconds) jump in apparent intensity, above a steady smoke background. However, observation of the test records showed continuous fluctuation in intensity, with duration of fluctuations being essentially random (Figure 31b).

The above results implied that the plume was much less uniform than previously supposed. At this point in the program it had been decided (for other reasons, Section 6.4.2) to take high speed motion pictures of the plume. The pictures revealed that the plume was less dense than supposed, and that smoke density was nonuniform (Figure 33). Thus one would expect to see more agglomerates through the light tube in the photometer system than previously supposed, and would expect to see also slower fluctuations in apparent intensity of the smoke cloud due to passage of

(a) Enhanced visibility of
    agglomerates due to short
    exposure.
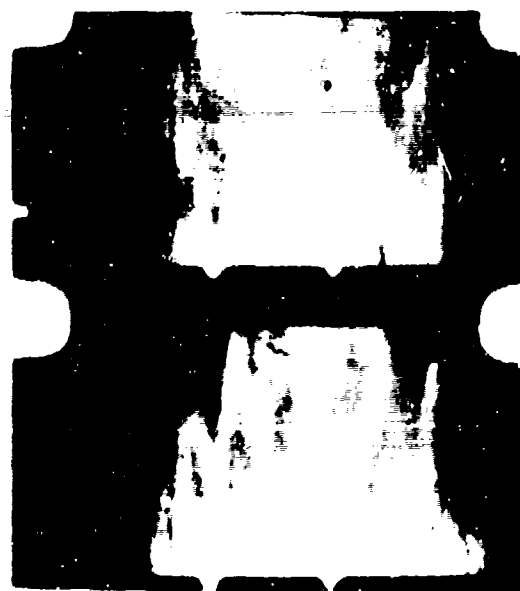
(b) Nonuniform smoke
    distribution.

Figure 33. High-speed pictures of details of the plume
           -- Region A.

nonuniform cloud past the field of view of the light tube. These results explained the intensity fluctuations in the photometer traces, but posed the problem (problem d of Section 6.3) that the field of view through the light tube was deeper than supposed (i.e., smoke was less dense) and would thus show more agglomerates than supposed. While this result is a positive contribution to knowledge of the fire environment, the realization of lower smoke density and higher agglomerate visibility serious complicates the interpretation of radiation measurements.

To examine the number of agglomerates to be expected in the field of view of the light tube, calculations were made of the number of agglomerates to be expected based on the aluminum droplet size and aluminum mass flow from the burning surface (Appendix C). This simple estimate of aluminum droplet population is summarized in Table 6. From the data shown, it

Table 6. Particles in a 1-cm^3 Field of View for a Photograph of Duration T.

Time (second) Diameter (μm)	1.0 second	1/10 second	1/100 second	1/1000 second	0.0 second
100	4.8×10^4	4.8×10^3	4.8×10^2	4.8×10	16
200	6×10^3	6×10^2	6×10	6	2
300	1.86×10^3	1.86×10^2	1.86×10	1.86	0.6

appears that a field of view from a 0.5-cm diameter light tube into a plume 1-cm thick would typically contain four, 100-μm agglomerates at any moment. In other words, radiation from the flame envelope around agglomerates would be visible in varying degree most of the time through the light tube. This is consistent with the conclusion of Section 6.3, i.e., that the thermal radiation reflects two sources at different temperatures (zones 1 and 3 of Section 5.2). Thus the experiments and theory indicate a variation in intensity with wavelength corresponding to concurrent contributions from a hot source (thermal zone 1, the flame envelope around

the burning agglomerate), and an appreciably cooler source (thermal zone 3,
the bulk gas smoke). The results also indicate a variation in time,
reflecting a photographically observable nonuniformity in smoke density,
and a density lower than expected. While no quantitative measurements
were made, an absorption coefficient of approximately 0.1/cm is estimated
from photographs.

6.4.2 Photography of Plume Optical Heterogeneity

One of the first problems encountered in this investigation was re-
solution of the burning agglomerates in the oxide smoke cloud (a classic
unsolved problem in rocket motor combustion studies). Figure 10 showed
how conspicuous the agglomerates were when the smoke was blown away, but
how inconspicuous they were in the smoke cloud. This was the reason the
smoke plume was assumed to be optically dense. However, this conclusion
was difficult to reconcile with other photographs that showed the plume
density to be low enough to discern objects through a 5-cm plume.

Resolution of the contradiction followed from more detailed considera-
tion of the exposure of the film during a single frame. Considering a
point on the film that is traversed by an agglomerate image during the time
the camera shutter is open, that point receives smoke radiation during the
entire time the shutter is open (Figure 34), but receives the radiation from
the agglomerate only briefly while its image traverses that point. Thus,
even though the agglomerate flame envelope is much brighter than the smoke,
its contribution to the total exposure at a point on the film can be small
compared to the smoke exposure (Figure 34). Hence within the combustion
plume the image of the agglomerate is a faint streak, hardly distinguish-
able from the smoke background, in spite of the greater brightness of the
agglomerate flame envelope.

The outcome of the foregoing considerations supports the repeated
observation that the flame envelope around the burning droplet is indeed
at high temperature, in spite of its low visibility in pictures of Region A
(Figure 1) of the plume. It also resolves the apparent contradiction
between photometric and photographic results regarding absorptivity of the

70
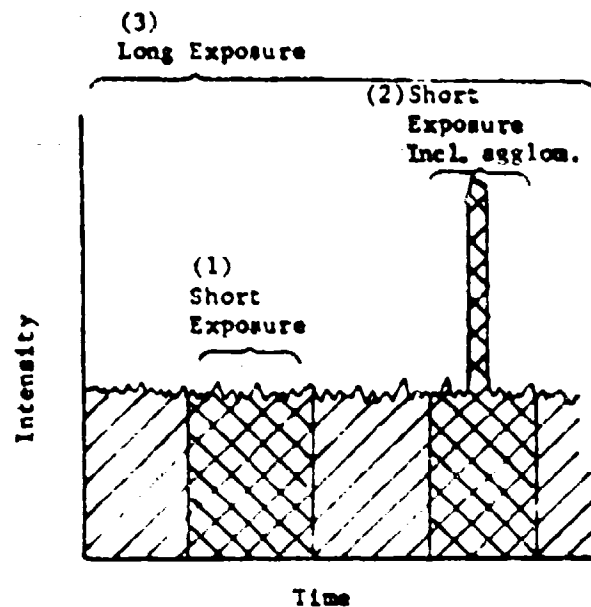
Intensity-time variation at a point on
the film traversed by an agglomerate image.
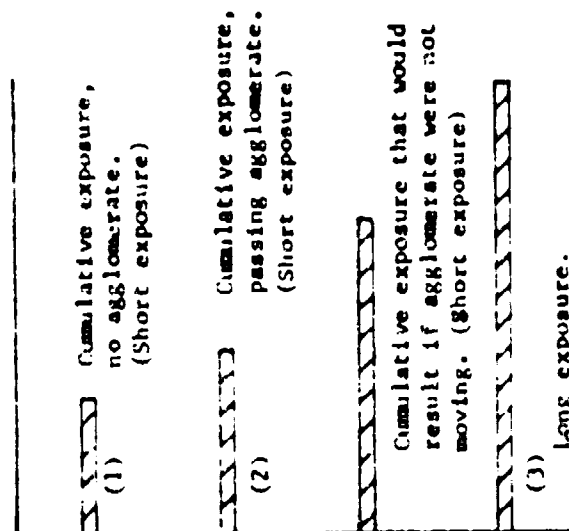
Total exposure at points on the film with
different exposure times and/or passage or
nonpassage of agglomerate image.

Figure 34.   Intensity versus time at a point on the photo-
graphic film during the time the shutter is
open.

smoke. Further, this interpretation suggests that pictures taken with a very short exposure time (comparable to the time for a moving agglomerate to travel only 2 or 3 diameters) would lead to high contrast between the hot agglomerate flame envelopes and the bulk smoke. This was verified by taking photographs at ~ 3000 frames per second with a high-speed motion picture camera. Figure 33a shows two successive frames of such a film, in which agglomerate streaks show against the smoke background. Figure 33b shows a sequence in which an inhomogeneity in the smoke cloud is also evident, as referred to in discussion of photometer records.

6.5   Status

The radiation field in the combustion zone shows spectral lines of several gaseous species, and a higher level of thermal radiation from the Al_2O_3 smoke cloud. Measurements of the smoke cloud[*] indicate a temperature of about $2800°K$, an emissivity of 0.03, and an absorption coefficient of about 0.1/cm. Intensity-emissivity measurements are wavelength-dependent, apparently due to presence of that small amount of smoke that is in the agglomerate flame envelopes, which is much hotter than the bulk volume. The methods of the present study could apparently be adapted to resolve the smoke and flame envelopes, but were not attempted in the work to date. Also, it is desirable to carry out a more systematic study of the smoke radiation as a function of location in the plume, as the contribution from flame envelopes is a function of distance from the burning surface.

The results clarified the details of spatial nonuniformity of luminosity due to agglomerates and nonuniformity of the smoke cloud, and the requirements for photography or photometric resolution of these nonuniformities. While these details are not particul [ly] important to effect of the fire environment, they are important to a consistent and mechanistically correct interpretation of test results, and design of future experiments.

---

[*] Observations 15-cm from the burning surface. A systematic measurement as a function of position in the plume was not completed.

7 VELOCITY, DENSITY AND MASS FLOW RATE

7.1 Introduction

In analyzing heat transfer (or mass deposition) on an object immersed
in the fire environment, the temperature plays a critical role (as in
Equation (1)). However, any detailed analysis of heat transfer calls for
further details of the flow such as flow velocity and density. As we have
seen, the heat transfer from two-phase flow involves velocity of both gas
and condensed phase, which may differ just as the temperature may differ.
Indeed, the behavior of the condensed phase is so important to the present
problem, that we have, and will in later Sections, dwelled at length on the
droplet size distribution that controls deposition. In the present section,
the arguments regarding the values of the classical variables in heat trans-
fer are collected from various analyses and measurements (some detailed
elsewhere in the report, e.g. Appendix F).

7.2 Mass Flow Rate, Gas Properties

The flow rate is governed by the burning rate of the propellant,
which was reported in Table 3 and observed to be about 0.127 cm/sec
(atmospheric pressure, 20^{c}C). The propellant density is 1.76 g/cm^3,
hence the mass flow rate from 1-cm^2 of burning surface is 0.224 g/cm^2 sec.
When the aluminum is completely unreacted, the mass flow rate of gas is
0.188 g/cm^2/sec and the mass flow rate of aluminum is 0.036 g/cm^2/sec.
When the aluminum is completely reacted, the mass flow rate of gas is
0.156 g/cm^2/sec, and the mass flow rate of Al$_2$O$_3$ is 0.068 g/cm^2/sec. These
figures are based on the assumption that the flow proceeds perpendicularly
from a flat burning surface. The spatial distribution of the transition
from all aluminum to all Al$_2$O$_3$ is discussed in Sections 8 through 11.

7.3 Density of the Flow

Near the burning surface, the values of temperature and molecular
weight of the gas given by the thermochemical calculations are 2350°K
and 23.8. Assuming a perfect gas, and negligible volume for the condensed
phase, the density of the gas is

$$\rho = \frac{pM}{RT}$$

where R is 82.05, for T in $^\circ K$, and p in atm. Thus for $M = 23.8$, $T = 2350^\circ K$ and $p = 1$ atm, $\rho = 1.23 \times 10^{-4}$ g/cm^3. For the gas in the region where all the aluminum is reacted to Al_2O_3, one gets $M = 18.7$, $T = 2990^\circ K$ and $p = 1$ atm, ρ is 0.75×10^{-4} g/cm^3.

7.3 Velocity

Following Sections 7.1 and 7.2, it is possible to calculate a corresponding plume velocity from the relation

$$\dot{m} = \rho v$$

The velocities obtained from this relation are shown in Table 7 for corresponding mass flow rates and densities. These are the velocities calculated from the thermochemical data (i.e., values of temperature and molecular weight), and pertain to a physical situation where flow is one-dimensional, with condensed material moving at the same speed as the gas. In experiments, the velocity may be more or less than these values, and are discussed below and in Appendix F.

Compared to the one-dimensional flow calculation, the real situation is considerably more complex. The inertia of the aluminum agglomerates is sufficient to require a significant portion of the burning time for them to come up to the speed of the gas flow. This velocity lag effect is calculated in Appendix F, and the dependence of droplet velocity on distance from the burning surface is shown in Figure 35 for various agglomerate sizes. From the standpoint of either experimental observation of velocity, or calculation of impingements on objects in the combustion zone, the velocity lag is a significant consideration. Beyond the combustion zone, the residual oxide droplets are near to the gas velocity.

In combustion studies with convenient size samples, the velocities may be below or above those in large-sample fires. In an open plume, velocities tend to be reduced by air entrainment, and experimental observations tend to emphasize these more visible slower agglomerates, which are not obscure by smoke. In enclosed plumes, velocities tend to be low near
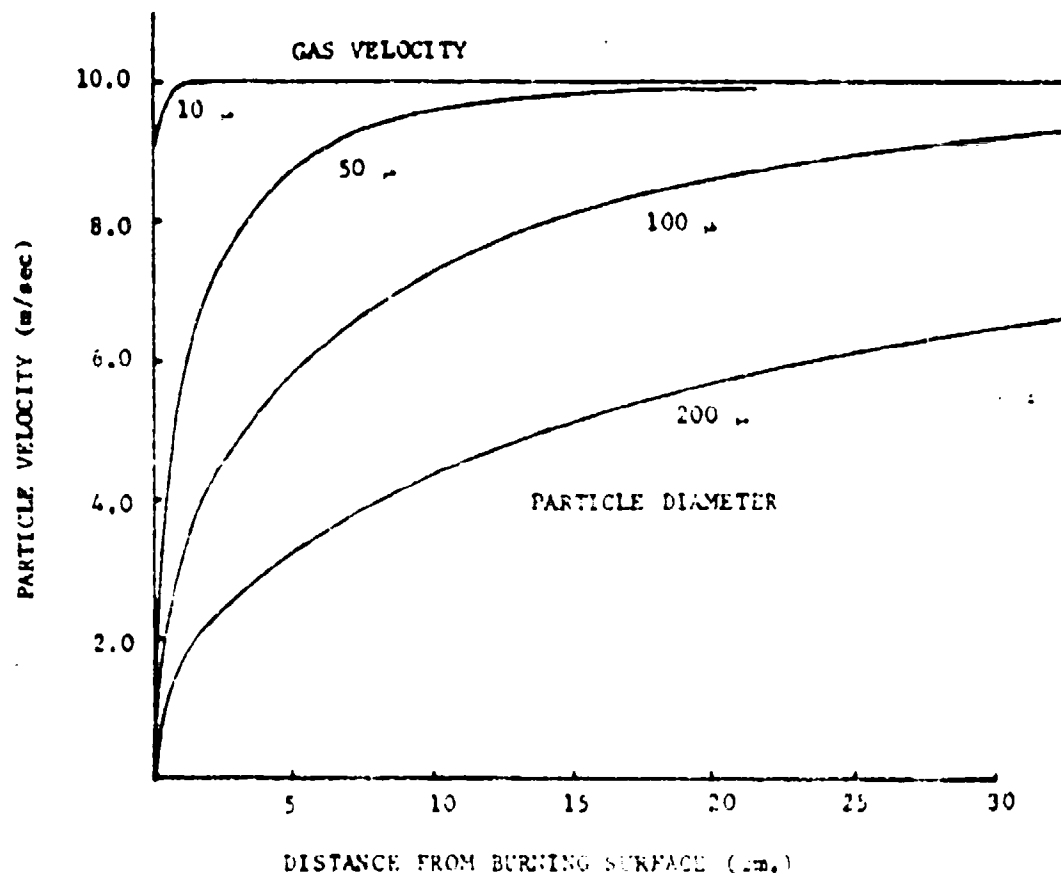
Figure 35. Velocity lag of agglomerates in the plume.

the tube wall, but can be higher than normal on the tube axis (Appendix F). As a result, experimental observations of velocity made on axis may give values higher than those in Table 7. Higher values may also result if the propellant sample burns irregularly with more than expected burning area.

Experimental observations were made by single frame snap shots, high speed motion pictures and streak camera methods (Appendix F). These methods collectively show velocities of agglomerates and smoke. The principal results are summarized in Table F-3 of Appendix F, and are in reasonable agreement with the results based on the thermochemical and velocity lag calculations.

In the event that a more refined determination of the velocity field for agglomerates were required, a more thorough series of measurements and calculations would be desirable--including more accurate determination of the initial agglomerate size distribution, and calculation of velocity lag allowing for changing size of the agglomerates as they move out in the plume.

Table 7. Conditions in the Flow Near the Burning Surface, and After All Aluminum is Reacted.

(Pressure = one atmosphere)

Location in plume	r cm/sec	$\overset{o}{m}$	$\overset{o}{m}_K$	$\overset{o}{m}_{Al}$	$\overset{o}{m}_{Al_2O_3}$	mole wt. M	T^oK	ρ g/cm³	v_g m/sec
			g/cm²/sec						
The burning surface	0.127	0.224	0.1877	0.036	0.0				
About 1 cm above the burning surface	---	0.224	0.1877	0.036	0.0	23.8	2350	1.23×10^{-4}	15.26
Beyond the aluminum combustion region	---	0.224	0.1558	0.0	0.068	18.7	2990	0.76×10^{-4}	20.50

77

8 BURNING HISTORY OF SINGLE
ALUMINUM DROPLETS

8.1 Introduction

The experimental determinations of spatial distribution of aluminum combustion and of aluminum and oxide droplet size distribution is a singularly difficult task, not yet fully accomplished in a quantitative sense. An analytical representation of the combustion of the aluminum droplet population is an important means of supplementing and summarizing experimental results. In the process, current and past experiments can be related to mechanistic arguments, and the analysis then provides a basis for representing collected results in a form needed for future studies of effect of the combustion environment on immersed objects. In the next three sections, an analytical procedure is developed for description of the evolution of the aluminum droplet cloud into an aluminum oxide cloud. In the present section, representation of the burning history of single drops is discussed and developed. In Section 9, the analysis is extended to the burning history of a population of droplets, and in Section 10 the development of the Al_2O_3 droplet population is described.

8.2 Aluminum Droplet Diameter vs Time

Much published work on droplet burning (e.g. References 19 and 20) describes results in terms of burning time of droplets. Although results are somewhat divergent, Equation (3a) approximates most experimental results

$$\tau = kD_o^{\,n} \tag{3a}$$

where τ is the time to burnout and D_o is the initial diameter.

---

19. Davis, A., "Solid Propellants: The Combustion of Particles of Metal Ingredients," Combustion and Flame, Vol. 7, No. 4, December 1963, p. 359-367.

20. Hartman, K. O., "Ignition and Combustion of Aluminum Particles in Propellant Flame Gases," Chemical Propulsion Information Agency Publication 220, Vol. I, November 1971, pp. 1-24.

Experimental values of n range from 1.5 to 2.0, and there is no com-
pelling argument for a specific value in this range. The factor k is
related to several variables, the most important being the concentration
of the oxidizing species.

In the present analysis it will be assumed that Equation (3b) applies
anytime during burning of droplet, i.e.,

$$\tau = kD^n \qquad (3b)$$

Since the droplet changes its character by accumulation of Al_2O_3 on the
droplet during burning, this assumption is not trivial, but there is no
way to validate it or make a more precise representation without further
research.

If time, t, is measured from the start of burning of the droplet,
then it can be shown from Equation (3b) that the droplet diameter decreases
with time (Appendix G) according to

$$\frac{D}{D_o} = \left(1 - \frac{t}{kD_o^n}\right)^{1/n} \qquad (4)$$

This relation continues until burnout given by $t = \tau = kD_o^n$, at which
time the surface oxide is presumed to consolidate into one, or a few
droplets that contribute to the local oxide droplet population (Section 10).

8.3   Aluminum Droplet Mass: Oxide Mass

For most practical purposes such as determining percent aluminum
burned, or impingement characteristics of droplets, the droplet mass is
more important (but harder to measure) than the diameter. For this
information, Equation (4) is easily used to obtain

$$\frac{m}{m_o} = \left(\frac{D}{D_o}\right)^3 = \left(1 - \frac{t}{kD_o^n}\right)^{3/n} \qquad (t < kD_o^n) \qquad (5)$$

Figure 36 shows the variation in diameter and mass of the aluminum droplet with time, based on Equation (5). Section 8.4 discusses briefly the significance of the accumulation of oxide in the agglomerate surface, and then attention is turned in Section 9 to the analytical representation of a population of agglomerates.

8.4   Oxide Resulting from Burning of Droplet

At all times the burned portion of aluminum is assumed to give Al_2O_3 and therefore at each time we have a certain amount of oxide produced. An α fraction of this goes away in the fine smoke form and $(1 - \alpha)$ portion remains accumulated on the droplet itself.

In the foregoing analysis it has been assumed that the aluminum droplet is spherical, an assumption motivated partly by lack of sufficient information for a better quantitative representation of agglomerates, and motivated partly by computational difficulties in use of more complex models. However, it is recognized from the start that the aluminum droplet has one or more oxide lobes of uncertain shape and size. It is assumed for convenience (and lack of evidence to the contrary) that each aluminum droplet has one oxide lobe, that this lobe contains a mass fraction $(1 - \alpha)$ of the total oxide produced by the droplet, that it is retained until burnout of the parent aluminum droplet, and then forms a single residual oxide droplet. When $t > kD_o^{n}$

$$\frac{D_{oxr}}{D_o} = \left[\frac{\rho_{Al}}{\rho_{Al_2O_3}} \frac{102}{54} (1 - \alpha) \right]^{-1/3} = c \tag{6}$$

In our computational scheme, the expression on the right is a constant, of value roughly 0.65 (Appendix G).
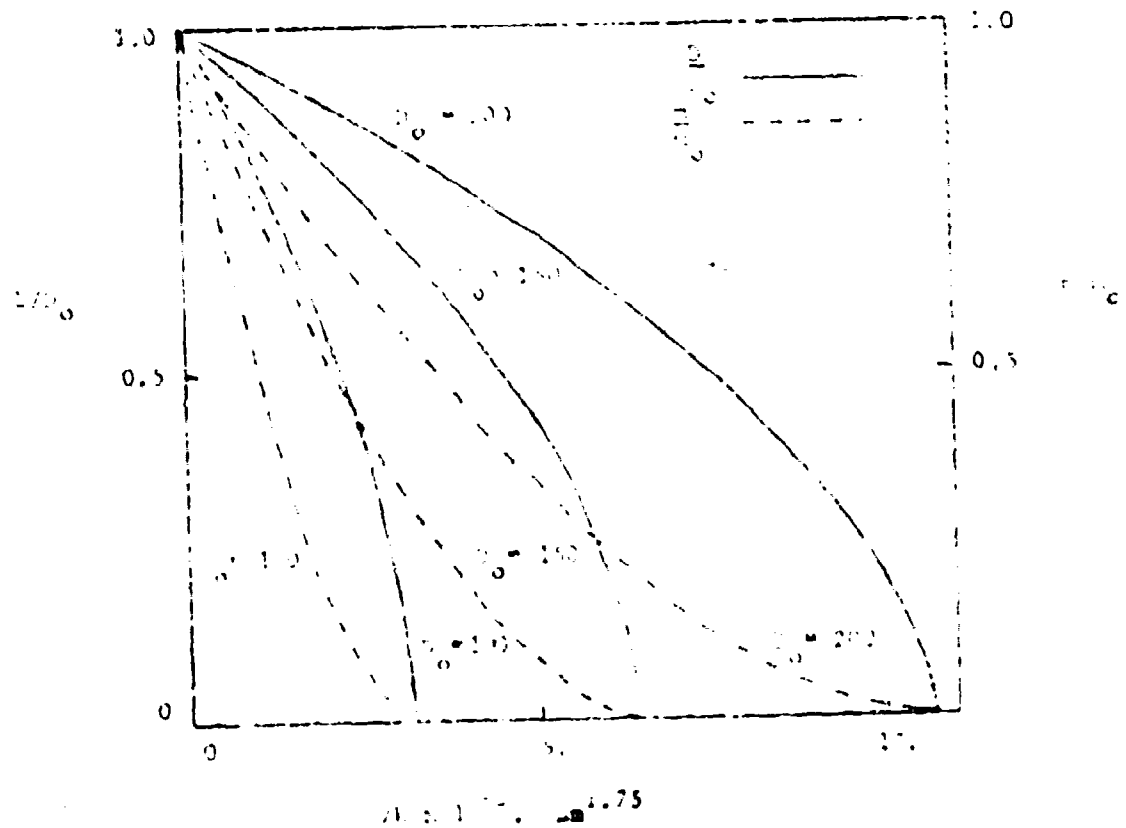
Figure 35. Diameter and mass of burning droplets versus time (Equations 4, 5, and 5).

9 BURNING HISTORY OF DROPLET POPULATION

9.1 General Trend of Population

As noted earlier, the nature of the droplet population starts with
some agglomerate size distribution leaving the burning surface, which can
in principle be measured by high speed, high resolution photography. The
population then proceeds to one of increasing oxide, which consists of
three distinct kinds of droplets (Figures 21 and 22).

a) burning agglomerates with lobes of molten oxide,

b) oxide droplets formed from the agglomerate oxide residual
   oxide droplets: e.g., droplets remaining when the aluminum
   burns to completion),

c) fine oxide droplets (smoke) formed in the detached flame
   envelope around the burning agglomerate.

The trends of these three parts of the droplet population are entirely
different as the material moves away from the burning surface. Further,
our interest in the parts of the population differ, as does our ability
to measure them. In the present section the trend of the aluminum popula-
tions is analyzed.

9.2 Strategy for Calculating Population

To calculate the droplet population versus position in the plume, it
is assumed that the initial droplet population is determined experimentally.
A widely used empirical burning rate law for aluminum droplets is used to
calculate the changing size of the agglomerates, with the parameters in the
law adjusted on the basis of results of various experimental investigation
(including particularly those of the present project).

Summation of the aluminum droplet population gives the aluminum con-
centration and fraction of aluminum burned--a quantity which is also
determined experimentally to permit a further check on selection of drop-
let burning parameters. Further, the percent-aluminum-burned figure permits
use of the chemical equilibrium data to determine the composition of gases,
the density, and temperature.

9.3 The Initial Droplet Distribution

A measurement of droplet size leaving the burning surface is obtained by measuring the diameter of all droplets for a period of time (Appendix C), over a small surface area. It is assumed that this is equivalent to measuring the size distribution over a large area of the surface in a short time interval, i.e., that surfacewise averaging is analagous to timewise averaging. The resulting measurements are tabulated as ΔN vs D_0, as illustrated in the sketch in Figure 37a, or as $\Delta N/\Delta D$ vs D as in Figure 37b. In Figure 37a, the number of droplets is indicated by the ordinate, while in Figure 37b, the number of droplets (in a ΔD interval) is indicated by the area under the curve

$$\Delta N = \text{Ordinate} \times \Delta D \tag{7}$$

and the total number of droplets in the volume samples is the area under the total curve. For the present purposes it is advantageous to normalize the distribution by dividing by the total number of droplets

$$\frac{\Delta D}{N} = \frac{\text{Ordinate}}{N} \times \Delta D \tag{8}$$

If the histogram is based on an adequate sample, it corresponds to a distribution function for the propellant, $\mathcal{J}_0(D)$ such that (see Appendix G)

$$\frac{dN_0}{N_0} = \mathcal{J}_0 \langle D_0 \rangle \, dD_0 \tag{9a}$$

Use of a differential notation implies that one is describing an indefinitely large sample, which is characteristic of the particular propellant and combustion environment. The subscript 0 refers to conditions near the burning surface, where the approximate size distribution is measured experimentally from high speed motion pictures (see Appendixes B and C).

For the present investigation, the mass-size distribution is probably of greater interest than the number-size distribution in Equation (9). The
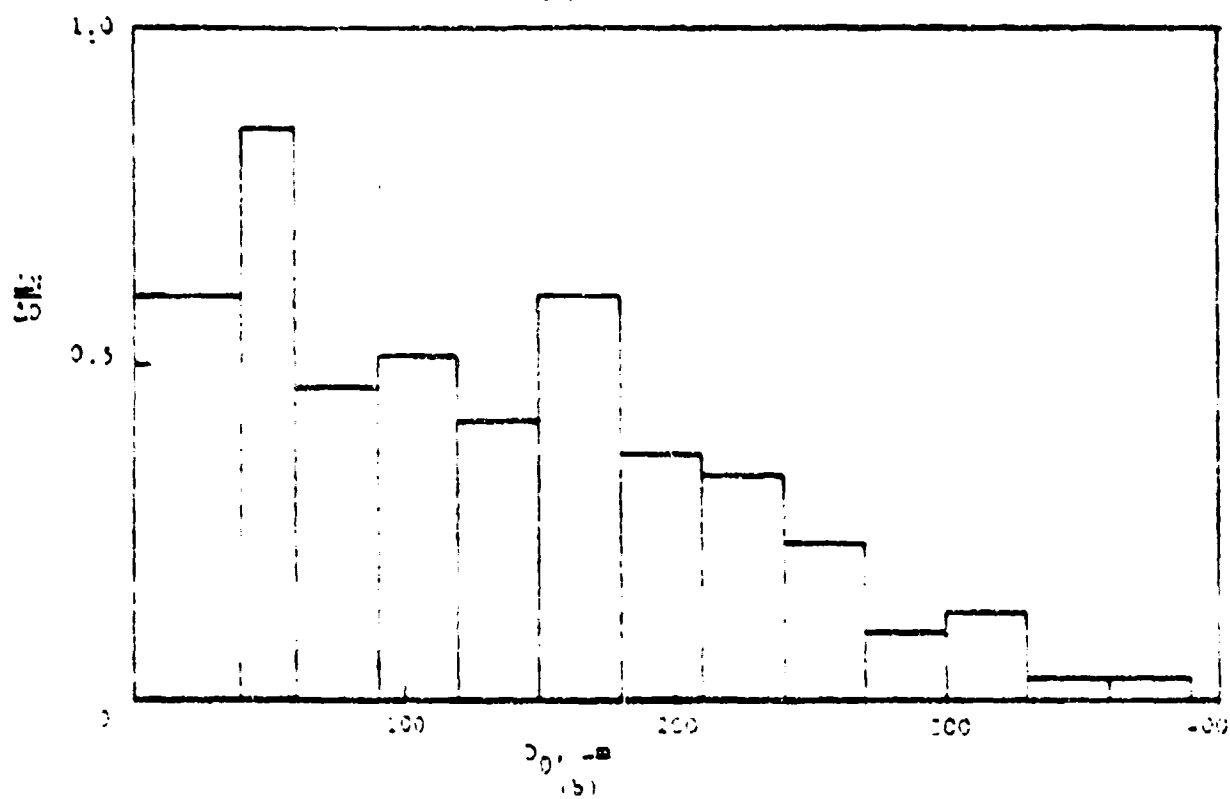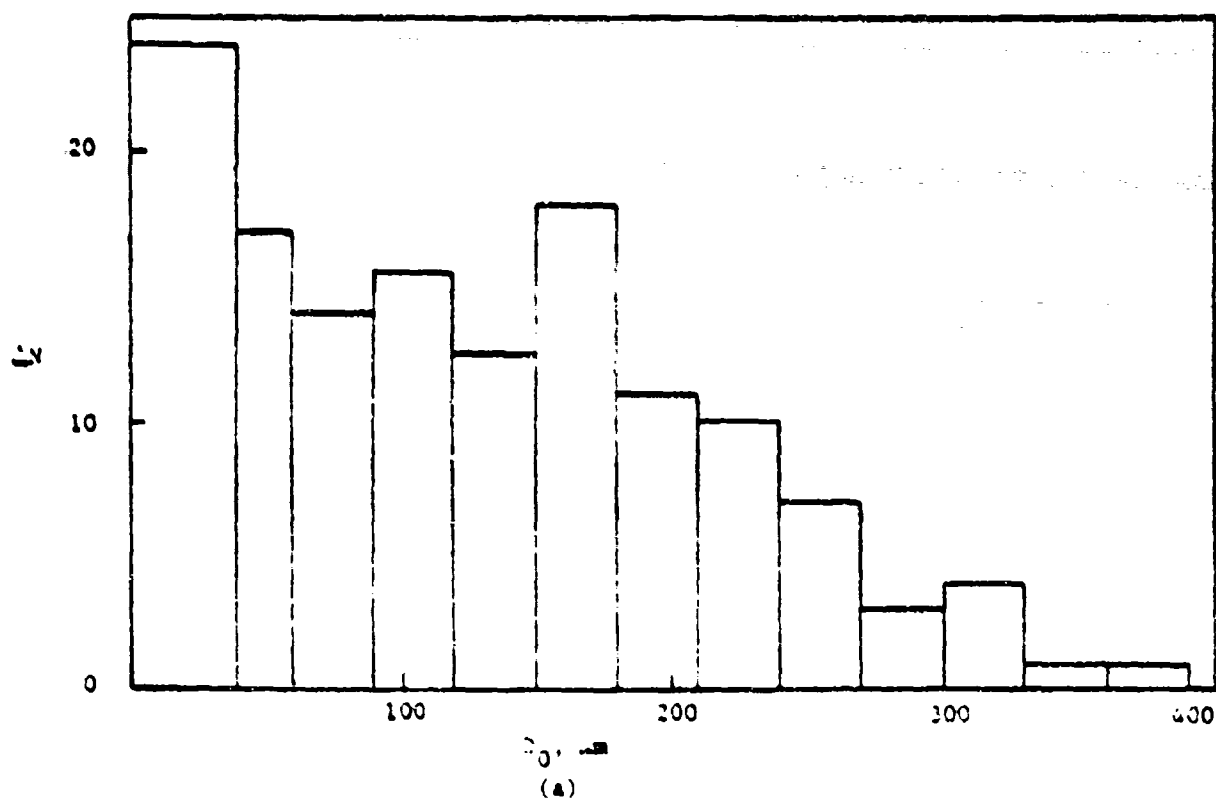
Figure 37. Measured initial size distribution, (corrected for flame stand-off).

mass-size distribution may be written in terms of the number-size distri-
bution as F_0 in

$$\frac{dm_0}{m_0} = F_0(D_0) \, dD_0 \tag{10a}$$

where

$$dm_0 = \frac{\pi}{6} D_0^3 \, dN = \frac{\pi}{6} D_0^3 N_0 \, \mathcal{F}_0(D_0) \, dD_0$$

and

$$m_0 = \int_{D_0=0}^{D_0=\infty} dm_0 = \frac{\pi}{6} N_0 \int_{0}^{\infty} D_0^3 \, \mathcal{F}_0(D_0) \, dD_0$$

Then

$$F_0(D_0) = \frac{D_0^3 \, \mathcal{F}_0(D_0)}{\int_{0}^{\infty} D_0^3 \, \mathcal{F}_0(D_0) \, dD_0} \tag{11a}$$

The distributions $\mathcal{F}_0(D_0)$ and $F_0(D_0)$ estimated from the motion pictures
taken near the burning surface are shown in Figure 36.

9.4   Change in Size Distribution with Time

As the aluminum droplets move away from the burning surface, their
sizes decrease due to burning (Section 8). The notation for the number, and
mass distribution functions is generalized to represent the changing popu-
lation as follows

$$\frac{dN}{N_0} = \mathcal{F}(D,t) \, dD \tag{9b}$$

$$\frac{dm}{m_0} = F(D,t) \, dD \tag{10b}$$

85
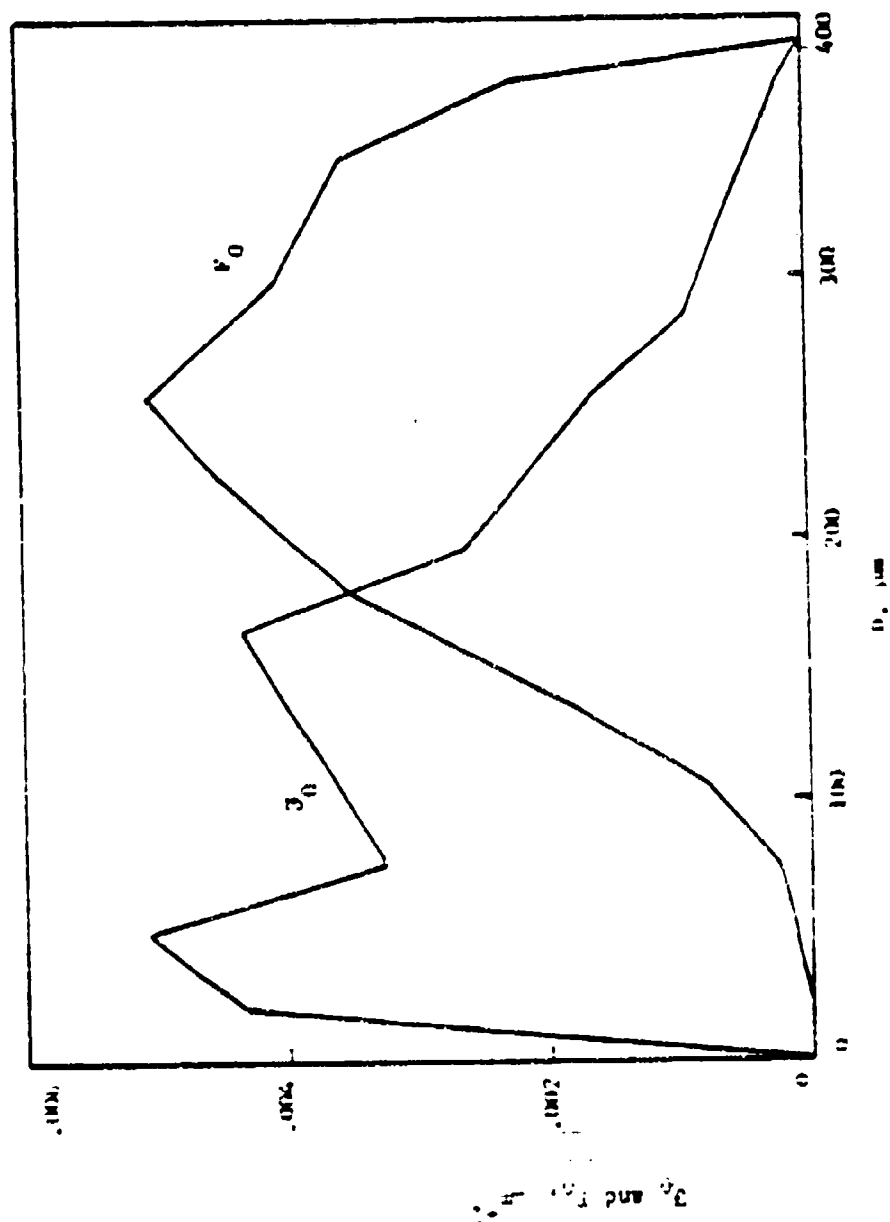
Figure 38. The population and mass distribution functions, $\mathfrak{z}_0$ and P_0, estimated from median pictures.

and by analogy with Equation (11a),

$$F(D,t) = \frac{D^3 \, \mathfrak{F}(D,t)}{\int_{\cdot}^{r^*} D_0^3 \, \mathfrak{F}_0\left(D_0\right) \, dD_0} \qquad (11b)$$

Thus the definitions of the distribution functions have been extended to apply to later times, after the initial droplet population has moved out in the combustion zone, and the relation between the number and mass distribution function has been correspondingly extended. It remains to show how these functions can be related to the initial distribution function so that they can be calculated from the experimentally determined initial distribution.

When the droplets burn, they are assumed here to follow the relation of Equation (4). A set of droplets dN in the initial size interval D_0 to $D_0 + dD_0$ must satisfy both Equation (9a) (at $t = 0$) and Equation (9b) at the later time*, i.e.,

$$\frac{dN_0}{N_0} = \mathfrak{F}_0\left(D_0\right) \, dD_0 = \mathfrak{F}(D,t) dD = \frac{dN}{N_0}$$

or

$$\mathfrak{F}(D,t) = \mathfrak{F}_0\left(D_0\right) \frac{dD_0}{dD} \qquad (12)$$

where dD is the interval in which the dN droplets are contained at time t. This differential can be obtained from Equation (4) in terms of dD_0 and t (Equation (G-10))

$$\left(dD/dD_0\right) = \left(1 - t/k \, D_0^n\right)^{(1-n)/n} \qquad (13)$$

_____

* This assumes that all droplets move out at the same speed.

Then, corresponding to Equation (G-13)

$$\Im(D,t) = \left(1 - t/k \, D_0^{\,n}\right)^{(n-1)/n} \Im_0\left(D_0\right)$$

$$\text{for} \quad D_0 > (t/k)^{1/n} \tag{14}$$

$$\Im(D,t) = 0 \quad \text{for} \quad D_0 < (t/k)^{1/n}$$

which gives the distribution function at time t in terms of t and the initial distribution function, $\Im_0$. The second equality, $\Im = 0$, corresponds to droplets that have burned out, and accounts for the decrease in N with time.

As noted before, we are concerned particularly with the mass-size distribution, now as a function of time starting with that in Equation (11a). The desired function is defined in Equation (11b), and the goal is (by analogy with Equation (14) to express it entirely in terms of the initial size distribution and time. Combinations of Equations (11b), (13), and (14) gives the desired result

$$\Im(D,t) = \frac{dm}{m_0} / dD = \frac{\left(1 - t/k \, D_0^{\,n}\right)^{(n+2)/n} D_0^{\,3} \, \Im_0\left(D_0\right)}{\int D_0^{\,3} \, \Im_0\left(D_0\right) dD_0}$$

$$\text{for} \quad D_0 > (t/k)^{1/n} \tag{15}$$

$$F(D,t) = 0 = \quad \text{for} \quad D_0 < (t/k)^{1/n}$$

Collectively Equations (14) and (15) provide the means to calculate the size distributions during burning, once the initial size distribution is known. The specific burning rate law for droplets is reflected in the coefficients involving $(1 - t/k \, D_0^{\,n})$ and in the burnout condition implicit in the limit $D_0 > (t/k)^{1/n}$. Figure 40 shows the number-size distribution

$\mathcal{J}(D,t)$ at several times during burning, based on the initial distribution shown in Figure 38. Figure 39b shows the corresponding mass-size distributions $F(D,t)$.

The areas under the $\mathcal{J}$ and F curves correspond to $\int \mathcal{J}dD$ and $\int FdD$, which in turn correspond to the proportion of droplets and droplet mass respectively at each time t. The areas are shown in Figure 41 as a function of time. The curves show, as one might expect, that the number of droplets decreases very rapidly as the smaller droplets burn out in large numbers-- while the mass decreases less rapidly because the original mass was in the larger diameter, longer-burning droplets. Fifty percent of the mass was burned in 0.045 second. For a flow velocity of 15 m/sec in the plume, this corresponds to 0.68 meter (25 inches) from the burning surface.

9.5 Relation of Other Aspects of the Problem

The aluminum droplet population is an important attribute for description of the fire environment for three reasons.

1. Combined with information on velocity, the population describes the size of aluminum droplets present to impinge on immersed objects.

2. The integrals of the distribution function give the net amount of aluminum burned, which is needed to use the chemical equilibrium calculations to get local temperature and composition.

3. The development of Al_2O_3 in the plume results from the changing aluminum population, and is described in the next section. The size distribution of the oxide droplets is important to the effect of the fire environment on immersed objects.

89
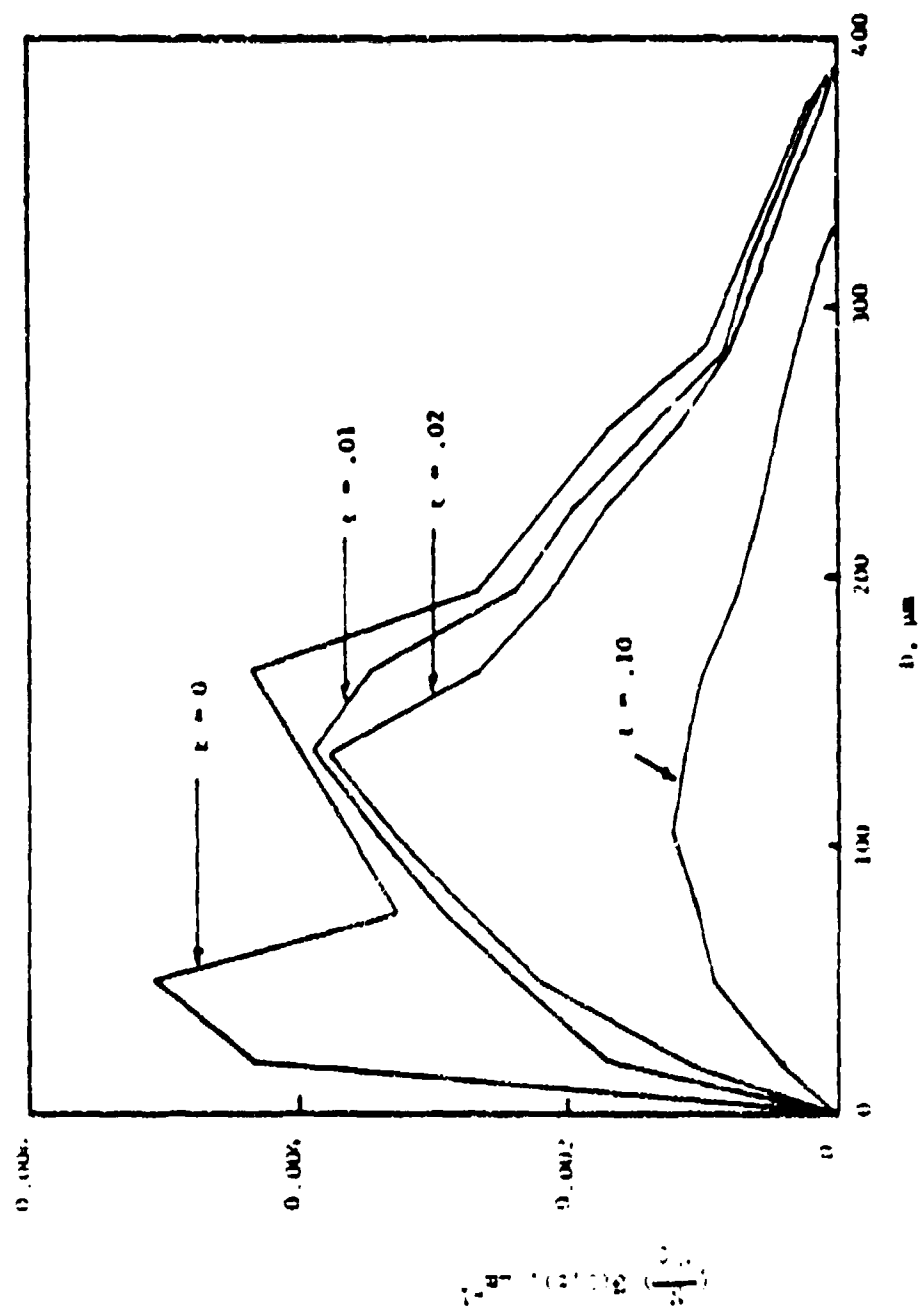
Figure 39. Droplet population distribution versus diameter at different times.
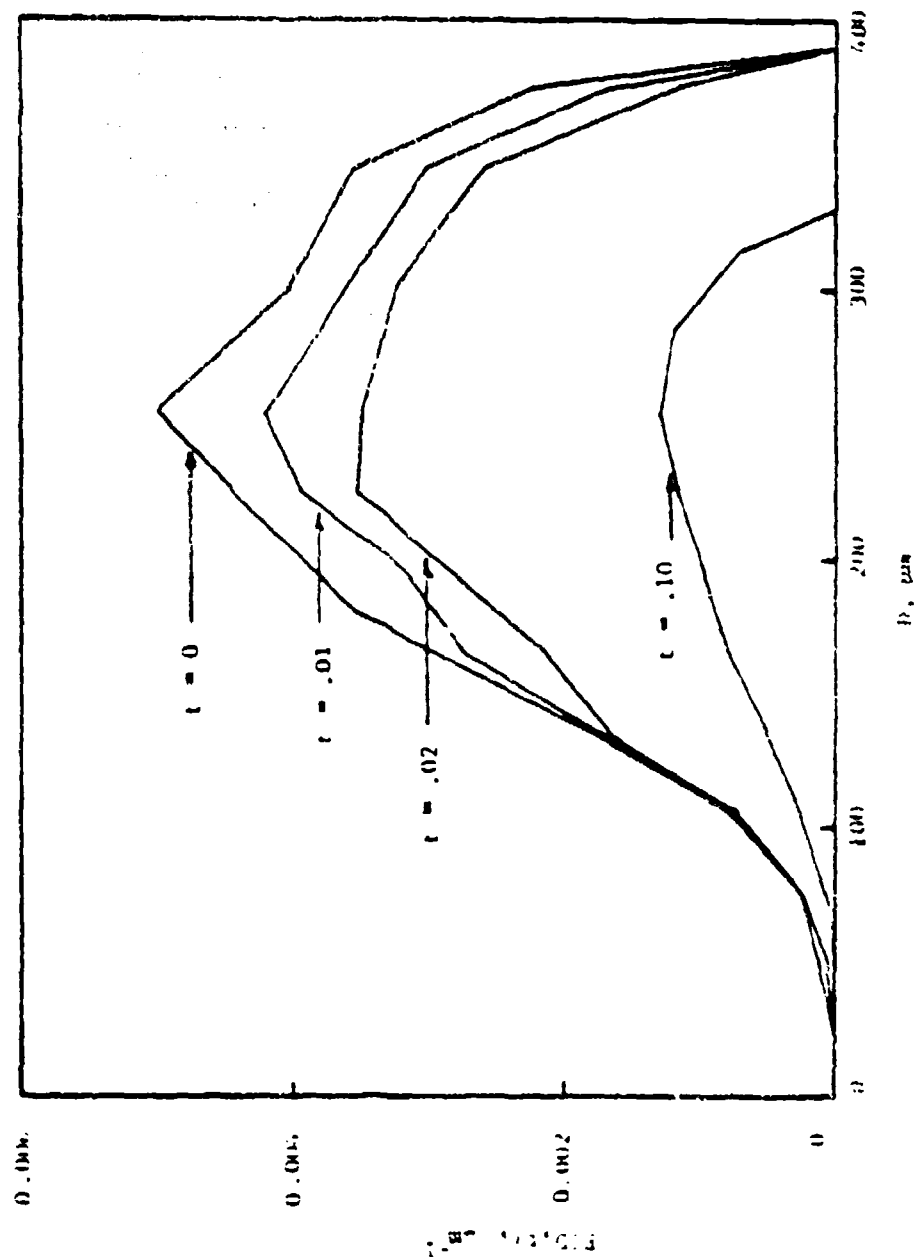
Figure 40. Mass distribution of agglomerates versus diameter at different times.
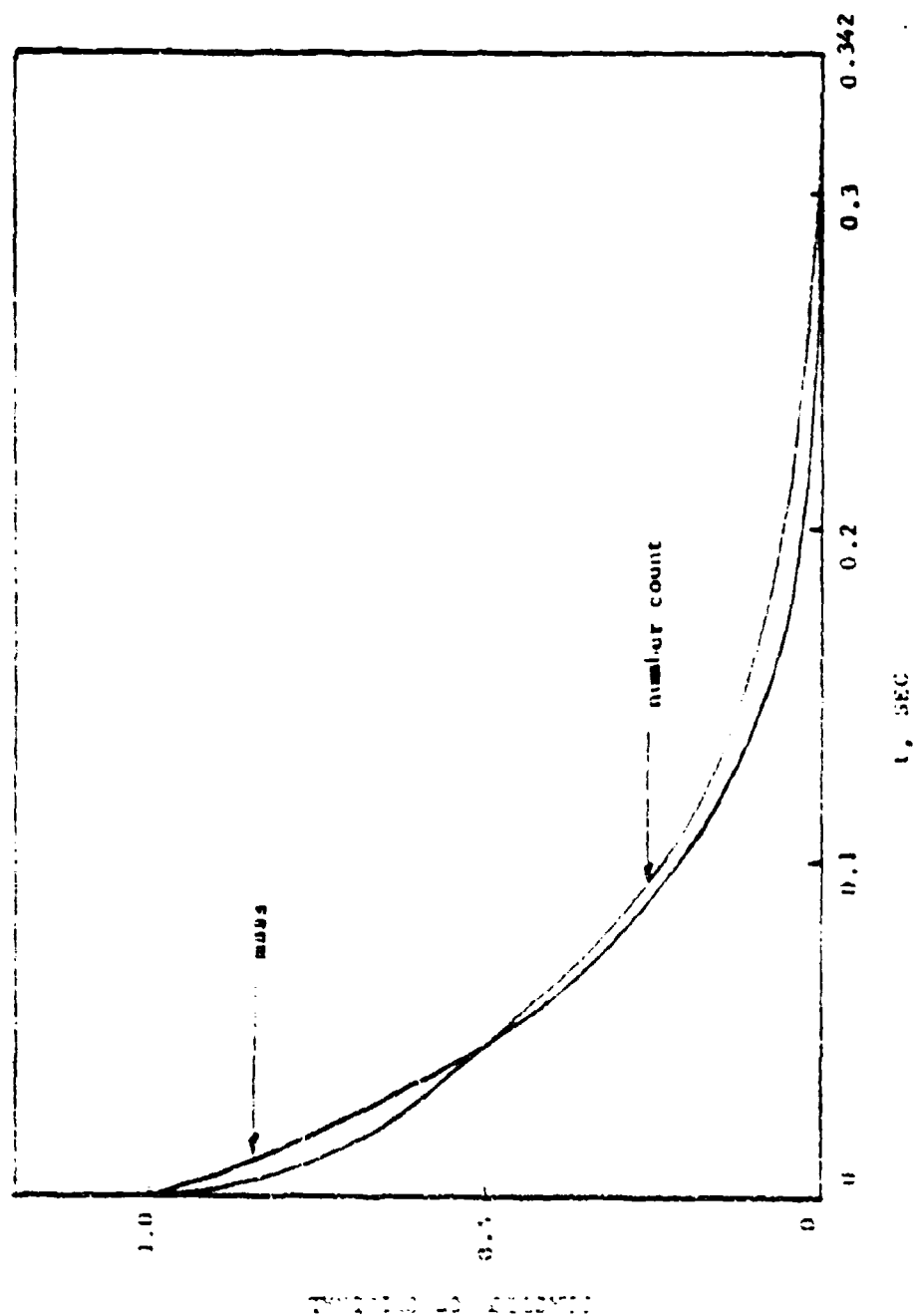
Figure 41. Values of integrals under the population and mass distribution curves versus time.

10 PRODUCT OXIDE POPULATION

10.1 Evolution of Agglomerates into Oxide Products

Given the initial aluminum agglomerate population, Figure 38, oxide products are formed at all subsequent times, Figure 42. Close to the burning surface, the condensed phase material will be mostly aluminum agglomerates with small oxide lobes. These agglomerates shift to fewer droplets of smaller sizes with more attached oxide as they move further from the propellant surface. The decreasing aluminum further from the surface is reflected in increasing oxide, in the forms of fine oxide smoke, surface oxide on the aluminum agglomerate, and residual oxide droplets formed from surface oxides of burned out agglomerates. The smoke droplet population is not really known, but it is believed to be insensitive to variables of interest except that the amount of smoke increases as the amount of aluminum decreases further from the surface. The size of smoke droplets is relatively unimportant for the present problem.

The residual oxide droplets are large enough so that a substantial portion will impinge on immersed objects. Their size distribution can be measured, at least roughly. The droplets formed early in the plume (i.e., near the propellant surface) probably result from burnout of unagglomerated aluminum particles and small agglomerates that burn out quickly.* Thus early residual oxide droplets tend to be rather small and dependent on original aluminum particle size. The residual oxide droplet population is enriched by increasingly larger droplets as they move away from the surface, as a result of burnout of agglomerates of increasingly larger original size.

---

* Some residual oxide droplets may actually result from expulsion from the agglomerate during burning (no evidence, but it occurs in some non-propellant laboratory experiments).
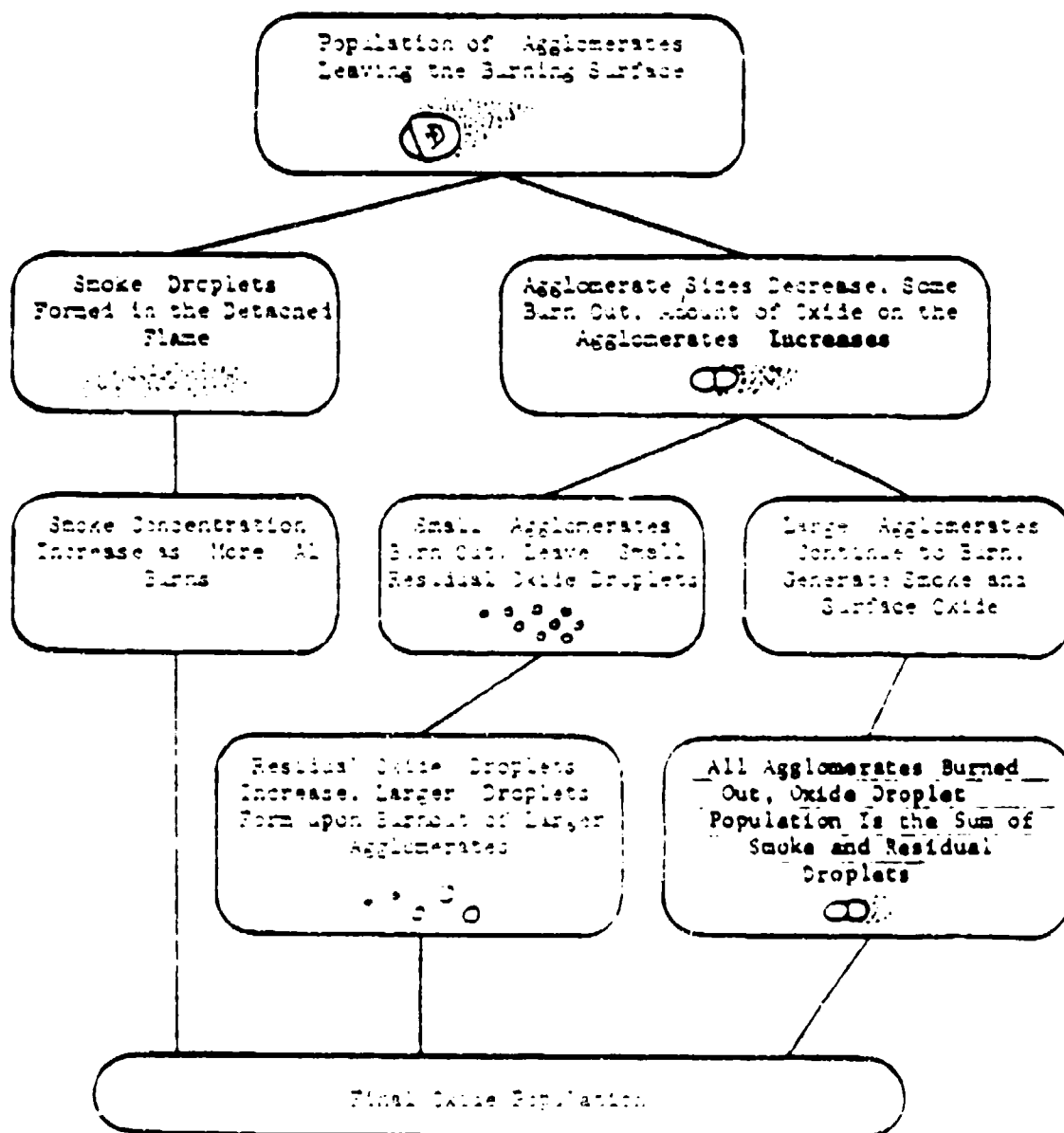
Figure 42. Diagramatic representation of the evolution of burning
agglomerates into oxides.

10.2 Aluminum Oxide Smoke

The aluminum oxide smoke formed in the detached flame around burning aluminum droplets has not been a subject of detailed interest because the droplets are so fine (< 2-μm diameter) that they flow around objects in the reaction zone without deposition. However, there is a need to estimate the *amount* of oxide smoke, in order to understand the radiation conditions in the plume, and in order to complete mass conservation arguments relative to other forms of oxide droplets of more direct interest.

Calculation of amount of oxide smoke is based on past experience, that shows approximately 80% of the oxide going into smoke form (References 21 and 22). For the present purpose it will be assumed that the proportion of smoke oxide to total oxide is α, to be evaluated experimentally in the sample collection studies. Then the amount of oxide smoke vs position in the plume is obtained from the amount of aluminum burned, portion going into smoke, and ratio of oxide mass to constitute aluminum. Figure 40 is used to get the required aluminum mass. Hence

$$m_{ox,S} = \frac{102}{54} \alpha \left(m_0 - m \right) \tag{16}$$

Subscript 0 on the right hand side refers to initial time, and m without an ox subscript means aluminum droplets. $m_{ox,S}$ vs time is shown in Figure 43 for $\alpha = 0.8$.

21. Grachukko, V. P., A. M. Stepanov, and A. A. Khvaltsev, "Estimate of the Dispersion of Products of Combustion of a Metal Particle," *Fizika Goreniya i Vzryva*, Vol. 12, No. 4, July-August 1976, pp. 519-530. (*Combustion, Explosion and Shock Waves*, translation copyrighted by Plenum Publishing Co.).

22. Eisel, J. L., E. W. Price and B. G. Brown, "Al_2O_3 Particles Produced During Solid Propellant Combustion," *AIAA Journal*, Vol. 13, No. 7, July 1975.
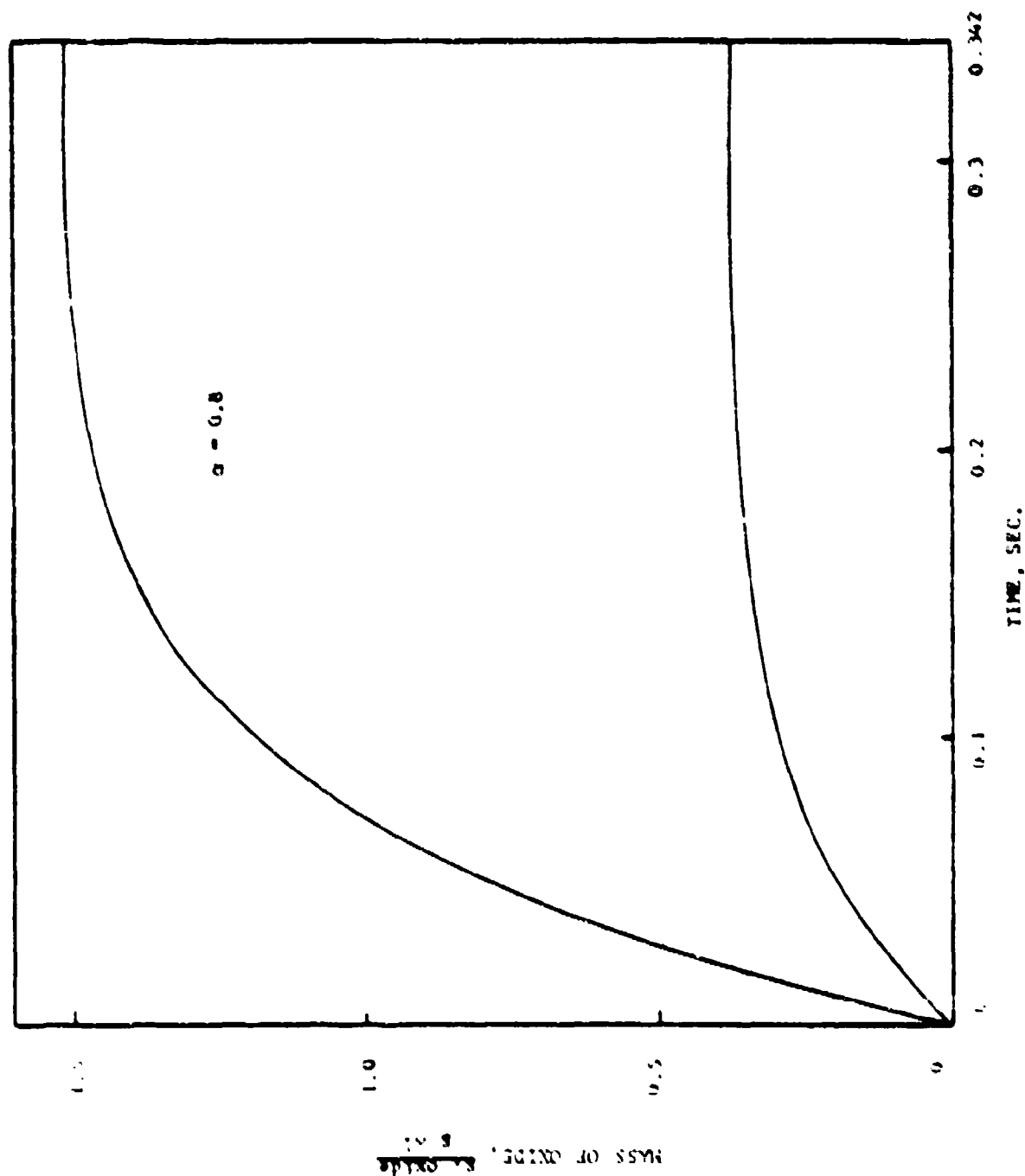
Figure 43. Formation of oxide in smoke and residual form during burning of the agglomerate population in Figure 37. σ is the fraction of oxide produced in the smoke form.

10.3 Residual Oxide, Amount

The balance of oxide is formed on the aluminum droplets (Figure 42; Sections 3 and 11), where it accumulates and forms larger droplets than the smoke (Appendix G). The total mass of that oxide is determined in a manner similar to the smoke oxide:

$$m_{ox,R} = \frac{102}{54} \left(1 - \alpha\right) \left(m_0 - m\right) \tag{17}$$

The resulting variation in the mass of residual Al_2O_3 with time is also shown in Figure 43. It should be understood that some of this residual oxide is in the form of droplets that have formed upon burnout of aluminum droplets (i.e., for which $D_0 < (t/k)^{1/n}$). Some of the residual oxide is still on the surface of burning aluminum droplets (those for which $D_0 > (t/k)^{1/n}$).

10.4 Size Distribution of Residual Oxide Droplets

When an aluminum droplet burns out completely, the surface-accumulated oxide forms one or more droplets whose diameters are different from the diameter of the original aluminum droplet. We will assume for simplicity here that only one oxide droplet results, whose diameter is smaller than that of the origianl aluminum droplet by a factor $\hat{z}$ (which depends on the densities of oxide and metal and the fraction of oxide that turns into smoke, α, and the stochiometric factor for Al_2O_3, 102/54; see Appendix G). As the population of aluminum agglomerates burns out it gives rise to the population of residual oxide. This means there is a one-to-one correspondence between original aluminum droplets and _final residual oxide_ droplets, so their _final distribution function_ has a similar correspondence amounting to linear transformation of the coordinate scales. This is demonstrated in Appendix G, and can be written

$$\mathfrak{I}_{ox}\left(D_{ox}, t\right) = \left(1/\hat{z}\right) \mathfrak{I}_o \left(D_{ox}/\hat{z}\right) \tag{18}$$

where $\mathfrak{I}_{ox}\left(D_{ox}, t\right)$ is defined on the usual way (e.g., like Equation (9)).

Equation (18) permits direct calculation of the residual oxide droplet distribution from the initial aluminum distribution function. This is illustrated in Figure 44.

The presence of a t in the functional notation on the left would be unnecessary if one were describing only the _final_ distribution of residual oxide droplets as outlined above; the t is needed when one is concerned with times when all aluminum droplets are not yet burned out. This is illustrated by the vertical line in Figure 44 at D_{ox} = 125. At a time $t = k(D_{ox}/8)^n$ all the aluminum droplets with initial diameter $D_{ox}/8$ or smaller are burned out, and all the residual oxide droplets with diameter D_{ox} or less are formed. In other words, that part of the oxide population curve to the left of the vertical line has been generated. As time progresses, the vertical line moves to higher diameter until all the aluminum population of the sample is burned and all the residual oxide droplets are generated. It is this aspect of the function $\mathfrak{J}_{ox}(D_{ox},t)$ that is time-dependent, and is elaborated in Figure 44 by the time scale at the top of the graph.

The _mass_-size distribution for the residual oxide droplets is developed in Appendix G from the definition

$$\frac{dm_{ox}}{m_0} = \mathfrak{J}_{ox}(D_{ox},t)\, dD_{ox}$$

The resulting relation to the number-size distribution is

$$F_{ox}(D_{ox},t) = 8^2 \frac{\rho_{ox}}{\rho_{Al}} F_0(D_{ox}/8) = \frac{\rho_{ox}}{\rho_{Al}} \frac{1}{8} \frac{D_{ox}^3 \mathfrak{J}_0(D_{ox}/8)}{\int_c^\infty D_0^3 \mathfrak{J}_0(D_0)\, dD_0}$$

$$= \frac{\rho_{ox}}{\rho_{Al}} \frac{D_{ox}^3 \mathfrak{J}_{ox}(D_{ox},t)}{\int_c^\infty D_0^3 \mathfrak{J}_0(D_0)\, dD_0} \tag{19}$$

98
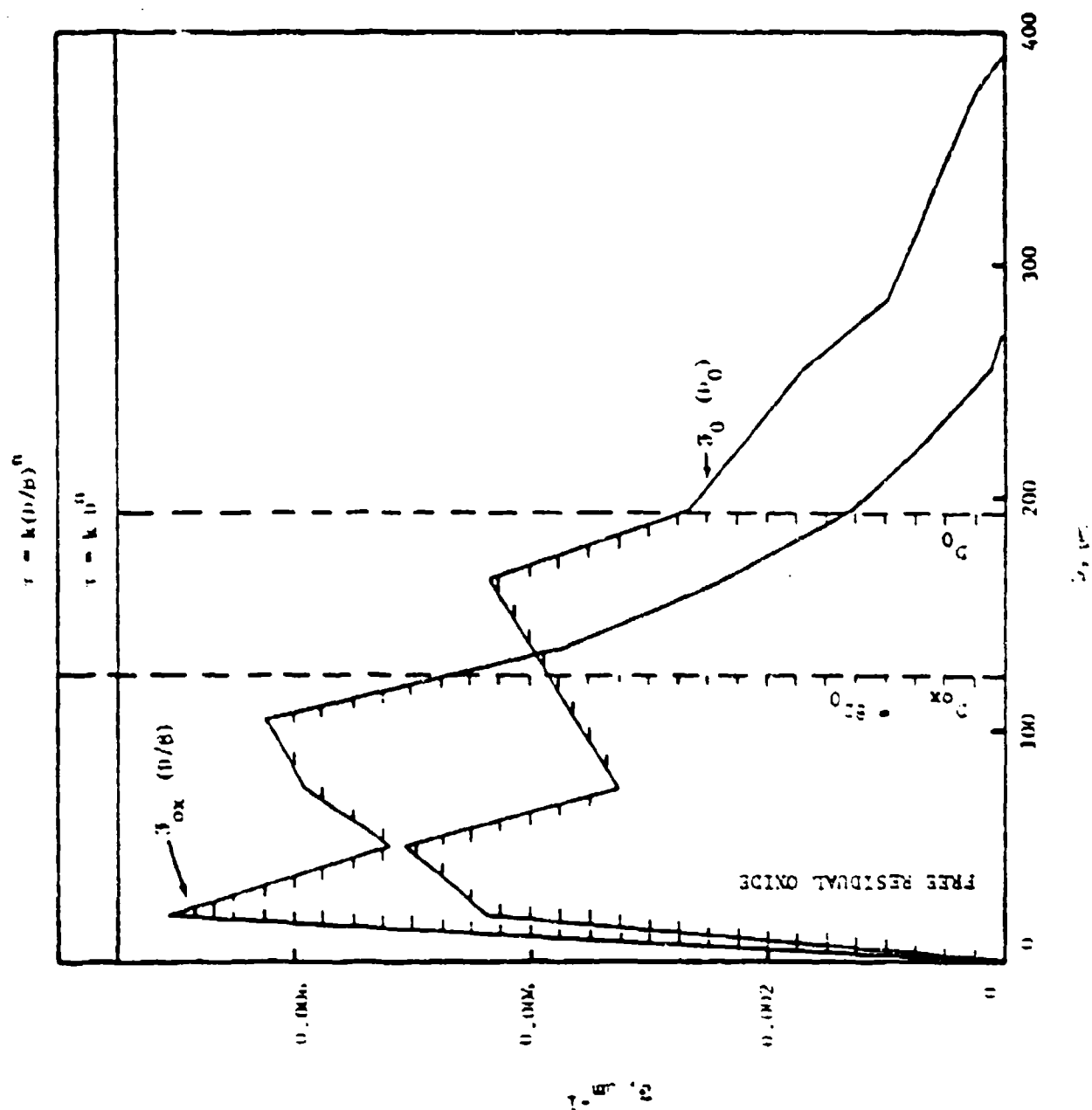
Figure 44. Population distribution function for residual oxide and original aluminum agglomerate.

This mass-size distribution is thus similar in form to $F_0(D_0)$ except for the linear scale transformations $\beta^2(\rho_{ox}/\rho_{Al})$ and $(1/\beta)$, as illustrated in Figure 45. As in the case of the number-size distribution, the population builds up from small droplets to larger ones, with the vertical line in the figure reflecting the limit of the population at a specific time (top scale).

10.5 Size Distribution of Surface Oxide

Part of the residual oxide calculated by Equation (17) is in the form of residual oxide droplets, but some is in the form of surface oxide on the larger, still-burning aluminum droplets. Thus to describe the population of burning droplets, one must also describe the amount of oxide on the droplets. At any given time during burning, the smallest aluminum droplets will be almost burned out, and the droplet will be largely oxide. The larger droplets will have a larger portion of their weight still in aluminum form.

In order to describe the surface oxide population as simply as possible for computational purposes, the weight on each aluminum droplet will be described as a sphere of diameter D_{oxs}, as if it were already an oxide droplet (but growing at the expense of the aluminum). Then according to the usual procedure, a mass distribution function can be defined by

$$F_{oxs}(D_0,t) = \frac{dm_{oxs}}{m_0} \frac{1}{dD_{oxs}} = \frac{\pi\rho_{ox}/6 \, D_{oxs}^3 \, DN}{m_0 dD_{oxs}}$$

Using the corresponding definition for the mass distribution function of the original aluminum droplets Equation (10a), one can obtain

$$F_{oxs} = \frac{\rho_{oxs}}{D_0} \left(\frac{D_{oxs}}{D_0}\right)^3 \frac{dD_0}{dD_{oxs}} F_0(D_0)$$

The objective is to get F_{oxs} in terms of D_0 and t, and the procedure is to get D_{oxs}/D_0 and dD_0/dD_{oxs} in terms of D_0 and t using Equations (4) and (17). This is described in Appendix G, and leads to the result

100
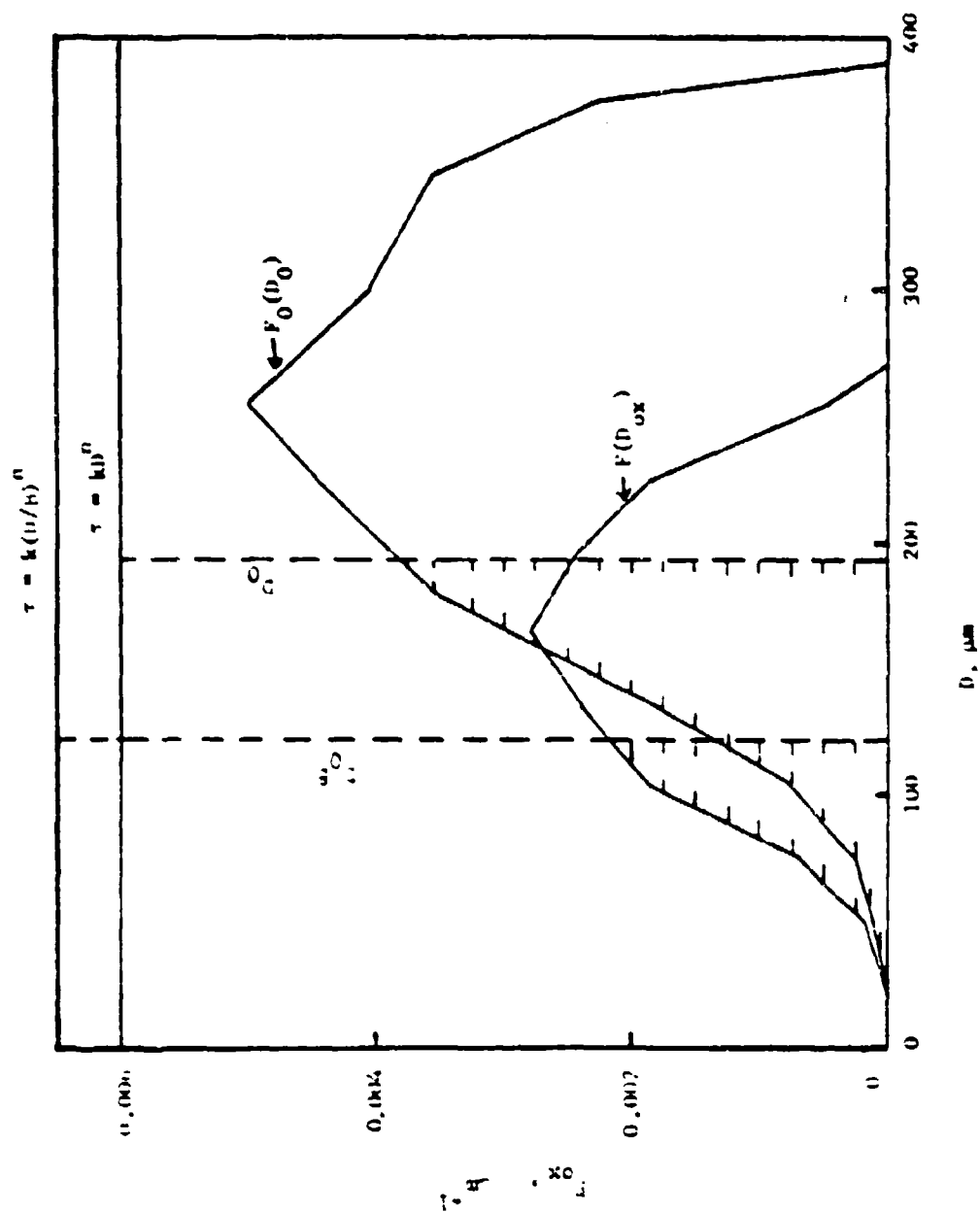
Figure 45. Mass distribution function for residual oxide and original aluminum agglomerates.

$$F_{oxs} = \frac{\dfrac{\rho_{ox}}{\rho_{Al}} \beta'^{2/3} \left[1 - \left(1 - t/kD_0^n\right)^{3/n}\right]^{5/3} F_0(D_0)}{\left[1 - \left(1 - t/D_0^n\right)^{3/n}\right] - \left(t/kD_0^n\right)\left(1 - t/kD_0^n\right)^{(3-n)/n}} \qquad (20)$$

Actual calculations of F_{oxs} were not made because of time limitations; however the trend of F_{oxs} is suggested by the sketched curves in Figure 46, which helps to clarify the meaning of the analysis. Curve A is the mass distribution function of the original aluminum droplets and Curve B is the mass distribution function of residual oxide droplets after aluminum burnout (Section 10.4). The point P on curve A corresponds to a particular size aluminum droplet, and the point P' is the corresponding residual oxide droplet. At the moment during burning when the droplet indicated by P burns out, the resulting oxide droplet at P' is formed, and is the largest one in the population at that point in the flow. Larger ones still consist of surface oxide and aluminum and will burn out later to give larger residual oxide droplets. This section is concerned with the amount of oxide on these larger droplets, which, to the right of P', is still increasing with time as indicated by Equation (20). The dotted curves in Figure 46 approximate this trend in amount of surface oxide at successively later times, a trend that culminates in the final residual oxide population upon burnout of the largest droplets.
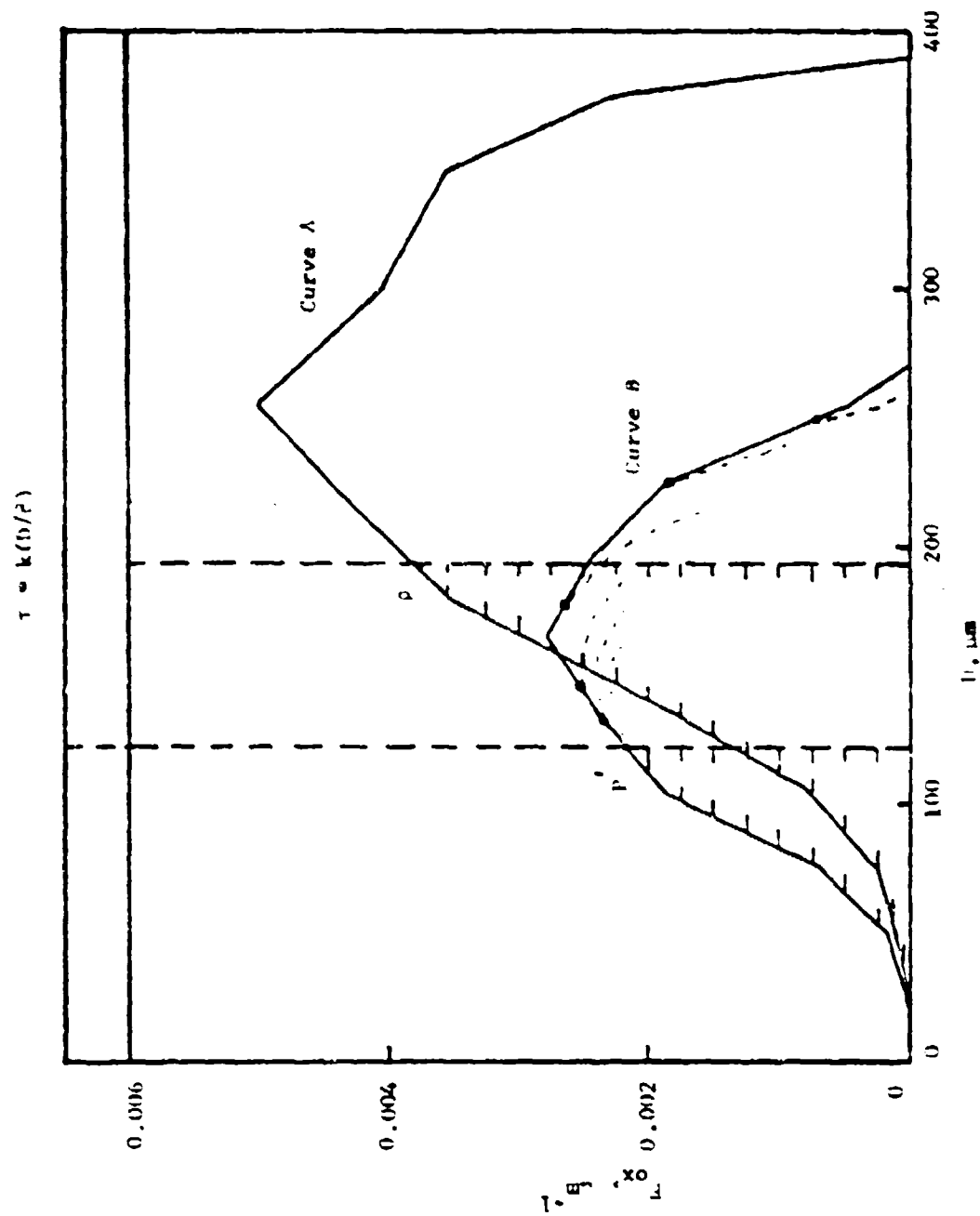
Figure 46. Mass distribution function for residual oxide and original agglomerates; and approximate curves for surface oxide mass distribution.

11 COLLECTION OF CONDENSED PHASE MATERIAL
IN THE COMBUSTION ZONE

11.1 Background

The importance of the condensed phase material to the heat transfer was demonstrated by the immersion probes (Section 4). The nature of the condensed phase material (Al and Al_2O_3) was described earlier (Sections 1, 3, 5, and 10). With initial droplet population obtained from the photographic method, the calculation of the droplet populations at subsequent times is dealt with in Sections 8 through 10. However, the basis for calculations needs to be supported by direct experimental measurements. To serve this need, extensive effort was devoted to obtain the droplet population at various sections of the plume.

Samples of condensed phase material are obtained by quenching the relevant portion of the combustion plume by appropriate means. The collected samples are used in population studies and to determine the free aluminum content in order to provide a check on the results of population calculation techniques and also to provide information for application of the thermochemical calculations (e.g., Figures 5 and 6) to the actual plume.

11.2 Test Procedure

The appropriate method of quench-collection of population samples was by no means obvious at the outset. Similar earlier efforts at rocket motor pressures (References 23 to 25) have remained of questionable validity.

23. Churchill, H. L., R. W. Fleming and N. S. Cohen, <u>Aluminum Behavior in Solid Propellant Combustion</u>, Air Force Rocket Propulsion Laboratory TR 74-13, May 1974.

24. Levashenko, G. I., and L. P. Bakhir, "Method for the Withdrawal of Particles Formed During the Combustion of Metalized Condensed Systems in a Constant-Pressure Chamber," <u>Fizika Goreniya i Vzryva</u>, Vol. 9, No. 2, March-April 1973, pp. 330-331.

25. Belyaev, A. F., B. S. Ermolaev, A. I. Korotkov and Yu V. Frolov, "Combustion Characteristics of Powdered Aluminum," <u>Fizika Geneniya i Vzryva</u>, Vol. 5, No. 2, June 1969, pp. 207-216.

However independent tests at atmospheric pressure prior to this project had shown that condensed material settled out of a horizontal combustion plume and quenched upon impact in a metal plate. Accordingly it was anticipated that in the present work, tests could be run with horizontal combustion plumes allowing aluminum agglomerates to settle out by gravity. However, with UTP 3001 propellant, quenching was not consistent (see Figure 9), and collection efficiency was indeterminate, negating the goal of determination of populations by this method. Accordingly, an experiment was developed in which the combustion plume, confined by a stainless steel tube of appropriate length, was directed into an alcohol bath that would quench burning droplets (Figure 47). Alcohol quenching was suggested by a technique developed by Russian investigators (Reference 25), although the experimental design was quite different because of the less demanding environmental situation (atmospheric pressure) and the larger combustion zone. The arrangement shown in Figure 47a was used in a series of tests using combustion tubes of different lengths. The small smoke particles (< 3 μ) are expected to travel with the gas around the tube opening into atmosphere, whereas, the bigger particles with greater weight, heat capacity, and aluminum content are expected to follow a gravitational path to the alcohol pool below.

11.3 Sample Preparation and Analysis

The sample, quenched and collected in the alcohol pool, is cleaned and dried for further study and analysis. The sample thus collected contains hydrochloric acid which is removed by repeatedly scrubbing the mixture with water and then the water in the sample is removed by repeated scrubbing of it with fresh alcohol. The technical details are described in Appendix C. The sample is finally dried and weighed.

1. A weighed subsample is removed and tested for free aluminum content. This involves solution of free aluminum into HCl and cleaning of $AlCl_3$ by scrubbing it with water and filtering. The remaining oxide is weighed. The loss of weight gives the amount of aluminum in the subsample (Appendix C).
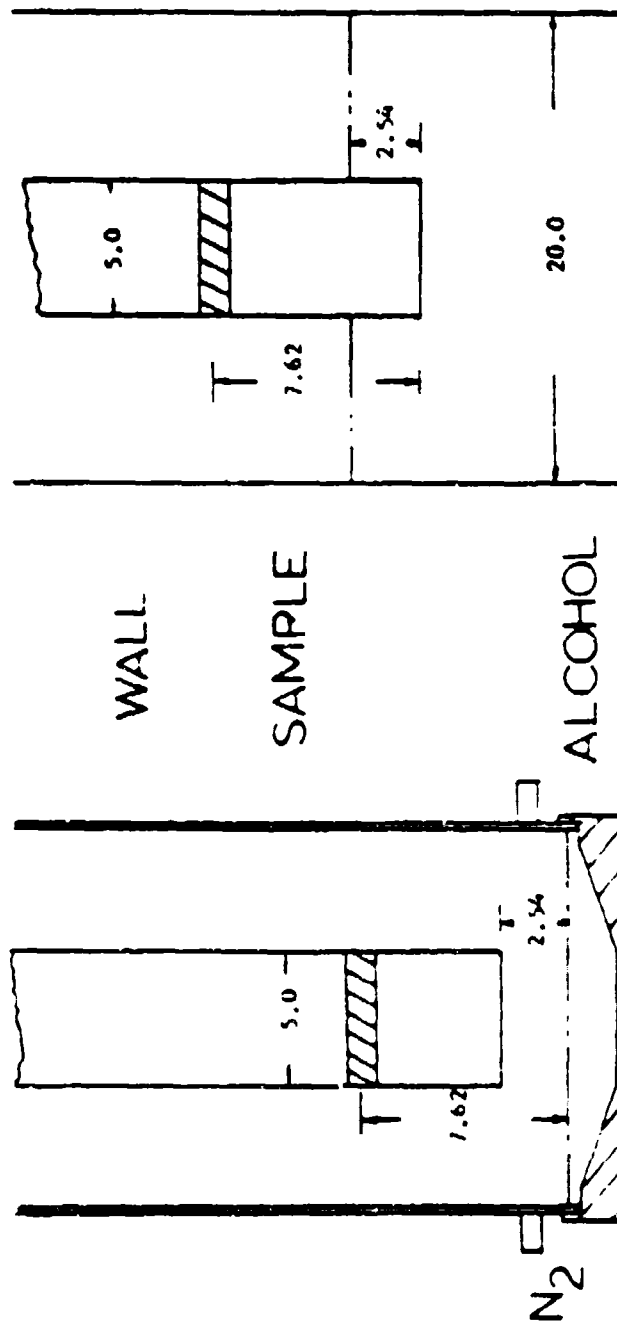
Figure 47. Sketch of experimental apparatus for quenching and collecting condensed phase material from the combustion plume using an alcohol bath: (a) initial arrangement, designed for collection of larger droplets; (b) present arrangement, designed to maximize collection efficiency. (Dimensions in cms)

2. The rest of the original sample is sieved through a series
of screens and the fractions then weighed, giving a rough mass size
distribution.

3. The sized fractions are examined microscopically to deter-
mine the nature of the population.

4. The sized fractions are tested for free aluminum content.

5. The results are compared with the analytical-computer model.

11.4 Results

During the present reporting period, some 80 tests were run. Mass-
size distributions of the entire samples for certain distances away from
the burning surface are shown in Figure 48. The results of the acid
etching of the subsample were used to plot the aluminum content in the
sample at various distances; see Figure 49. Typical photographs of the
samples collected are shown in Figure 50.

11.5 Discussion

Direct quantitative comparison of the experimental results with the
results predicted by theory is not made. Such a comparison was not consi-
dered justified because the sample collection method was found to be in-
efficient, and suspected of being selective (i.e., did not give an unbiased
sampling of kinds and sizes of droplets present in the plume).

Qualitative examination was made of samples collected at different
distances from the propellant surface, to see if the evolutionary process
of burning droplets described in Figure 42 was evident. The inevitable
decrease in agglomerate size with distance was evident, along with the
increasing size of residual oxide particles (Figure 50). The oxide lobes
on agglomerates were evident in samples everywhere in the plume. Relative-
ly few examples were seen of agglomerates in which the oxide lobe had
become the dominant   t of the agglomerate; it was speculated that such
droplets might be fragmenting, but no fragmentation was observed, and it
may be that the rapid burnout of such configurations makes their observa-
tion improbable.

A modified collection method (Figure 47b) was adopted and used in
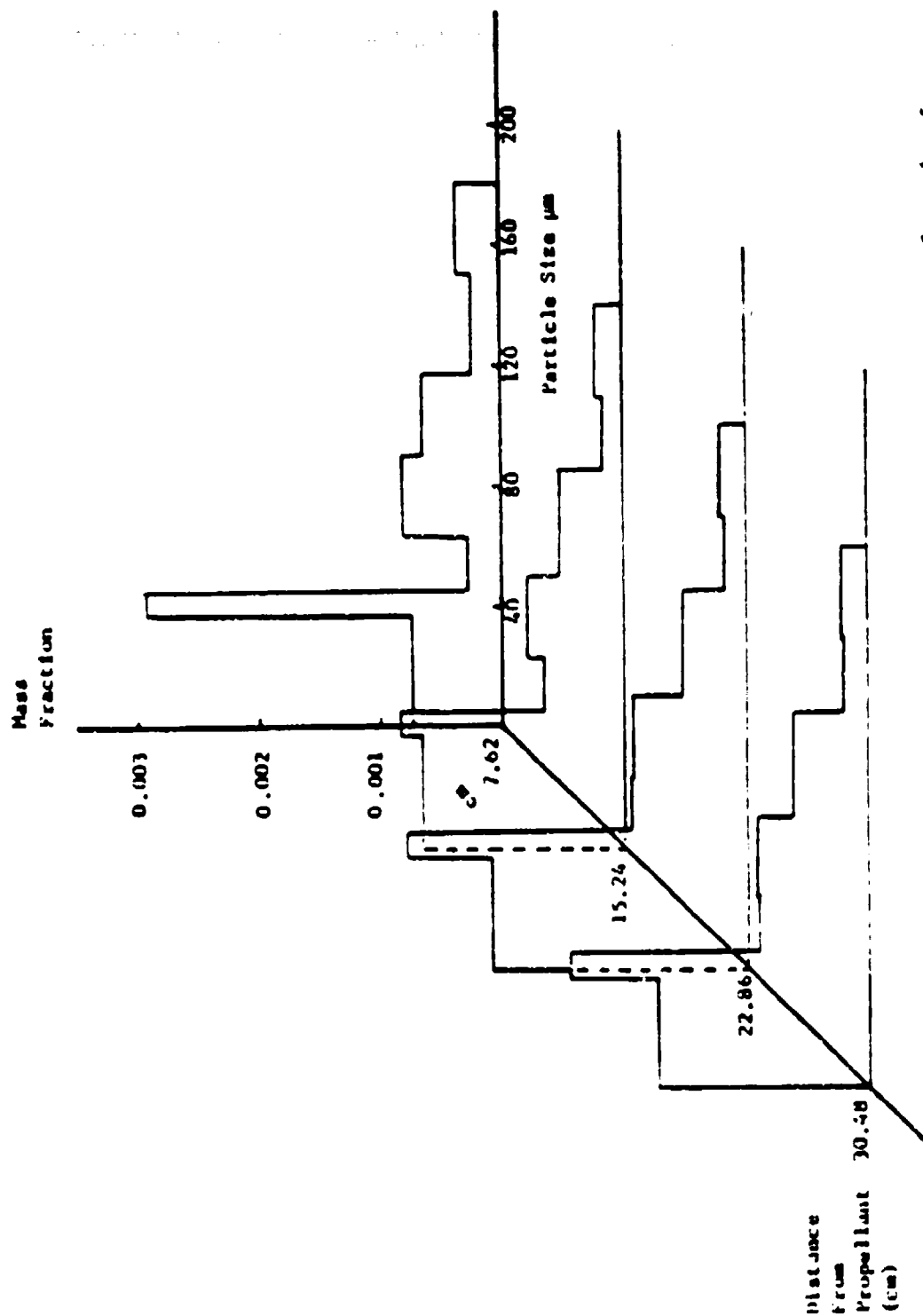
Figure 48. Mass-size distributions obtained by sieve-separation of samples from the experiment shown in Figure 47.
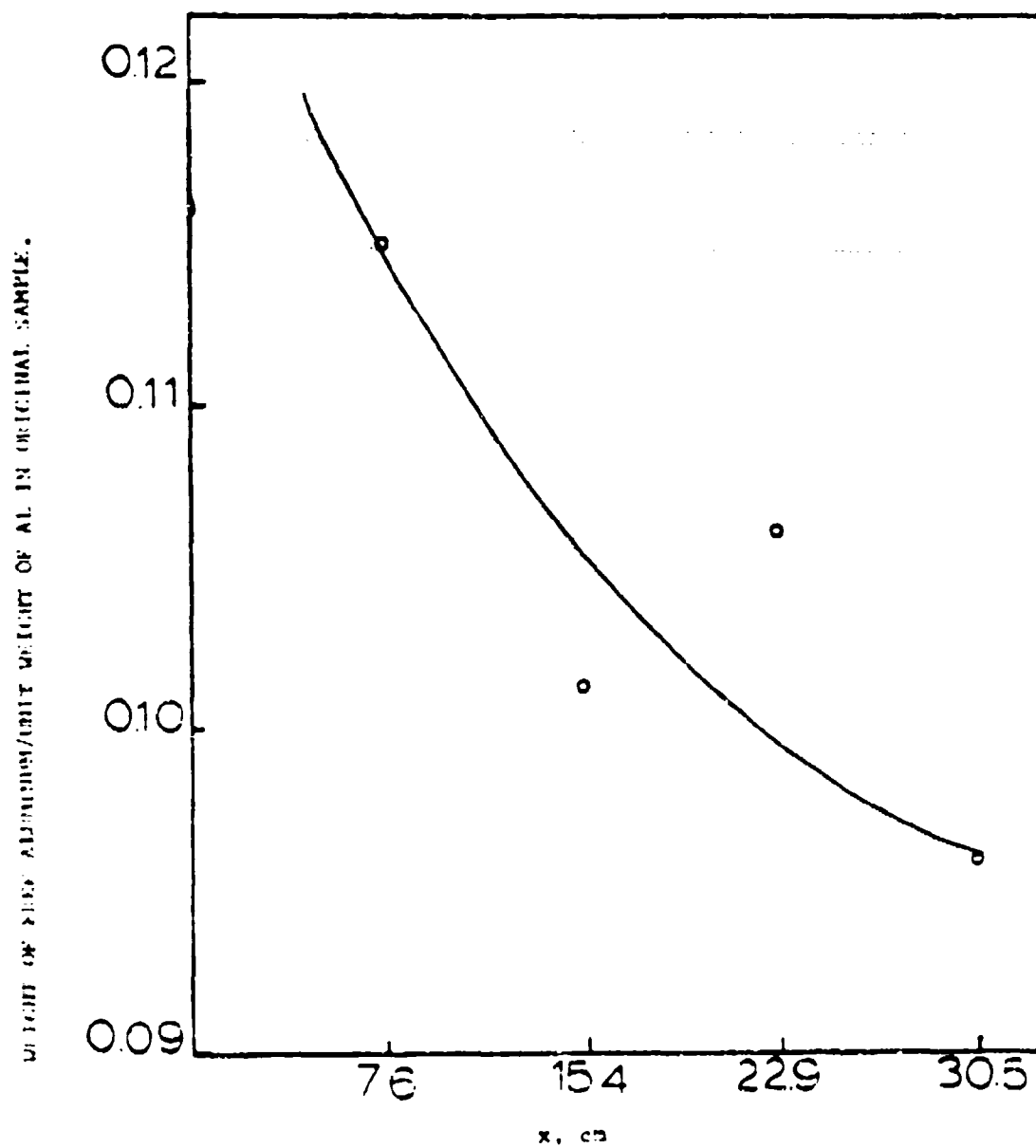
Figure 42. Free aluminum vs distance from the burning surface, determined by weighing samples before and after removal of free aluminum by acid solution method.

109
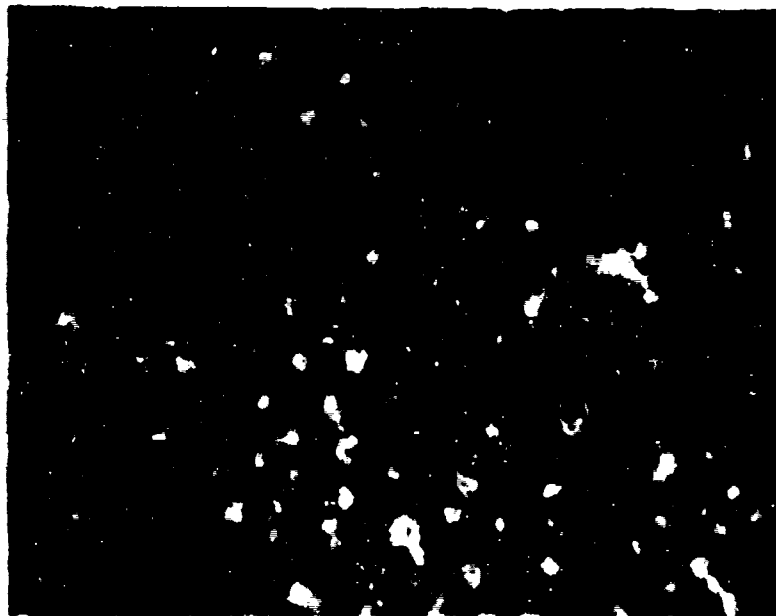
Figure 50. Condensed material from alcohol quench sampling 7.6 cm from the burning surface (most of material is aluminum). Magnification 40x.

preliminary experiments that yielded high collection efficiency. Samples collected by this method are believed to be suitable for quantitative comparison with the analyses of Sections 8 through 10, but such studies were not made.

12 INITIAL SIZE DISTRIBUTION OF
ALUMINUM AGGLOMERATES

12.1 Introduction

The importance of droplet size of aluminum in the combustion zone
has been noted in preceding sections. It relates to the dimensions of
the combustion zone and nature of droplets contributing to interactions
with immersed objects. The sizes of the agglomerates leaving the burning
surface constitute the initial condition to the population calculations
in Sections 9 and 10. Fortunately, the size distribution is susceptible
to measurement by photographic means in the vicinity of the burning sur-
face, because the droplets are still moving relatively slowly, and because
the general oxide smoke density is still relatively low and doesn't obscure
the individual agglomerates. This is evident from Figures 29b and B-2.
In the present study, sizes of aluminum agglomerates were measured from
high-speed motion pictures, and a size distribution esti   ed for use in
calculation of size distributions further away from the burning surface (Sections
8 through 10).

12.2 Procedures

The photographic method used is described in Appendixes B and C.
A 16-mm Hycam camera was used, with 2 to 1 image-to-object size and a frame
rate of 2150 frames per second. Propellant samples for these tests were
7.6-mm high by 6.6-mm wide by 2-mm thick. The pictures showed the larger
agglomerates for several frames as they moved out of the field of view
(Figure B-2).

The first step in population determination was to project the frames
onto a screen where the enlarged images of the droplets could be measured.
The field of view was limited by masking, to show a column 4.4 cm wide
(actual width 1.1 mm) perpendicular to the burning surface. In this
column, the sizes of all droplets leaving the surface were measured and
tabulated for typically 100 frames. The resulting data were used to
construct a distribution function. However, some corrections to the
measurements were made first, as described below.

112

Photography by self-luminosity shows the aluminum droplet as a brilliant sphere with a convective tail (Figures 29b and B-2). The diameter of this sphere is indicative of the flame envelope, with the aluminum droplet being smaller. The present photography does not usually show the droplet itself. Measurements of the ratio of flame envelope diameter to droplet diameter are reported in scattered comments in the literature, but are the explicit topic of Reference 26. Results of that reference were used (Appendix C, Part 4) to convert the present flame envelope diameter to droplet diameters, to be used in determining the size distribution (Sections 9 and 10, and Appendix G).

12.3 Initial Size Distribution

Figure 51a shows the droplet size distribution obtained by dividing the diameter range (Appendix C) into intervals, tabulating the number of droplets, ΔN, falling on each interval, and drawing the corresponding histogram of $\Delta N/N\Delta D$ where $N = \Sigma\Delta N$. This corresponds to a sample from a population represented by the number count size distribution function $\mathfrak{J}(D_0,0)$ referred to in Section 9. For the present purposes the mass size distribution is probably more significant, and the droplet sizes were also tabulated in Appendix C as $m/\upsilon = c_{Al} D_0^3$. The area diameter range was divided into intervals and the combined droplet mass in each interval, Δm, was tabulated. From these results (Table C-1) a histogram of $\Delta m/m_0 D$ vs D is shown in Figure 51b. This corresponds to a sample from a population represented by the mass-size distribution function $F(D_0,0)$.

It is the change in $\mathfrak{J}$ and F during burning that is sought in Section 9, and it is the histograms from the photographic studies above that are used to approximate $\mathfrak{J}_0$ and F_0. The total area under the histogram is one for $t = 0$. At later times (Section 9, Figures 38b and 39a and b) the area will be the mass fraction of aluminum remaining.

---

26. Boreisho, A. S., A. V. Ivashchenko, and G. G. Shelukkin, "Problem of Determining the Sizes of Burning Metal Particles," Fizika Goreniya i Vzevva, Vol. 11, No. 4, July-August 1975, pp. 659-660.
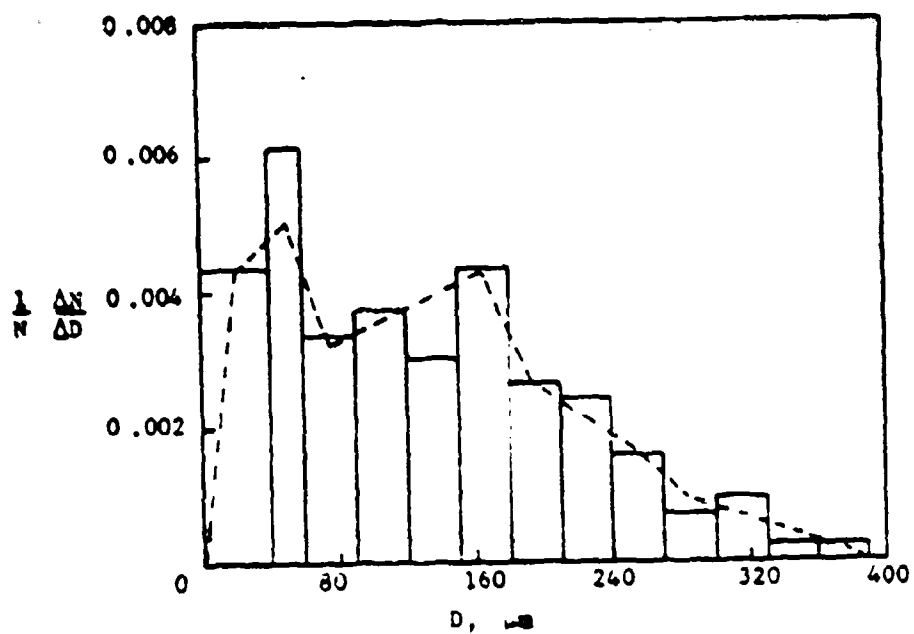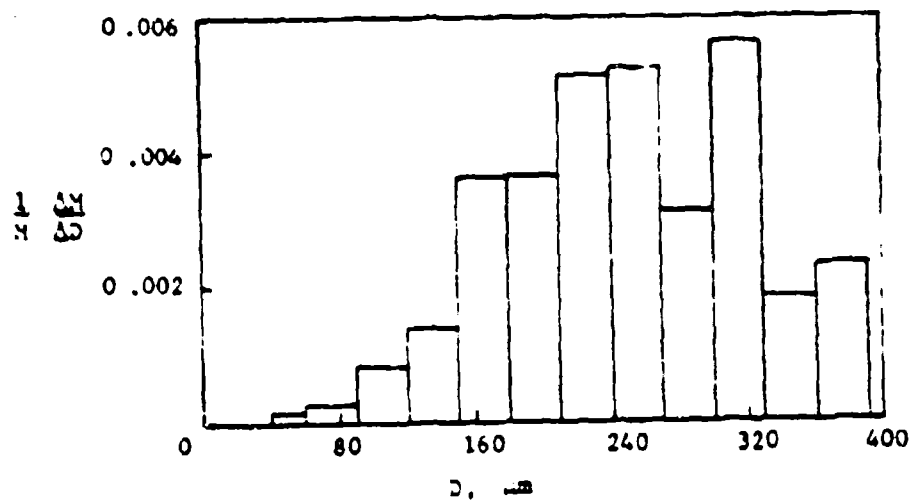
Figure 51. Number count (a) and mass-size distribution of agglomerates leaving the burning surface (sample data from combustion photography corrected for flame standoff).

13   GAS ANALYSIS OF THE COMBUSTION ZONE

13.1 Introduction

Composition of the gas mixture in the combustion zone is of interest
for two reasons. First, future choices of materials for radioisotope
thermoelectric generators (RTGs) may be optimized by consideration of
reactability in the propellant product flow. Second, the gas composition
is an indicator of the state of aluminum combustion (ac) and of air
admixture (aa). As noted in Section 2., the gas composition can be cal-
culated from theory, except for the uncertainty as to extent of ac and aa.
In this respect, measurement of gas composition provides a supplementary
means of estimating ac and aa.

No previous measurements of gas composition in metalized propellant
combustion were found, and there are some profound difficulties in measure-
ment because of the presence of HCl and Al_2O_3. However, it was decided
that gas samples could be withdrawn into sample bottles without Al_2O_3 by
sampling through a porous plug filter, and that HCL could be inactivated
by including a suitable neutralizer in the sample bottle. If this could
be done, determinations could be made of relative concentrations of other
gases versus position in the plume, using a gas chromatograph method.
In the following and Appendix G, the results of such measurements are
reported.

13.2 Experimental Arrangement for Sampling

The general arrangement for sampling is shown in Figure 52. Evacuated
sample bottles were equipped with valves (stopcocks) and connected to a
sampling tube that extended into the combustion zone through a hole in the
combustion tube. This probe contained the filter plug to collect condensed
material. The stopcock was opened after the propellant sample was burning,
and closed before burn out (e.g., open 15 seconds). The sample bottle was
kept cool in order to condense w   . vapor and retard further reactions.
One sample was taken fo, each test, and the test was repeated for different
distances from the propellant surface. Samples were collected until ready
for gas analysis. There was some indication in the test results that the
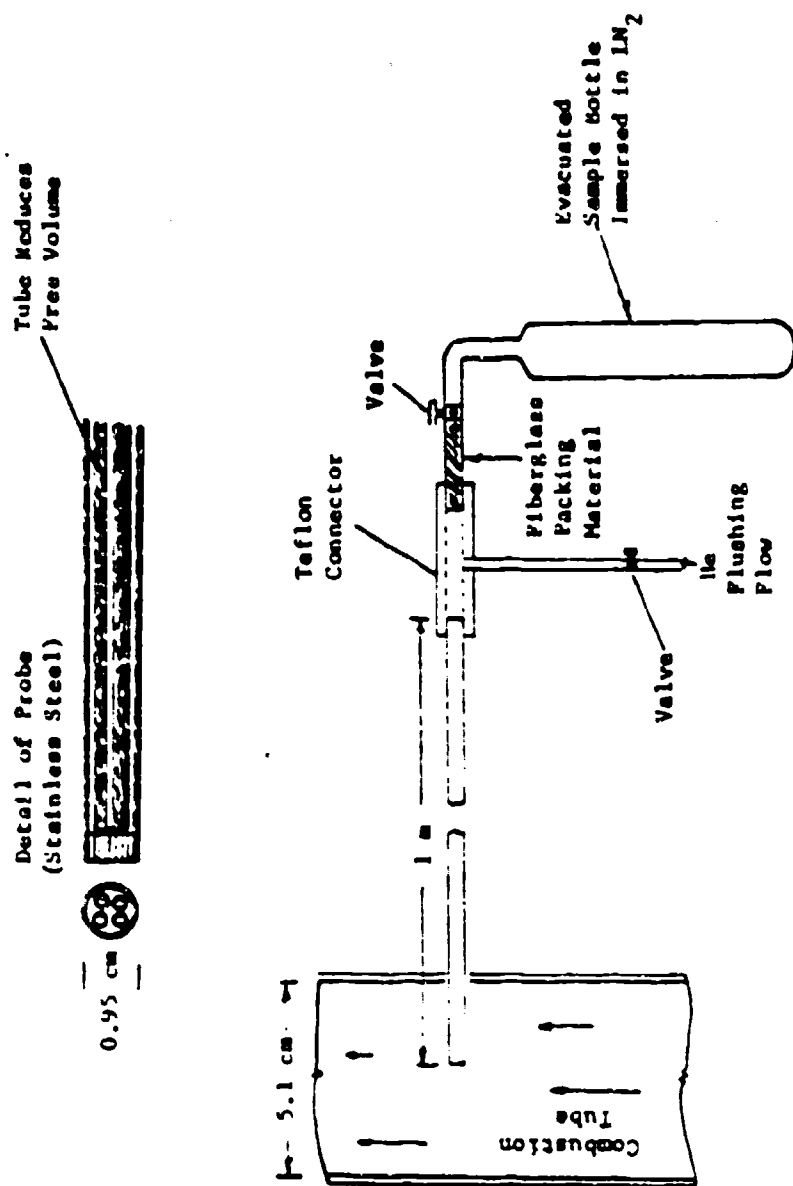
Figure 52. Arrangement for sampling gas from the combustion zone.

116

samples contained air, indicating leakage during storage (the indication was the presence of O_2, which is not believed to be present in the product flow inside the combustion tube).

13.3 Gas Analysis and Results

Details of the gas analysis are presented in Appendix H. Figure 53 shows a sample gas chromatograph record and Figure 54 shows the trend in concentration of H_2, CO and CO_2 with distance from the propellant surface (the ordinate scale is in arbitrary units). The expected trends are exhibited, with the decrease in CO_2 and increase in CO with distance reflecting the reaction with aluminum. The increasing H_2 reflects the reaction of aluminum with water to give Al_2O_3 and H_2. The data suggest that the aluminum reaction is substantially complete at 15 cm. However this may be deceptive, as the aluminum droplet population measurements and calculations show a large portion of aluminum that is in the large (slow burning) part of the droplet population.

Measurement of water content was complicated by condensation of an unknown amount in the sampling tube. Further the presence of HCl was a more serious problem in measuring water. However a gas chromatographic method was evaluated that can probably be used successfully. Preliminary results (Figure 54) exhibited the expected trend of H_2O concentration decreasing with distance from the propellant surface.

13.4 Discussion

Gas analysis showed the expected trends in concentration of CO, CO_2, H_2, and H_2O, the principal species involved in oxidation of the aluminum. The methods used can almost surely be upgraded to give quantitative results, but the measurements obtained in the current project are regarded as only qualitatively valid. They suggest that the gas phase approximates equilibrium, validating use of the thermochemical calculations of Section 2. The results further suggest rather rapid aluminum combustion (e.g., in the leveling off of the H_2, CO and CO_2 curves beyond 15 cm in Figure 54). This conclusion is not supported by all the results (e.g., H_2O concentration, Figure 54).

117
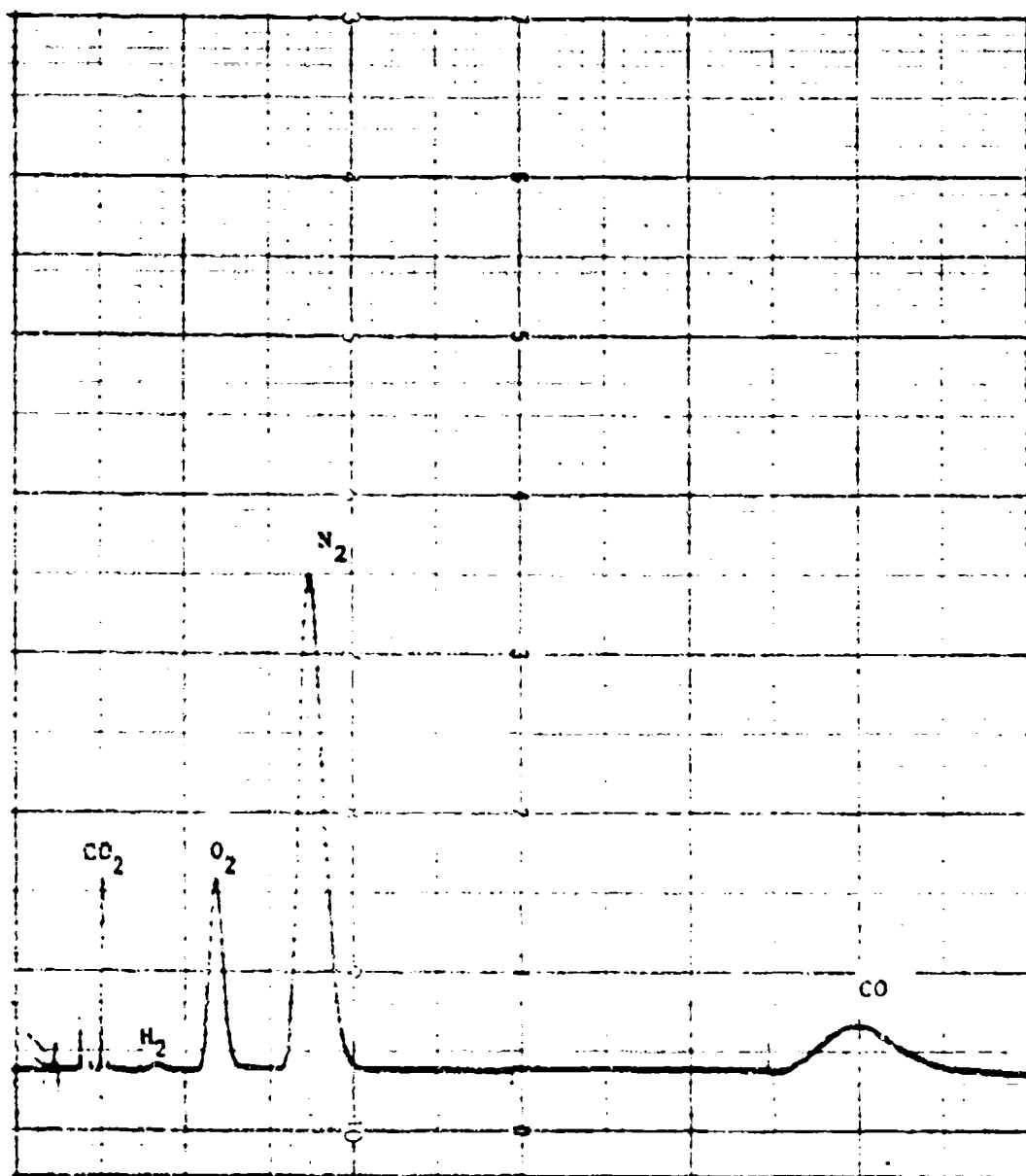
Figure 53. Sample gas chromatograph record of combustion products.
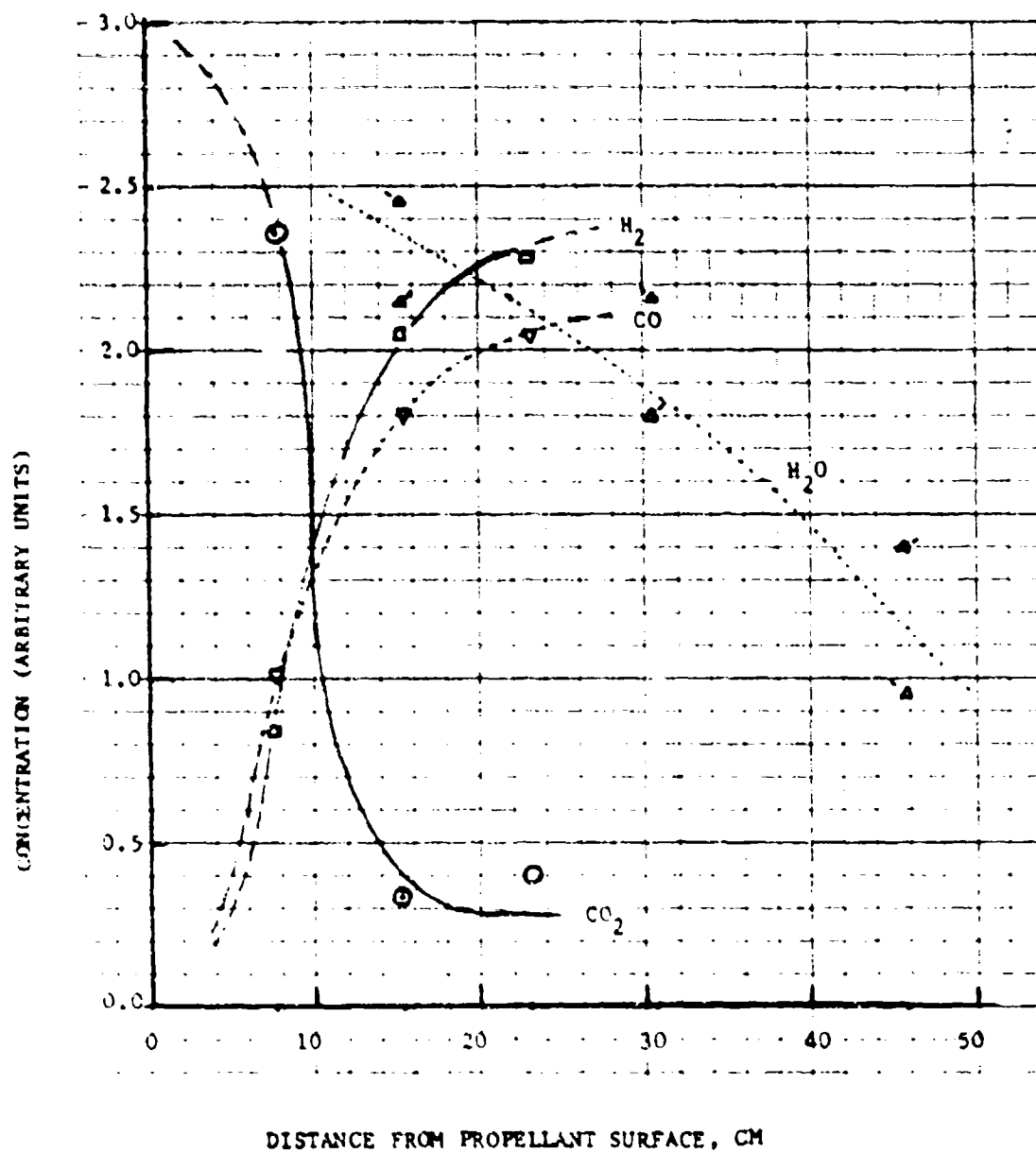
Figure 54. Variation in product gas composition with distance from the burning surface, as measured by gas chromatographs of collected samples.

NOMENCLATURE

SYMBOLS

C   Constants in grey body radiation law

C_p Effective heat capacity of an immersed object or probe

D   Diameter of a droplet

f Mass-size distribution function, $dm/m_o dD$

$\mathfrak{Z}$ Number-size distribution function, $dN/N_o dD$

H   Coefficients in heat transfer equation, Equation (1)

I   Radiation intensity

k   Constant in the droplet burning time law, Equation (3)

m   Mass; of a droplet (Equation (5)) or a collection of droplets

N   Number of droplets

n   Exponent in the droplet burning time law, Equation (3)

T   Temperature

t   Time

t^* $t^* = t/k$

x   Distance, e.g., from propellant burning surface

v   Velocity

α Portion of oxide occurring in smoke form

β Ratio of diameters of residual oxide droplets and parent aluminum droplets (in turn equal to
$$\left[\left(\rho_{Al}/\rho_{Al_2O_3} \right)\left(102/54 \right)\left(1 - \alpha \right)\left(1/\eta \right) \right]^{1/3}$$

β' $= \eta\beta$

η Number of residual oxide droplets per aluminum droplet

λ Wavelength of light

τ Burning time of an aluminum droplet

SUBSCRIPTS

Al   Aluminum

Al_2O_3 Aluminum oxide

bo   at, or after burnout

0   initial, time = 0, at start of droplet burning

ox   oxide, may refer to all oxide or residual oxide, see context

ox,S   oxide smoke

ox,R   refers to all residual oxide, both free droplets and surface

oxs   surface oxide on a burning droplet

oxr   refers to free residual oxide droplet (i.e., parent aluminum is burned out)

g   gas

p   probe; propellant

APPENDIX A

TWO DIMENSIONAL MIXING LAYER CALCULATION

A-1 Technical Basis

The combustion products of UTP 3001 are reasonably fuel rich and are capable of reaction with the surrounding air, even if the aluminum has burned. A reacting mixing layer between the hot propellant gases and the surrounding air may therefore develop. For a large block of propellant a substantial length above the propellant will exist where an essentially two dimensional mixing layer is a good model for the mixing process. This layer is assumed bounded on one side by the equilibrium products of propellant combustion, but with the aluminum in various stages of complete combustion, and on the other side by quiescent air.

It is known that at the prevalent conditions the mixing layer will become turbulent within only a small distance (small fraction of an inch) above the surface, so a turbulent mixing layer will be assumed. For simplicity, the presence of aluminum will be ignored in the mixing layer, thus neglecting the mass, momentum and energy source/sink for the gas phase in the mixing layer. Consideration of the effect is beyond the scope of the program. The equilibrium computations of Figure A-1 show that the thermal effect of aluminum combustion in the presence of air is reasonably weak (approximately 20% effect on absolute temperature). The neglect of this effect sets the spirit of accuracy of the present analysis, where several approximations will be introduced.

Two limits will be considered: a) the gas phase reactions between fuel rich propellant combustion products and air are nonexistent (pure mixing case) and b) the reactions take place with infinite rate. In both cases a distributed reaction within the mixing layer need not be considered, but in case b) reaction will occur at a mathematical surface in space, because fuel (CO and H_2 primarily) and oxidizer cannot coexist at any point. This latter case will be treated by what is known as the collapsed flame approximation. In both cases the boundary layer equations with the turbulent exchange modelled in Boussinesq form with turbulent Prandtl and Schmidt

123
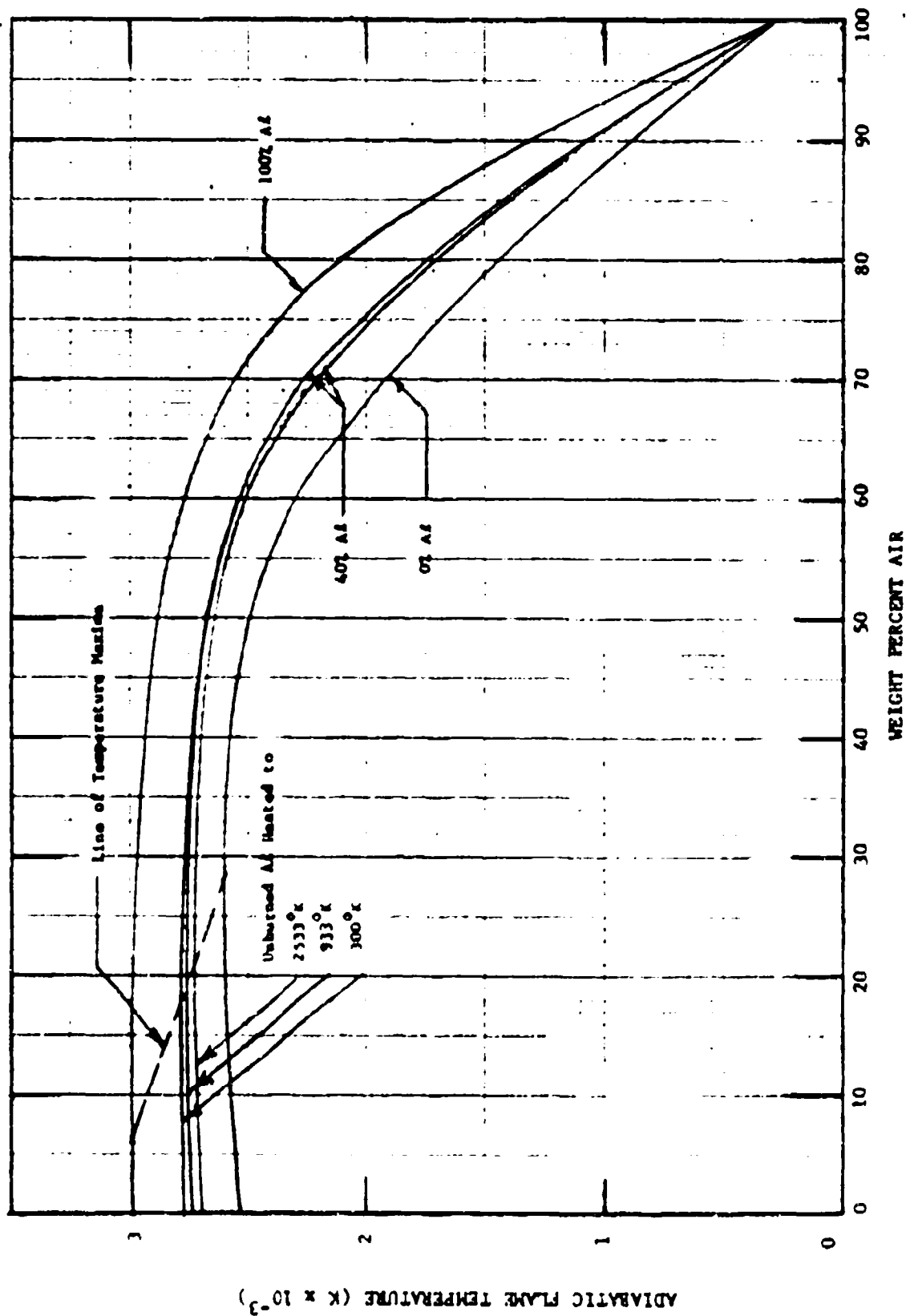
Figure A-1. Temperatures for equilibrium reaction of UTP 3001 propellant in air, assuming varying degrees of completeness of aluminum combustion.

numbers of unity are

Continuity

$$\frac{\partial (\rho u)}{\partial x} + \frac{\partial (\rho v)}{\partial y} = 0 \tag{A-1}$$

Axial Momentum

$$\rho u \frac{\partial u}{\partial x} + \rho v \frac{\partial u}{\partial y} = \frac{\partial}{\partial y} \left(\rho \varepsilon \frac{\partial u}{\partial y} \right) \tag{A-2}$$

Vertical Momentum

$$\frac{\partial p}{\partial y} = 0 \tag{A-3}$$

Energy

$$\rho u \frac{\partial h}{\partial x} + \rho v \frac{\partial h}{\partial y} = \frac{\partial}{\partial y} \left(\rho \varepsilon \frac{\partial h}{\partial y} \right) \tag{A-4}$$

Species Conservation

$$\rho u \frac{\partial Y_i}{\partial x} + \rho v \frac{\partial Y_i}{\partial y} = \frac{\partial}{\partial y} \left(\rho \varepsilon \frac{\partial Y_i}{\partial y} \right) \tag{A-5}$$

Perfect gases will be assumed so that

$$p = \rho \frac{R_o}{W} T \tag{A-6}$$

$$h = \int_{T^o}^{T} c_p (T) \, dT \tag{A-7}$$

The reference state enthalpies will be taken from Reference A-1. From an

---

A-1. *JANAF Thermochemical Tables*, Dow Chemical Company, Midland (continuous update).

125

inspection of the thermochemical equilibrium calculations supplied by AFWL, the dominant species to be considered are given for the propellant gases for two limits of aluminum combustion in Table A-1. Also shown in the table are temperatures and velocities of the gases for the propellant gas flow, which will be termed the core flow. These conditions form the boundary conditions on Equations A-1 through A-5 at $y = +\infty$. At $y = -\infty$ the conditions are cold quiescent air at $T = T^o$ and $Y_{N_2} = 0.767$, $Y_{O_2} = 0.223$.

Table A-1. Compositions and Temperatures Used for the Propellant Combustion Gases in the Limits of 0 and 100% Complete Combustion of Aluminum.

Species	Mole Fractions	
	0% Al Burned	100% Al Burned*
H_2O	0.32	0.12
H_2	0.14	0.34
CO	0.23	0.29
CO_2	0.08	0.01
N_2	0.08	0.09
HCl	0.15	0.15
Molecular Weight	23.7	19.4
c_p	0.435 cal/g.^{o}K	0.452 cal/g.^{o}K
Temperature	2500K	3000K
Enthalpy, h_∞	861 cal/g	1143 cal/g
Velocity	18.5 m/sec	25.1 m/sec

* H and Cl are also present in a minor amount and have been lumped into the components shown.

Equations A-4 and A-5 admit the solutions

$$h = A + B u/u_\infty \tag{A-8}$$

$$Y_i = C_i + D_i u/u_\infty \tag{A-9}$$

as may be checked by direct substitution. Here A, B, C_i and D_i are constants of integration. Consequently, the solution to the problem is reduced to finding a solution to Equations A-1 and A-2 with the boundary conditions on u that

$$u(\infty, x) = u_\infty (x) \qquad u(-\infty, x) = 0$$

$u_\infty (x)$ will be later determined by a separate equation concerning alumi-num consumption.

The eddy viscosity will be chosen as

$$\rho^2 \epsilon = \rho_{-\infty}^2 \epsilon_o(x) = \rho_{-\infty}^2 K_\epsilon u_\infty x \tag{A-10}$$

which is a form with empirical support (Reference A-2). With this choice, where K_ϵ is an empirical constant to be determined, one further assump-tion allows a rather simple solution to the problem. The assumption is one of local similarity by introduction of the variables

$$z = \int_0^y (\rho/\rho_{-\infty}) \, dy \qquad \eta = z/x K_\epsilon^{1/2} \tag{A-11}$$

and a solution is sought for flow variables depending on η alone, rather than x and z. This is found permissible if u_∞ is a slowly changing func-tion of x. By slowly is meant that the length scale over which u_∞ changes substantially (aluminum consumption length) is much larger than the mixing

---

A-2. Alber, I. E., "Integral Theory for Turbulent Base Flows at Subsonic and Supersonic Speeds," Ph.D. Dissertation, California Institute of Technology, 1967.

layer thickness, a fact which may be checked a *posteriori*. Introducing the variables

$$\Psi = u_\infty x \, K_\ell^{1/2} \, f(\eta)$$

$$\frac{\partial \Psi}{\partial x} = u = u_\infty f'$$

$$\frac{\partial \Psi}{\partial x} = -v = K_\ell^{1/2} \, u_\infty \, (f - \eta f')$$

$$v = \frac{\rho v}{\rho_{-\infty}} + u \int_0^y \frac{\partial \rho / \partial x}{\rho_{-\infty}} \, dy \qquad (A-12)$$

Equation A-1 is automatically satisfied and Equation A-2 collapses to the ordinary differential equation

$$f''' + f \, f'' = 0 \qquad (A-13)$$

with the boundary conditions

$$f'(\infty) = 1 \qquad f'(-\infty) = 0 \qquad (A-14)$$

While Equation A-13 subject to Equation A-14 may be solved numerically, in the spirit of the approximation used here, an appropriate analytical solution is desired. Before doing this, however, a common problem should be noted; the third order differential equation has only two boundary conditions in Equation A-14. Therefore, the problem is ill-posed as it stands. This is really a strong interaction problem where the behavior of the universe around the mixing layer can influence the cant or tilt of the mixing layer relative to the horizontal axis. An additional condition will be imposed here that there are no lateral forces acting on the shear layer. A careful examination of the transverse momentum equation reveals that an additional boundary condition is

$$v(\infty) = 0 = \lim_{\eta \to \infty} (f - \eta f') \qquad (A\text{-}15)$$

This now makes the problem solution unique.

Inspection of Equation A-14 shows that the asymptotic forms of f are

$$\eta \to \infty \quad f \to \eta$$

$$\eta \to -\infty \quad f \to f_{-\infty} , \text{ a constant}$$

Insertion of these forms in Equation A-13 above and below $\eta = 0$, respectively, converts Equation A-13 to a linear ordinary differential equation. Demanding continuity of f, f' and f'' at $\eta = 0$, the two solutions may be uniquely matched at $\eta = 0$. The solution which satisfies Equations A-14 and A-15 is

$$\eta \geq 0$$
$$f' = 0.5694 + 0.8613 \int_0^\eta e^{-\eta^2/2} \, d\eta$$
$$\eta \leq 0$$
$$f' = 0.5694 \, e^{0.6035\,\eta} \qquad (A\text{-}16)$$

where $f_{-\infty} = -0.6035$. Equation A-16 is plotted on Figure A-2.

For the case of no reaction Equations A-8 and A-9 yield

$$\frac{h}{h_\infty} = f'$$

$$Y_{O_2} = Y_{O_{2-\infty}} (1-f')$$

$$Y_{HC\ell, \ H_2O, \ H_2, \ CO, \ CO_2} = Y_{HC\ell, \ H_2O, \ H_2, \ CO, \ CO_{2\infty}} f' \Bigg\}$$

$$Y_{N_2} = Y_{N_{2\infty}} + f' (Y_{N_{2\infty}} - Y_{N_{2-\infty}}) \qquad (A\text{-}17)$$

129

Collapsed Flame Position for 0% Al' Burned

Position of Zero Lateral Mass Flow

Collapsed Flame Position for 100% Al Burned

u/u_
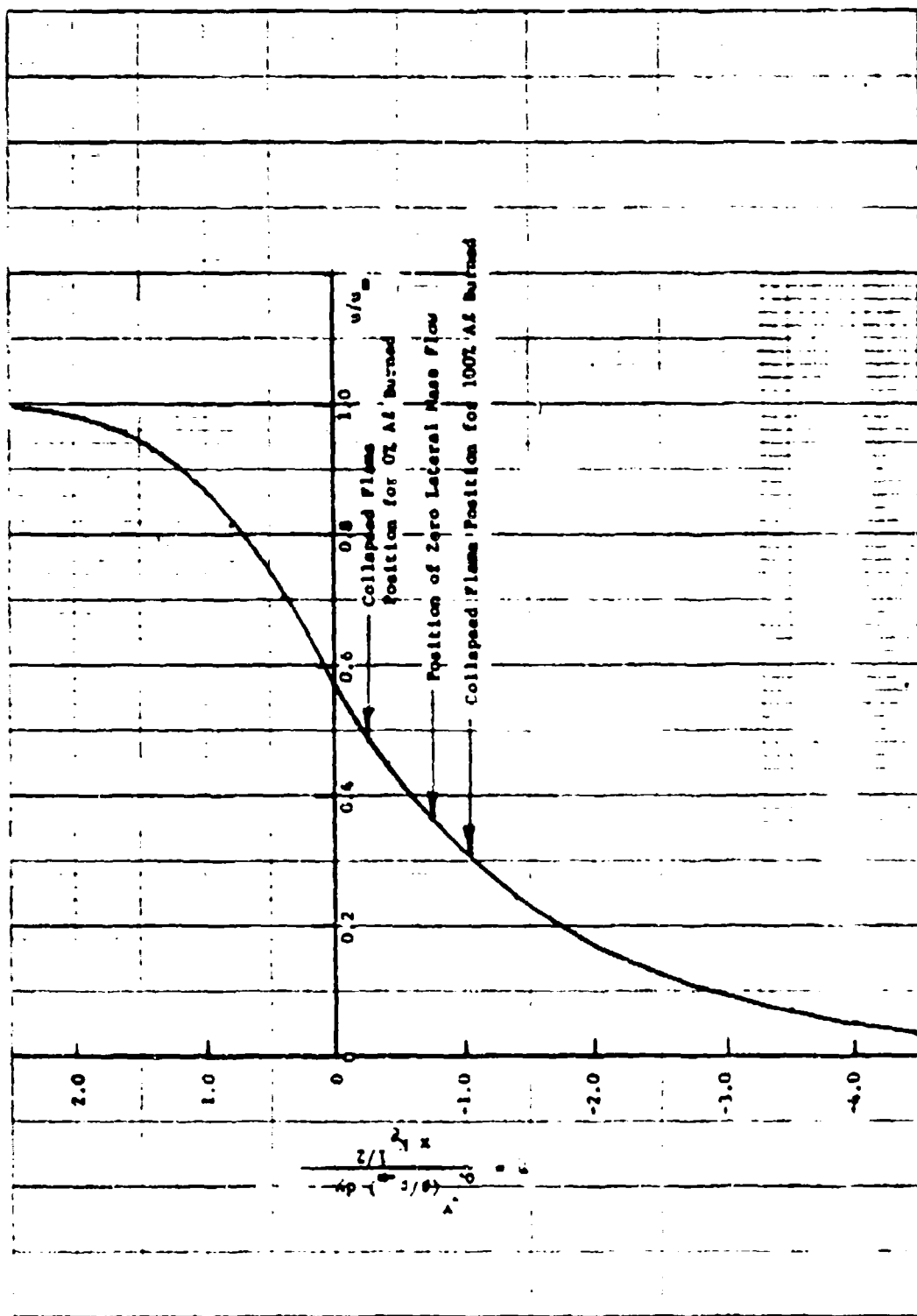
Figure A-2. f' versus η

From Equation A-7, if an average specific heat is used,

$$\frac{h}{h_e} \approx \frac{T - T_{-\infty}}{T_e - T_{-\infty}} \qquad (A-18)$$

For zero Aℓ consumption $\bar{c}_p = 0.391$ cal/g.$^{\circ}$K and for 100% Aℓ consumption $\bar{c}_p = 0.423$ cal/g.$^{\circ}$K, where these are calculated on the basis that

$$h_e = \bar{c}_p (T_e - T_{-\infty})$$

and h_e is calculated from Reference A-1 and the composition of Table A-1.

For the case of reactions between O_2, CO and H_2 the computation of the enthalpy and mass fraction profiles is more complex. The reaction considered is the one step irreversible reaction

$$O_2 + a \ CO + b \ H_2 \rightarrow b \ H_2O + a \ CO_2 \qquad (A-19)$$

at the collapsed flame surface. From Table A-1 it may be calculated that

a = 1.24		a = 0.92
	0% Aℓ burned		100% Aℓ burned
b = 0.76		b = 1.08

From Reference A-3 it is known that the functions

$$\theta_{H_2} = \frac{Y_{H_2}}{W_{H_2}(-b)} + \frac{Y_{O_2}}{W_{O_2}}$$

$$\theta_T = \frac{h}{\Sigma_i \ h_i^o \ W_i \ (\nu_i' - \nu_i'')} + \frac{Y_{O_2}}{W_{O_2}}$$

A-3. Williams, F. A., "Combustion Theory," Addison-Wesley, Reading, pp. 9-13 (1965).

131

satisfy

$$\hat{\theta} = \hat{\theta}_\infty + (1 - f')(\hat{\theta}_{-\infty} - \hat{\theta}_\infty) \qquad (A-20)$$

everywhere in the field, even if reaction is occurring. By calculations, the sum in the denominator of $\hat{\theta}_T$ is approximately 1.3×10^5 cal/mol for both limiting cases of Table A-1 and is assumed a constant. Since at the flame surface $Y_{H_2} = Y_{O_2} = 0$, Equation A-20 determines f' at the flame surface location.[2] These points are shown in Figure A-2. $\hat{\theta}_T$ may then be calculated from Equation A-20 and is shown on Figure A-3 for the two limiting cases of Table A-1. It is seen that the primary effect of the reactions is to extend the core temperature into the mixing layer and effectively widen the hot zone. Figure A-3 essentially shows the brackets on temperature to be expected in the mixing layer.

So far, results have been expressed in terms of the similarity variable η. To get the results in physical $y-x$ space requires the inversion which follows from Equation A-11.

$$\frac{y}{x R_c^{1/2}} = \int_0^\eta (\rho_{-\infty}/\rho) \, d\eta$$

where $\rho_{-\infty}/\rho$ is calculated from Equation A-6. For the three cases of no reactions, 0% Aℓ burned with reaction and 100% Aℓ burned with reaction, the inversion to physical space is shown in Figure A-4.

The final relation necessary to complete the mixing layer computation is the $u_e = u_e(x)$ relation, which is determined by a calculation of aluminum consumption in the core flow. Because the temperature in the core is nearly linear with the amount of aluminum consumption (see Figure A-1), a linear relation between the velocity and amount of aluminum consumption is quite accurate; viz,

$$u_e = u_{e_0} + (m/m_0)(u_{e_1} - u_{e_0}) \qquad (A-21)$$

132
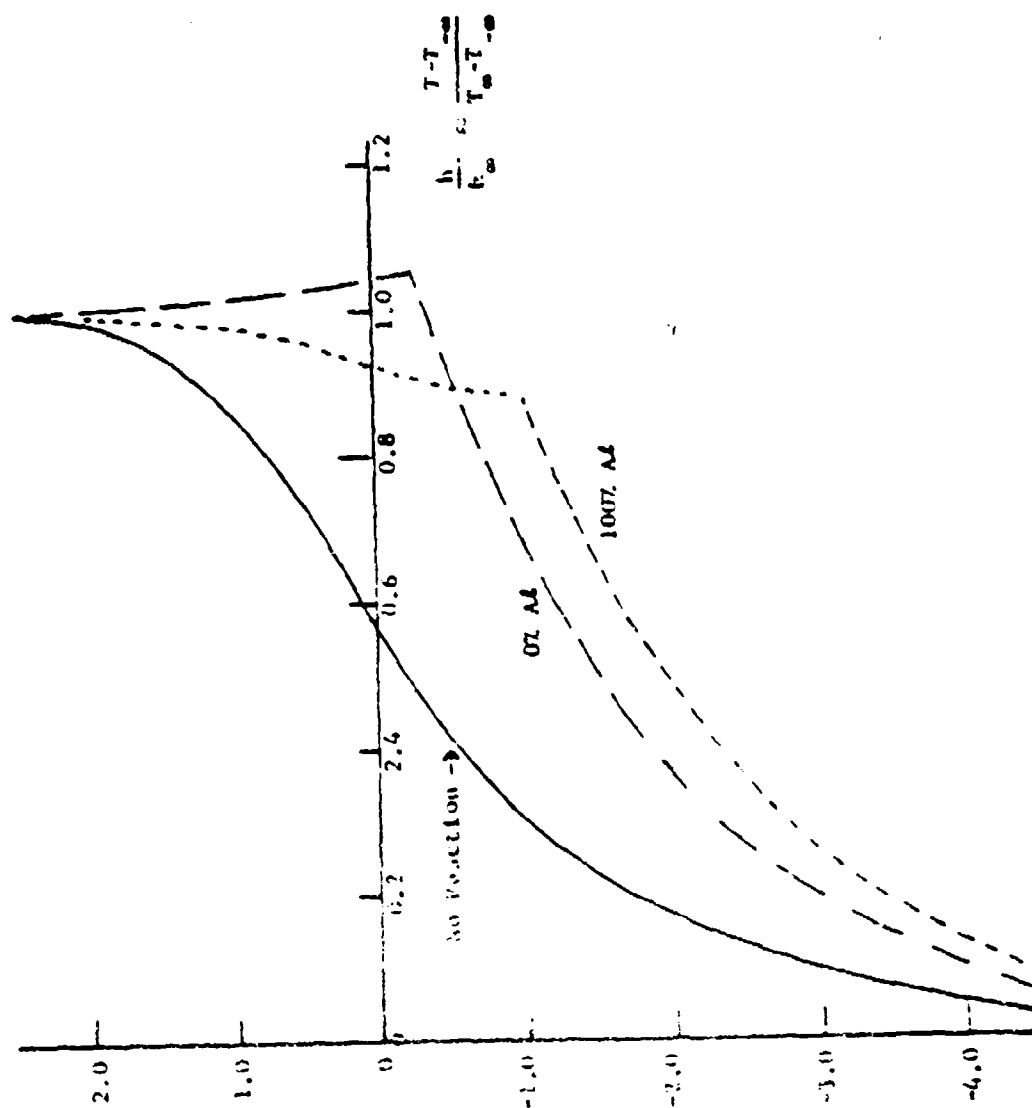
Figure A-3. Enthalpy profiles under various assumptions concerning reactions.
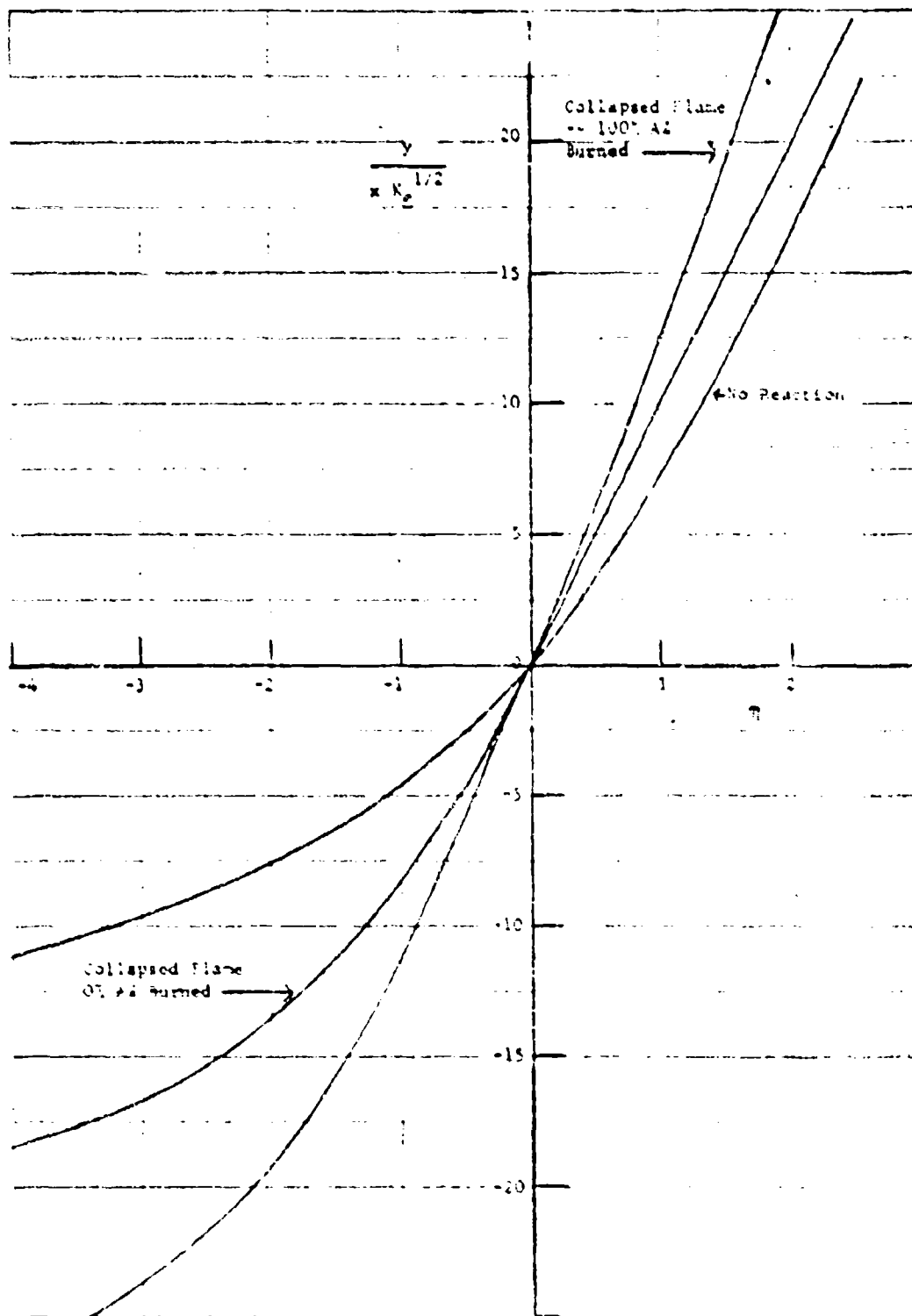
Figure A-4. Relation between η and the physical space variables.

where u_∞ and u_{∞_1} are given in Table A-1. The aluminum will be assumed in velocity equilibrium with the core gases and the consumption time for an aluminum agglomerate will be assumed to be (Reference A-4)

$$\tau \text{ (sec)} = 6.7 \times 10^{-6} \, D_o^n / \alpha_k^{0.6}$$

$$n = 1.5$$

$$\alpha_k = 0.6$$

$$D_o \text{ in } \mu m$$

Assuming that the overall time to burn is the overall result of the process

$$\frac{dm}{dt} = K \, D^n$$

where K and n are constant, it may readily be worked out that

$$\frac{d(m/m_o)}{dt} = u_\infty (x) \frac{d(m/m_o)}{dx} = \frac{2}{\tau} (m/m_o)^{1/2}$$

Upon integration and use of Equation A-2 the formula for aluminum consumption is

$$x = u_{\infty_1} \tau \left[1 - (m/m_o)^{1/2}\right] + \frac{2}{4} (u_{\infty_o} - u_{\infty_1}) \tau \left[1 - (m/m_o)^{3/2}\right] \quad (A-22)$$

A-2   Sample Calculation

To proceed with an actual calculation, two things are necessary; a) an experimental definition of the outer edge of the mixing zone, and b)

A-4.   Belyaev, A. F., B. S. Ermolaev, A. I. Korotkov and Yu V. Frolov, "Combustion Characteristics of Powdered Aluminum," Fizika Goreniya y Vzryva, Vol. 5, No. 2 (1969), (translation in Combustion, Explosion and Shock Waves, Plenum Publishing Co., 1972).

an assumption or experimental statement of the extent of reaction between O_2, CO and H_2. In this example a) the outer edge is defined as the straight line where h/h_∞ has dropped to 0.1 (the temperature has fallen 90% of the original temperature difference) and b) there is no reaction between the O_2, CO and H_2.

Concerning the aluminum, this calculation assumes a unimodal agglomerate size distribution. For this calculation $D_o = 100$ μm is assumed. Furthermore $T_\infty = 300^\circ$K is assumed.

Step I

a) T_m/T_∞ is computed as a linear function of m/m_o, using Figure A-1. This is plotted in Figure A-5a.

b) $u_m(x)$ is computed from Equation A-21. This is plotted in Figure A-5a.

c) m/m_o is plotted as a function of axial distance from the propellant from Equation A-22 and is plotted in Figure A-5a.

Step II

a) From the assumed measurement, take $y_{90}/x = -\tan 10^\circ$ as the equation of the straight line defining the outer edge of the mixing zone.

b) From Figure A-3 the no-reaction case (assumed), $h/h_\infty = 0.1$ at $\eta = -2.8$.

c) From Figure A-4 for the no-reaction case $y/x\hat{n}_c^{1/2} = -9.2$ at $\eta = -2.8$.

d) From Steps a) and c) the value of the mixing coefficient $\hat{n}_c^{1/2} = 0.019$

e) From Figure A-3 for the no-reaction case $h/h_\infty = 0.9$ at $\eta = 1.2$. This defines the inner edge of the mixing zone. From Figure A-4 $y/x\hat{n}_c^{1/2} = 9.7$ at the inner edge, yielding $y_{10}/x = 0.17$ from the known mixing coefficient. The two straight lines defining the mixing region are shown on Figure A-5b. From Figure A-5a, several positions of various aluminum consumption are shown on Figure A-5b.
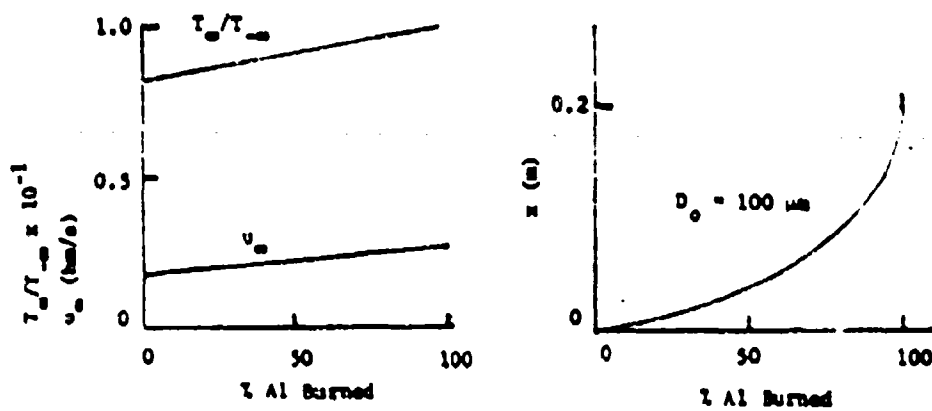
(a) Core velocity, ratio of core to cold temperature and physical axial distance as a function of mass of Al burned.
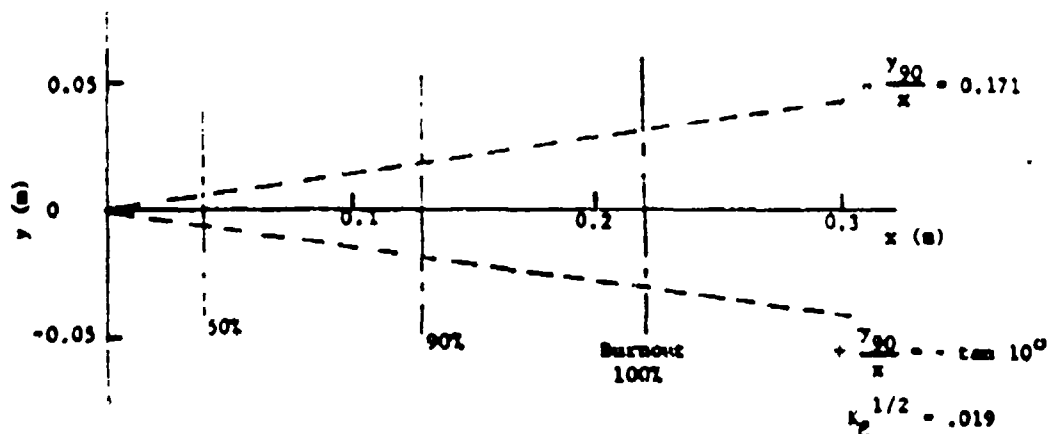
(b) Assumed spread of the mixing region versus axial distance and illustration of axial locations of various Al % consumption.
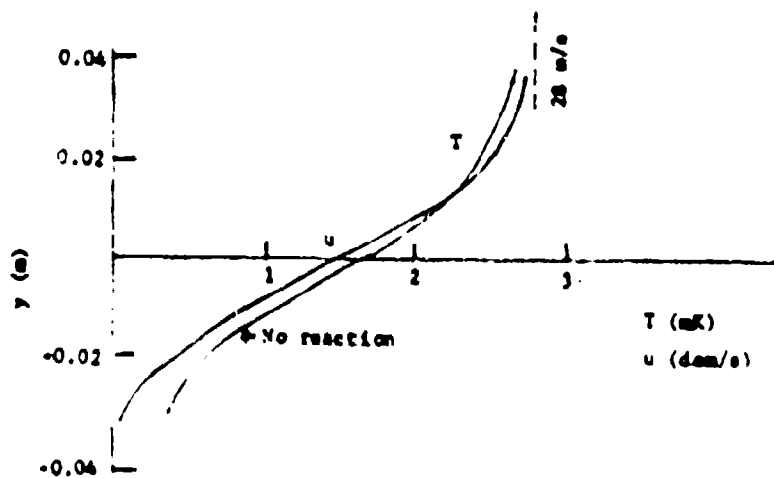
(c) Calculation of velocity and temperature profiles at the 90% Al consumption point assuming no reaction of air with the Al.

Figure A-5. Sample calculation of mixing zone.

137

Step III

a) Choose a particular axial station, here chosen as the x -
position for 90% aluminum consumption.

b) u is calculated from f' vs η on Figure A-2 with $u = u_\infty f'$,
u_∞ taken from Figure A-5a and the η to y conversion taken
from Figure A-4. The result is plotted on Figure A-5c.

c) The enthalpy profile is taken from the Figure A-3, the assump-
tion is made that $h/h_\infty \approx \dfrac{T-T_{-\infty}}{T_\infty - T_{-\infty}}$; the η to y conversion
is taken from Figure A-4. The result is plotted on Figure A-5c.

For the case where infinite reaction rates between the O_2 and CO
and H_2 are assumed the calculation procedure proceeds as above, but the
calculation of the enthalpy profile and the edge of the mixing layer are
slightly more complex. The edge of the mixing layer will be slightly curved
in this case, and in Step II-a it is necessary to specify not only that the
90% point is known but the amount of aluminum consumption at the x-point.
The reason is that in Step II-c an interpolation between two $y/xK_c^{1/2}$ vs η
curves is required to define $K_c^{1/2}$. In Step II-c an interpolation between
two h/h_∞ vs η curves is required. In Step III-b an interpolation is re-
quired on Figure A-4. In Step III-c interpolations are required on Figures
A-3 and A-4. It is recommended that the value of K_c deduced in Step II-a
be taken as a constant which will yield a slightly curved edge to the mixing
zone, owing to the continuous shift in the curve used in Figure A-4.

The mass fraction of the various species may be calculated using
Equation A-17 or Equation A-20 depending upon the reaction state which is
considered. In Equation A-20

$$\bar{B}_{CO} = \frac{Y_{CO}}{W_{CO}}(-a) + \frac{Y_{O_2}}{W_{O_2}}$$

$$\bar{B}_{H_2O} = \frac{Y_{H_2O}}{W_{H_2O}} + \frac{Y_{O_2}}{W_{O_2}}$$

$$B_{HCl} = Y_{HCl}$$

$$B_{CO_2} = \frac{Y_{CO_2}}{W_{CO_2}} + \frac{Y_{O_2}}{W_{O_2}}$$

139

NOMENCLATURE

(Appendix A)

c_p Specific heat at constant pressure

D Aluminum agglomerate diameter

h_i^o Enthalpy of formation of species i at T^o

h Sensible enthalpy above reference state, $\int_{T^o}^{T} c_p \, dt$

K_e Eddy diffusivity coefficient

m Mass of aluminum agglomerate

p Pressure

T^o Reference temperature (air temperature)

u Velocity in x-direction

v Velocity in y-direction

w Transformed vertical velocity

W Molecular weight

x Axial coordinate parallel to propellant side

y Coordinate perpendicular to propellant side with origin at the propellant

Y_i Mass fraction of ith, species

z Transformed vertical coordinate

ε_v Turbulent eddy diffusivity

ε_o Incompressible eddy diffusivity

v_i Stoichiometric coefficients of reaction equation

ρ Density

Ψ Stream function

τ Aluminum burn time

Subscripts

90 Point at which h/h_∞ has dropped to 0.1

10 Point at which h/h_∞ has dropped to 0.9

$\bullet$ Hot propellant core conditions

$-\infty$ Cold atmospheric conditions

i Species i

Subscripts (continued)

0   Conditions at $x=0$

1   Conditions at 100% aluminum consumption

Superscript

'   Left hand side of reaction equation

''   Right hand side of reaction equation

APPENDIX B
PHOTOGRAPHIC METHODS

B-1   Introduction

Photography was used extensively as a research tool during the course of this investigation for numerous reasons. Photography, especially with the use of telephoto lenses, is a remote data acquisition system and thus no components are threatened with destruction by the hostile environment of the propellant fire. It also provides a permanent record which can be analyzed to determine plume height and burning conditions such as one-dimensionality of the burning surface, crosswind effects, etc. Photography is used to magnify specific areas of interest within the combustion zone and reduce the light intensity thus revealing details which are not visible to the naked eye. A sequential recording of events such as deposition on a test object which occurs over a relatively long period can be obtained using a 35-mm camera with motorized film advance. Sequential events such as aluminum shedding from the burning surface which occurs over very short time periods can be recorded using a high speed motion picture camera. More importantly, photography can stop action, that is, it can reproduce an image which exists for as short a time as 10^{-5} second; an image which the human eye cannot resolve.

The photographic equipment used in this research is described in Section B-2. In Sections B-3 through B-6 the appropriate combinations of cameras and lenses for photographing various regions of the propellant fire are described. Shutter speeds and aperture settings for various films are also given in these sections. In Section B-7 a brief explanation of factors governing the selection of films, shutter speeds and filters is presented.

B-2   Description of Equipment

Burning samples of UTP 3001 were photographed using still 35-mm cameras with either manual or motorized film advance and with a 16-mm Hycam motion picture camera. Three high-resolution Nikkor lenses and two Vivitar lenses were used interchangeably for the still and motion picture cameras.

B-2.1 Cameras:

Nikon F-1. The Nikon F-1 is a single-lens reflex 35-mm camera
with through the lens light meter readings and shutter speeds of 2 seconds
to 0.001 second. This camera was fitted with a Nikon motorized back which
automatically advances the film and cocks the shutter. Using the motorized
back, photographs can be exposed singly or as a sequence of photographs at
either 1, 2, 3, or 4 pictures per second (pps). This back holds bulk film
rolls which will permit 250 exposures per roll.

Nikkormat EL. The Nikkormat is also a single-lens reflex 35-mm
camera with shutter speeds of 2 seconds to 0.001 second. This camera
has automatic exposure control which uses a between the lens light meter
to select the correct shutter speed. The light meter, however, averages
the light intensity between the bright plume and the dark background and
thus overexposes the plume and underexposes the background. Thus, best
results were obtained by manual selection of aperture and shutter speed.

Honeywell Pentax Spotmatic. The Pentax is also a 35-mm single-
lens reflex with through the lens light metering. The Pentax was used
primarily as a backup camera for tests with 10-cm diameter propellant
samples.

Red Lake Hycam. The Hycam is a 16-mm rotating prism motion picture
camera. Normal motion picture cameras (pin-type intermediate speed fram-
ing cameras) operate on a principle similar to the Nikon F-1 with motorized
back, only at higher rates. Thus the film advances, stops, the shutter is
opened and the film exposed, the shutter closes and the film advances.
Cameras of this type are limited to about 500 pps. The Hycam (rotating
prism camera) moves the film continuously between two reels and the image
is synchronized with the film movement by the use of a rotating prism.
If it were not for the prism, the image would be smeared across the film
as in a streak camera. In fact, by reversing the optics and avoiding the
prism, the Hycam can be used as a streak camera. The Hycam is capable of
filming rates of up to 11,000 pps with exposure times of 4×10^{-5} second.

3-2.2 Lenses:

All lenses were used interchangeably with all of the above cameras (both 35-mm still and 16-mm movie) using adapters.

Nikon Zoom Nikkor (200-to 600-mm) f/9.5 to f/32. This lens was the most useful one for these tests. Using this lens, it was possible to photograph agglomerates (200 microns) on the burning surface from a distance of 2.5 meters. It was also used for photographing agglomerate streaks in tube tests.

Nikon Zoom Nikkor (43- to 86-mm) f/3.5 to f/22. Used with chopper for plume photography.

Nikon Micro Nikkor (50-mm) f/3.5 to f/32. Used to photograph apparatus and overall plume height photos.

Vivitar Automatic Zoom (80- to 230-mm) f/4.5 to f/22. Used with Pentax as second camera in tests of large (10 centimeters) propellant samples.

Vivitar Automatic 85-mm lens, f/1.8 to f/16. Used with Hycam camera to photograph agglomerates leaving the burning surface in the window bomb.

3-2.3 Films:

All photography was carried out using Kodak films. For the 35-mm cameras, high-speed Ektachrome (EH-135, ASA 160), Ektachrome 200 (ED-135, ASA 200), and Ektachrome X (EX-135, ASA 32) color films and Plus-X (PX-135, ASA 160) black and white film were used. The motorized back was loaded with 250-exposure rolls of Ektachrome ER (ASA 160), a color film, similar to high-speed Ektachrome, available in bulk rolls. The Hycam camera was loaded with either Ektachrome EF-430 (ASA160) or EFB-430 (ASA 125) color films or Tri-X TXR (ASA 160) black and white film.

3-3   Photography of the Entire Plume

Initial photographic experiments involved photography of the entire plume to determine plume height and methods of obtaining columnar plumes, i.e., avoid edge burning. For these tests either the Nikkormat EL camera with an 86-mm lens or the Pentax camera with the 80- to 230-mm lens was used. These same cameras and lenses were also used in the chopper tests

(see Figure 10). When using fast films (ASA 125-200) camera settings
were 0.001 second at f/16 and when using moderate films (ASA 32) settings
of 0.001 second at f/3.5 or f/4.5 were acceptable. All settings should
be considered as base line settings. During the run several shots at the
next larger and next smaller aperture settings should be taken. For exam-
ple, with Ektachrome X (ASA 32) with a shutter speed of 0.001 second,
several exposures would be made at apertures of f/3.5, f/4.5, and f/5.6.

B-4   Photography of the Burning Surface

Still photographs of the burning surface were taken with a Nikon
camera with the 600-mm Nikkor lens. These photographs were taken to ob-
serve aluminum burning on the surface (see Figures 12, 14, and 23), to
test the effectiveness of edge burning inhibitors (Figures 9 versus 13)
and smoke trails from agglomerates on the surface (Figure 13). For fast
films (ASA 125-200) a shutter speed of 0.001 second and aperture of f/32
and for moderate films, a shutter speed of 0.001 second and aperture of
f/11 or f/16 are recommended as base line settings with the 600-mm lens.

For detailed examination of aluminum agglomeration on the surface,
a small sample (7.6-mm by 6.6-mm by 2-mm) of UTP 3001 was mounted in the
combustion bomb. The combustion bomb (see Figure B-1) had two quartz
windows, one for additional illumination of the sample from a 2500 watt
Xenon lamp and the other for photography. A nitrogen flushing flow was
used to prevent smoke obscuration. The burning surface was photographed
with the Hycam movie camera set for 2,000 pps. The Vivitar 85-mm lens
was reversed and mounted on a 70-mm extension tube to obtain a 2 to 1
magnification ratio. Using Tri-X film (ASA 160) and the Xenon lamp, an
aperture of f/4 gave a satisfactory exposure. These movies (see Figure
B-2) were used to measure the size of agglomerates leaving the burning
surface.

B-5   Photography of Agglomerates in the Plume

The apparatus used for photography of agglomerates at different
distances from the burning surface is described in Appendix F. Initial
photography was by Nikon camera with the 600-mm lens using Panatomic X

Figure B-1.   Combustion bomb with Hycam camera and xenon lamp.

|← 1 mm →|

Figure B-2.   Agglomerates burning on the surface of UTP 3001.

(ASA 32) film at 0.001 second and f/16 to f/32. For motion pictures using the Hycam camera, Ektachrome EFB film, and the 600-mm lens set at f/22, a framing rate of 4,000 ppe is recommended for distances of 15 cm or less from the burning surface and 2,000 ppe for distances greater than 15 cm. In Section B-7, the reason for decreasing exposure time is discussed.

B-6   Photography of Deposition of Condensed Phase Material on Test Objects

As noted in the text, deposition of condensed phase material is a major source of heat transfer to objects in the fire environment. Several exploratory tests were conducted with simple test objects (rods) immersed in the plume at various distances from the surface. Sequences of photographs were taken (see Figure 24) using the Nikon F with motorized back and the 600-mm Nikkor lens. The film was automatically exposed for 0.001 second every second (1 ppe) using an aperture of f/32.

B-7   Resolving Moving Objects

The subject field to be photographed in these studies was self-luminous, and bright, hence easy to photograph. However, the motion of the objects to be resolved and their small size poses a severe problem of stopping the motion. In addition, the field of view consists of a cloud of aluminum oxide smoke (droplets too small to resolve) and burning aluminum droplets (which need to be resolved); the smoke tends to obscure the aluminum droplets. Some skill is required to assure image contrast between the aluminum droplets and the smoke.

B-7.1 Stopping Motion

Relative to stopping motion, the problem is that resolution is required for droplets 150 μm in diameter moving 15000000 μm per second. Even if the goal were merely to limit smear of the image to 10% of the droplet diameter, this would require an exposure time of one microsecond or less. No effort was made to achieve this. Instead, photography of droplets was done near to the burning surface, where velocity of droplets was still low (Figure 35). There, motion pictures at 2,150 frames per

second were used (Section 12). For photography further out in the plume, pictures of droplets consisted of bars or streaks, the length of which was used for velocity measurement. At 15 m/sec, a 150-μm droplet moves 10^5 diameters per second, or 100 diameters in a 0.001 second camera exposure. While there are custom-built drum cameras that take pictures at speeds high enough to stop motion (resolve) of the aluminum droplets, they are not generally available, involve other experimental problems, and were not critical to the objectives. In the present work still camera shots at 0.01 to 0.001 second exposures were used. In addition, the Hycam motion picture camera was used at 2,150 pictures per second, and can be used in future tests at rates up to 10,000 pictures per second.

B-7.2 Proper Film Exposure

Another problem in resolving the aluminum droplets was the presence of an Al_2O_3 smoke cloud, which tended to obscure the embedded aluminum droplets. The smoke cloud was part of the combustion plume, and was hot and luminous. There was a tendency to expose the film properly for the smoke luminosity, which left very little latitude in the film response to resolve the brighter aluminum droplets (see Section 5), which were then overexposed. This was not such a serious problem in the high-speed motion pictures because of the short exposure time, and low smoke density in the case of pictures near the burning surface.

B-7.3 Contrast for Moving Object-Continuous Background Situation

There was a more subtle problem than overexposure involved in resolving burning aluminum droplets in the smoke field, which was described briefly in Section 6.4. The problem arose from the fact that the total radiation reaching a point on the film consisted of radiation from both smoke and burning aluminum droplets. The earlier discussion showed that the radiation from the droplet lasted only about 10^{-5} second, whereas the smoke field illumination lasted for the full open-shutter time. This resulted in a very low contrast between droplet streak and smoke background, unless the agglomerate was much brighter than the smoke or the camera

shutter time was very short (e.g., 10^{-5} second), or both.

The foregoing is illustrated by the simple analysis of film exposure. If the radiant flux reaching the film is i_1 for smoke and i_2 for agglomerates, then the total exposure (per unit area) at a point where an aluminum droplet image passes during exposure is

$$Q = Q_1 + Q_2 = \int_{t=0}^{t=\Delta t} i_1 \, dt + \int_{t=0}^{t+\delta t} i_2 \, dt = i_1 \Delta t + i_2 \delta t \qquad (B-1)$$

where Δt is the shutter-open time; δt is the time for the image of a burning droplet to move one diameter ($\delta t = D/v$); and i_1 and i_2 are assumed to be time-averaged values. It was noted earlier that D/v was of order 10^{-5} second, but larger near the burning surface where v is low.

Now the contrast between image points where a burning droplet passes and adjoining points is given by

$$\frac{Q}{Q_1} = \frac{Q_1 + Q_2}{Q_1} = \frac{i_1 \Delta t + i_2 \delta t}{i_1 \Delta t} = \frac{i_2}{i_1} \frac{\delta t}{\Delta t} \qquad (B-2)$$

From this expression, the contrast is high if (i_2/i_1) $(\delta t/\Delta t)$ is large compared to 1. As noted in Sections 5 and 6, (i_2/i_1) may be quite large; however $\delta t/\Delta t$ tends to be very small. Good pictures of burning droplets in the plume region require that very short exposure times be used, or that pictures be taken at locations where droplet velocity is still low, or that the smoke be blown away as in Figure 10. As a matter of interest, operation of the Hycam camera as a streak or smear camera is one way to reduce Δt down to the same order as δt, since Δt becomes the time for a point on the moving film to traverse the width of the viewing slit.

B-7.4 Selection of Film and Filters

Choice of film (if a choice is available) is governed by two constraints. It must be fast enough to be exposed during the short exposure

times and it must be slow enough so that it is not overexposed.

Kodak manufactures three films for the Hycam camera: EF and EFB (color films); and Tri-X (black and white). EFB is balanced for tungsten illumination and this film was used primarily for photographing agglomerates in the plume since the tungsten balancing makes EFB more sensitive to i_2 thereby increasing the ratio of i_2 to i_1 over EF film.

There is a much larger selection of films for 35-mm still cameras. Exposure guidelines for some of these films have been reported in Sections 3-3 through 3-6. Acceptable results have been obtained for most films.

In Section 3-6 it was recommended that a shutter speed of 0.001 second and aperture of f/32 be used with fast films when using the 600-mm lens to photograph the plume. Even with these settings, the film is slightly overexposed but since this is the minimum exposure time and minimum aperture it is necessary either to use a neutral density filter or use a slower color film. Since filters for the 600-mm lens are very expensive and very hard to obtain, the use of a slower color film is recommended.

Filters would also be useful in maximizing contrast as expressed by Equation 5-2.

3-7.5 Color Contrast

The temperature responsible for the agglomerate luminosity was much higher than the temperature of the smoke background (Figure 29). As a result, the ratio i_2/i_1, which varied as the fourth power of the ratio of these temperatures, tended to be much larger than 1. In addition, the agglomerate radiation was shifted to shorter wavelength (Figure 30). As a result the ratio of intensities at short wavelength was greater than the ratio of total radiation. Thus narrow band photography at short wavelength by use of filters would give better contrast. This technique was explored only superficially, but would probably help in marginal situations.

NOMENCLATURE

(Appendix B)

D   Diameter of agglomerate

i_1 Radiant flux from smoke per unit area per unit time reaching camera

i_2 Radiant flux from agglomerates per unit area per unit time reaching the camera

pps   Pictures per second

Q   Film exposure per unit area from smoke and an agglomerate

Q_1 Film exposure per unit area from smoke

Q_2 Film exposure per unit area from an agglomerate

V   Velocity of agglomerate

t   Time

Δt Increment of time the shutter is open

δt Time for image of an agglomerate to move one agglomerate diameter

APPENDIX C
EXPERIMENTAL DETERMINATION OF
DROPLET SIZE DISTRIBUTIONS

C-1 Introduction

Given the importance of droplet impingement as a means of damaging objects immersed in the fire environment, considerable effort was devoted to determination of the droplet population. This was done by observation of the initial population (near the burning surface) photographically. This led to an initial size distribution that was needed for calculation of downstream populations (Sections 9 and 10). In addition, samples were collected directly from the plume at different distances from the burning surface, and studied for size distribution, mass, portion that is aluminum, and nature of droplets. In the following, the sample collection is described first, and then the photographic studies are detailed.

C-2 Collection of Sample

The purpose was to obtain samples of aluminum and aluminum oxide from enclosed plumes of burning 5-cm diameter samples of aluminized propellants. The objective was to collect bigger particles (3μ-diameter and up) and to keep the samples as clean as possible for subsequent study of size and mass distribution.

C-2.1 Experimental Setup

The products from a down-flowing plume of a solid propellant piece, burning upside down in a 5-cm diameter stainless steel tube, were received into a bowl of alcohol.* Alcohol was used here as it quenched the condensed droplets without shattering them. A part of the whole plume was quenched depending on the method. The sample collected in alcohol was washed and dried after the test.

The tests described were developed over a period of time. __Three__ __methods__ of collecting the quenched particles were considered. The sample of solid propellant used in those three methods was the same shape and size.

The sample was of 5-cm diameter and 1.25-cm thick, weighing approxi-

---

* Ethanol

155

mately 45 g. It was placed in a stainless steel tube backed up by epoxy
to hold it in place. The samples were inhibited around the cylindrical
face by paper tape and no igniter paste was used. The average burning
surface of the sample was placed at a given distance (7.6 cm, 15.2 cm,
22.8 cm, 30.5 cm) away from the alcohol surface.

The alcohol to quench the condensed phase material was in a collection
bowl. The collection bowl for each of the three methods differed because of
the nature and position of the plume to be quenched in each case.

The first of the collection methods involved the whole plume imping-
ing onto an alcohol pool. The heavy particles were expected to go down
under gravity, while the lighter smoke particles were expected to turn
with the gas flow and escape. The collection bowl for this is shown
in Figure 47a. The base consisted of a steel dish with a frustrum shaped
interior to increase the depth of alcohol just below the sample. The outer
diameter of this dish was approximate 13 cm. It held and supported another
steel cylinder that provided an adequate wall to confine the fire.

The exit of the steel tube holding the sample was about 2.5 cms
above the alcohol level. Directly under the sample where alcohol dc
was the greatest, a Teflon disc of 5.0-cm diameter was placed to avoid
any sintering of the condensed phase material onto the metal bottom. The
tendency towards this decreased as the distance from the burning surface
increased.

The outer cylinder was provided with a helium flush for the purposes
of avoiding combustible alcohol-air mixtures in the apparatus, and extin-
guishing alcohol fires after the test.

It was observed during tests that substantial amounts of burning
aluminum were present in the deflected flow from the apparatus during
tests. Weighings of the collected material in the quench reservoir showed
collection efficiency of only about 16%, an outcome that raised some ques-
tions about the interpretation of results, as noted in later discussion.
Although it was concluded that a modification of the experiment would yield
more decisive results, most of the experimental results were obtained with
the first setup.

The second collection setup was contrived to avoid unwanted properties of the first setup. The second setup (Figure C-1) was designed to collect samples on the axis of the combustion plume, where it was postulated that:

a) The sample was least affected by the wall effects of the combustion tube.

b) The collected sample was least deflected by radial deflection in the exhaust flow, hence might be most representative of undisturbed flow.

c) The sample would be quenched in an inert gas before impingement on the alcohol.

Limited tests by this method yielded particles that seemed to be good representatives of the flow, but no systematic tests or optimization of design were carried out.

A third method was developed concurrently with the second one, and was designed to collect more of the condensed phase material in the alcohol. The arrangement (Figure 47b) was much like the first one, except that provision was made for a larger reservoir of alcohol and percolation of the entire propellant exhaust through the reservoir. Preliminary tests in this experimental setup yielded a 100% collection efficiency, but the number of tests was too few for systematic processing of samples. Alcohol-air fires were more of a problem in this arrangement.

C-2.2 Test Procedure

In each of the experimental setups, the propellant sample was weighed before the test. It was mounted in the combustion tube at the desired distance from the exit. The sides of the sample were inhibited by vaseline or paper tape or both. The paper tape was sometimes used to make the sample fit snugly in the tube. Ignition was accomplished by using ignition wire which heated the surface of the propellant locally to a temperature at which the propellant ignited. In order to ensure that fire spread all over the surface quickly, an igniter paste was used. The combustion products of the igniter paste were blown away or were washed away in the cleaning of the sample.
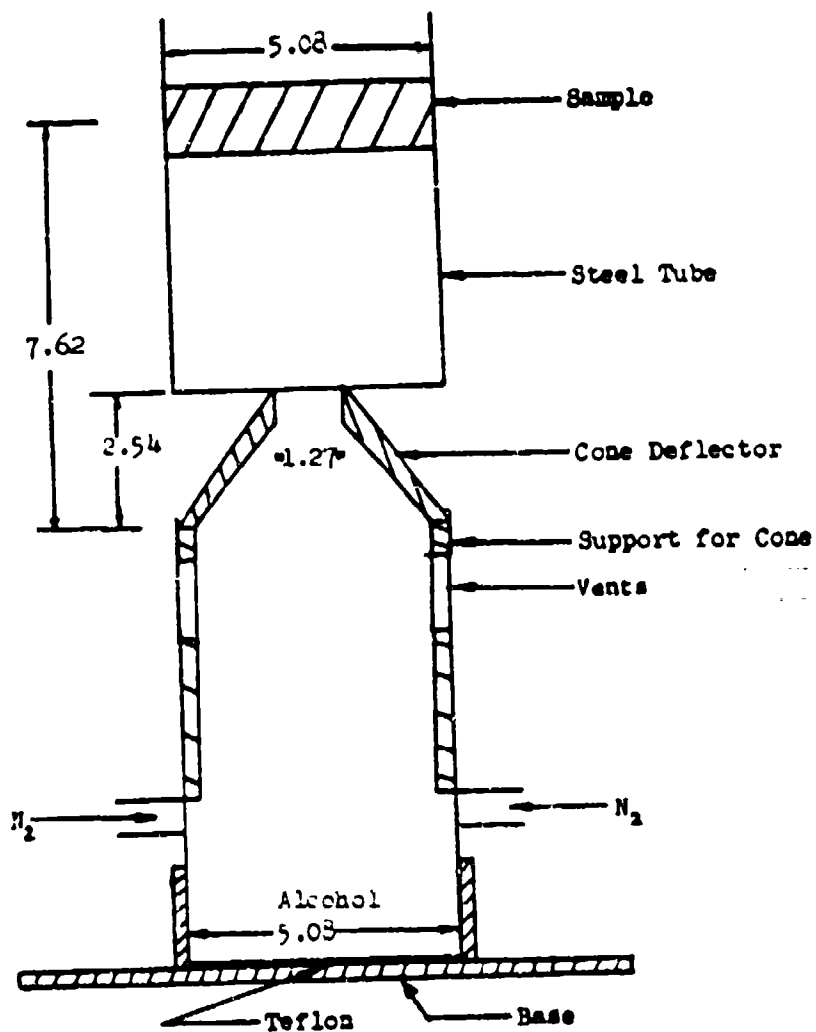
Figure C-1. Experimental setup for on-axis collection.
(All measurements in centimeters.)

C-2.3 Cleaning and Drying the Sample

The samples collected at the end of tests contained mainly alcohol, suspended particles and other chemicals such as HCl. It was necessary that particles of interest be separated from active ingredients. In order to do that, the acids and other soluble chemicals were scrubbed off with water. Then the water moist suspension was scrubbed with alcohol again in order to remove moisture and make drying easier.

A general procedure is described below.

1. Pour and rinse the contents of the collection bowl into a glass jar.

2. Remove the liquid from the mixture. This can be done using a syringe after allowing it to settle for some time. In the third method, however, filtering is required to remove the liquid as the volume of liquid involved is too large to be handled by the syringe. Also, it takes too long and reactions might occur which are not desirable.

3. Wash the residual with water and remove liquid again, either by a syringe or by filtering. This way major amounts of chemicals soluble in water are removed. Three or four repetitions of water-scrubbing will assure a sample almost free of HCl and other such chemicals.

4. The residual sample from step 3 is washed with alcohol to remove water. Again, three or four repetitions will remove almost all of the moisture.

5. Pour out the mixture of alcohol and particulate matter onto a flat dish (usually a petri dish) and allow it to dry.

C-3 Characterization of Sample

The entire sample was weighed initially. The weight was normalized with respect to the unit weight of aluminum in the original propellant sample (m). A plot of this quantity against the burning distance for the first alcohol impingement plume method is presented in Figure C-2.

C-3.2 Microscopic Observation and Photography of Unsized Sample

The entire sample was observed under microscope and comments were made regarding its appearance and other visual characteristics. The sample
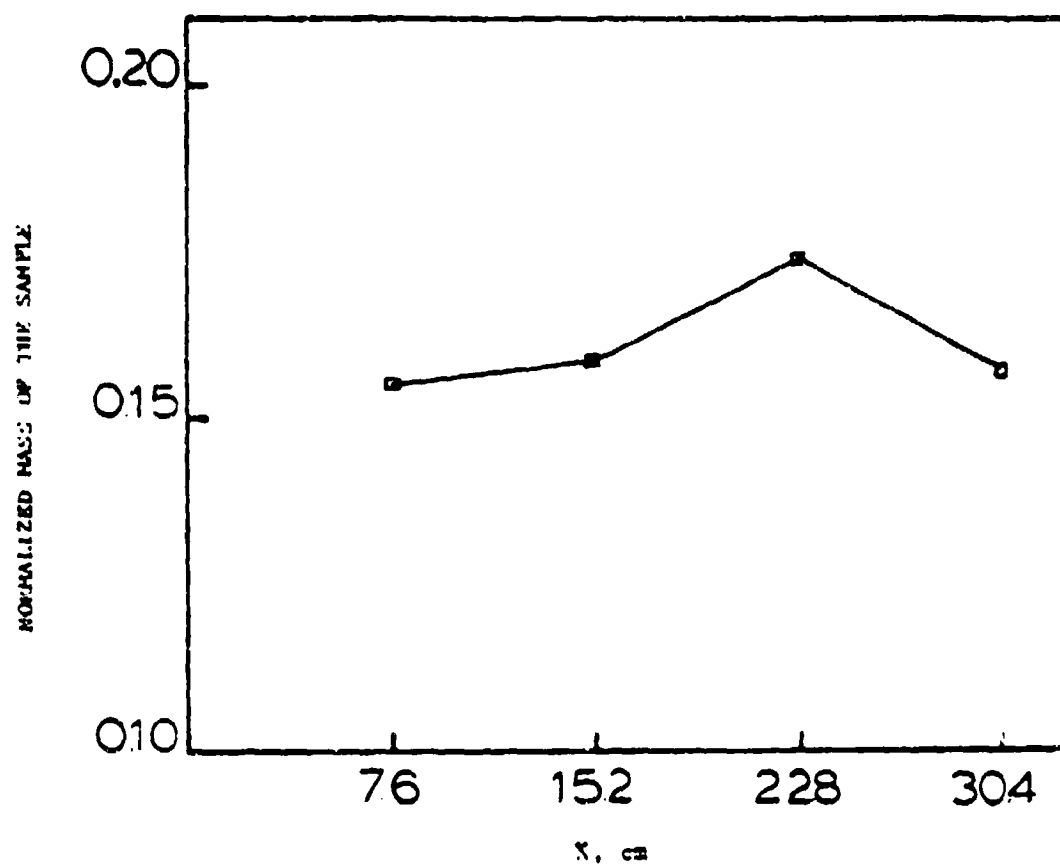
Figure C-2. Normalized mass of total collected sample versus the distance from the burning surface.

contained the following types of particles:

Shiny particles of irregular shapes, mostly sintered together.
This part contained mostly aluminum and had hardly had a chance to burn.
These came in large sizes (150 _ up).

Shiny and gray aluminum balls with oxide caps on them. These
came in all sizes. They were essentially spherical. They contained more
aluminum than oxide, but the oxide proportion was not necessarily small.

Translucent oxide balls with little or no aluminum attached to them.
These are called the residual oxides in the text. These resulted from
complete burn-out or possible spewing of oxide from large aluminum drop-
lets. They were mostly smaller than about 30 _. Typical pictures are
shown in Figure C-3.

C-3.3 Mass and Size Distribution Analysis

In order to study the burning history and further fire characteris-
tics, the size, shape and mass distribution of the particles had to be
known. The collected sample was, therefore, divid d into subintervals of
varying sizes by sieving the sample through a number of screens. The grid
column used in the present analysis is shown in Figure C-4. The sample
was placed on the topmost screen and the column was shaken so that loosely
sticking particles would separate.

The weights of samples on top of each screen were noted. The parti-
cles bigger than 600 _ were always some combination of smaller particles.
Therefore, the weight of the particles in this interval was distributed to
all the intervals in proportion of their individual weights. Thus we had
a set of corrected weights for all the intervals. The weights were nor-
malized by the amount of aluminum present in the original propellant sample.
The mass distribution over unequal intervals was hard to compare. There-
fore, the normalized weights in each interval were further divided by the
size of that interval, thus arriving at the following quantity (weight of
the sample per micron of the interval per unit weight of aluminum in
original sample).

Plotted over the particle size, this gave us the histograms shown
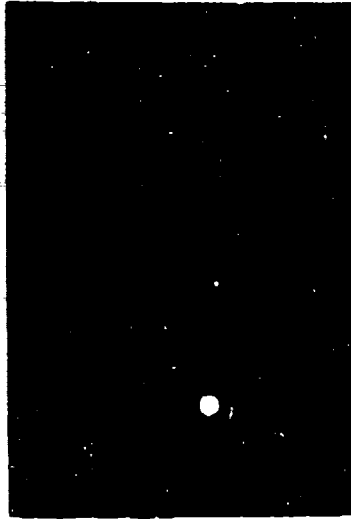
(b) Gray and shiny balls.

(d) Translucent residual oxides.

(a) Irregularly shaped material.

(c) Balls with oxide caps.

Figure C-3. Pictures of typical particles seen in the sample.

600 < D
180 < D < 600
149 < D < 180
125 < D < 149
90 < D < 125
63 < D < 90
45 < D < 63
37 < D < 45
0 < D < 37

Figure C-4. Grid column used to separate the sample into size intervals. (All figures in microns.)

in Figure 48.

Plots of this mass fraction against the burning distance for a given interval are shown in Figure C-5.

C-3.4 Microscopic Observation of Each Interval for Impinging Plume Method

A sample in each interval was separately observed in the microscope in order to make comment on its visual characterization.

1. Size interval D > 600 μ.

This interval mainly contained irregularly shaped shiny material and smaller balls sintered together.

2. Size interval 180 μ < D < 600 μ.

This interval contained irregularly shaped shiny pieces and spherical particles. Some of the balls were sintered together with the shapeless material.

3. Size interval 149 μ < D < 180 μ.

This interval mainly contained spherical particles. Some of the spherical particles were gray with oxide caps attached to them and others appeared metallic and shiny. Some smaller shiny balls were found sintered together with irregularly shaped shiny particles.

4. Size interval 125 < D < 149 μ.

This interval mostly contained spherical particles both gray and shiny. The spherical particles had oxide caps on them. Small amounts of irregularly shaped shiny material were sometimes found sintered on the spherical particles.

5. Size interval 90 μ < D < 125 μ.

This interval contained gray spherical particles with oxide caps. There were a few shiny balls present along with irregularly shaped shiny material.

6. Size interval 63 μ < D < 90 μ.

This interval contained gray spherical particles with oxide caps on them. There were some shiny balls connected together with other shiny material.

7. Size interval 45 μ < D < 63 μ.
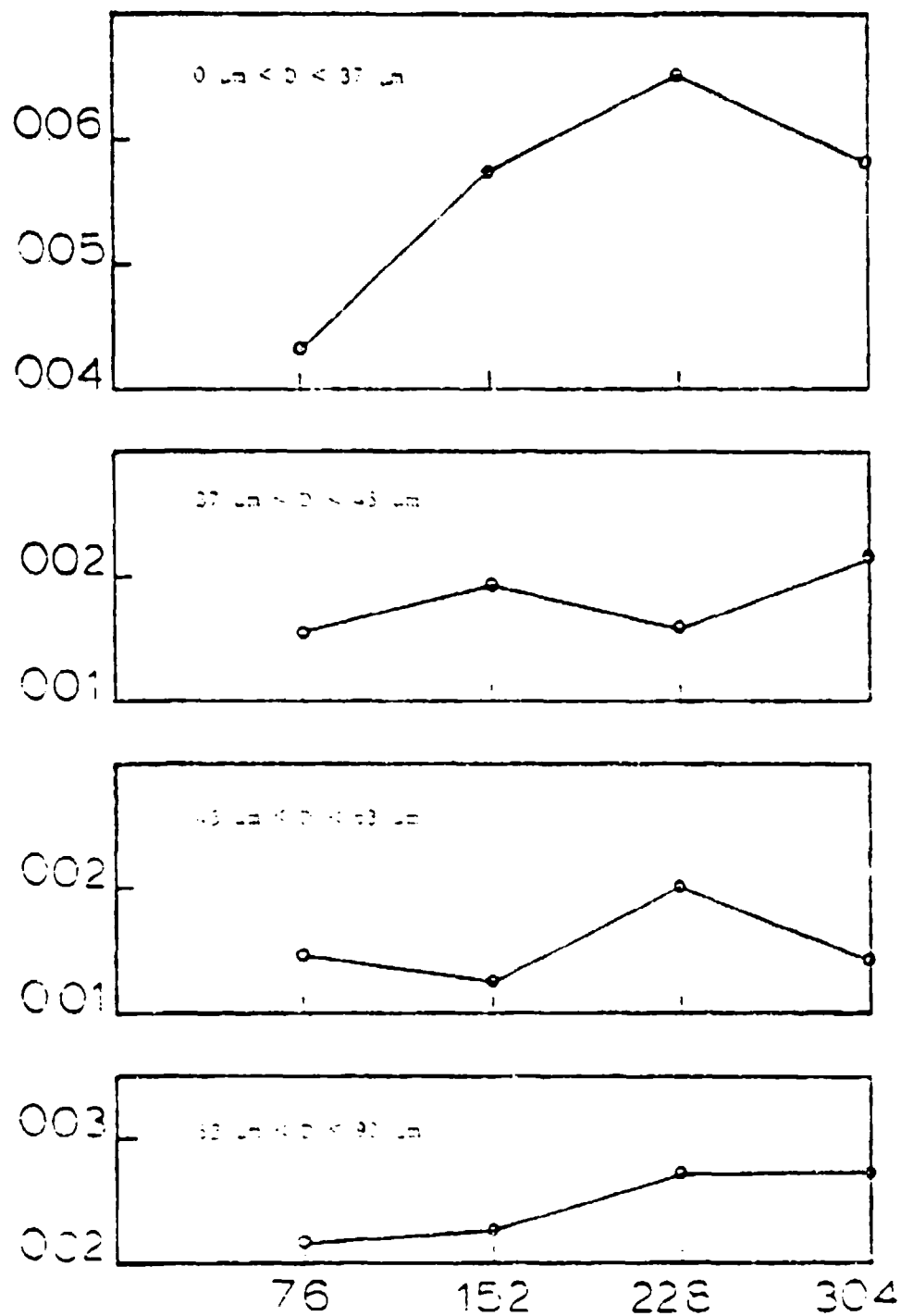
Figure 3-8. Mass fractions of the collected sample versus the distance
from the burning surface for different intervals.
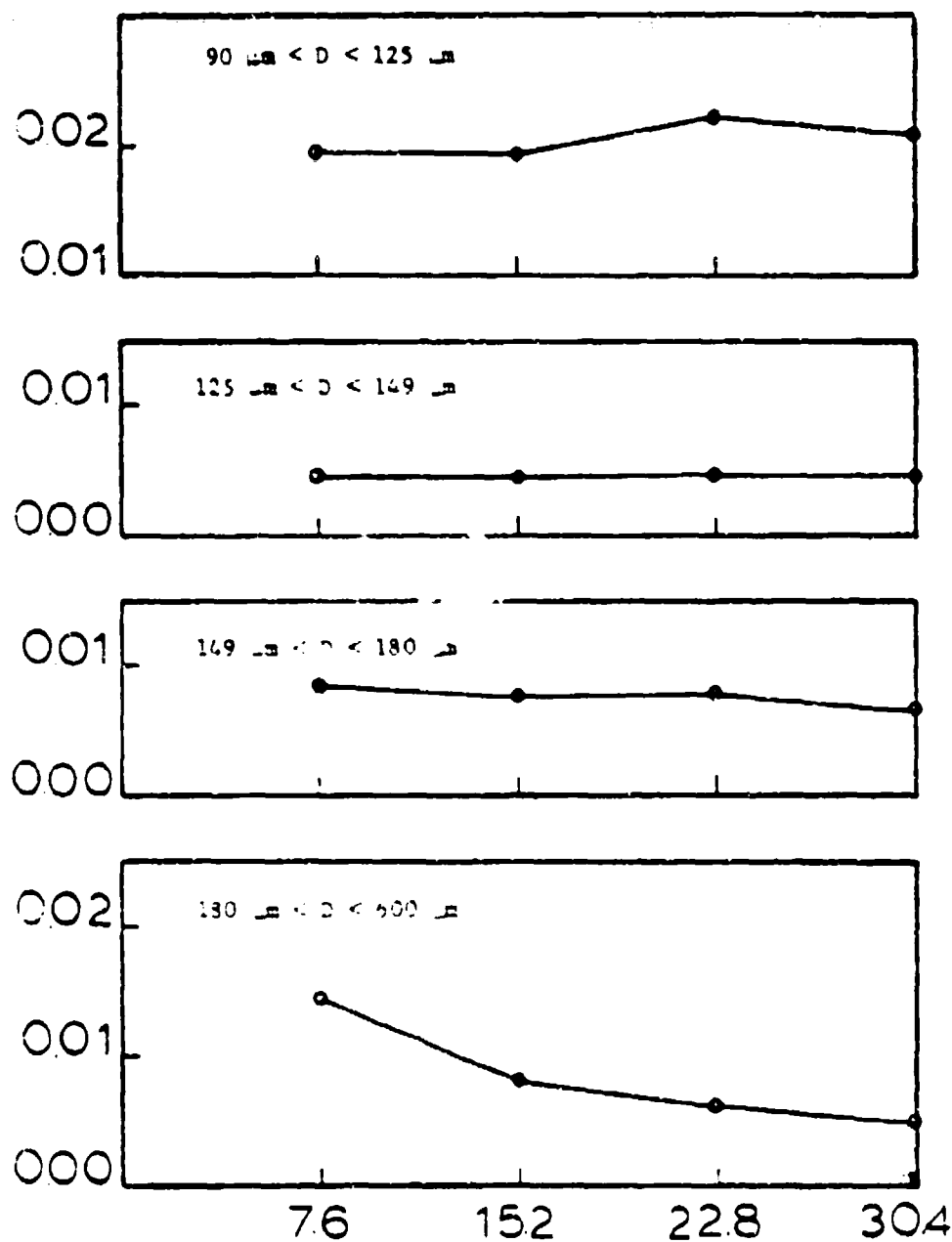
Figure C-5 (cont.). Mass fractions of the collected sample versus the distance from the burning surface for different intervals.

This interval contained mostly spherical particles and little irregularly shaped material. Gray and shiny balls were seen in various sizes. Additionally, some white translucent balls were evident in this size interval. These were non-metallic in their appearance.

8. Size interval 37 μ < D < 45 μ.

This interval contained gray and shiny balls in equal proportion. Some translucent oxide balls were also observed.

9. Size interval 0 < D < 37 μ.

The fraction of white translucent balls in this interval was more than the previous one. All the particles were regular in their shape.

Typical photographs are shown in Figure C-6.

C-3.5   Analysis of Amounts of Aluminum Present in the Collected Sample

The collected sample contained the following types of particles.

1. Aluminum particles with thin layer of oxide.

2. Aluminum particles with thick layers of oxide or oxide caps.

3. Oxide balls with little or no free aluminum on them.

The size distribution of the total sample, therefore, did not give the entire picture of the aluminum content as the smaller intervals had more oxide balls than in the larger intervals.

To find the actual aluminum content of the sample, one must separate oxide from the metal and this is very difficult without destroying the sample. A flotation method is thought to be possible, but has not been explored. Instead, a relatively easy method of acid etching the sample chemically was used. Since the aluminum in the sample was eaten away, this test was performed after all the other observations were made (photography, etc.).

The procedure was to allow the HCl (20%) to react with the sample for about 15 minutes. At this strength, HCl has relatively no reaction with the bigger oxides or thick oxide layers. It does, however, break through the gaps in the thin oxide layer and react with the metal. Vigorous bubbling followed by slower reaction takes place. The gas given out is hydrogen so care must be taken while conducting these tests.

164

$37~\mu < D < 45~\mu$

$63~\mu < 90~\mu$

$0 < D < 37~\mu$
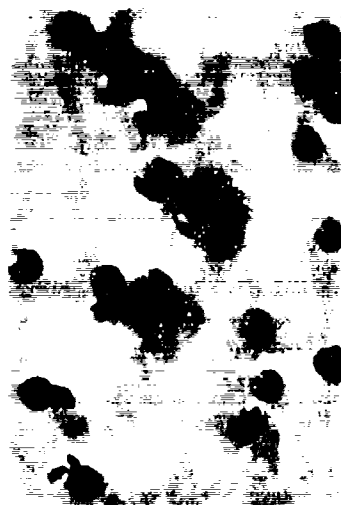
$45~\mu < D < 63~\mu$
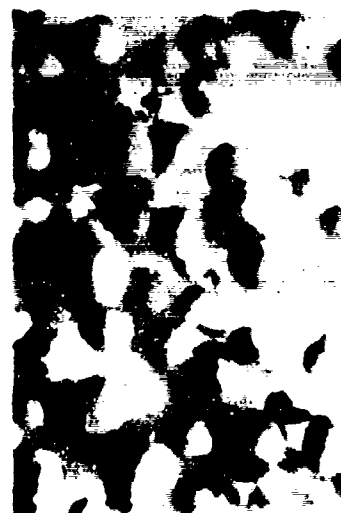
Figure C-6. Pictures of portions of collected samples in various intervals.

165

125 μ < D < 149 μ

180 μ < D < 600 μ

90 μ < D < 125 μ

149 μ < D < 180 μ

Figure C-6 (cont.). Pictures of portions of collected samples in various intervals.

After about 15 minutes, almost all of the aluminum is reacted to soluble Al Cl. This mixture is filtered and rinsed with water several times. The residue on the filter paper is dried in a desiccator and weighed. The difference between the weight of original sample and this residue gives the weight of aluminum in the sample.

This gives the fraction or percent of aluminum in that sample. These figures are used to calculate the weight of aluminum metal in the corrected weight of sample in each interval. This, then, is normalized with respect to the weight of aluminum in the original sample. The sum of weights in all the intervals gives total aluminum at that distance which is shown against distance in Figure 49.

C-4   Photographic Determination of Initial Droplet Size

Determination of the population of condensed phase material in the combustion zone has two general purposes. One is to know from direct observation what is present that is likely to experience impingement on objects in the flame. The other is to verify the conceptual pattern of how the population of droplets occurs, and how it changes with location in the combustion zone. Sections 8 through 10 establish an analytical scheme, embodying the concepts of how the population changes during burning, a procedure by which the results of experiments and of analysis can mutually support and correct each other. However, the population calculation procedure presumes that the initial aluminum droplet size distribution is determined independently and adequately. The most accurate means available appeared to be high-resolution photography of the aluminum immediately above the burning surface, where observational conditions are, fortunately, quite favorable. The following describes the procedures used, and results.

Combustion photography near the burning surface was widely used, and the procedure used here was fairly routine. The physical setup is described in Section 12 and Appendix B. The motion of the droplets was slow enough, and density of smoke low enough near the surface to give fairly clear pictures of agglomerates (e.g., Figure B-2). These were measured by first projecting on a screen for further enlargement.   Two difficulties were:

167

1. Unequal velocities of droplets of different sizes. This made the size distribution in single pictures nonrepresentative of the true population, and required sequential frame observation to identify each droplet and count it once only.

2. Obscuration of the aluminum droplets by the luminous flame envelope of the droplet. A diameter correction was applied using flame standoff data from the literature (see Section 12).

Table C-1 summarizes the measured droplet sizes observed over a period of time. Also shown are the diameters corrected for flame standoff and the grouping of the data in diameter increments corresponding to the histograms in Figure 51. These data were used elsewhere in the report for the initial aluminum droplet size distribution.

It was noted late in the investigation that the aluminum mass flow calculated from the droplet count data was substantially less than would be expected from the observed propellant burning rate and aluminum mass fraction. Since no such calculation has been reported in prior work, there was no basis for determining whether this anomaly reflected a corresponding failing in the droplet determinations. However, it is deemed desirable to make more extensive observations that might show sample-to-sample variations in population and mass flow rate. Further, it is of comparable importance that the flame envelope standoff be determined for this specific propellant (standoff versus droplet size). Photography with pulsed monochromatic back lighting should provide the necessary experimental results for standoff measurement.

Table C-1. Tabulation of Agglomerate Sizes (from Combustion Photography) and Calculation of Droplet Size Distribution. (Diameters in Micrometers.)

#	Observed Droplet Diameter	Corrected Droplet Diameter	Frequency	ΔN	$\dfrac{\Delta N}{N}$	$\dfrac{1}{N}\dfrac{\Delta N}{\Delta D}$	ΔM	$\dfrac{\Delta M}{M}$	$\dfrac{1}{m}\dfrac{\Delta M}{\Delta D}$
1	25	8.6	9						
2	37	15.0	1						
3	38	15.1	1						
4	40	16.0	2						
5	43	17.9	1	24	0.174	0.00435	0.00054	0.000495	0.000012
6	50	22.7	2						
7	55	26.2	2						
8	58	29.0	1						
9	60	30.1	1						
10	65	33.0	2						
11	68	37.8	2						
12	75	44.1	5						
13	80	50	2						
14	83	51.9	4	17	0.1232	0.00616	0.00313	0.00298	0.000149
15	85	53.4	1						
16	88	58.7	3						
17	90	60.0	4						
18	93	64.1	1						
19	95	65.1	1						
20	100	71.4	3						
21	103	75.2	3	14	0.1014	0.00338	0.00869	0.00829	0.000276
22	105	77.8	1						
23	108	81.5	1						
24	110	84.6	2						
25	115	90.2	2						
26	117	94.4	1						
27	118	95.0	1						
28	120	96.0	1						
29	125	104.2	4	15.5	0.1123	0.00375	0.02588	0.02469	0.00823
30	130	110.2	2						
31	130	113.2	2						
32	135	116.4	2						
33	138	120	1						
34	140	121.7	1						
35	145	128.3	2						
36	148	133.3	1	12.5	0.0906	0.00302	0.04401	0.04198	0.0014
37	150	136.4	4						
38	155	140.9	2						
39	160	146.8	2						

Table C-1
(continued)

#	Observed Droplet Diameter	Corrected Droplet Diameter	Fre-quency	ΔN	$\dfrac{\Delta N}{N}$	$\dfrac{1}{N}\dfrac{\Delta N}{\Delta D}$	ΔM	$\dfrac{\Delta M}{M}$	$\dfrac{1}{m}\dfrac{\Delta N}{\Delta D}$
40	163	150.9	4						
41	165	154.2	1						
42	168	157.0	3						
43	170	160.4	2						
44	172	162.2	1	18	0.1304	0.00435	0.11526	0.10995	0.00366
45	173	163.2	1						
46	180	169.8	2						
47	185	175.2	3						
48	185	179	1						
49	190	182.9	3						
50	193	183.8	2	11	0.0797	0.00266	0.11599	0.110624	0.00369
51	200	190.5	1						
52	205	195.2	1						
53	213	195.2	2						
54	215	205	2						
55	225	214.3	1						
56	230	219	2	10	0.0725	0.00242	0.16175	0.15429	0.00514
57	243	231.5	2						
58	245	233.3	1						
59	247	235.5	1						
60	250	238.1	3						
61	253	243.3	1						
62	255	245.4	1	7	0.0507	0.00169	0.16465	0.15098	0.005029
63	260	256.5	1						
64	270	259.5	1						
65	280	269.5	3						
66	287	275.3	1	3	0.02174	0.00075	0.09846	0.09392	0.003131
67	300	288.5	2						
68	312	302.4	1						
69	313	303.9	1	4	0.0290	0.00097	0.11714	0.16898	0.00563
70	325	315.4	1						
71	328	318.4	1						
72	350	339.8	1	1	0.00724	0.1002	0.03815	0.0527	0.00184
73	375	376.6	1	1	0.00724	0.3024	0.07563	0.075	0.0025

$$N = 138 \qquad m = 1.04831 \text{ mg}$$

APPENDIX D
MEASUREMENTS WITH IMMERSION
HEAT PROBES

D-1 Introductory Comment

There were no illusions at the outset of the investigation that the fire environment could be characterized by a unique temperature, or that such a property could be measured by insertion of a thermometer in the plume. On the other hand, it was clear that a heat-sensitive device in the fire would respond, and would be responding to an experience similar to that of any test object (radioisotope thermoelectric generator) in the fire. Accordingly, several experiments were made on immersion devices ranging from bare thermocouples to water-cooled calorimeter tubes. Much of this was reported in Section 5.

D-2 Bare Thermocouples

At the outset, a number of tests were run with thermocouples immersed directly in the combustion zone. These thermocouples experienced direct impingement with droplets in the flow, gave very erratic readings, and survived only briefly (the most heat resistant thermocouples were of the platinum/platinum rhodium type). The results foretold later conclusions, that impingement-deposition processes were major factors in measurements. Some measurements made in the wake of deflectors (a region relatively free of condensed material, see Figure 16) survived longer and gave better records--however, it was not clear how the temperature there could be related to the free stream temperature, even if the thermocouples survived.

D-3 Immersion Calorimeter

In measurement of heat in high-temperature flows where immersion probes deteriorate, measurements may be based on the heat-up rate of the probe during temporary immersion. This amounts to operating the probe as a calorimeter. A probe was designed for this purpose, and was used to calculate heat transfer in the fire environment. This work is described in Section 4, and the purpose of this portion of Appendix D is to describe how

the recorded probe temperature data is handled to obtain an effective
plume temperature

The details of the probe are shown in Figure 25, and typical thermo-
couple output curves are shown in Figure 26. Equation 1 was used to calcu-
late plume temperature, neglecting the radiant heating term and rewriting
as follows

$$T_g = A \frac{dT_p}{dt} + B(T_p - T_o) + C(T_p^4 - T_o^4) \qquad (D-1)$$

The quantity T_p is measured, and the quantity T_o is the room temperature
($296^\circ K$). The coefficients A, B, and C were determined by calibration of
the probe in combustion gases of known temperatures, where only A, B, and
C are unknown.

The values of A, B, and C were calculated in a manner illustrated
in Table D-1. The table shows a set of 5 data points (T_p vs t) (from a
calibration run) and shows calculated values of dT_p/dt. This leads to
three sets of T_p, dT_p/dt and t which should satisfy Equation D-1. When
substituted in Equation D-1, these sets give three equations in A, B, and
C (Table D-1, center), which can be solved to give values of A, B, and C
(Table D-1, bottom). These values are then used in the calculation of T_g
from Equation D-1 and tests in propellant combustion plumes. The calibration
procedure was carried out on each probe, before and after each test. The
calibration gas flow was $1659^\circ K$. The results of calibration after tests
were much different than those before tests, because of deposition on the
probe. Lacking any better guide, the assumption was made that the change
in A, B, and C with time were linear functions of time during tests.

In the propellant plume test, a temperature versus time curve (e.g.,
Figure 26) is obtained from the thermocouple in the probe. A set of 6 points
or so is measured, tabulated, and converted from millivolts to temperature
(Table D-2) in $^\circ K$ using thermocouple response tables or independent cali-
bration. From these points, corresponding values of dT_p/dt are calculated.
The resulting data are substituted into Equation D-1 to determine T_g. In
this calculation the linear interpolation of the parameters A, B, and C

Table D-1. Data Reduction From the Before-Test
Calibration of Test Number 170.

Part A. Test Data

t (sec.)	MV	T^oC	T_p^oK	$\dfrac{dT_p}{dt} \dfrac{^oK}{sec}$
30	1.55	213		
40	2.125	278	551	6.40
50	2.7	341	614	5.80
60	3.2	394	667	5.25
70	3.7	446		

Part B. Evaluation of Parameters From
Equation D-1 and Part A of This
Table: $T_g = 1659^oK$.

$$6.40\ A + 255\ B + 8.45 \times 10^{10}\ C = 1102$$

$$5.80\ A + 318\ B + 1.34 \times 10^{11}\ C = 1045$$

$$5.25\ A + 371\ B + 1.90 \times 10^{11}\ C = 992$$

Part C. Values of Parameters Before Test Number 170.

A	B	C
161	0.135	5.07×10^{-10}

between pre- and post-test calibration is made for each time during burn-
ing (Part B of Table D-2). The Table shows (last column) the indicated
gas temperature at four times during the test, and these temperatures are
shown in the graph of Figure 27, plotted at the 7.6-cm position above the
burning surface.

Many tests like number 170 were run, including ones in which the probe
location was at 14.2 and 23 cm from the burning surface. Various problems
were encountered such as failure of the probe, anomalous propellant sample
burning, or shedding of the deposits from the probe before the second cali-
bration. However, satisfactory tests were obtained at the 7.6-, 14.2-, and
23-cm locations above the burning surface. The results are summarized in
Section 4 (Figure 27), and discussed there. The following arguments are
advanced:

    1. The indicated plume temperatures are inordinately high
because extensive heat transfer is produced by deposition of hot
oxide and aluminum and by oxidation of deposited aluminum, whereas
all heat transfer in Equation 1 is assigned to convection from a
gas at temperature T_g (and heat transfer coefficients are eval-
uated in a clean gas).

    2. The decrease in indicated temperature with distance from
the propellant surface is due to cold air mixing with the plume,
decreased deposition on the probe, and decrease in aluminum oxida-
tion on the probe.

    3. The trend of increasing indicated temperature with time
is due to increasing accumulation and oxidization rate of aluminum,
an argument that is supported by the reduced time dependence at 23
cm, where the availability of aluminum is substantially less.

The principal result of these particular tests was to bring out the
importance of deposition and reaction of condensed material, and the dif-
ficulties in trying to represent the fire environment in terms of a simple
flow of a high temperature medium. Clearly, the effect on immersed objects
is strongly dependent on the impingement-retention-reaction-shedding of
condensed material, which in turn depends on the composition and size of

Table D-2. Data Reduction for Test Number 170.
Test Burning Time Was 26 Seconds.

Part A. Temperature Data

t (sec.)	MV	$T^{\circ}C$	T_p $^{\circ}K$	$\frac{dT_p}{dt}$ ($\frac{^{\circ}K}{sec}$)
9	3.2	394		
10	3.55	441	714	51.5
11	4.2	497	770	55.5
12	4.75	552	825	57.0
13	5.35	611	884	56.0
14	5.9	664		

Part B. Correction of Parameters for Deposition-Calculation Of Gas Temperature From Equation D-1.

t (sec)	A	B	C	T_g $^{\circ}K$
10	216	-0.72	2.94×10^{-9}	12,278
11	221.5	-0.81	3.18×10^{-9}	13,773
12	227	-0.89	3.43×10^{-9}	14,856
13	232.5	-0.98	3.67×10^{-9}	15,541

droplets present.

D-4 Water Cooled Probe

It was noted earlier that one way to assure survival of an immersion probe was to use a calorimeter type system and limit immersion time. This approach was used in Section D-3. Two major problems were: slow response time, which limits the amount of measurements (i.e., the plume cannot be tested at several locations in one test); change in calibration during measurement due to buildup of deposit.

An alternate means of assuring survival of a probe is by cooling it to limit its temperature rise. Such a probe would measure coolant temperature rise and flow rate, as a means of measuring heat transfer. Response time could be low enough to permit operation in a traversing mode; alternately, if deposition changed calibration drastically, measurements could be made with short enough duration to minimize change in calibration during individual measurements. Further, the change in calibration could be characterized on a time continuous basis by simply noting the change in heat transfer with time during a long test with stationary probe.

These considerations motivated exploratory tests on a system shown diagramatically in Figure D-1. While the tests were not extensive enough to develop systematic data, they showed the following promising characteristics.

1. Deposition was much less than for the uncooled calorimeter probe.

2. Cooling water temperature rise of $30^\circ C$ occurred with a convenient water flow rate of 10 g/sec.

3. Steady temperatures were reached in 2 seconds, indicating relatively short time response.

Analytically, the response of this probe can also be represented by Equation 1. However, one would normally operate it as a steady state device, eliminating the need for the dT_p/dt term. In addition, temperatures would remain low enough to eliminate need for a radiation term, and the heat conduction out would be modified to reflect convection out by the water
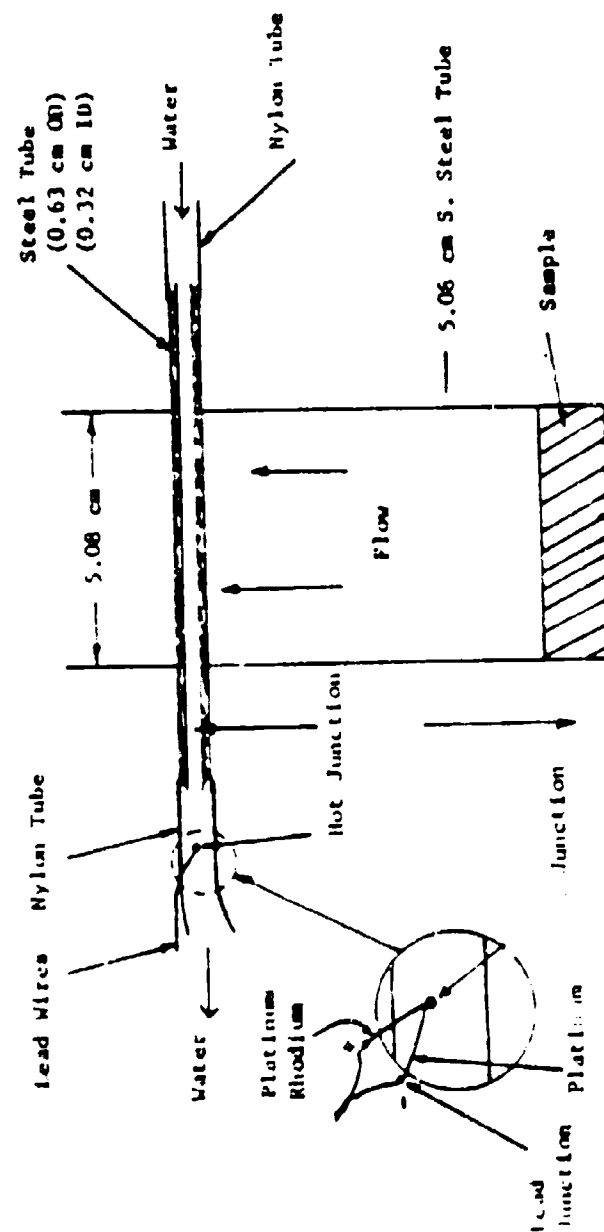
Figure II-1. Schematic of the watercooled probe setup.

flow. Thus

Convective transfer, gas to probe surface	Transfer by deposition of con- densed material	Heat transfer through tube walls

$$H_g \, (T_g - T_p) \quad + \quad H_c \, (T_c - T_p) \quad = \quad H_t \, (T_p - T_o) \quad =$$

Heat removal by coolant	Heat removal by conduction

$$= \overset{o}{m} \, C_v \Delta T_w \quad + \quad H_o \, (T_p - T_o) \tag{D-2}$$

If one assumes that the heat convected out by coolant is much larger than the heat conducted out, then the $H_o \, (T_p - T_o)$ term can be dropped. Then we have two equations. One is

$$H_g T_g + H_c T_c = (H_g + H_c) \, T_p + \overset{o}{m} C_v \Delta T_w$$

$$T_g \, (1 + \frac{H_c}{H_g} \frac{T_c}{T_g}) = (1 + \frac{H_c}{H_g}) \, T_p + \frac{\overset{o}{m} C_v \Delta T_w}{H_g} \tag{D-2a}$$

Eliminating T_p in favor of T_o, using the second equation in D-2,

$$H_t \, (T_p - T_o) = \overset{o}{m} C_v \Delta T_w$$

$$T_p = \frac{\overset{o}{m} C_v}{H_t} \Delta T_w + T_o \tag{D-2b}$$

Then equations D-2a and D-2b give

$$T_g \, (1 + \frac{H_c T_c}{H_g T_g}) = (1 + \frac{H_c}{H_g}) \, (\frac{\overset{o}{m} C_v}{H_t} \Delta T_w + T_o) + \frac{\overset{o}{m} C_v}{H_g} \Delta T_w$$

$$\mid T_g = \left(\frac{1 + \frac{H_c T_c}{H_g T_g}}{1 + \frac{H_c}{H_g}} \right) T_g = (\frac{1}{H_t} + \frac{1}{H_g}) \, \overset{o}{m} C_v \Delta T_w + T_o \tag{D-3}$$

In this expression, the coefficient of T_g is indicative of the relative importance of heat transfer by gas convection and by deposition of condensed material, being of value one when there is no condensed material. The coefficient of the first term on the right can be determined by calibration of the probe in a clean flame, where T_g, $\overset{\circ}{m}$, ΔT_w and T_o would be measured, and

$$(\frac{1}{H_t} + \frac{1}{H_g}) = \frac{T_g}{\overset{\circ}{m} c_w \Delta T_w + T_o} \tag{D-4}$$

With this result and the measured values of $\overset{\circ}{m}$, ΔT_w and T_o in a propellant test, one can obtain ΓT_g from Equation D-3. Indeed, the behavior of ΓT_g could be observed as a function of position in the plume (traversing probe) or as a function of time (monitoring effect of accumulating deposit). As in the case of the uncooled immersion calorimeter, the values of ΓT_g would presumably be greater than the true temperatures due to deposition heating. In this case the effect is localized explicitly in the factor Γ for study by suitable experiments. However, this line of investigation could not be pursued within the limitations of the present project.

NOMENCLATURE

(Appendix D)

A,B,C   Coefficients in Equation D-1, related to heat transfer

C_w Heat capacity of water

H_c Coefficient of heat transfer due to deposition of condensed material (Equation D-2)

H_g Coefficient of heat transfer due to convection from gas (Equation D-2)

H_t Coefficient of heat transfer through tube walls (Equation D-2)

$\overset{\circ}{m}$ Flow rate of water (Equation D-2)

T_g Temperature of flowing gas

T_p Temperature of probe outer surface (Equation D-2)

T_o Temperature of surroundings

T_w Temperature of coolant water (initially T_o)

t   Time

f   Coefficient (Equation D-3) reflecting relative contribution of condensed material deposition to calculated temperature.

APPENDIX E

RADIATION FROM DROPLETS

E-1   Introduction

The majority of the radiation in the combustion zone originates from Al_2O_3 smoke. As a result, efforts were made to obtain quantitative measurements of smoke radiation. At the outset, it was expected that the smoke would be optically dense, and mostly near the temperature of the gas in the same region. Accordingly, it was assumed that if intensity at 2 or 3 wavelengths could be made (by comparison with a laboratory standard lamp of known temperature), a meaningful measure of bulk temperature and droplet emissivity could be determined. In the following, a summary is given of the analytical basis, experimental procedures, and results of measurements of temperature and emissivity of the plume based on intensity at three different wavelength regions. Specifically, the radiation is measured by means of three photomultiplier tubes fitted with narrow band-pass interference filters. The wavelengths selected are 4050 $\overset{o}{A}$, 5050 $\overset{o}{A}$, and 6000 $\overset{o}{A}$. In addition, a fourth wavelength can be monitored using a monochromator. The intensities emitted by the plume at these wavelengths are compared with the corresponding intensities emitted by a tungsten ribbon filament lamp at a known temperature. The ratios of plume intensity to lamp intensity at the three wavelengths are then used to determine temperature of the Al_2O_3 smoke by three techniques:

1. Using measurements at one wavelength and an assumed emissivity.
2. Using measurements at two wavelengths and assuming a gray body.
3. Using measurements at three wavelengths and using an assumed dependence of emissivity upon wavelength.

Each of these techniques will be discussed separately.

E-2   Data Reduction Techniques

E-2.1 Assumed Emissivity

For radiation normal to a hot surface, the radiant intensity in the wavelength band between λ and $\lambda + d\lambda$ is given by the Planck radiation

law:

$$I_\lambda = \left\{ \frac{2 \, \epsilon_\lambda c_1 \lambda^{-5}}{e^{c_2/\lambda T} - 1} \right\} A d\lambda \qquad (E-1)$$

where

ϵ_λ = emissivity at wavelength λ

c_1 = first radiation constant = 0.588×10^{-12} W/cm^2

c_2 = second radiation constant = 1.438 cm/°K

λ = wavelength (cm)

A = area of radiating surface (cm^2)

T = temperature of the radiator in °K

I_λ = the intensity in watts per unit solid angle

For practical calculations a close approximation to Planck's law is given by Wien's law:

$$I_\lambda = 2\epsilon_\lambda A c_1 \lambda^{-5} e^{-c_2/\lambda T} d\lambda \qquad (E-2)$$

which holds with sufficient accuracy as long as λT is less than 0.5 cm°K. For the temperatures and wavelengths considered in this study, this criterion is met and Equation E-2 will be used.

In order to determine temperature using Equation E-2 a calibration standard is needed, since absolute intensity measurements are difficult. A tungsten ribbon filament lamp with a known temperature versus current curve is used as a standard. The ratio of intensities $I_\lambda/I_{\lambda c}$ is determined from Equation E-2 as'

$$I_\lambda/I_{\lambda c} = \frac{\epsilon_\lambda}{\epsilon_{\lambda c}} e^{c_2/\lambda \left(\frac{1}{T_c} - \frac{1}{T} \right)} \qquad (E-3)$$

where $I_{\lambda c}$ is the radiant intensity of the calibration lamp, and $\epsilon_{\lambda c}$ and T_c are the corresponding known emissivity and temperature of the tungsten ribbon.

If a value of the emissivity of the Al_2O_3 smoke is assumed, Equa-

tion E-3 can be solved for the temperature T to yield:

$$1/T = 1/T_c - \frac{\lambda}{c_2} \ln \left[\frac{I_\lambda}{I_{\lambda c}} \frac{\epsilon_{\lambda c}}{\epsilon_\lambda} \right]$$ (E-4)

E-2.2 Gray Body

The emissivity of a cloud of fine Al_2O_3 particles differs from the emissivity of bulk Al_2O_3; it is a function of particle concentration, optical path length, and particle size distribution. Consequently, the emissivity is an unknown that must also be measured. If the emissivity is assumed to be independent of wavelength (i.e., gray body), then measurements at two wavelengths are sufficient to determine ϵ and T. This is done by writing Wien's law (i.e., Equation E-3) for two different wavelengths λ_1 and λ_2, taking logarithms and rearranging to obtain:

$$\ln \epsilon - \frac{c_2}{\lambda_1 T} = \ln \left[\epsilon_{1c} \left(\frac{I_1}{I_{1c}} \right) \right] - \frac{c_2}{\lambda_1 T_c}$$ (E-5a)

$$\ln \epsilon - \frac{c_2}{\lambda_2 T} = \ln \left[\epsilon_{2c} \left(\frac{I_2}{I_{2c}} \right) \right] - \frac{c_2}{\lambda_2 T_c}$$ (E-5b)

Eliminating $\ln \epsilon$ from Equations E-5a and E-5b yields the solution for temperature:

$$1/T = 1/T_c + \frac{\lambda_1 \lambda_2}{c_2 (\lambda_1 - \lambda_2)} \ln \left[\left(\frac{\epsilon_{1c}}{\epsilon_{2c}} \right) \left(\frac{I_1/I_{1c}}{I_2/I_{2c}} \right) \right]$$ (E-6)

where ϵ_{1c} and ϵ_{2c} are obtained from the known emissivity of tungsten at temperature T_c. Using the value of T computed from Equation E-6, Equation E-3 is then solved to obtain ϵ:

$$\epsilon = \epsilon_{\lambda c} \left(\frac{I_\lambda}{I_{\lambda c}} \right) e^{-\frac{c_2}{\lambda} \left(\frac{1}{T_c} - \frac{1}{T} \right)}$$ (E-7)

183

where λ is either λ_1 or λ_2.

E-2.3 Three-Color Technique

For a cloud of particles, the emissivity will in general depend upon wavelength and the gray body approximation is not applicable. This wavelength dependence can be calculated from the Mie theory of light scattering (Siddall and McGrath) if the complex refractive index of Al_2O_3 particles is known. Since no data is available on the optical properties of small Al_2O_3 droplets at high temperatures, an empirical formula must be used. Such an approach is used by Siddall and McGrath to describe the emissivity of soot particles in flames.

Following Siddall and McGrath, the monochromatic emissivity, ϵ_λ, of a cloud of particles is given by

$$\epsilon_\lambda = 1 - e^{-K_\lambda L} \tag{E-8}$$

where K_λ is the extinction coefficient and L is the thickness of the cloud (assumed homogeneous). If the concentration of particles is high and/or the cloud is thick (optically thick cloud), then $K_\lambda L$ is large and $\epsilon_\lambda \approx 1$; that is, the cloud radiates like a black body.

For optically thin clouds, the variation of ϵ_λ with wavelength must be taken into account in the determination of temperature by radiation measurements. For soot particles it has been found that a good approximation for K_λ is given by

$$K_\lambda = k\lambda^{-\alpha} \tag{E-9}$$

where k is a constant of proportionality that depends on the volume of particles per unit volume of cloud, and α is approximately a constant for visible light. Substituting Equation E-9 into Equation E-8 gives:

$$\epsilon_\lambda = 1 - \exp\left(-kL\lambda^{-\alpha}\right)$$

or lumping kL into a single parameter B:

$$\epsilon_\lambda = 1 - \exp\left(-B\lambda^{-\alpha}\right) \qquad (E-10)$$

From measurements of emitted radiation at three wavelengths, the parameters B and α, as well as the temperature T can be determined, provided that Equation E-9 is a good approximation to the actual wavelength dependence of K_λ.

Assuming that the cloud of Al_2O_3 particles is adequately described by Equation E-10, the following algorithm is used to determine B, α, and T from measured values of $I_\lambda / I_{\lambda c}$ at the three wavelengths:

Step 1: Guess a value for ϵ_1 ($\lambda_1 = 4050$ Å).

Step 2. Calculate T from Wien's law (Equation E-4) using I_1/I_{1c} and the assumed value ϵ_1.

Step 3: Calculate ϵ_2 and ϵ_3 from Wien's law (Equation E-7) I_2/I_{2c}, I_3/I_{3c}, and the temperature T calculated in Step 2.

Step 4: From the values of ϵ_1 and ϵ_2 calculate B_1 and α_1 from Equation E-10. The appropriate formulas are:

$$\alpha = \frac{\ln\left|\dfrac{\ln(1-\epsilon_1)}{\ln(1-\epsilon_2)}\right|}{\ln(\lambda_2/\lambda_1)} \qquad (E-11)$$

$$B = -\ln(1-\epsilon_i)\,\lambda_i^{\alpha} \quad (i = 1 \text{ or } 2) \qquad (E-12)$$

Step 5: Repeat procedure of Step 4 using ϵ_2 and ϵ_3 to calculate B_2 and α_2.

Step 6: Calculate $y = \alpha_2 - \alpha_1$. If $y = 0$ (or $|y|$ less than a specified tolerance δ), then B_1, α_1, and T is the required solution. If $|y| > \delta$ proceed to Step 7.

185

Step 7: Select a new guess for ϵ_1 and repeat Steps 2 through 6. Improved guesses of ϵ_1 may be obtained by linear interpolation (or extrapolation) based on previous guesses of ϵ_1 and their corresponding y values.

The above procedure will fail to converge if:

(1) The actual variation of emissivity with wavelength departs significantly from that postulated by Equation E-10.

(2) Experimental errors in the measured intensities are sufficiently large that no solution exists or that a solution exists only for $\epsilon_1 < 0$ or $\epsilon_1 > 1$ (physically meaningless).

E-3   Description of Apparatus for Emission Measurements

The optical system used for emission measurements of the solid propellant plume consists of a viewing tube with a diaphragm, an achromatic objective lens, and a photomultiplier detector array. The optical system, which is mounted on an optical bench, is shown in Figure E-1.

The viewing tube consists of a 5.08-cm O.D. aluminum tube 15.24 cm long which is connected to the combustion tube by a 0.95-cm O. D. stainless steel tee fitting at one end. The 2.54-cm diameter optical window is mounted at the front end of the viewing tube. A nitrogen purge is introduced through the tee fitting to prevent the hot plume gases and particles from entering the viewing tube. The flow rate of the nitrogen is not high enough to appreciably disturb the plume.

An iris diaphragm is mounted directly in front of the view tube window to restrict the cone of light collected by the objective lens to about 4.5° (1.27 cm aperture). This restriction on viewing aperture is greater than that imposed by the tee fitting, which is necessary because the tee fitting cannot be used when viewing the calibration lamp.

The light from the solid propellant plume or calibration lamp is focused by the achromatic objective lens (85-mm focal length) upon a pinhole aperture (iris diaphragm at smallest setting, 0.8 mm). Thus the light entering the photomultiplier array is restricted to that emitted from a small area of the plume or calibration lamp filament. Since the

(1) Beam Splitter Cube   (6) Iris Diaphragm
(2) Interference Filter   (7) Optical Window
(3) RCA 931A PM1   (8) View Tube
(4) Iris Diaphragm   (9) 0.95-cm Tee
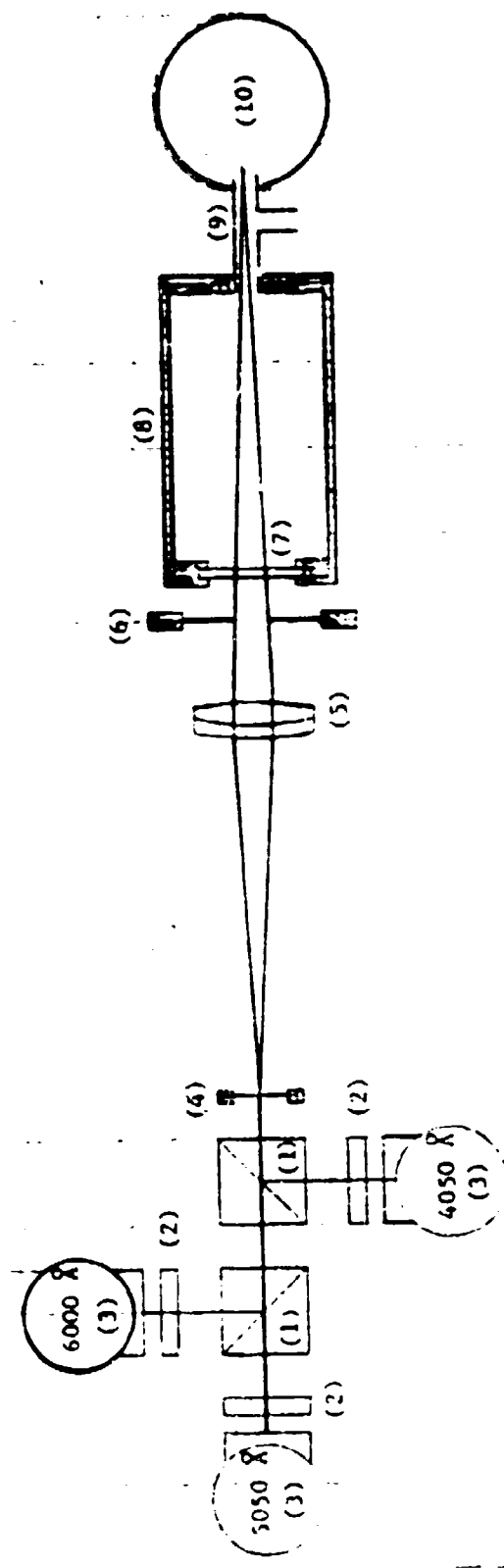(5) Achromat (85 mm f.l.)   (10) Combustion Tube

Figure E-1. Optical system for emission measurements of solid propellant plumes.

distance from the detector aperture to the lens (image distance) and the distance from the lens to the lamp filament or plume (object distance) is the same for both calibration and for test firings, the area of the emitter is the same in both cases. This allows direct comparison of the intensities measured during test firings with the calibration intensities in order to determine the temperature and emissivity of the plume.

The detector array consists of three RCA 931A photomultiplier tubes (PMTs) equipped with interference filters (100 $\AA$ bandwidth) centered at 4050 $\AA$, 5050 $\AA$, and .000 $\AA$. Two beamsplitter cubes in series are used to direct the incoming beam to the three PMT detectors. All of these components are mounted on a minioptical bench and are shielded with a black cloth to eliminate stray light.

The photomultiplier tubes are operated at 500 volts supplied by a regulated DC power supply. The output currents from the PMTs are passed through 100,000 ohm resistors and the resulting voltages are amplified (Neff Type 122 DC amplifiers) with gains of 1-50. The amplified signals from the PMTs are then recorded using three channels of a Hewlett-Packard Model 3968A 8-channel tape recorder. The recorded outputs are later plotted for data reduction.

E-4   Test Procedure

The optical system is set up in a fume hood for safe removal of the solid-propellant combustion products. The optical window is removed from the viewing tube and placed on the front of the calibration lamp housing. The lamp is then placed in the fume hood with the front of the window mount in contact with the large iris diaphragm. With the lamp on, the system is aligned so that the pinhole aperture is centered on the image of the ribbon filament. The lamp current is set at 36A, which corresponds to a filament temperature of 2600°K, and the output signals are recorded. Toward the end of the record the lamp is turned off and the background is recorded. The calibration data is then plotted before proceeding to the test firing.

For the test firing, the calibration lamp is removed and the optical window placed on the viewing tube. The viewing tube is then attached

to the combustion tube and the whole assembly is then mounted in the hood with the front of the window mount in contact with the large iris diaphragm. To align the system a small lamp with a frosted bulb is lowered into the combustion tube and the pinhole aperture is centered on the small circular image of the bulb in contact with the tee fitting. The lamp is then removed and the nitrogen flow is turned on. The tape recorder is started about ten seconds before ignition, the propellant is then ignited and the PMT signals are recorded for the duration of the test (about 15 seconds). The test data is then plotted for later reduction.

E-5   Test Results

Two test firings have been conducted for which plume emission measurements have been made. The output signals of the three PMTs are shown in Figure E-2 for the first of these tests. The data was reduced in two ways: (1) using the gray body technique, and (2) using the three color technique. The temperatures and emissivities obtained by these two methods will now be discussed.

E-5.1 Gray Body Technique

By assuming that the Al_2O_3 smoke particles radiate as a gray body, temperatures and emissivities were calculated using each of the three possible pairs of measurements: (1) 4050 $\overset{o}{A}$ and 5050 $\overset{o}{A}$, (2) 4050 $\overset{o}{A}$ and 6000 $\overset{o}{A}$, and (3) 5050 $\overset{o}{A}$ and 6000 $\overset{o}{A}$. The highest temperatures and lowest emissivities were obtained when the two shortest wavelengths were used. For this case calculated temperatures were between $3420^{o}K$ and $4060^{o}K$ (mean $3760^{o}K$), and emissivities ranged from 0.001 to 0.008. Somewhat lower temperatures were obtained when the 4050 $\overset{o}{A}$ and 6000 $\overset{o}{A}$ measurements were used (mean $3330^{o}K$), and emissivities fell between 0.006 and 0.025. The lowest temperatures were obtained when the two longest wavelengths were used, and the corresponding emissivities were the largest. These latter results are shown in Figure E-3 for the first test. Here measured temperatures fluctuated between $2760^{o}K$ and $2960^{o}K$ with a mean temperature of $2840^{o}K$. During the first part of the burn, the emissivity was roughly
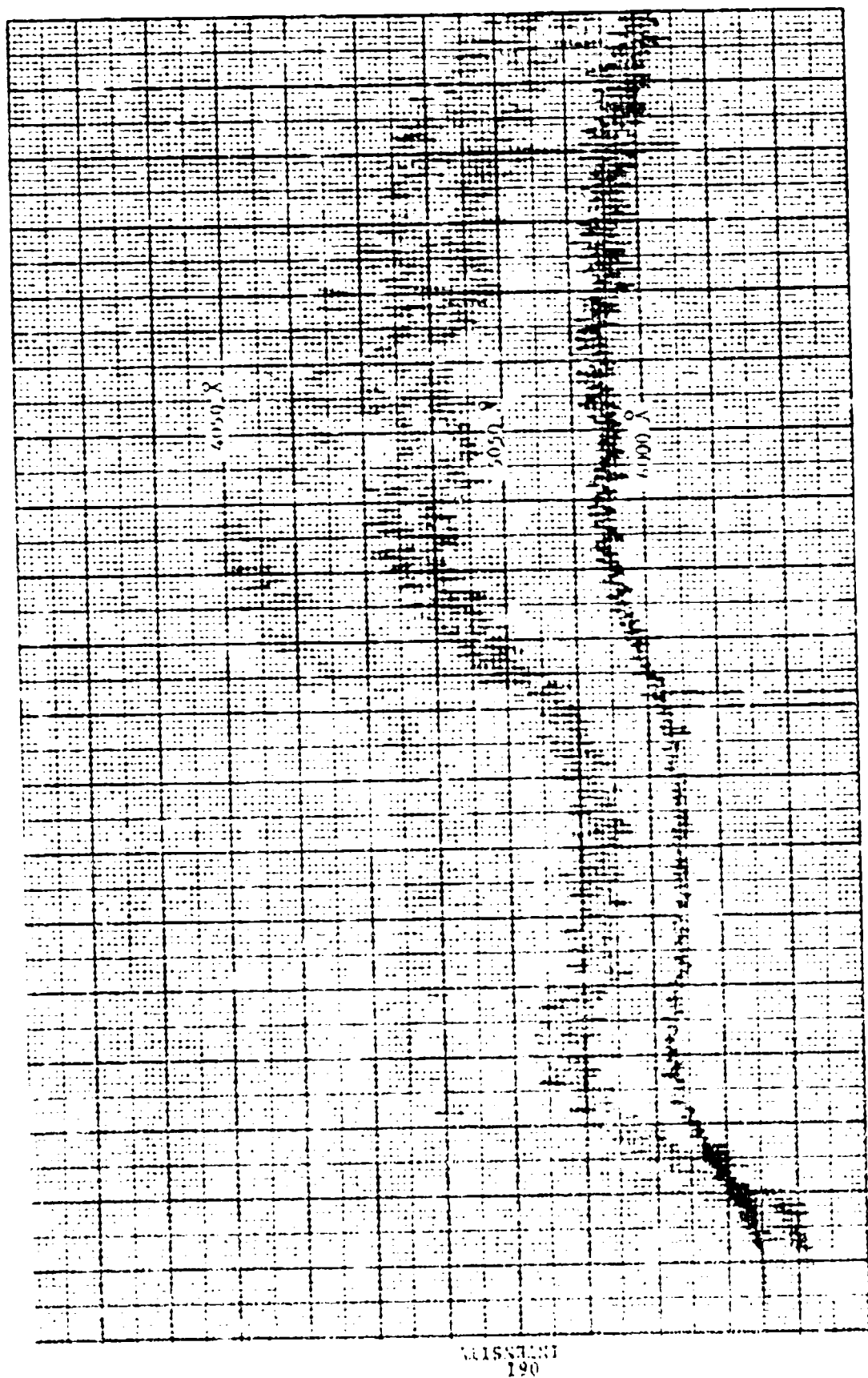
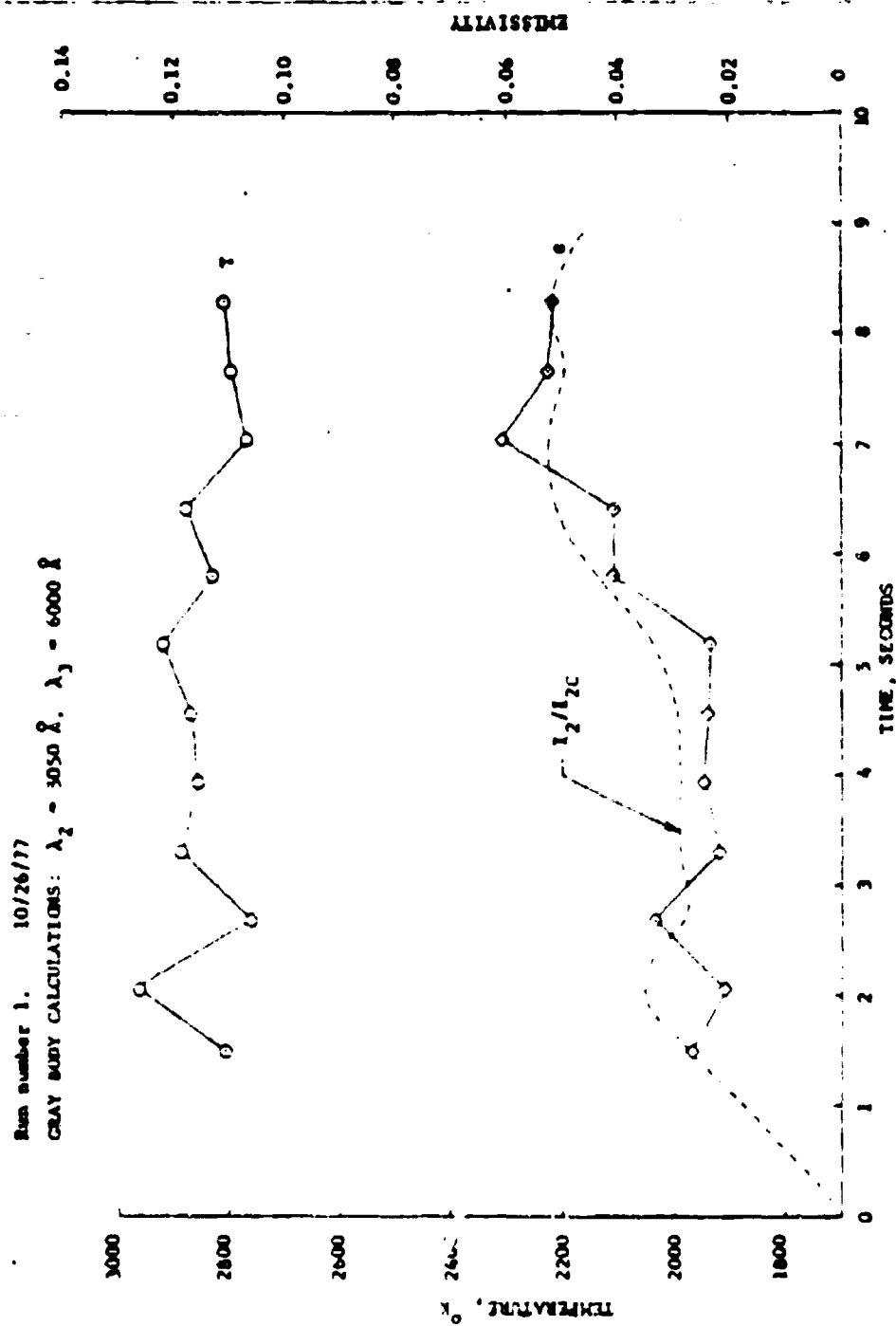Figure F-2. Emission intensities in three colors for run number 1.

Figure E-3. Gray body values of temperature and emissivity for run number 1.

0.025, with a sharp rise to about twice this value after five seconds. The increase in emissivity during the middle of the burn correlates well with the rise in measured light intensity for each of the three wavelengths.

The above results were obtained for the first test firing; for the second test similar results were obtained. For each of the three pairs of wavelengths, somewhat lower temperatures and higher emissivities were obtained in the second test, but again higher temperatures were obtained when the 4050 $\overset{o}{A}$ measurement was used. The results for the second test are shown in Figure E-4 for 5050 $\overset{o}{A}$ and 6000 $\overset{o}{A}$, where again increases in brightness seem to arise from increases in emissivity rather than temperature. The emissivity variations are probably due to variations in smoke particle concentration during the burn.

The results obtained using the gray body technique are inconsistent, because the same temperature and emissivity are not obtained for each pair of wavelengths. This discrepancy cannot be accounted for by a simple dependence of plume emissivity upon wavelength, since the three color technique fails also, as discussed below. The measurements indicate excess radiation at short wavelengths (4050 $\overset{o}{A}$), which cannot be accounted for by gray body emission of Al_2O_3 particles. The excess blue radiation could arise from the presence of burning aluminum agglomerates which are several hundred degrees hotter than the aluminum oxide smoke.

E-5.2 Three Color Technique

As mentioned above the three color technique fails to give meaningful results. The data does not fit the assumed functional form of the dependence of emissivity with wavelength, and no solution can be found for B, σ, and T. Assuming an emissivity of 0.03 at 4050 $\overset{o}{A}$, the data indicates a decrease in emissivity at 5050 $\overset{o}{A}$ followed by an increase in emissivity at 6000 $\overset{o}{A}$. This is clearly inconsistent with the monotonic dependence of emissivity upon wavelength assumed in the three color technique.
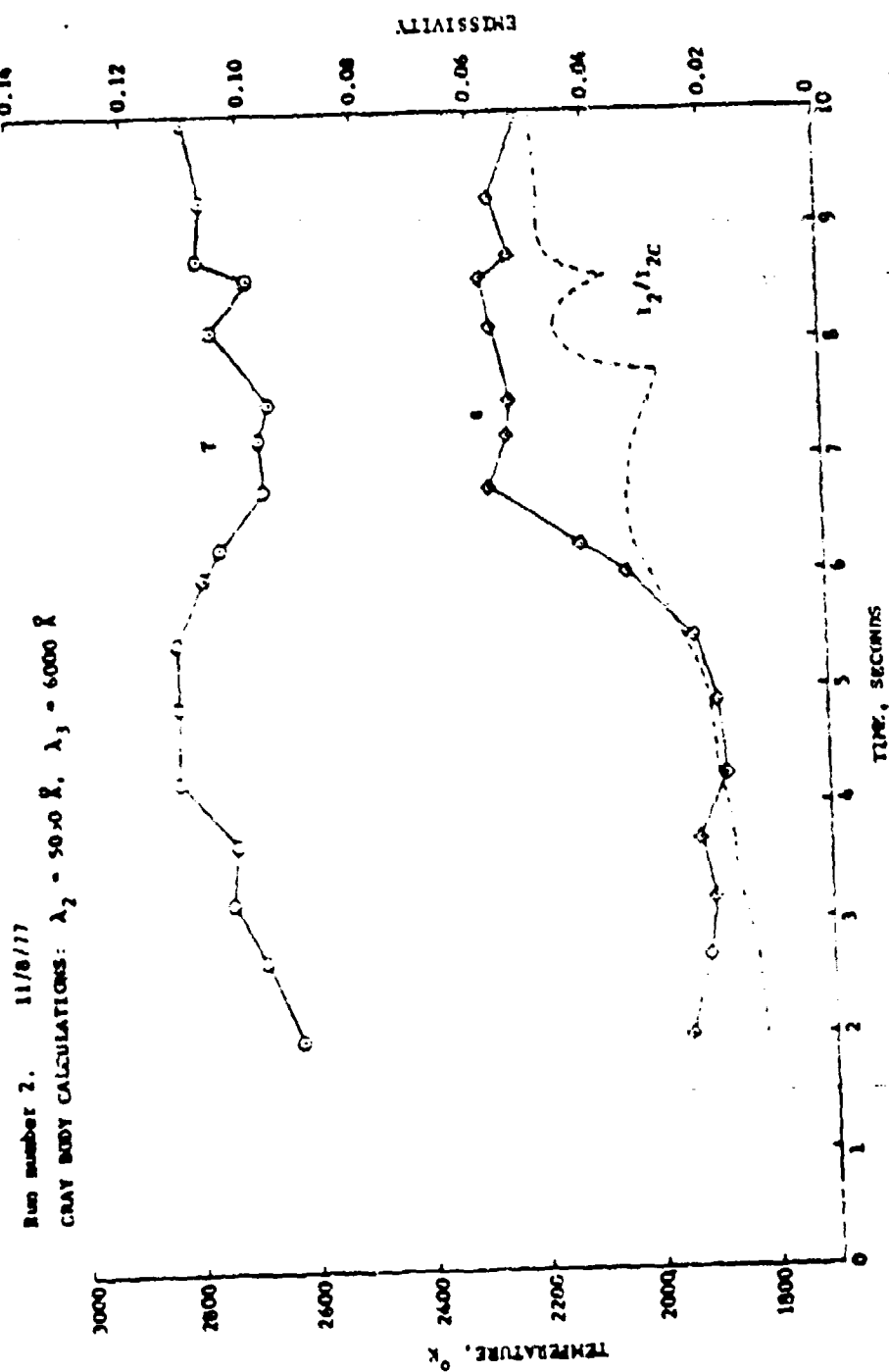
192

Figure E-4. Gray body values of temperature and emissivity for run number 2.

193

E-6   Conclusions

The methods used in these studies seem to hold considerable promise.
Indeed, if measurements had been confined to the longer two wavelengths,
one would be tempted to conclude that a temperature of about $2800^{\circ}K$ had
been measured, with an emissivity of about 0.040. The tendency for the
emissivity to rise in the later part of the test might be interpreted as
an increase in smoke density (reason unknown).

In the course of the investigations, it became apparent that the
smoke plume was not optically dense. This would lead to a deceptively
low indicated value of emissivity. It also implies that the radiating
material seen by the photomultiplier may include more than an occasional
burning agglomerate, which is much brighter than the smoke cloud. In
other words, the plume consists of a heterogeneous flow with radiating
condensed phase material of widely different temperatures. While the
temperatures of $2800^{\circ}K$ or so determined from the longer wavelength data
may give a useful measurement of the general oxide smoke cloud, the shorter
wavelength then reflects a much higher temperature, probably that of the
aluminum flame envelopes around agglomerates. The procedure for analysis
of the measurements does not provide for a two-temperature measurement,
and the measurement of emissivity is severely compromised. Further, mea-
surement of the expected determination of wavelength-dependence of emis-
sivity (due to Mie scattering) was frustrated by the two-temperature plume.
In the future it would be worthwhile to explore the possibility of deter-
mining both temperatures, and emissivity versus wavelength, using a modi-
fied analysis and measurements at additional wavelengths as needed.

In spite of these difficulties, the experimental technique seems to
have performed well, and the temperature values of $2800^{\circ}K$ and $3600^{\circ}K$ are
compatible with the expected temperatures of radiating droplets in the
combustion plume. The values of emissivity are more difficult to recon-
cile, because values were essentially unknown at the outset, and because
in the method of calculation from the measurements, the calculated emis-
sivity is very sensitive to errors in intensity.

194

APPENDIX F

DETERMINATION OF VELOCITIES
IN THE COMBUSTION ZONE

F-1   Introduction

In the combustion zone, the gaseous reaction products of the pro-
pellant accelerate quickly in their reaction region within about 1 cm of
the burning surface. The condensed phase material accelerates less rapid-
ly, in a manner dependent on droplet inertia, drag of the gas flow, and
gravitational force. The oxide smoke droplets accelerate quickly to very
near gas velocity, while 200-μm aluminum agglomerates move relatively
slowly away from the surface and require several cm to approach gas velo-
city. Determination of these velocities is important because it affects
the interaction with immersed objects. In the present investigation, an
analysis of droplet motion (Section F-2) was made to serve as one source
of information and serve as a means of interpreting experimental results.
In addition, three photographic techniques were used to obtain direct
information on velocity (Section F-3). In addition, the resulting state
of knowledge is summarized (Section F-5) and some comments are made on
possible improved methods of velocity determination.

F-2   Relative Velocities of Gas and Particles
F-2.1   Acceleration of a Particle in a Uniform Gas Flow

Consider a gas of uniform temperature flowing vertically with a
constant velocity, V_g. At time $t = 0$, a spherical particle of density,
ρ_p, diameter, D_p, and mass, m_p ($= \rho_p \pi D_p^3/6$), is released at $y = 0$
with initial velocity $V_p = 0$, and allowed to accelerate upwards to a
steady velocity. In this analysis it is assumed that the mass remains
constant, i.e., the particle does not burn. Since the particle is spher-
ical, there are no fluid induced forces normal to the gas flow and the
motion of the particle is in the y-direction.

The drag force exerted by the gas flow on the particle is

$$F = C_D \left[\tfrac{1}{2} \rho_g (V_g - V_p)^2 \right] \frac{\pi D_p^2}{4} \qquad (F-1)$$

where C_D is the drag coefficient. For spheres, the drag coefficient is a function of the Reynolds number

$$Rey = \frac{\rho_g (V_g - V_p) D_p}{\mu_g} \tag{F-2}$$

where μ_g is the coefficient of viscosity of the gas. Using values of μ_g and ρ_g obtained from the thermochemical calculations described in Section 2, it is estimated that a 10-micron sphere will have a Reynolds number equal to 0.113 at $y = 0$ where $V_p = 0$. As the particle accelerates, the particle velocity increases and the Reynolds number decreases further.

For Reynolds numbers less than 0.1, the drag coefficient is given by Stokes' law:

$$C_D = \frac{24}{Rey} \tag{F-3}$$

The use of Stokes' law greatly simplifies the solution of the equations and is accurate except for very large particles near the burning surface where the particle velocity is nearly zero.

Newton's third law of motion states that the force on a particle (fluid drag minus the weight) is equal to the change in momentum of the particle:

$$F_D - m_p g = m_p \frac{dV_p}{dt} \tag{F-4}$$

where g is the acceleration of gravity. Substituting Equations F-1, F-2, and F-3 into Equation F-4 and rearranging terms gives:

$$\frac{dV_p}{dt} + \frac{18\mu_g}{\rho_p D_p^2} (V_p - V_g) + g = 0 \tag{F-5}$$

196

F-2.2 Calculation of Velocities

Notice that Equation F-5 provides two sources of information: If the gas velocity is known, the motion of the particle can be obtained. Alternatively, if the particle velocity and acceleration are known, the gas velocity can be calculated. These two cases will be investigated separately.

F-2.2.1 Motion of a Particle in a Gas Stream of Known Velocity

When V_g is known, the solution to Equation F-5 is

$$V_p = \left[V_g - \frac{\rho_p D_p^2 g}{18 \mu_g} \right] \left[1 - \exp\left(\frac{-18 \mu_g t}{\rho_p D_p^2} \right) \right] \qquad (F-6)$$

which gives the velocity of the particle at any time, t. The position of the particle at time, t, is

$$y = \left[V_g - \frac{\rho_p D_p^2 g}{18 \mu_g} \right] \left[t + \frac{18 \mu_g}{\rho_p D_p^2} \left[\exp\left(\frac{-18 \mu_g t}{\rho_p D_p^2} \right) - 1 \right] \right] \qquad (F-7)$$

Calculations have been made for 10-, 50-, 100-, and 200-micron diameter aluminum spheres ($\rho_p = 2.382$ g/cm^3) moving through UTP 3001 combustion prod·:ts at T = 2841 K ($\rho_g = 8.977 \times 10^{-5}$ g/cm^3 and $\mu_g = 7.8883 \times 10^{-4}$ g/cm/sec) and $V_g = 1000$ cm/sec. The results are shown in Figure F-1. It is clear that the velocity lag for the larger particles is significant even 30 cm _rom the burning surface.

It is also clear that there is a limiting diameter for particles leaving the surface such that particles larger than this diameter will not be lifted off the surface by the gas flow. In this case, the diameter is large enough so that the Stokes' law approximation is not applicable and the diameter must be found by trial and error, i.e., a diameter is assumed, a Reynolds is computed and the drag coefficient is found from a graph of drag coefficient versus Reynolds number for spheres. A drag force is then calculated using Equation F-1 and the particle weight is computed. The
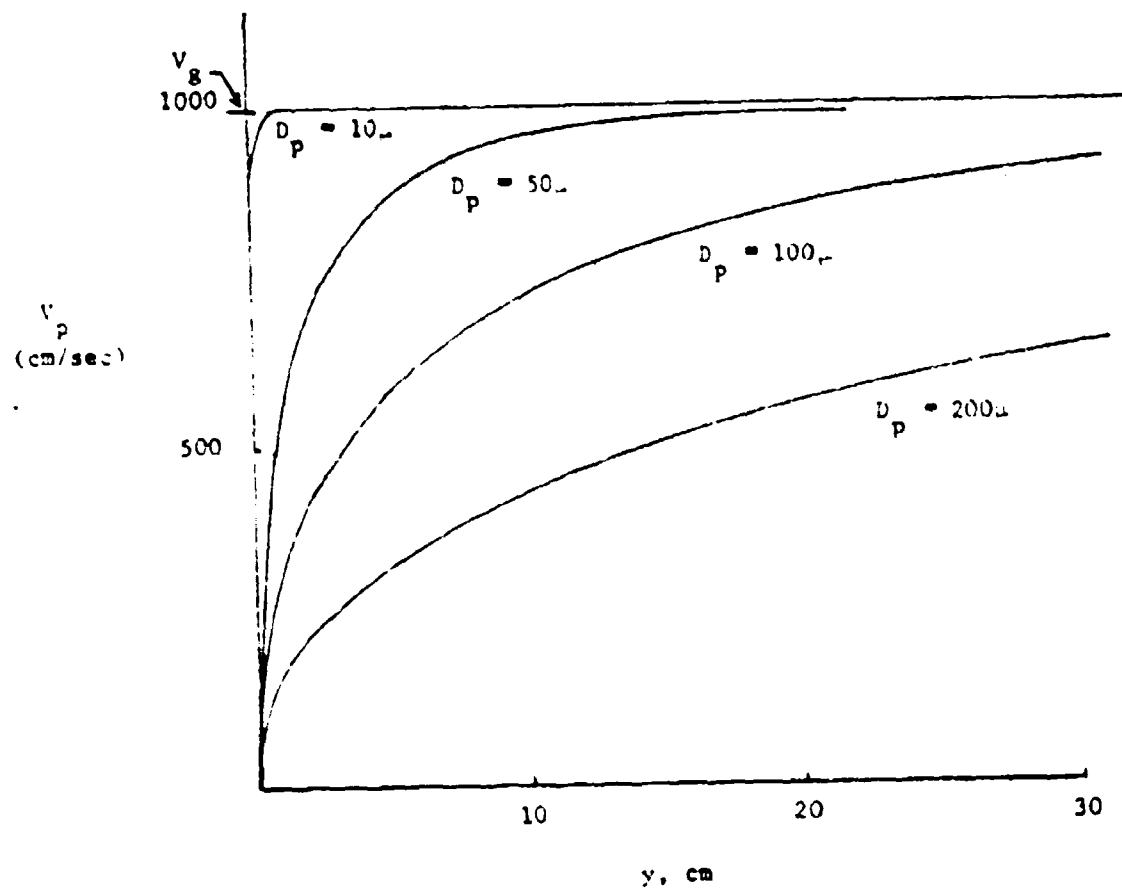
197

Figure F-1. Particle velocities for 10-, 50-, 100-, and 200-micron spheres as a function of distance.

198

cutoff diameter is found when the drag force equals the particle weight, which for the previously prescribed conditions is about 2 cm.

F-2.2 Calculation of the Gas Velocity from Observed Particle Velocity and Acceleration

If the particle velocity is known as a function of y, the particle acceleration can be determined from

$$\frac{dV_p}{dt} = V_p \frac{dV_p}{dy} \qquad (F-8)$$

Substituting Equation F-8 into Equation F-5 and rearranging terms gives

$$V_g = V_p + \frac{\rho_p D_p^2}{18\mu} \left[V_p \frac{dV_p}{dy} + g \right] \qquad (F-9)$$

This equation is used in the next section to calculate the gas velocity using particle velocities at four vertical locations.

F-3 Experimental Determination of the Gas Velocity and Particle Velocities

Standard methods of gas velocity determination rely on the measurement of static and stagnation properties (pressure or temperature) using a probe submerged in the flow. The gas velocity is then computed using relationships between the gas velocity and the difference between static and stagnation conditions. In the two-phase flow of concern in this study, such probes are quickly destroyed by deposition of molten aluminum and alternative methods must be explored.

In the present studies such difficulties were avoided by use of photographic methods. The plume contains condensed phase material in the form of irregularly shed clouds of fine particles and burning aluminum agglomerates. The velocity of the fine particles in the clouds should be very nearly equal to the gas velocity and the velocity of these clouds can be determined from high speed motion pictures of the plume. The velocity of the

burning aluminum agglomerates lags the gas velocity due to the inertia of
the agglomerates. These agglomerates, however, leave very bright streaks
which can be observed on either still photographs or single frame analy-
sis of high speed motion pictures. The single frame analysis of high-speed
motion pictures is preferred since single frame exposures of 0.006 to 0.0001
second are possible while 35-mm still cameras are limited to 0.001 or 0.002
second, and the shorter exposure times are needed to allow the streaks to
be seen against the background radiation from the fine Al_2O_3 smoke. Indeed,
velocity calculations using both single-frame agglomerate streak measure-
ments and frame-to-frame cloud velocity measurements can be obtained from
high-speed motion pictures.

F-3.1 Test Apparatus and Procedures

High-speed motion pictures have been made of the plume at the exit
of 5.1-cm-diameter stainless steel tubes 7.6, 15.2, 22.9, and 30.5 cm long.
Wafers of propellant 5 cm in diameter and 1.3 cm thick were cut and a coil
of igniter wire was attached with igniter paste (see Figure 11). The wafers
were wrapped with masking tape to insure a snug fit into the tube. The
wafers were then pressed into the tube with the igniter wire emerging
through insulated holes in the tube and the propellant was secured along
the bottom with a coating of epoxy. Before the test, the tube (propellant
end down) was pressed into a base plate which was secured to the counter
top of a fume hood. Two notches approximately 0.64 cm apart (exact dis-
tances were recorded) were filed into the open end of each tube. These
notches are used to determine exact magnification factors in motion pictures.

High-speed motion pictures were made with a Hycam camera and a
Nikon 200-to-600-mm zoom lens. The Hycam camera is capable of filming rates
up to 11,000 pps using a full frame format. Filming rate and aperture set-
tings were obtained by trial and error, and it was concluded that for the
5.1-cm-diameter tube tests, using Kodak Ektachrome T (tungsten) film and
the lens set for 600-mm and an aperture of f/22, filming rates of 2,000 to
4,000 pps produced the desired bright agglomerate streaks against the smoke
clouds. It should be noted that the camera does not run at a constant rate,

but approaches the set framing rate in an exponential manner and then
oscillates slightly about the set rate. A rate of 2,000 pps can be main-
tained over approximately 70% of a 30-meter film roll. The exact film-
ing rate at any frame can be determined from timing marks printed onto the
edge of the film at 0.001 second intervals by a light-emitting diode (LED)
timing mark generator. The Hycam camera was mounted on a tripod approxi-
mately 3 meters from the tube. The Nikon zoom lens was mounted on an ex-
tension bracket which was then mounted to a second tripod. The two tripods
were adjusted until the lens and camera were aligned, whereupon the lens
was connected to the camera. The stainless steel tube was positioned
within the fume hood so that the camera was aligned with the tube axis
slightly above the tube exit with the notches just visible at the bottom
of the frame with the lens focal length set at 600 mm. The lens was focused
halfway between the center of the tube to the front edge. The filming rate
was set at 2,000 pps and the lens aperature set at f/22.

The ignition wires were connected to the igniter circuit and the
propellant was ignited. The propellant was allowed to burn for 10 seconds
to heat up the tube and establish steady flow. After 10 seconds, the camera
was started and the 30-meter film roll exposed in two seconds. Cine-photo-
graphy in the streak mode followed the same general procedure, only the
camera housing was reversed and a special film gate installed.

F-3.2 Data Reduction

The processed films were viewed with an LW 16-mm motion analyzer
(movie projector) with a frame counter and projection speeds of 16 pps,
24 pps, variable slow rates of 1 to 10 pps, and frame-by-frame stop motion.
A single-frame image was projected onto the portable screen and the magni-
fication ratio determined from measurement of the distance between notches.

For measurement of agglomerate streaks, the film was advanced 500
frames (to allow the film speed to stabilize) and the initial film rate
(i.e., the distance between timing marks) was recorded. The film was then
advanced frame by frame until 25 streaks (see Figure F-2a for a sample
streak) were measured and recorded. When the 25th streak was recorded a

Figure F-2a. Agglomerate streak at tube exit.
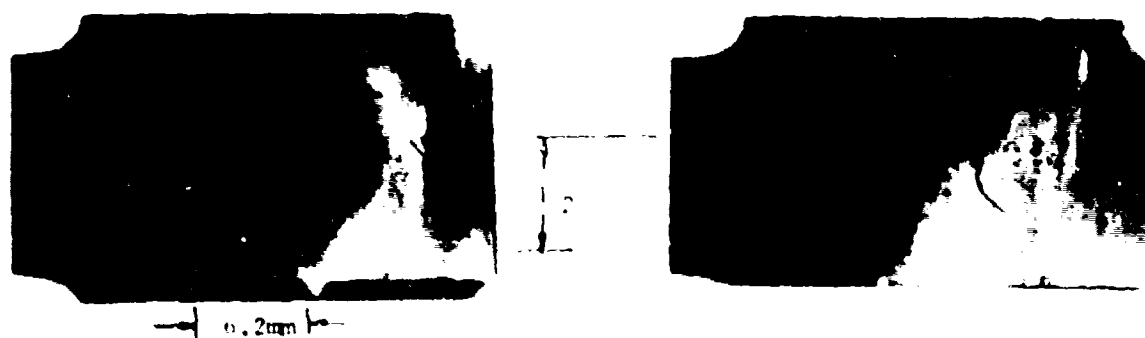$\dot{C}_p = 1_1$ (2.5 x filming rate)

Figure F-2b. Smoke (Al_2O_3) in successive frames at tube exit $(C_{smoke} = 1_2/$filming rate$)$.
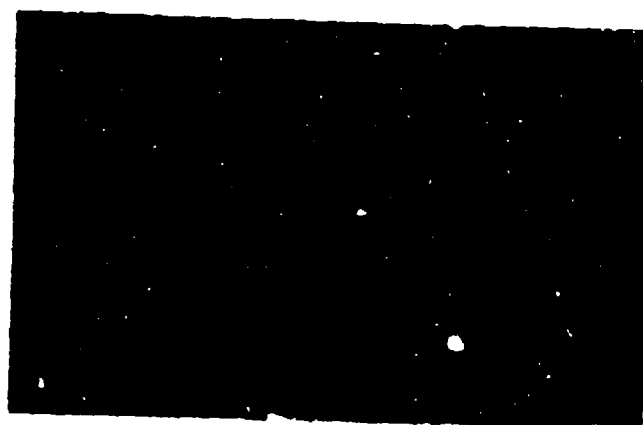

Figure F-2c. Diagonal lines from streak movie.

final filming rate was recorded. The film was then advanced to the 800th
frame, an initial filming rate was recorded, 25 streaks measured and re-
corded and a final filming rate recorded. This procedure was repeated
beginning at the 1,500th and 1,800th frames to give a total of 100 streaks.
Each group of 25 streaks was averaged to obtain a group average streak
length and the film speed at the beginning and end of each group was aver-
aged to obtain a group film speed. The exposure time for a single frame
is $1/(2.5 \times$ group film speed). Using these values, a group streak velo-
city, $\bar{\bar{V}}_p$ was calculated for each of the 16 groups (four for each tube).
Finally, the four groups from each tube were averaged to obtain an average
particles speed for each tube, $\bar{V}_p$.

   As shown in Figure F-2b, a single frame contains the bright agglom-
erate streaks and a rather blotchy mottle of Al_2O_3 smoke. The smoke usual-
ly distorts between frames due to velocity gradients within the tube and
diffusion, but it is possible (after a considerable amount of searching)
to find a distinct point (between light and dark spots) which can be iden-
tified in two consecutive frames. The distance traveled between frames is
measured, the filming rate determined, (the time of travel is now the in-
verse of the film speed), and a velocity obtained. This velocity is refer-
red to as the smoke velocity and should be equal to the gas velocity due
to the negligible mass of the smoke particles.

   The background smoke in the 7.6-cm tube was too bright to permit
selection of a clearly identifiable spot for frame to frame analysis. How-
ever, a movie was made using the 7.6-cm tube with the Hycam camera in the
streak mode. A section of this film is shown in Figure F-2c. The film
speed is calculated, and the angle of the diagonal lines is measured. The
speed of the bright object leaving the streaks is equal to the film speed
multiplied by the tangent of the angle.

   In Table F-1, the values of $\bar{\bar{V}}_p$ and $\bar{V}_p$ as well as $V_{p\ max}$, the
longest agglomerate streak measured in each tube, are presented. Also
given are values of V_g (smoke) for the 15.2-, 22.9-, and 30.5-cm tubes
and V_g (streak) for the 7.6-cm tube. It should be noted that V_g (smoke)
is averaged from only two to four measurements for each tube and V_g (streak
mode) is averaged over about 25 lines.

Table F-1. Comparison of Velocities at the Exit of Four Tubes

Tube length, (cm)	$\bar{\bar{V}}_p$ (m/sec)	$\bar{V}_p$ (m/sec)	$\bar{V}_{p\ max}$ (m/sec)	$\bar{V}_{g\ smoke}$ (m/sec)	$V_{g\ streak}$ (m/sec)
7.6	10.96	.....	.....	.....	.....
	10.04	9.95	21.23	.....	16.13
	9.61	.....	.....	.....	.....
	9.21	.....	.....	.....	.....
15.2	11.99	.....	.....	.....	.....
	10.85	11.21	19.80	16.18	.....
	10.46	.....	.....	.....	.....
	11.53	.....	.....	.....	.....
22.9	11.74	.....	.....	.....	.....
	11.57	11.82	19.60	14.24	.....
	11.75	.....	.....	.....	.....
	12.20	.....	.....	.....	.....
30.5	12.65	.....	.....	.....	.....
	13.08	13.01	16.13	15.74	.....
	12.61	.....	.....	.....	.....
	13.69	.....	.....	.....	.....

$\bar{\bar{V}}_p$ — Agglomerate velocities averaged over 25 frames

$\bar{V}_p$ — Agglomerate velocities averaged over 100 frames

$\bar{V}_{p\ max}$ — Velocity of fastest moving agglomerate

$\bar{V}_{g\ smoke}$ — Velocity of smoke cloud

$\bar{V}_{g\ streak}$ — Velocity from streak movie

F-3.3 Corrections for Tube Velocity Profiles

Since the propellant is burning inside a tube, the gas velocity will not necessarily be uniform. If the tube length is very short compared to the tube diameter, and/or the kinematic viscosity is low, the velocity will be uniform except for a negligibly thin region near the tube wall. If the tube is much longer than its diameter and/or the kinematic viscosity is very high and the temperature is uniform throughout the tube, the velocity will have a parabolic velocity distribution. Since the tubes used in these tests have tube lengths comparable to their diameters and the kinematic viscosity is high, the velocity profiles lie somewhere in between uniform and parabolic. Therefore, correction factors will be obtained for uniform velocity profiles (zero length tube) and parabolic velocity profiles (infinitely long tubes). Next, using the two extreme cases correction factors for intermediate length tubes will be presented.

Three characteristic velocities are useful in describing the velocity in nonuniform flow. First, $\overline{V}$, is the velocity averaged over an Area A of the tube and defined by

$$\overline{V} = \frac{\int V(r)r\,dr}{\int r\,dr} \tag{F-10}$$

Second, $[V]$ is the mean or mass average velocity which is the velocity given by Equation F-10 when A is the entire area of the tube. Finally, V_o is the velocity on the centerline of the tube.

F-3.3.1 Uniform Velocity Profile

When the tube length is much less than the tube diameter, the velocity is very nearly uniform over the entire cross sectional area of the tube. Therefore

$$\overline{V} = V_c \tag{F-11}$$

$$[V] = V_o \tag{F-12}$$

F-3.3.2 Parabolic Velocity Profile

When the tube length is much greater than the tube diameter the velocity profile is parabolic:

$$V = V_o \left[1 - \left(\frac{r}{R} \right)^2 \right] \qquad (F\text{-}13)$$

In the previous section on photographic results, average particle velocities $\bar{V}$ were measured over a portion of the tube. The area, A, viewed in the movies is shown in Figure F-3. Substituting Equation F-13 into Equation F-10 and performing the required integration gives

$$\bar{V} = 2 V_o \left| \frac{\frac{1}{4} \sin^{-1} L + \frac{5}{12} L \sqrt{1 - L^2} - \frac{L^3}{6} \sqrt{1 - L^2}}{\sin^{-1} L + L \sqrt{1 - L^2}} \right| \qquad (F\text{-}14)$$

If the entire area of the tube had been photographed, ($L = 1$), the mean velocity in the tube would have been obtained, i.e.

$$[V] = \frac{V_o}{2} \qquad (F\text{-}15)$$

This is a well known result from the theory of laminar flow in tubes. The three reference velocities are thus related by

$$[V] = \frac{\bar{V} \left[\sin^{-1} L + L \sqrt{1 - L^2} \right]}{\left[\sin^{-1} L + \frac{5}{3} L \sqrt{1 - L^2} - \frac{2}{3} L^3 \sqrt{1 - L^2} \right]} = \frac{V_o}{2} \qquad (F\text{-}16)$$

For the tube movies described in the previous section these relationships are

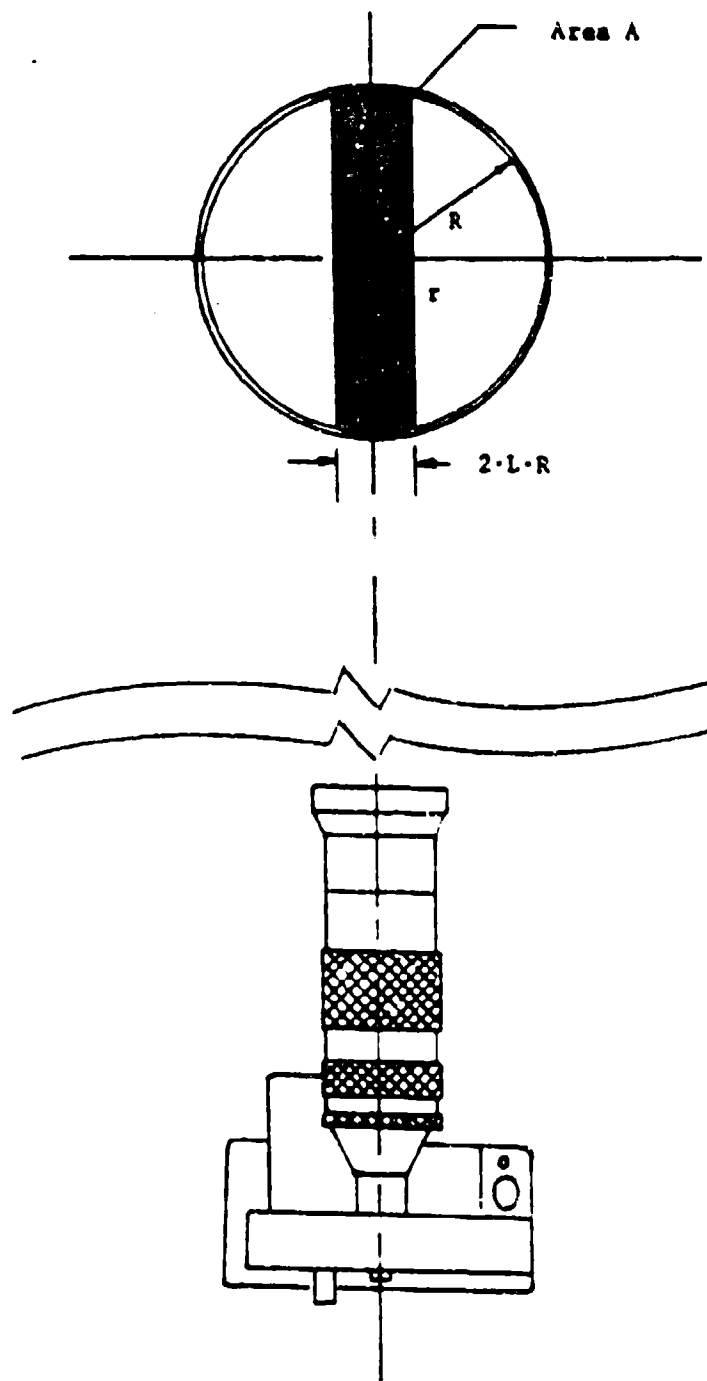$$[V] = .787 \bar{V} = .5 V_o \qquad (F\text{-}17)$$

206

Figure F-3.   Cross sectional area photographed by
Hycam.

As previously described, due to the high kinematic viscosity and the low ratio of tube length to diameter, the actual correction factors lie between these two extremes. Schlichting has shown that the transition from uniform to parabolic profile proceeds as a function of the parameter

$$\lambda = \frac{\mu_g \ell}{\rho_g R^2 [V]} \tag{F-18}$$

where ρ_g and μ_g are the gas density and viscosity, ℓ is the tube length, and R is the tube outer radius. Schlichting also presents curves of $V/[V]$ as a function of λ for several radial locations. (The curve for $r = 0$ represents $V_o/[V]$.) Using values of ρ_g and μ_g from the thermochemical calculations described in Section 2 and assuming $[V] = 1000$ cm/sec, $\rho_g = 8.977 \times 10^{-5}$ g/cm^3 and $\mu_g = 7.8883 \times 10^{-4}$ g/cm sec at 2841°K, velocity profiles for the four tubes are obtained from Schlichting's plots and presented in Figure F-4.

The correction factors are written

$$[V] = .5 \left[1 + F(\lambda) \right] V_o \tag{F-19}$$

and

$$[V] = \left[.797 + .203 \, F(\lambda) \right] \bar{V} \tag{F-20}$$

A value of $F(\lambda)$ for each of the four tubes can be obtained from Equation F-19 and Figure F-4. These values of F are then used to obtain the correlation between $[V]$ and $\bar{V}$ using Equation F-20.

Values of $\bar{V}_p$, $V_{p\,max}$, $V_{g\,(smoke)}$, and $V_{g\,(streak\,mode)}$ presented in Table F-1 are corrected for nonuniform velocity profiles and given in Table F-2 as values of $[V]$. $\bar{V}_p$ represents the average velocity of 100 streaks in the region shown in Figure F-2 and thus this value is corrected by Equation F-20. Values of $V_{p\,max}$ represent the largest particle velocities measured in the tubes. Since the largest gas velocity in the tube
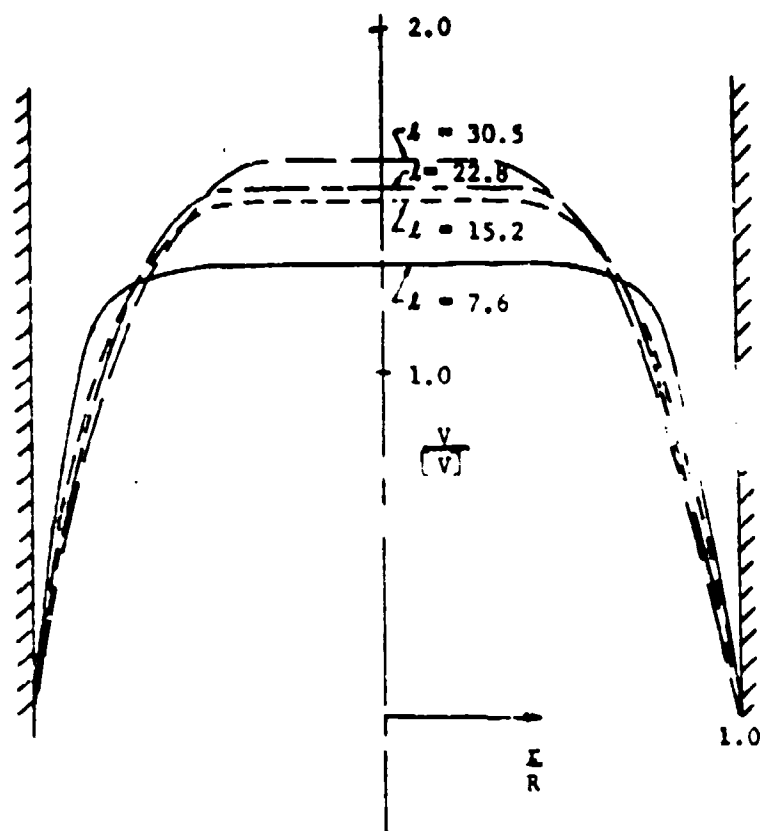
NOTE: l (length of tube) is in centimeters.

Figure F-4. Theoretical velocity profiles in cylindrical ducts of various lengths.

is V_o, these values are corrected by Equation F-19. Reduction of data for streak mode photographs and cloud velocities is not as well defined. Therefore this data is presented corrected by Equation F-19 and Equation F-20. Interpretation of these results is presented in a following section. Using the values of $[V_p]$ for the four tube lengths it is possible to estimate the particle acceleration by fitting an exponential curve to the results. Using the values $\mu_g = 0.78885 \times 10^{-3}$ g/cm sec and the density of aluminum (liquid) $\rho_g = 2.392$ g/cm, $[V_g]$ can be related to $[V_p]$ for different particle diameters. Results are shown in Table F-3.

Table F-2. Mean Velocities at the Exit of Four Tubes.

ℓ Tube length, (cm)	(1) $[V_p]$ from V_p (m/sec)	(2) $[V_g]$ from $\eta_{p\ max}$ (m/sec)	(3) $[V_g]$ (Eq. F-19) from streak mode or cloud (m/sec)	(4) V_g (Eq. F-20) from streak mode or cloud (m/sec)
7.6	9.02	16.21	12.31	14.50
15.2	9.80	13.66	11.15	14.14
22.9	10.19	1? 89	9.37	12.26
30.5	11.03	10.08	9.84	13.35

Tables F-2 and F-3 represent the current status of this research with respect to velocity measurements. Columns 2, 3, and 4 of Table F-2 represent estimates of the mean gas velocity at various distances from the burning surface. Column 1 of Table F-2 represents the average velocity of large condensed phase material at various distances from the burning surface. In order to calculate the gas velocity from the condensed phase material velocities, it is necessary to know the size (diameter) of the condensed phase material at various distances from the burning surface. At the

Table F-3. Mean Gas Velocities for 10-, 20-, 50-, 100-, and 200-Micron Particles

Tube length, (cm)	$[V_g]$ (D=0) (m/sec)	$[V_g]$ (D=10μ) (m/sec)	$[V_g]$ (D=20μ) (m/sec)	$[V_g]$ (D=50μ) (m/sec)	$[V_g]$ (D=100μ) (m/sec)	$[V_g]$ (D=200μ) (m/sec)
7.6	9.02	9.06	9.19	10.10	13.37	26.46
15.2	9.80	9.82	9.87	10.24	11.58	16.92
22.9	10.19	10.20	10.25	10.59	11.99	16.63
30.5	11.03	11.04	11.09	11.44	12.65	17.55

present time, particle collection techniques have not been refined so that the average particle diameter can not be determined experimentally with acceptable accuracy. Table F-3, therefore, uses the condensed phase material velocities from column one of Table F-2 to predict the gas velocity for various sized particles. For example, if subsequent tests indicate that the aluminum agglomerates have an average diameter of 100 microns at a distance of 7.6 cm from the burning surface, Table F-3 predicts a gas velocity of 13.37 m/sec.

F-4   Discussion of Results

In the previous sections, high-speed motion picture films of the plume of burning UTP 3001 have been used to estimate the mass average gas velocity at different distances from the burning surfaces. The velocities of large (burning aluminum agglomerates) and small (aluminum oxide smoke) particles of condensed phase material have been measured from the films and several analyses have been used to estimate average gas velocities based on the local condensed phase velocity.

There are still several areas of uncertainty for each measurement technique relating to three phases of the analysis, namely measurement of

condensed phase velocities, relationship between measured local average velocities and the mean velocities over the entire plume, and the relationship between condensed phase velocities and gas velocities. In the following sections, the areas of uncertainty for each of the individual measurement techniques and subsequent analyses will be discussed briefly and possivle improvements will be suggested.

F-4.1 Estimation of Gas Velocities from Average Condensed Phase Particle Velocities

Determination of the velocity of large (50- to 200-micron) agglomerates is quite accurate if camera speed is correctly averaged. However, when using Equation F-10 to relate velocities averaged over a restricted area to velocities averaged over the entire plume it is assumed that all streaks between the front edge of the tube and the centerline of the tube (or the back edge of the tube) are visible and measurable. While this is true for the 22.8- and 30.5-cm tubes where the back edge is visible, the background Al_2O_3 smoke is very bright in the 7.6- and 15.2-cm tubes and the depth of view cannot be determined. Because of this uncertainty, the extrapolation of local mean velocities to average mean velocities over the entire tube is only approximate. Further, the previously discussed difficulties in obtaining satisfactory experimental data on mean particle diameter as a function of distance from the burning surface precludes the determination of gas flow velocity using this technique at this time.

F-4.2 Estimation of Gas Velocities from Smoke Clouds

The principal difficulties with this method are in the determination of the distance a smoke cloud travels between motion picture frames and the relationship between smoke velocities and average gas velocities. As can be seen in Figure B-2, the edge of a smoke cloud is a somewhat vague gray region. Since it is difficult to def'~ a point or edge in any single motion picture frame there is a 'igree of ~icertainty in the distance this point travels between successive frames. In movies at the exit of 7.6- and 15.2-cm tubes, the background radiation is very bright and only very small (about 0.5 mm across) dark blotches, apparently near the edge of the tube,

could be observed. In this case, it seems appropriate to use Equation
F-20 to determine the average gas velocity since the smoke velocities re-
present local values. In the 22.8- and 30.6-cm-long tubes, the background
radiation is less intense and larger (~5 mm across) smoke clouds can be
seen. For larger clouds, near the center of the tube, the use of Equation
F-19 is correct since the visible leading edge would travel at V_0. The
smoke travels at gas velocity so there is no ambiguity in relating con-
densed phase material velocity to gas velocity.

F-4.3 Estimation of Gas Velocities from the Fastest Particle

It is difficult to conceive of a situation in which the condensed
phase material moves faster than the gas. Thus, this analysis simply
assumes that the fastest particle, $V_{p\ max}$, found in a movie is traveling
at the fastest gas velocity, V_0. Note that this velocity is not time
averaged since only one velocity is used for each tube. However, this
method seems to have the least uncertainty.

F-4.4 Determination of the Gas Velocity from Streak Movies

Using the Hycam camera in the streak mode presents several difficul-
ties. The film must be loaded emulsion side up and thus no timing marks
are printed on the film. Camera speed must be estimated from similar rolls
exposed with emulsion side down. Further, after focusing and aligning the
camera, it must be disconnected to load the film so that alignment with the
tube centerline is no longer assured. Further, since no distinct image is
formed on the film, it is not possible to determine what is being photo-
graphed--smoke or agglomerates. It should be noted that most of these
difficulties might be circumvented by the use of a special streak camera
rather than a Hycam with add-on attachments. In any event, this method
presents the most ambiguities with regard to results and is not recommended
for further consideration.

F-5 Conclusions

At the present time, the most plausible results seem to be the fastest
particle velocities. Using these results (column two from Table F-2) the

gas velocity as a function of distance from the burning surface is presented in Figure F-5. Bars are also given at each of the four locations to indicate the data spread from columns 2, 3, and 4 in Table F-2. Also presented are theoretical predictions from Section 7. It is seen that initial gas velocities appear correct, but due to heat loss through the tube walls the gas velocities in the tube tests decreases. The heat loss to the tube is very evident in the movies where the decrease in light intensity in longer tubes is significant. Subsequent tests should employ better insulation of the tube walls.
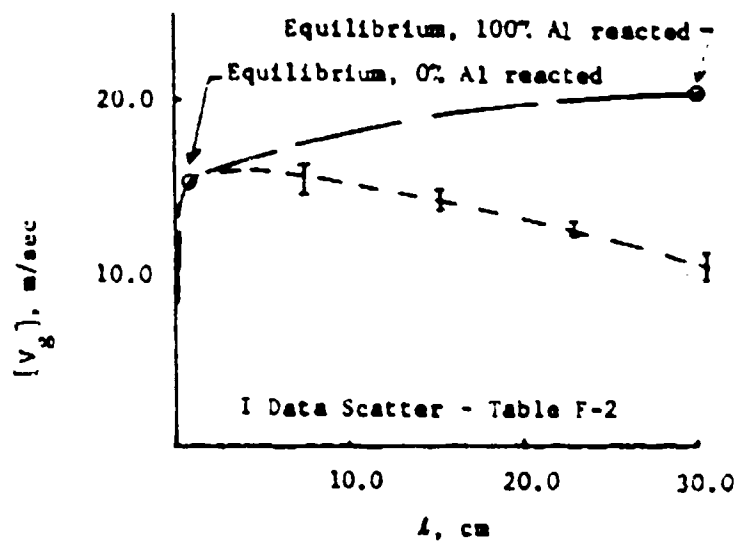
Figure F-5. Comparison of average gas velocity versus distance from burning surface as computed from equilibrium calculations and measured at the exit of 5-cm diameter tubes.

215

NOMENCLATURE

(Appendix F)

C_D Drag coefficient

D_p Diameter of particle

F Drag force

$F(\lambda)$ Function of λ

g Acceleration due to gravity

1 Tube length

m_p Particle mass

r Radial coordinate

R Tube radius

Rey Reynolds Number

t Time

T Temperature, $^{\circ}K$

V_g Gas velocity

V_0 Velocity at $r = 0$

V_p Particle velocity

$V_{p\ max}$ Fastest agglomerate streak found in motion picture

$\bar{V}_p$ Agglomerate velocities averaged over 25 motion picture frames

$\bar{V}_p$ Agglomerate velocity averaged over 100 motion picture frames

$[V]$ Mass average velocity, Equation F-10

y Distance away from burning surface

λ Transition parameter, Equation F-18

μ_g Viscosity of gases

ρ_p Density of particle

APPENDIX G

DROPLET POPULATION CALCULATIONS

G-1   Introduction

While this study did not cover the mechanism of aluminum and oxide droplet interaction with objects in the fire environment, the results of Section 4 and Appendix D showed the importance of impingement of droplets. This result is also observed in erosion of rocket motor components (Reference G-1). However, the impingement phenomenon and its effect on exposed objects are dependent on the composition, size and temperature of the droplets in the flow, and this in turn is dependent on the progress of burning of the aluminum droplets. Efforts to determine this information by experimental means are described in Section 11 and Appendix C. However, the unreliability of such experiments dictates a complementary effort to calculate the droplet populations. Such an approach has the advantage of producing a systematic framework with which to organize results and predict behavior, and also brings to bear a backlog of fundamental knowledge that augments the empirical results of direct measurement.

Calculation of droplet populations depends first on an experimentally determined aluminum droplet size population near the propellant burning surface, as described in the latter part of Appendix C. At this location, relatively little Al_2O_3 has formed, and the aluminum agglomerates are relatively easy to measure. Given this droplet size distribution, a burning rate law for the droplets is used in the following to calculate droplet diameters versus time, amount of aluminum remaining, amount of oxide formed, and oxide droplet distribution.

G-2   Burning of Individual Droplets

Various investigators have studied aluminum droplet combustion exper-

---

G-1.   Shchubin, V. K., A. I. Moronov, V. A. Filin and N. N. Koval'nogov, "Intensity of Heat Transfer Between Two-Phase Flow and Nozzle Walls as Function of Particle Motion Parameters," Izvestiya VUZ, Aviationnaya Tekhnika, Vol. 19, No. 1, 1976, pp. 109-114.

imentally and theoretically (e.g., References G-2, G-3, G-4, G-5). Most investigators report results in terms of a correlation between initial diameter and time to burnout, in the form

$$\tau_o = k \, D_0^{\, n} \tag{G-1}$$

While agreement on values of the parameters k and n are less than ideal, values of

$$k = 10^{-5} \, sec/(\mu m)^{1.75}$$

$$n = 1.75$$

seem reasonable for the present purposes (they are for τ in seconds, and D_0 in micrometers, and all the values were chosen to fit burning times observed in the present study).

It should be noted that Equation G-1 is usually intended to relate burning time to _initial_ droplet diameter. We will assume here that the equation holds for any time during the droplet burning, not just for D_0.

G-2. Davis, A., "Solid Propellants: The Combustion of Particles of Metal Ingredients," _Combustion and Flame_, Vol. 7, No. 4, December 1963, pp. 359-367.

G-3. Hartman, K. O., "Ignition and Combustion of Aluminum Particles in Propellant Flame Gases," _Chemical Propulsion Information Agency Publication 220_, Vol. I, November 1971, pp. 1-24.

G-4. Friedman, R., and A. Maček, "Combustion Studies of Single Aluminum Particles," from _Ninth Symposium (International) on Combustion_, Academic Press, 1963, p. 709.

G-5. Brzustowski, T. A., and Irvin Glassman, "Vapor-Phase Diffusion Flames in the Combustion of Magnesium and Aluminum: I. Analytical Developments; and II. Experimental Observations in Oxygen Atmospheres," AIAA Progress in Astronautics and Aeronautics, Vol. 15, _Heterogeneous Combustion_, Academic Press, New York, 1964, pp. 75-158.

Then

$$\tau = k\, D^n \qquad\qquad (G\text{-}2)$$

If the time to burn from D_0 to D is designated by t,

$$t = \tau_0 - \tau = k\,(D_0^{\,n} - D^n) = kD_0^{\,n}\,(1 - D^n/D_0^{\,n})$$

$$\frac{D}{D_0} = (1 - \frac{t}{kD_0^{\,n}})^{1/n} \qquad (t < kD_0^{\,n}) \qquad (G\text{-}3)$$

Equation G-3 describes the droplet diameter as a function of time from $t = 0$ at the start of burning, until $t = \tau_0$ at burnout. Variation of diameter with time is graphed in Figure G-1. As a matter for future discussion, it is worth noting that droplets burn out very rapidly after their diameters are down to 40% of initial value.

It is to be understood that, while the droplet is nearly spherical and mostly aluminum at $t = 0$, it is accumulating aluminum oxide during burning. In the usage here, the diameter, D, refers to an effective aluminum droplet size in the sense of correctly describing the amount of unreacted aluminum.[*] In addition there is accumulating oxide, which will be discussed later.

While the droplet diameters are usually the experimentally determined measures of droplet size, we are often concerned in practical problems primarily with droplet mass. This is given as a function of time from Equation G-3. Thus

$$\frac{m}{m_0} = (\frac{D}{D_0})^3 = (1 - \frac{t}{dK_0^{\,n}})^{3/n} \qquad (t < kD_0^{\,n}) \qquad (G\text{-}4)$$

---

[*]   If one were to seek improvement on this procedure, it would no doubt be necessary to go back to the assumption yielding Equation G-2 from Equation G-1; this would require information not presently available.
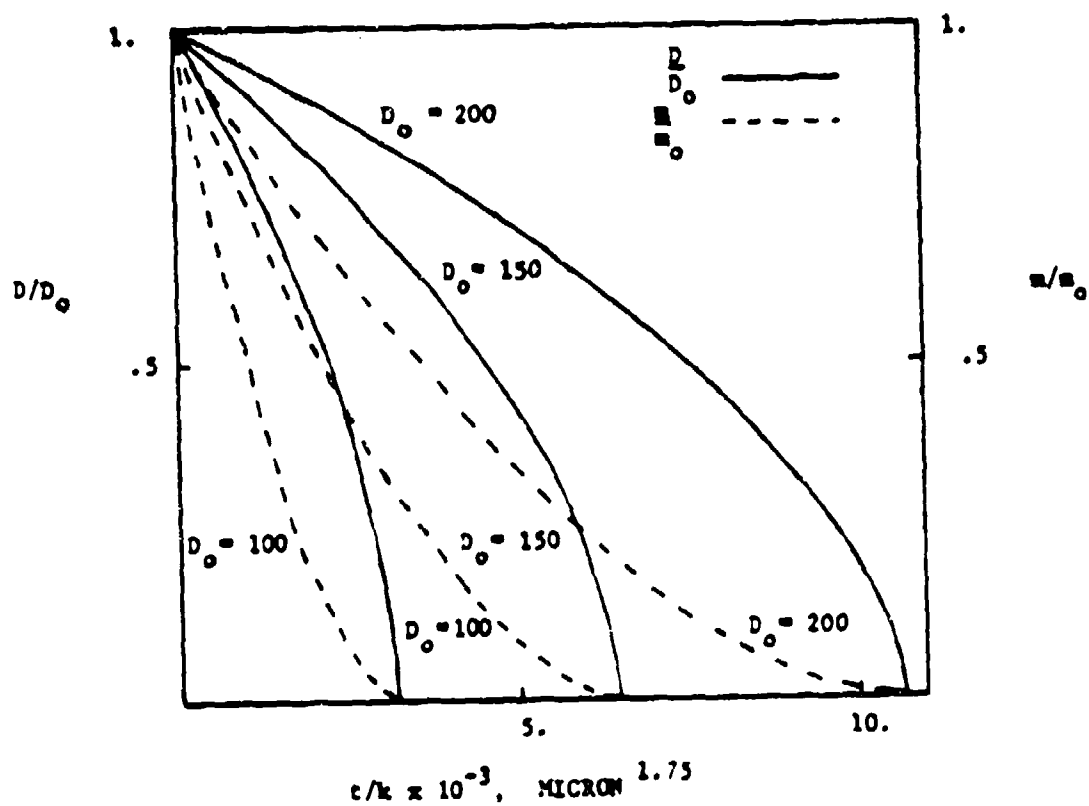
Figure G-1. Diameter and mass of burning droplets versus time. (Equations G-3 and G-6). (D_0 in μm).

The corresponding dependence of droplet mass fraction versus time burned is shown as the solid curves in Figure G-1.

G-3   Formation of Product Oxide

The qualitative nature of aluminum droplet combustion in propellant atmospheres is now established beyond doubt, and UTP 3001 is no exception. It is clear that fine oxide droplets (smoke) form in the detached flame about the droplet, and that oxide also forms on the droplet surface. At, or near the burnout of the aluminum droplet, the surface oxide forms one or more droplets of much larger size than those in the detached flame. These residual oxide droplets are small when formed from small agglomerates, larger when formed from large agglomerates. Since the large agglomerates are the last to burnout, the large residual oxide droplets are the last to form free of agglomerates. In the following we will be calculating the populations of these droplets, so it will be necessary to make some assumptions about them that may remain quantitatively argumentative. However, the assumptions are not critical to the calculations, in the sense that they will be represented by adjustable parameters.

The _first_, or _major assumption_ is that the smoke droplets form in a mass fraction α (smoke mass to total oxide mass), at all times. No detailed consideration will be given to smoke droplet size because it is so small that impingement is minimal. The residual oxide mass fraction is therefore $(1 - \alpha)$. Experimental results suggest that α ranges between 0.70 and 0.90 (Reference G-6).

The _second assumption_ is that surface oxide does not separate from the agglomerate, but forms η droplets of equal size upon burnout. At all times the residual oxide may be assigned an effective diameter for the purpose of defining the droplet size, but it is understood that its actual shape may vary greatly during burning of the agglomerate. After burnout,

---

G-6. Kraeutle, K. J., and H. H. Bradley, "Combustion of Aluminized Propellants: The Influence of Pressure and Propellant Composition on Formation of Aluminum Combustion Residue," _CPIA Publication 292_, Volume I, 1977.

the oxide droplets do become spherical. Their mass will then be

$$m_{oxr} = m_0 \left(\frac{102}{54} \right) \left(\frac{1-\alpha}{\eta} \right) \tag{G-5}$$

where 102/54 is the mass ratio of Al_2O_3 to its ingredient Al_2. The volume of the droplet is

$$\frac{m_{oxr}}{\rho_{Al_2O_3}} = \frac{m_0}{\rho_{Al}} \left(\frac{102}{54} \right) \left(\frac{1-\alpha}{\eta} \right)$$

and the diameter ratio of residual oxide droplet to parent agglomerate droplet is

$$\frac{D_{oxr}}{D_0} = \left[\frac{\rho_{Al}}{\rho_{Al_2O_3}} \frac{102}{54} \left(\frac{1-\alpha}{\eta} \right) \right]^{1/3} = \beta$$

$$= \left[1.38 \frac{(1-\alpha)}{\eta} \right]^{1/3} \tag{G-6}$$

In many of the later calculations, values of α and η will be assumed to be 0.20 and 1.0 respectively. The evidence indicates these assumptions for α and η to be reasonable. The result is a value of $D_{oxr}/D_0 = \beta = 0.65$.

G-4   Populations of Droplets

The microstructure of the solid propellant is an important factor in determining aluminum agglomerate size, and the disorder of the structure results in a wide range of agglomerate sizes. In Section 11 and Appendix C the size of these agglomerates was reported as a histogram representing numbers of droplets observed in certain diameter intervals (Figure 37a). It was noted that a normalized form of the histogram is more suitable for applications (Figure 51a). In general, one may assume that a histogram of

222

this kind represents a sample from a large population which is _characteristic of the propellant_. This large population can be represented by a frequency function $\mathcal{J}(D,t)$, such that

$$\frac{dN}{N_0} = \mathcal{J}(D,t)dD \qquad\qquad (G-7)$$

where dN/N_0 is the portion of all droplets in the size interval dD, or $\mathcal{J}$ is the portion of droplets per unit diameter. The functional notation $\mathcal{J}(D,t)$ means that $\mathcal{J}$, as a property of a droplet cloud moving away from the propellant surface, describes the number of droplets versus D, and means that the whole distribution changes with time (due to droplet burning). The experimentally determined initial droplet size distribution corresponds to $\mathcal{J}(D,t)$ evaluated at $D = D_0$ and $t = 0$, and will be denoted by $\mathcal{J}_0(D_0)$. Development of an initial distribution from an experiment is described in Section 12 and Appendix C, and the results are presented there for UTP 3001 propellant burning at atmospheric pressure.

If one were interested primarily in the effect of type of propellant or combustion environment, a comparison would be made of $\mathcal{J}_0(D_0)$, a function whose integral (area under the $\mathcal{J}, D_0$ curve) is always one, but whose shape reflects the size distribution. In the present investigation we are interested in how both $\mathcal{J}$ vs D and $\mathcal{J}dD$ change with time for our particular propellant, and will determine this in paragraph G-5 by imposing the droplet burning rate results of paragraph G-2 on the initial distribution of Section 12.

Recalling our practical concern with **mass**-size distributions, one may develop a mass-size distribution function corresponding to $\mathcal{J}(d,t)$.

$$\frac{dm}{m_0} = \frac{(\pi_0/6)\, D^3 dN}{(\pi_0/6)\int_0^{\infty} D_0^{\,3} dN_0} = \frac{D^3 \mathcal{J}(D,t)dD}{\int_0^{\infty} D_0^{\,3} \mathcal{J}_0(D_0) dD_0}$$

$$\frac{dm}{m_0} = F(D,t) = \frac{D^3 \mathfrak{J}(D,t)dD}{\int_0^\infty D_0^3 \mathfrak{J}_0(D_0)dD_0} \qquad (G-8)$$

Equation G-8 gives the mass-size distribution as a function of the number-size distribution function at any time that the latter is known, including time $t = 0$ when $D = D_0$, $dD = dD_0$, and $\mathfrak{J}(D,t) = \mathfrak{J}_0$. In Figure G-2, a Gaussian distribution curve is shown to represent $\mathfrak{J}_0$ versus D_0, and a second curve is shown that represents the corresponding mass-size distribution F_0 versus D_0. In the next section we examine how $\mathfrak{J}(D,t)$ can be related to the initial distribution $\mathfrak{J}_0$, through the burning rate law.

G-5   Change in Population with Time

In the combustion plume, the population of agglomerates changes due to burning as the agglomerates move out from the burning surface. We will assume that all size agglomerates move out at the same speed (not too good an assumption near the burning surface) (see Appendix F). If one follows a set of droplets dN in the size range designated dD, the number dN is constant, so from Equation G-7,

$$dN_0 = N_0 \mathfrak{J}_0(D_0) \, dD_0 = N_0 \mathfrak{J}(D,t)dD = dN \qquad (G-9)$$

where dN and dN_0 are the same droplets, so $dN = dN_0$ but $dD \neq dD_0$. From this relation the general distribution function can be expressed in terms of the initial distribution and Equation G-3. Thus

$$\mathfrak{J}(D,t) = (dD_0/dD) \, \mathfrak{J}_0(D_0)$$

From Equation G-3,

$$(dD/dD_0) = (1 - t/kD_0^n)^{(1-n)/n} \qquad (G-10)$$

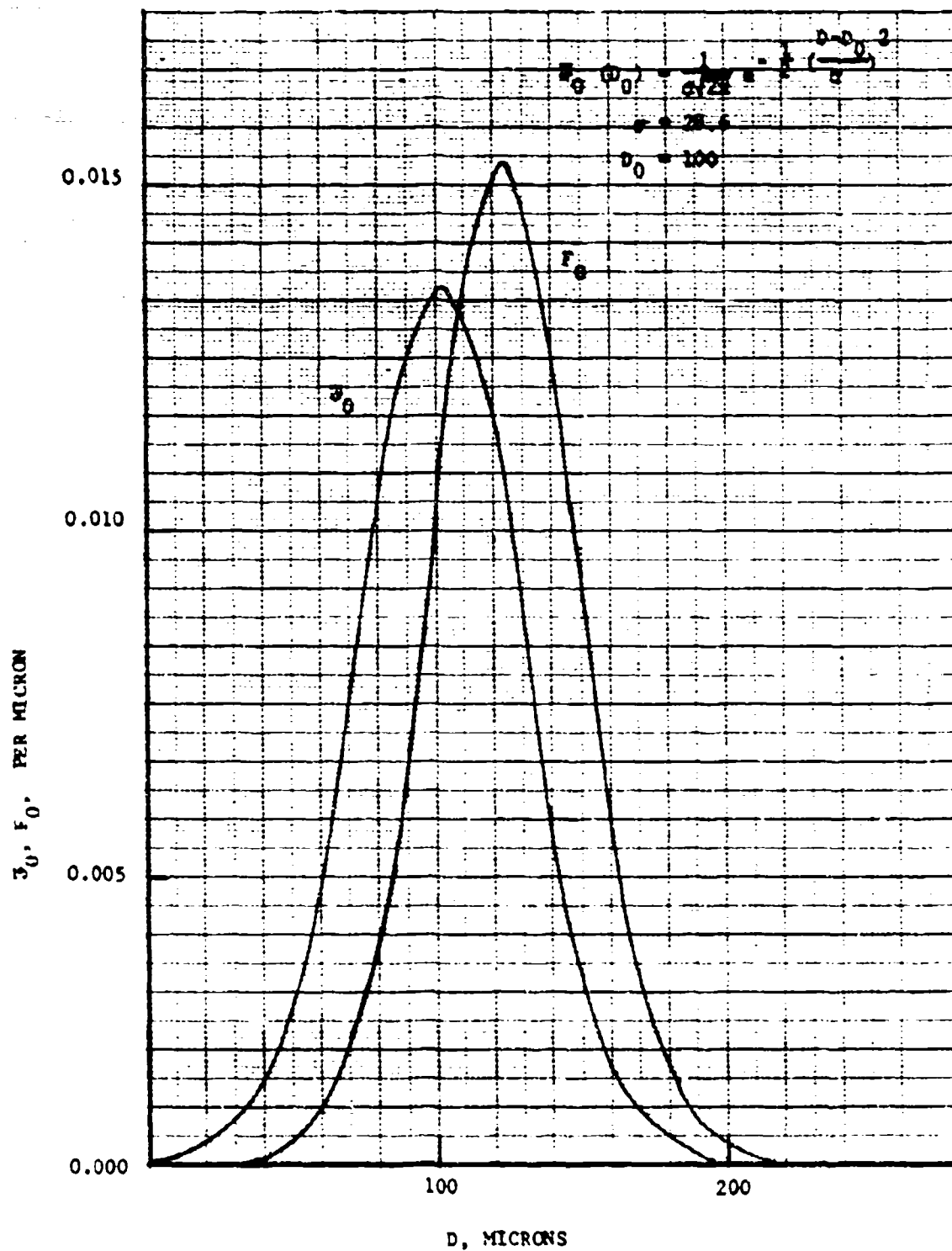$$\mathfrak{J}(D,t) = (1 - t/kD_0^n)^{(1-n)/n} \mathfrak{J}_0(D_0) \qquad (G-11)$$

224

Figure G-2. Distributions functions $\mathfrak{F}$ and F, where $\mathfrak{F}$ is chosen to be a Gaussian distribution of mean diameter. $D_0 = 100$ μm.

225

which, in combination with Equation G-3, gives $\mathfrak{F}(D,t)$ in terms of D_0, $\mathfrak{F}_0$ and t, and the parameters n and k of the burning rate law. This number-size distribution function is shown in Figure G-3a at several times during burning, using the Gaussian distribution in Figure G-2 as an initial distribution. A corresponding development based on the measured initial size distribution for UTP 3001 is shown in Figure 38a.

The mass-size distribution varies with time as indicated in Equation 8, which can be expressed completely in terms of initial distribution function time and D_0 using Equations G-3, G-8, and G-10, thus

$$\frac{dm}{m_0} = \frac{D_0^3 (1 - t/kD_0^n)^{\frac{3}{n} + \frac{n-1}{n}} \, \mathfrak{F}(D_0) \, D_0 (1 - t/kD_0^n)^{\frac{1-n}{n}}}{\int_0^\infty D_0^3 \mathfrak{F}_0(D_0) \, dD_0} \, dD_0$$

$$\frac{dm}{m_0} = F(D,t)dD = \frac{D_0^3 (1 - t/kD_0^n)^{\frac{1}{n}} \, \mathfrak{F}(D_0)}{\int_0^\infty D_0^3 \mathfrak{F}_0(D_0) \, dD_0} \, dD_0 \qquad (G-12)$$

Figure G-3b hows the variation in this mass-size distribution for the initial Gaussian distribution in Figure G-2. Figure G-3c shows the area under the population curves versus time, which amounts to a graph of mass fraction of aluminum unburned, versus time. The comparable curves for UTP 3001 are shown in Figures 38b and 39.

G-5   Product Oxide Population

In Section G-3, the qualitative nature of the product aluminum oxide droplets was described in terms of parameters α, β, and η, along with assumptions regarding physical behavior determining these parameters or implicit in the use of them. Briefly,

α = mass fraction of oxide in the < 2 μm-diameter range, characteristic product of the detached flame envelope (value roughly 0.7 to 0.9, assumed to be 0.8 in some calculations here).

226

$$3_0 = \frac{1}{6\sqrt{2\pi}} e^{-1/2} \left(\frac{D-\bar{D}_2}{6}\right)^2$$

$$6 = 28.57, \qquad \bar{D}_0 = 100 \qquad\qquad k = 10 \times 10^{-6} \; sec/micron^{1.75}$$
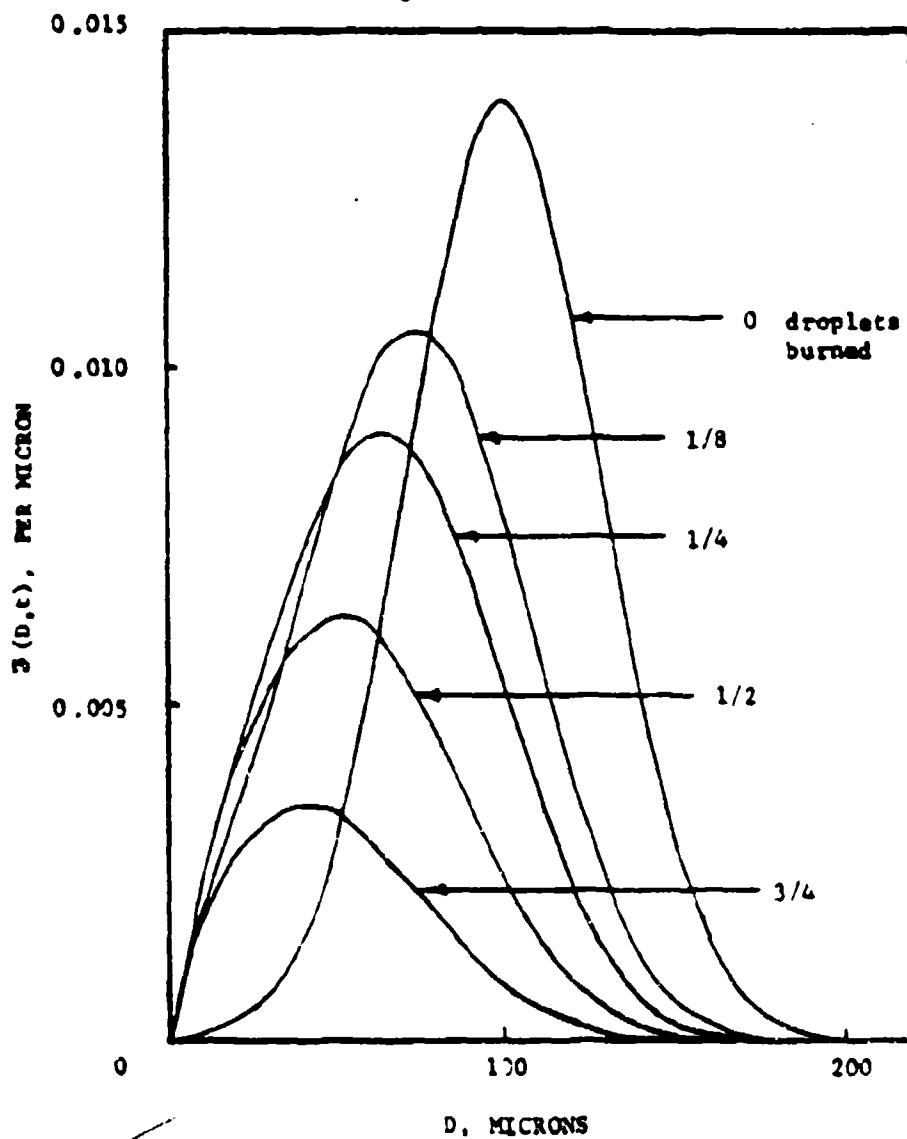

Figure G-3a. Change in number-size distribution with time for a Gaussian initial distribution.

227

$$m_o = \int_{-\infty}^{\infty} D_o^3 \, \mathcal{J}_o \, dD_o \qquad\qquad P_o = \frac{D_o^3 \mathcal{J}_o(D_o)}{m_o}$$

$$\mathcal{J}_o = \text{Gaussian Normal}$$

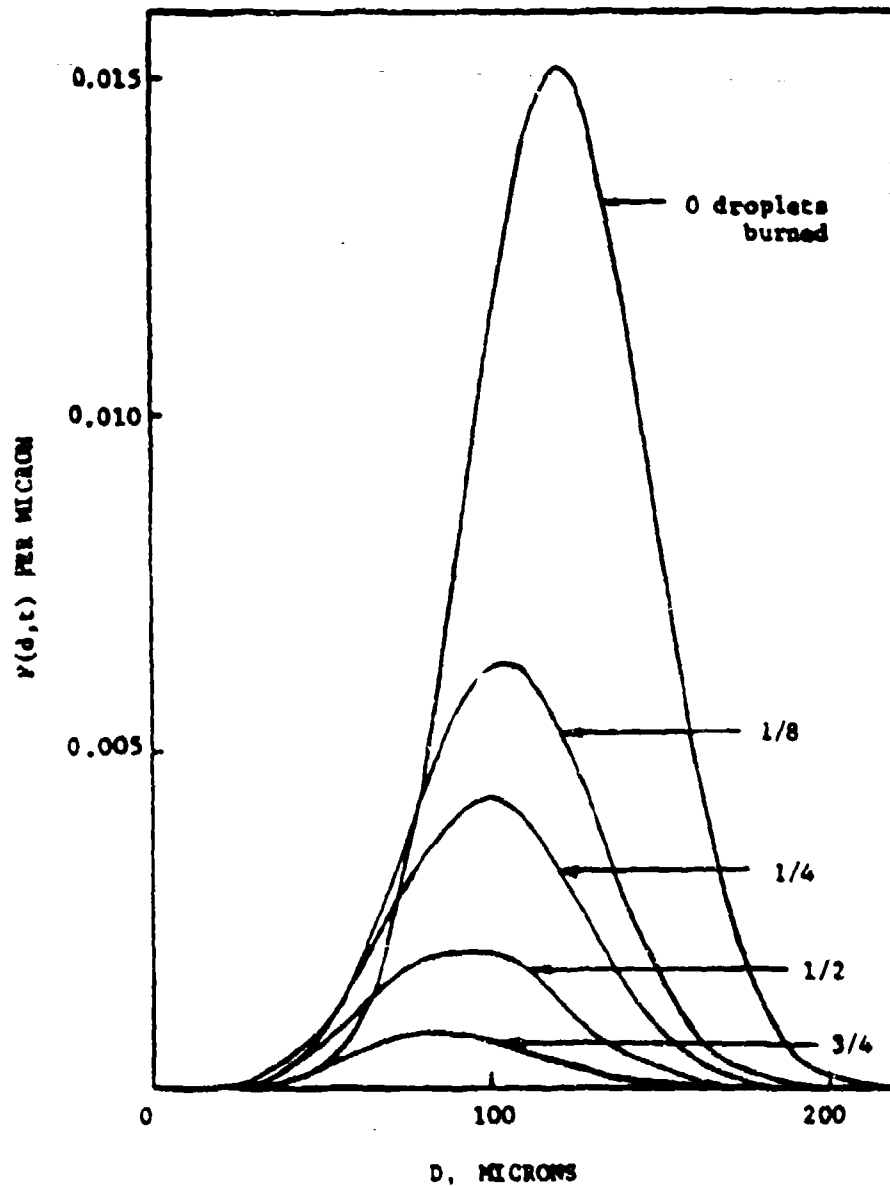$$n = 1.75 \qquad\qquad k = 10 \times 10^{-6} \ \text{sec/micron}^{1.75}$$

Figure G-3b. Change in mass-size distribution with time for a Gaussian initial number-size distribution as shown in Figure G-3a.
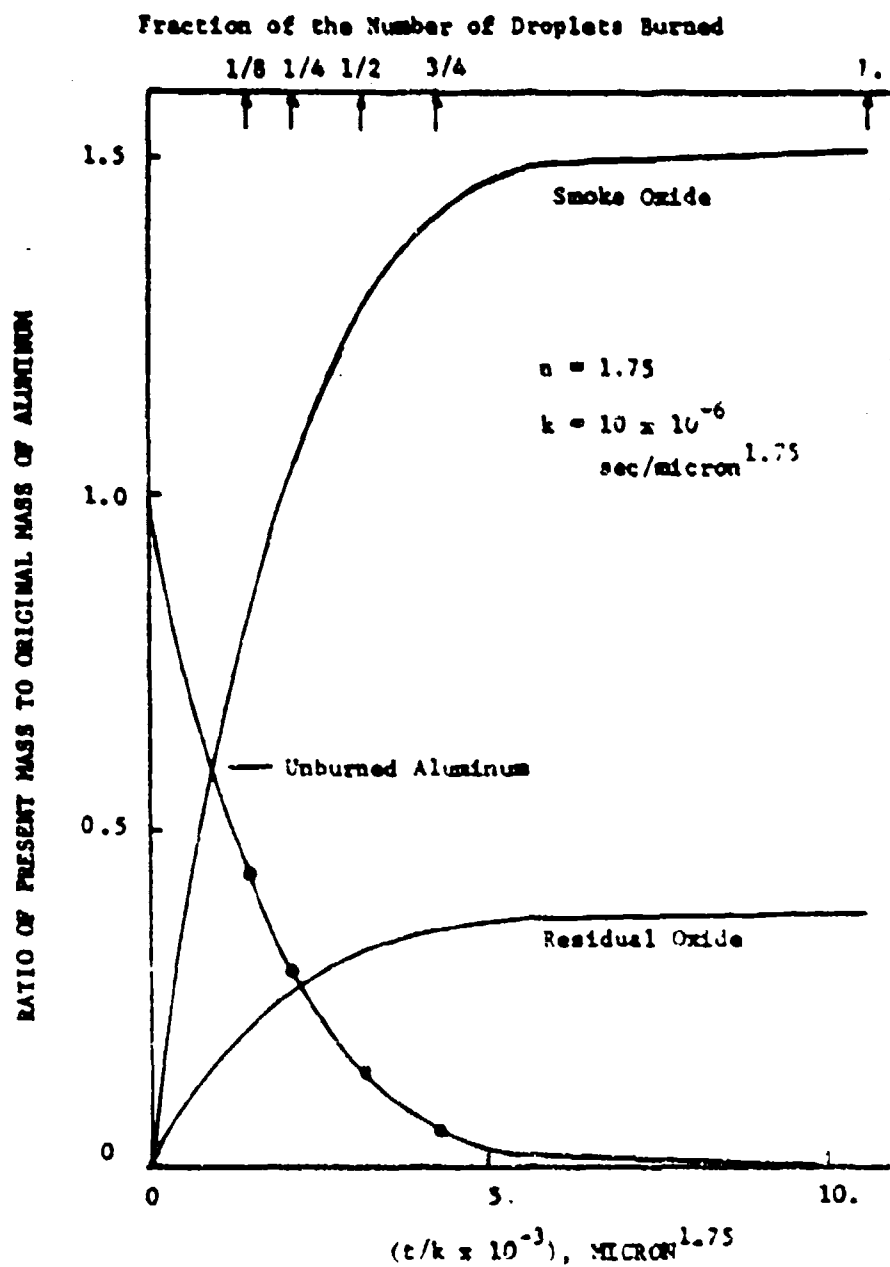
Figure G-3c. Mass fraction of droplets remaining for Gaussian initial population-size distribution and resulting oxide fraction in the smoke and residual form.

η = the number of the larger, surface-formed residual oxide droplets resulting from one aluminum droplet (assumed to be one in most calculations).

β = the diameter ratio of residual oxide droplet to parent aluminum droplet. (Usually for η = 1.0, when β = 0.65 when α = 0.8).

The correct values for α, β, and η for UTP 3001 (or any other propellant) are not known accurately. In the present work, efforts to determine these parameters by collection of droplets in the combustion plume were thwarted by low collection efficiency. However, the specific values of 0.8, 0.65 and 1.0 noted above were suggested by earlier work, and are compatible with the present results. Thus the product oxide can be described as consisting of 80% smoke droplets < 2 μm in diameter and 20% residual oxide > 2 μm in diameter.

Having developed the equations for the aluminum droplet population versus time (e.g., Equation G-12) the determination of _amount_ of oxide versus time follows from the calculations leading to Figure G-3c, and the above assumptions and definitions, that

$$m_{ox} = \frac{102}{54} (m_o - m) \qquad (G-13a)$$

$$m_{ox,S} = \frac{102}{54} \alpha (m_o - m) \qquad (G-13b)$$

$$m_{ox,R} = \frac{102}{54} (1 - \alpha)(m_o - m) \qquad (G-13c)$$

Figure G-3c shows how the oxide mass varies with time when the initial aluminum droplet size distribution is the Gaussian one in Figure G-1.

In Equation G-13b, these smoke oxide droplets are so small they follow the gas streamlines around objects in the flow with minimal impingement. Accordingly, no effort was made to determine their size distribution (it was verified that they were in the < 2-μm range). On the other hand, the residual oxide droplets are relatively large, and their size distribution will be considered in the following.

230

The most gross aspect of the residual oxide is the question (Equation G-13c) of how much is in the form of free oxide droplets and how much is still present as surface oxide on burning aluminum droplets. This question can be answered by examining how much of the initial aluminum population is burned out at a given time t, i.e., that part for which $D_0 < (t/k)^{1/n}$. Referring to Figure G-2, if the diameter corresponding to $D_0 = (t/k)^{1/n}$ is located, the droplets at lower D_0 have all burned out and the area under the F_0 curve to the left of this D_0 is the portion of the aluminum involved that has contributed to residual oxide droplets. This amounts to integrating the initial distribution function from $D_0 = 0$ to $D_0 = (t/k)^{1/n} = (t^*)^{1/n}$

$$m_{bo} = \int_{D_0=0}^{D_0=(t^*)^{1/n}} \frac{dm}{m_0} = \int_0^{D_0=(t^*)^{1/n}} F_0(D_0) \, dD_0 = \frac{\int_0^{} D_0 \mathcal{J}_0(D_0) dD_0}{\int_0^{\infty} D^3 \mathcal{J}_0(D_0) \, dD_0}$$

$$m_{oxr} = \frac{102}{54} (1 - \alpha) m_{bo}$$

(G-13)

The number-size distribution of residual oxide droplets (after all aluminum has burned) is, within limits of assumptions about α and η, determined directly by the initial aluminum droplet size distribution. Thus, if we define the number-size distribution by $\mathcal{J}_{ox}^*$, then

$$\frac{dN_{ox}}{N_0} = \mathcal{J}_{ox} (D_{ox}, t) \, dD_{ox}$$

---

* The subscript "ox" is used here to mean oxide after aluminum burnout, and refers to free residual oxide droplets. During aluminum burning an additional subscript will be used to distinguish residual oxide from that on the surface of aluminum droplets.

231

where dN_{ox} corresponds to residual oxide droplets in a diameter increment dD_{ox}, droplets that in turn correspond to a number $dN = (dN_{ox})/\eta$ of parent aluminum droplets of initial diameter D_0 in the diameter increment dD_0. The population $\mathcal{J}_{ox}(D_{ox})$ is related to the initial aluminum droplet population by

$$\mathcal{J}_{ox}(D_{ox},t)\ dD_{ox} = \frac{dN_{ox}}{N_0} = \eta\ \frac{dN_0}{N_0} = \eta\mathcal{J}_0(D_0)\ dD_0$$

or

$$\left.\begin{aligned}
\mathcal{J}_{ox}(D_{ox},t)\ dD_{ox} &= \eta\mathcal{J}_0(D_0)\ dD_0 \\[2mm]
D_0 &< (t/k)^{1/n}
\end{aligned}\right\} \qquad \text{(G-14a)}$$

The second (burnout) part of Equation G-14a provides the time-dependence of $\mathcal{J}_{ox}(D_{ox},t)$, with the __final distribution__ being given by taking large t so all aluminum droplets are burned out. To be useful, Equation G-14a must be modified or supplemented by a relationship between D_{ox} and D_0 such as that in Equation G-6, from which one may rewrite G-14a as

$$\left.\begin{aligned}
\mathcal{J}_{ox}(D_{ox},t) &= \eta/\beta\ \mathcal{J}_0(D_{ox}/\beta) \\[2mm]
D_{ox} &< (1/\beta)(t/k)^{1/n}
\end{aligned}\right\} \qquad \text{(G-14b)}$$

From this equation it is evident that the final residual oxide distribution function differs from the original aluminum droplet distribution by simple linear scale changes, illustrated in Figure G-4a for the Gaussian distribution for values of η and β of 1.0 and 0.65 respectively. Note that for times when the aluminum is not all burned out, not all of the final popula-
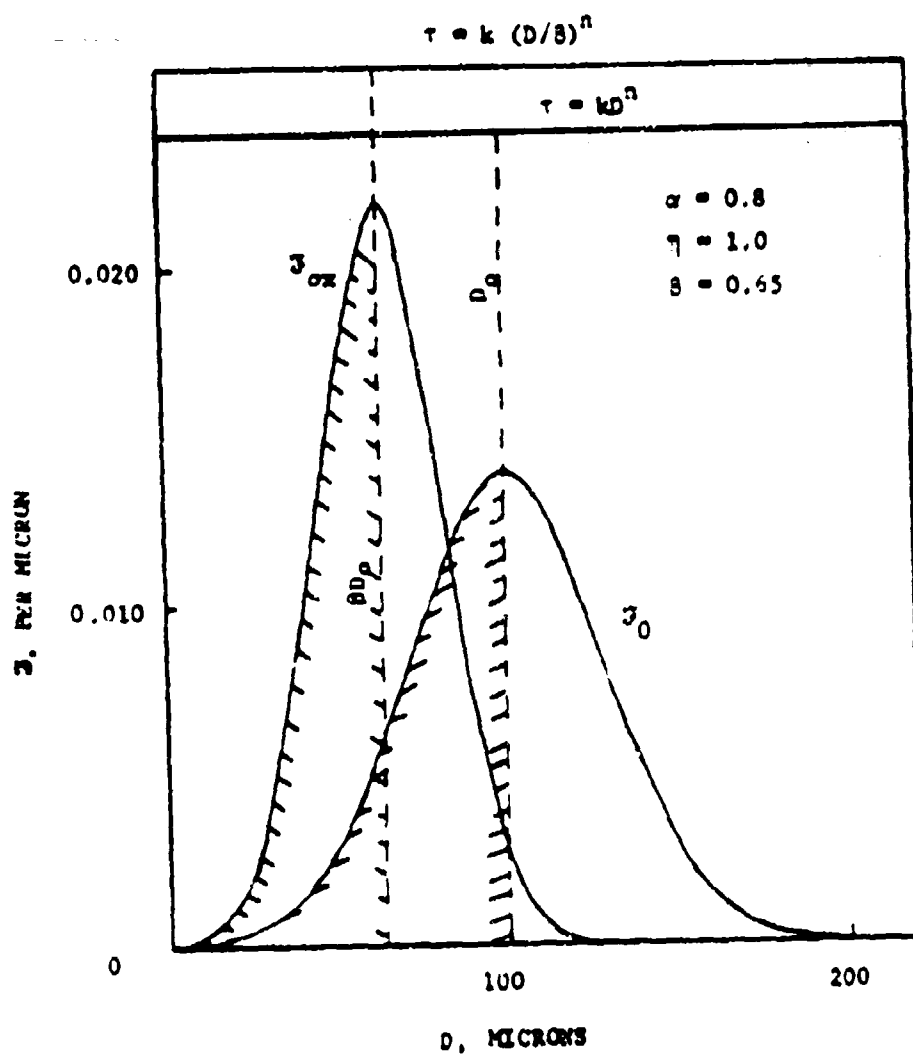
232

Figure C-4a. The number-size distribution for residual oxide and initial agglomerate population.
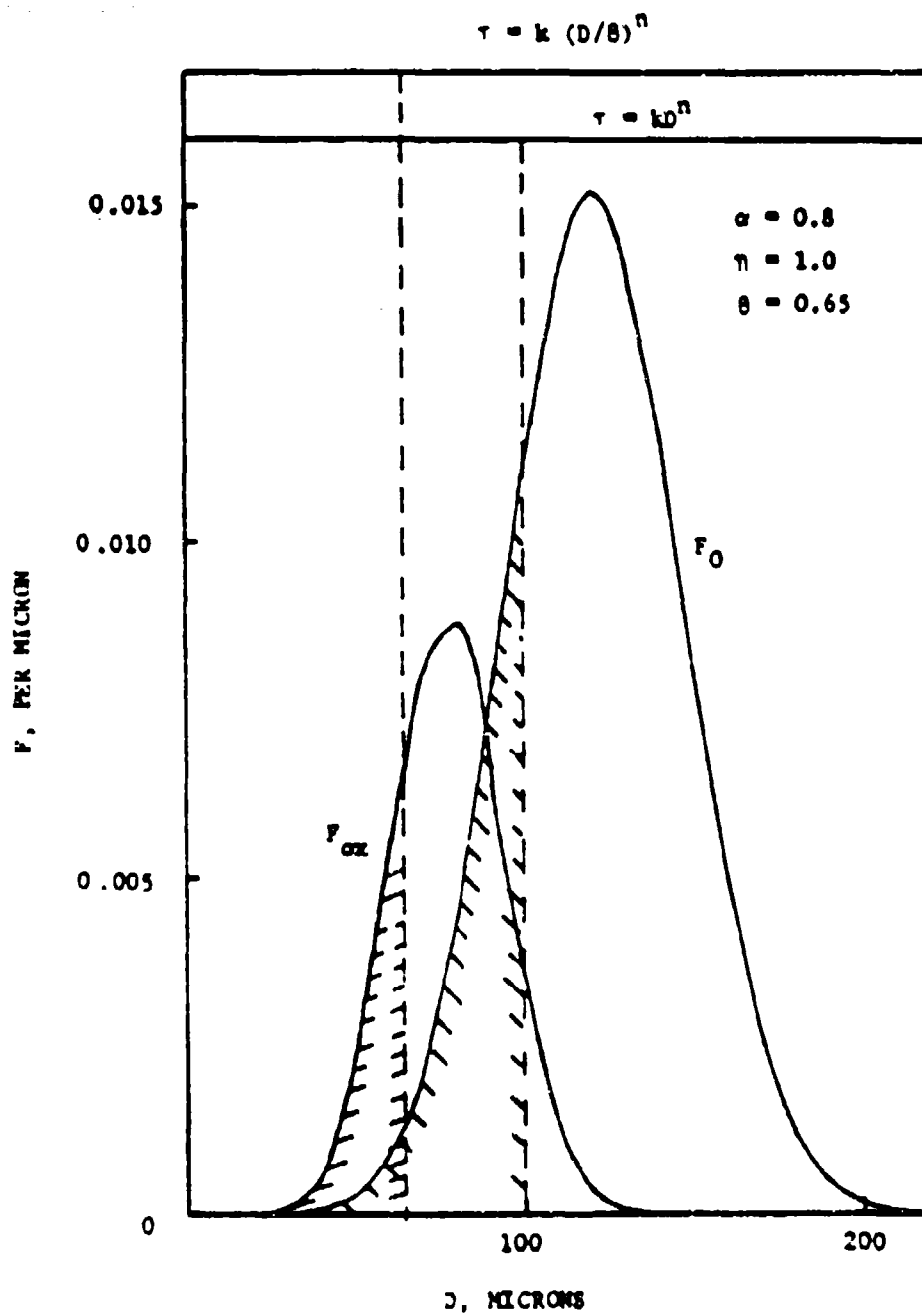
Figure G-4b. Mass-size distribution for residual oxide and initial agglomerate population.

tion of free oxide droplets is yet formed. In particular, the large drop-
lets, which form from initially large aluminum droplets, are not yet free
of the aluminum. Specifically, at a given time after the population left
the burning surface, the second part of Equation G-14b applies, and larger
droplets have not yet entered the population. This is illustrated by the
abscissa scale at the top of Figure G-4a, which allows one to find the por-
tion of the droplet population that applies at any time after the droplet
population starts burning.

The mass-size distribution of the residual oxide droplets can be
developed from the number-size distribution of the oxide or the initial
aluminum population, and will have the same size-cutoff time dependence
as the number-size distribution. Thus

$$F_{ox}(D_{ox}, t) = \frac{dm_{ox}}{m_o} \frac{1}{dD_{ox}} = \frac{(\pi\rho_{ox}/6) D_{ox}^3 dN_{ox}}{m_o dD_{ox}}$$

$$= \frac{(\pi\rho_{ox}/6)\beta^3 D_0^3 \eta dN_0}{\beta m_o dD_0} = \eta\beta^2 \frac{\rho_{ox}}{\rho} \frac{(\pi\rho/6)D_0^3 dN_0}{m_o dD_0}$$

$$= \eta\beta^2 \frac{\rho_{ox}}{\rho} \left(\frac{dm_o}{m_o} \frac{1}{dD_0} \right) = \eta\beta^2 \frac{\rho_{ox}}{\rho} F_0(D_0)$$

$$F_{ox}(D_{ox}, t) = \eta\beta^2 \frac{\rho_{ox}}{\rho} F_0 (D_0)$$

$$= \eta\beta^2 \frac{\rho_{ox}}{\rho} F_0 (D_{ox}/\beta)$$

$$D_{ox} < (1/\beta) (t/k)^{1/n}$$

(G-15a)

or from Equation 14 (or Equation G-12 with $t = 0$)

$$F_{ox}(D_{ox}, t) = \eta \beta^2 \frac{\rho_{ox}}{\rho} \frac{D_0^3 \mathfrak{J}_0(D_0)}{\int_0^\infty D_0^3 \mathfrak{J}_0(D_0) \, dD_0}$$

$$= \frac{\eta}{\beta} \frac{\rho_{ox}}{\rho} \frac{D_{ox}^3 \mathfrak{J}_0(D_{ox}/\beta)}{\int_0^\infty D_0^3 \mathfrak{J}_0(D_0) \, dD_0} \left. \right\} \qquad \text{(G-15b)}$$

$$D_{ox} < (1/\beta)(t/k)^{1/n}$$

Thus the residual oxide droplet population is described in terms of the original aluminum droplet population and certain approximations involving droplet combustion embodied in the parameters η and β. Reasonable estimates of these parameters are 1.0 and 0.65 respectively.

One more aspect of droplet distributions is the amount of surface residual oxide on burning droplets. As noted earlier, we have chosen to ignore this oxide in describing the aluminum population versus time. However, this oxide is expected to be a factor in impingement on objects in the combustion zone, and during part of the burning history of a population, involves more oxide mass than the free residual oxide population. In the following development, the surface oxide is assigned a diameter, in order to follow the formalism used for the other populations. However the diameter is simply a means of specifying mass without getting involved in describing the shape of the surface oxide. Thus, using the previous conventions on notation,

$$F_{oxs}(D_{oxs}, t) = \frac{dm_{oxs}}{m_0} \frac{1}{dD_{oxs}} = \frac{\pi \rho_{oxs}}{6} \frac{D_{oxs}^3 dN_{oxs}}{m_0 \, dD_{oxs}}$$

$$= \left(\frac{\rho_{oxs}}{\rho_{Al}} \right) \left(\frac{D_{oxs}}{D_0} \right) \left(\frac{dN_{oxs}}{dN_0} \right) \left(\frac{dD_0}{dD_{oxs}} \right) F_0(D_0) \qquad \text{(G-16)}$$

236

In this expression the ratio of dN_{oxs}/dN_0 will be taken to be 1.0, as it relates to the distribution of the surface oxide on the aluminum droplet and we are concerned only with total mass. The ratio of differentials can be calculated from D_{oxs}/D_0, so it remains to determine the relation of D_{oxs} to D_0 and time, which follows from Equation G-13c expressed in terms of diameter

$$\rho_{oxs}(D_{oxs})^3 = \frac{102}{54} \rho(1 - \alpha)(D_0^3 - D^3)$$

$$\frac{D_{oxs}}{D_0} = \beta' \left[1 - \left(\frac{D}{D_0} \right)^3 \right]^{1/3}$$

$$\frac{D_{oxs}}{D_0} = \beta' \left[1 - (1 - t/kD_0^n)^{3/n} \right]^{1/3} \qquad (G-17)$$

where β' is β (see Equation G-6) with $\eta = 1$, and Equation G-17 is the desired relation of D_{oxs} to D_0 and t. Now the ratio of diameter differentials in Equation G-16 can be obtained from Equation G-17, and when the results and Equation G-17 are substituted back in Equation G-16, one obtains

$$F_{oxs}(D_{oxs}, t) = \frac{(\beta')^{2/3} (\rho_{ox}/\rho_{A1}) \left[1-(1-t/kD_0^n) \right]^{3/n} \quad {}^{5/3} \quad F_0(D_0)}{\left[1-(1-t/kD_0^n)^{3/n} \right] -- (t/kD_0^n)(1-t/kD_0^n)^{3-n/n}}$$

$$D_0 = \left\{ \beta' \left[1 - (1-t/kD_0^n)^{3/n} \right]^{1/3} \right\}^{-1} D_{oxs} \qquad (G-18)$$

$$D_0 > (t/k)^{1/n}$$

This set of equations defines a mass-size distribution function for the

surface oxide, as a function of the initial aluminum distribution function F_0, a pseudo-diameter D_{oxs} (or real diameter D_0 of parent droplet), and time. The third equation in the set separates the droplets that are all oxide from the ones with aluminum still burning. In other words, the surface oxide corresponds to the larger droplets to the right of $D_0 = (t/k)^{1/n}$ in Figure G-4. However, the droplets are not fully developed yet, so the distribution function is below the final one, approaching it as in the sketch in Figure G-5.

G-6   Summary of Population Calculations

The population calculations start with an experimentally determined distribution of aluminum droplets leaving the burning surface,[*] and a burning rate law for droplets. From this the size distribution is calculated as a function of time, along with the total mass of aluminum remaining and oxide formed. In addition, the mass-size distributions of the product oxide droplets, and of accumulations on burning droplets are calculated versus time. Thus one knows the percent aluminum burned, and the size distribution of aluminum and oxide droplets and the amount of oxide attached to the aluminum droplets. This time dependence can then be converted into a spatial dependence by considering the velocity field (Section 7). From the standpoint of an object in the fire environment, this describes the physical character of the condensed material that may participate in impingement, heat transfer and further reaction. It also provides the information on percent aluminum burned, which is needed to use the thermochemical equilibrium calculations (Figures 5 and 6) to obtain estimates of gas composition, temperature, molecular weight, viscosity, etc. This sequential synthesis of results is outlined in Figure G-6.

---

[*] A Gaussian distribution was assumed in this Appendix; an experimental distribution was used in the corresponding calculations for the text.

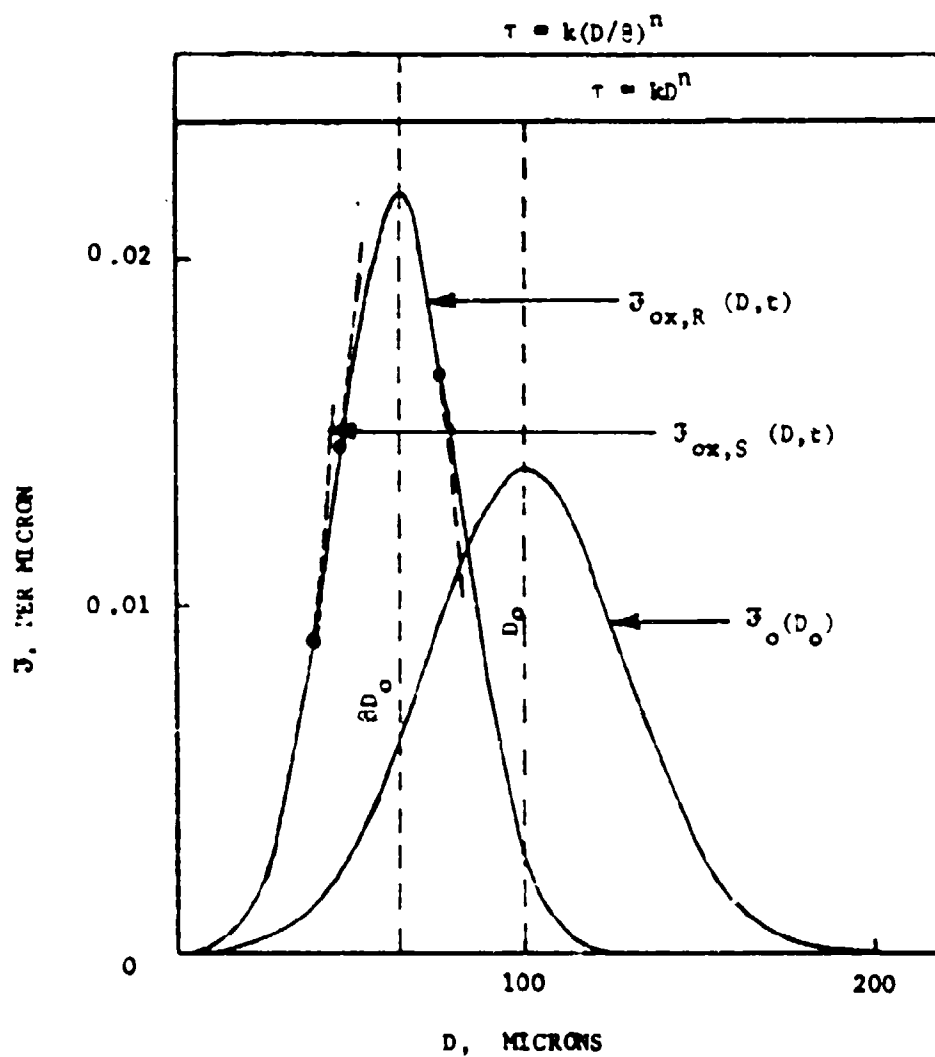Figure G-5. Approximate extensions of the number-size distri-
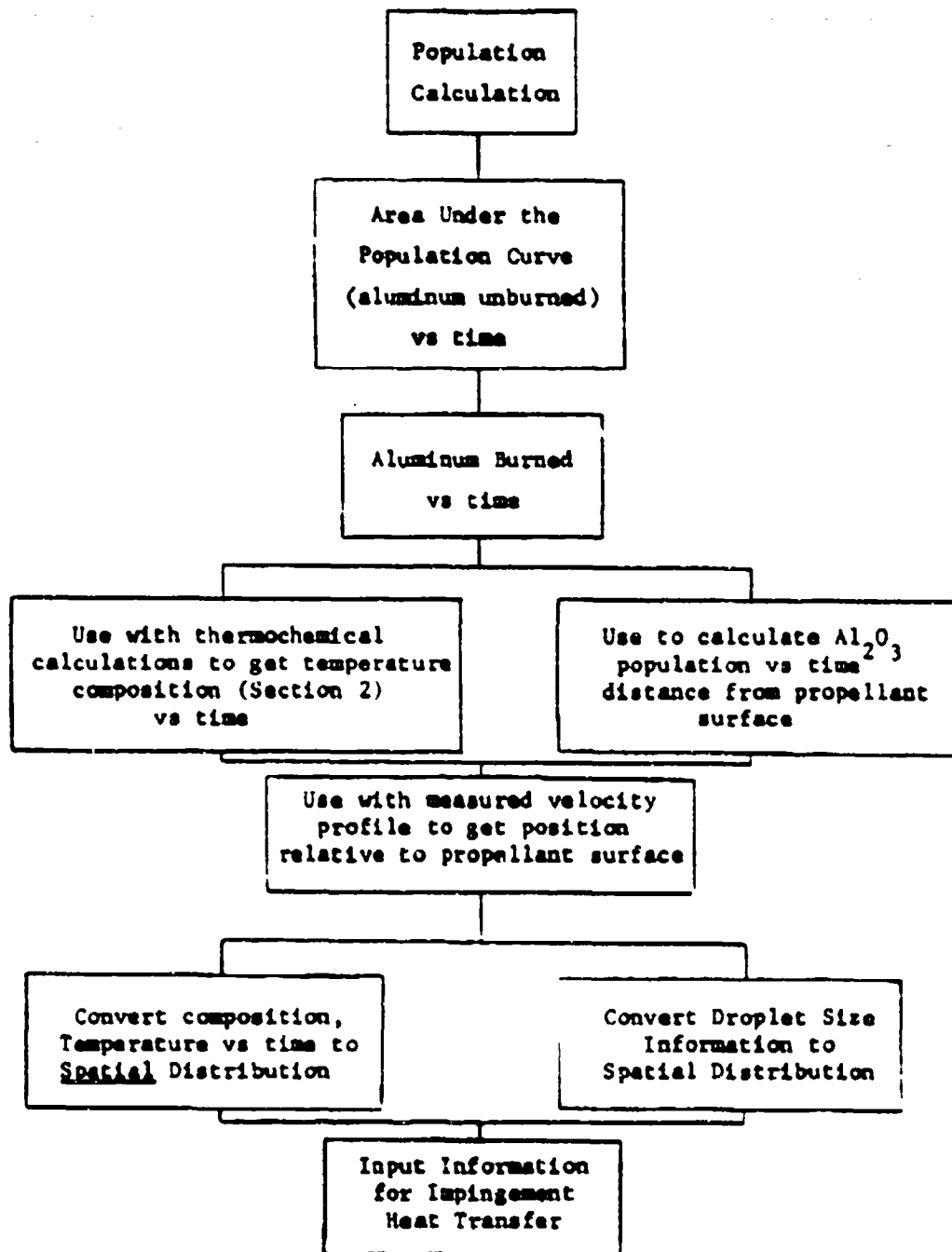bution curves to represent surface oxide distribution.

239

Figure C-6. Use of population curves brings together various
data to give spatial distribution of fire environment.

NOMENCLATURE

(Appendix C)

SYMBOLS

D   Diameter (of a droplet)

F   Mass-size distribution function; $F = dm/m_0 dD$

3   Number-size distribution function; $3 = dN/N_0 dD$

k   Coefficient in the droplet burning law $\tau = kD_0^n$

m   Mass of a droplet, or a set of N droplets; $m = \int_0^\infty dm$
        Refers to aluminum when no subscript

N   Number of droplets in a specified set or population

n   Exponent in the aluminum droplet burning law; $\tau = kD_0^n$

P,P'   Points on the population curve for $D = (t/kD_0^n)$.

t   Time (from start of burning of a droplet)

x   Distance from propellant burning surface

α Portion of oxide produced in smoke form

β Diameter of residual oxide droplet divided by diameter of parent
        aluminum droplet (for case of $\eta = 1$)

β' $= \eta\beta$

η Number of oxide droplets from each aluminum droplet

ρ Density; aluminum unless subscript

τ Burning time of aluminum droplet

SUBSCRIPTS

Al   Aluminum: mass and diameter without subscript, or with subscript
        0 are also aluminum

Al_2O_3 Aluminum oxide; usually denoted by subscript ox

bo   Refers to burned out material or state

0   Value at $t = 0$, the start of burning

ox   Oxide

oxR   All surface-formed or residual oxide

oxr   Oxide droplets free of the parent aluminum droplet

oxS   Smoke oxide (droplets < 2 μm)

oxs   Surface oxide still on the aluminum droplets

241

APPENDIX H
GAS ANALYSES

H-1   Objective

The chemistry effort of this project is divided into the following tasks:

   1. Development of a sampling device for the combustion of gases.

   2. Development of an analytical procedure for the analysis of the gaseous combustion produc s such as hydrogen, carbon dioxide, carbon monoxide, water, and volatile hydrocarbons.

   3. Plotting the relative concentrations of the above gases and vapors at different heights from the surface of the burning propellant and comparison of the experimental results with those of equilibrium calculations.

H-2   The Sampling Device

In designing a sampling device for the combustion gases we must take into consideration the conditions of the combustion. The combustion, for example, of the propellant sample is complete within a few seconds during which the gaseous sample must be collected. The temperature above the burning propellant is very high, and this limits the choice of materials that could be used. During the combustion of the propellant, large amounts of corrosive hydrogen chloride is produced from the decomposition of ammonium perchlorate.

The presence of the hydrogen chloride in the reaction gases makes it impossible to use any chromatographic method for their analysis, because it will destroy the chromatographic column and the detector. It is therefore very important that the hydrogen chloride be either excluded from the sample or be removed after the collection and before the analysis.

With these considerations in mind the following sampling device (Figure 52) was constructed. It consists of a glass ampule with a Teflon valve. The inlet of the ampule was packed with glass wool and it was connected into a stainless steel tubing packed with fritted stainless steel. Before sampling, the ampule is evacuated using a high vacuum pump, and then

242.

it is connected with the stainless steel tube through a Teflon sleeve.

Immediately before sampling, the stainless steel tube is flushed with helium to remove the air. The propellant sample is burned on the bottom of a stainless steel pipe placed vertically inside an exhaust hood.

During the combustion, the end is introduced into the center of the combustion effluent through an opening on the wall of the stainless steel pipe. Then the Teflon valve of the ampule is opened and a sample is drawn into the ampule. In order to stop any reaction between the components of the sample, the ampule is immersed in liquid nitrogen during sampling. Any base used to neutralize it such as sodium hydroxide or calcium hydroxide would also neutralize the carbon dioxide.

Successful removal of the hydrogen chloride was accomplished by filling the sampling ampule with powdered sodium oxalate according to the equation:

$$C_2O_4Na_2 + 2\ HCl \rightarrow C_2O_4H_2 + 2\ NaCl \qquad (H-1)$$
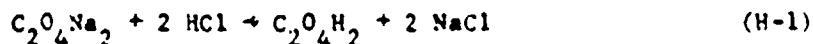
H-3   Analysis of the Gases

There are several methods available for the analysis of gases. The preferred one, however, is gas chromatography.

Preliminary testing indicated the presence of hydrogen, carbon monoxide, carbon dioxide and water in the combustion gases. Methane was found among the reaction products when the combustion of the propellant sample took place inside a phenolic resin pipe. Combustion inside a stainless steel pipe produced no methane or any other hydrocarbon.

From the beginning of the analytical work, it became obvious that in addition to the hydrogen, carbon monoxide, carbon dioxide and water, there were always present oxygen and nitrogen among the combustion products, in a ratio approximately that of air. Since there is no appreciable free oxygen expected in the combustion zone, it was concluded that the samples were contaminated with air. This affected the choice of subsequent procedures, as the analysis was now required to distinguish oxygen and nitro-

gen from other constituents.

Since the chromatographic column is responsible for the separation, the choice of the column was the most important decision in developing the methodology for the analysis of the gaseous products. There is no one single chromatographic column capable of separating all the combustion gases and air. Molecular sieves, for example, are very effective for the separation of hydrogen, oxygen, nitrogen and carbon monoxide. They absorb, however, the carbon dioxide and the water. The porous organic polymers, on the other hand, such as porapacks, do not absorb the carbon dioxide and the water, but the separation of the other gases is very poor, and the water peak is very broad and flat, difficult to quantitate.

To overcome all these difficulties, we decided to analyze the water separately from the permanent gases and to use a combination of chromatographic columns for the analysis of the gases.

Such a combination is a CTR column, available commercially from Alteck Associates. A CTR column is a combination of two concentric columns. The inner column has a 0.95 cm OD and it is packed with molecular sieve. The sample injected into the CTR column is split between the porapack and the molecular sieve columns. The portion of the sample entering the molecular sieve will be separated and will elute the H_2, O_2, and CO, followed by a peak due to CO_2. It is therefore possible to separate all the gases with one injection (Figures 53 and 54).

H-4   Determination of Water

The quantitation of the water in the combustion gases is complicated by the presence of hydrogen chloride.

There is also the danger of condensation of the water vapor on the walls of the sampling device.

An attempt was made to trap the water on anhydrous salts such as magnesium sulfate and then determine its amount by the weight gain of the salt. The results, however, were not consistent.

A chromatographic method, on the other hand, showed more promise. The sample glass ampule used to collect the combustion gases was

244

also used to collect a sample for the determination of water. However, instead of the sodium oxalate used to neutralize the hydrogen chloride, 5 grams of anhydrous barium hydroxide was added into the ampule. Before sampling, the ampule was heated to 120°C and was pumped overnight in a vacuum system.

The barium hydroxide neutralizes and removes the hydrogen chloride and the carbon dioxide from the gaseous products.

After sampling, the inlet of the ampule is plugged with a rubber septum and the ampule is heated again to 120°C in order to keep the water in the vapor phase.

A sample for chromatographic analysis is drawn through the septum with a syringe. The chromatographic column used for the quantitation of water was a 2 m x 0.95 cm chromasorb 104. The water elutes out of the chromosorb after the gases, and as a rather sharp peak which can be easily quantitated. The results, however, of the water determination were not very reproducible. This may be due to an observed tendency for the water to condense inside the stainless steel tube of the sampling device. The reproducibility of the injected volume of sample into the GC is also questionable since the sample is drawn at 120°C into a syringe of much lower temperature. Further refinements in the experiment will be required before a valid comparison can be made of water concentration in samples from different sites in the combustion plume.

H-5   Determination of Amount of Unreacted Aluminum in Samples Collected from the Plume

The progress of aluminum combustion can be most directly determined by simply intercepting, quenching, collecting and analyzing the condensed material at different locations in the plume. The samples that were collected were examined in many ways (see Appendix C), but the aluminum content in particular was examined by two methods. The first was reaction of the aluminum by HCl and rinsing to remove the dissolved products. Comparison of dried sample weights before and after such processing showed a weight loss corresponding to the unreacted aluminum weight of the original sample. This method, and results, are described in Appendix C.

The second method of determining aluminum weight was contrived to circumvent the fact that some Al_2O_3 reacts with HCl during the previously described test (possibly a negligible amount). The second method measures the gas formed by the HCl reaction. This method depends on the reaction scheme

$$2Al + 6 HCl \rightarrow 2AlCl_3 + 3H_2 \qquad (H-2)$$

$$Al_2O_3 + 6 HCl \rightarrow 2AlCl_3 + 3H_2O \qquad (H-3)$$
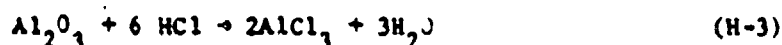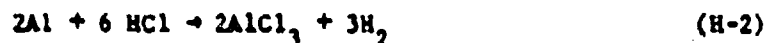
Although both aluminum and Al_2O_3 yield $AlCl_3$ when dissolved by HCl, the aluminum metal also yields hydrogen gas, whereas the Al_2O_3 yields water. Measurement of the volume of hydrogen produced from a known amount of sample will enable us to calculate the amount of aluminum in the sample from Equation H-2.

Using the second method, a very simple device was used for the dissolution of the aluminum and collection of hydrogen gas.

The aluminum sample was trapped inside a glass fiber filter and placed inside a 100-ml burette graduated to 0.1 ml. Then the burette was filled with hydrochloric acid diluted 1 to 3 through a reservoir connected to the tip of the burette with a plastic tubing. The top of the burette was plugged with a rubber septum.

As the aluminum dissolved and hydrogen gas is produced, the surface of the liquid in the burette moved down. The reservoir was lowered from time to time in order to keep its surface on the same level with the liquid inside the burette. It took 75 minutes for the reaction to be completed.

The volume of the hydrogen was read on the burette at the ambient temperature. Then it was corrected for the pressure of the water vapor inside the burette and it was converted into a volume under standard conditions of 1 atm and $0°$ Kelvin.

The amount of aluminum corresponding to a certain correct volume of hydrogen was calculated from Equation H-2 from which resulted in

246

$$1.12 \text{ ml } H_2/\text{mg Aluminum}$$

This procedure for determing aluminum content in a sample was judged to be practical, but was not used extensively because the method described in Appendix C was preferred.